GEOCHEMISTRY OF HAWAIIAN DREDGED LAVAS

by

PHILIPPE C. GURRIET
Ingénieur, Ecole Nationale Supérieure de Géologie
(1984)

SUBMITTED IN PARTIAL FULFILLMENT
OF THE REQUIREMENTS OF THE
DEGREE OF

MASTER OF SCIENCES
IN EARTH AND PLANETARY SCIENCES

at the

MASSACHUSETTS INSTITUTE OF TECHNOLOGY
May 1988

Signature of Author _____
Department of Earth and Planetary Sciences

Certified by _____
F. A. Frey
Thesis Supervisor

Accepted by _____
W. F. Brace
Chairman, Department Committee

GEOCHEMISTRY OF HAWAIIAN DREDGED LAVAS

by

PHILIPPE C. GURRIET

Submitted to the Department of Earth and Planetary Sciences
on May 5, 1988 in partial fulfillment of the
requirements for the Degree of Master of Science in
Earth and Planetary Sciences

ABSTRACT

40 tholeiitic basalts dredged off the main island of Hawaii are analysed for major and trace element abundances and radiogenic isotope ratios. The major element variability of these lavas is controlled by a typical Ol–Ol+Plag–Ol+Plag+Cpx paragenesis associated with variable amounts of clinopyroxene fractionation, and massive accumulation of non-equilibrium olivines. Individual volcanoes are characterized by different incompatible trace element ratios (*e.g.* La/Zr) and isotopic ratios. In particular, samples from Mauna Loa rift zone define two separate groups that vary in trace element ratios beyond what was ever seen in subaerial lavas. Although these Mauna Loa lavas trend toward Kilauea, they are not mixtures of recent Kilauea and Mauna Loa compositions. Overall, compositional differences between Hawaiian tholeiitic shields require heterogeneities in their source material that are not understood yet.

Thesis Supervisor: F. A. Frey, Professor of Geochemistry

Pour Valérie

ACKNOWLEDGEMENTS

I express my sincere gratitude to Fred for his scientific expertise and personal support.

I also thank Eric for one night of hard work.

TABLE OF CONTENTS

1. INTRODUCTION

A characteristic of Hawaiian lavas is a wide compositional variability confined to a small area. This variability is two fold. First, intravolcano differences in the traditional sequence of eruption stages (tholeiitic, pre-erosional alkalic and post-erosional alkalic) are expressed in major element and trace element abundances and ratios, and radiogenic isotope ratios. These differences have been modeled using a homogeneous source (Feigenson *et al.*, 1982) or a variable proportion mixture of distinct source materials (Chen and Frey, 1985). Physical models (*e.g.* Gurriet, 1986) involving a "plume" component mixing with incipient melts from the heated lower lithosphere provide support for the mixing model. Also, the homogeneous source model is not consistent with the systematic variations in isotopic ratios between lavas from the different volcanic stages. In contrast, systematic intervolcano differences in the abundant shield building tholeiitic lavas seem to reflect heterogeneities in their source material (Wright, 1971; Tilling *et al.*, 1979; Budahn and Schmitt, 1985; Rhodes, 1983). This apparently simple explanation raises profound questions on: (1) the mechanisms of volcanic eruptions in Hawaii. In particular, how do erupting melts consistently preserve source characteristics on a lengthscale of a few tens of kilometers (*e.g.* Mauna Loa systematically lower in TiO_2 than Kilauea) after

their extraction through the lithosphere, and (2) the processes responsible for the creation of these compositionally distinct sources.

Because most studies of Hawaiian volcanoes, except for Loihi, have been on subaerial samples, our present knowledge is limited to the upper 10% of the volcanic edifice. This restricted sampling also biases the age range of the samples studied. For example, Mauna Kea and Hualalai volcanoes are completely covered by post-shield volcanism. In order to obtain samples formed at earlier stages of volcano growth, we studied 40 submarine samples dredged around the big island of Hawaii. The objectives of this work are: (1) to document variations in major elements, trace elements and radiogenic isotope ratios in submarine lavas and compare them to the data set for subaerial lavas, (2) to evaluate the role of partial melting, crystal fractionation and other petrological processes responsible for the chemical variability of these rocks, and (3) to identify and attempt to explain composition differences required in the source regions of different Hawaiian volcanoes.

2. SAMPLING AND ANALYTICAL TECHNIQUES

The samples were recovered by dredging the main rift zones associated with the five volcanoes of the big island of Hawaii (Figure 2.1). Glassy rims of the pillow basalts were selected for rare gas analysis and electron microprobe studies (Lupton and Garcia, respectively). In most cases, because of the small quantities of glass available, crystalline material adjacent (within a few cm.) to the glassy rims was used for whole-rock major element, trace element and isotope analysis. It is assumed that the glass is chemically equivalent to the groundmass in the corresponding whole rock. Each sample was broken into 1 cm. sized chips that were hand picked to exclude altered zones and crushed to powder in a tungsten carbide shatter box at the University of Hawaii. Also, samples ML4–3, ML4–9, ML4–22 and duplicates of ML4–10 and ML4–11 were crushed separately in an agate shatterbox at MIT and are labeled with an asterisk (*e.g.* ML4–3*) throughout this study.

Major element abundances were obtained by X-Ray fluorescence (XRF) on fused disks at the University of Massachusetts, with BHVO-1 included as a standard in each run of 4 samples. The precision given by replicate analysis (10) of BHVO-1 is better than 0.1% relative error for SiO_2, Al_2O_3, Fe_2O_3, CaO and TiO_2, and better than 0.5% relative error for MgO. The reported values for Na_2O, rare earth

elements, Hf, Ta, Sc, Co and Cr were determined by instrumental neutron activation (INAA) at MIT with a precision that can be estimated by replicate analysis (3) of sample ML1–1 (Table 2.1). The elements V, Ni, Zn, Ba, Zr, Nb and Sr were analysed for by XRF (Au tube) at the University of Massachusetts with a precision based on replicate analyses of BHVO-1 (included in each run) and reported in Table 2.2. These data were obtained in two different batches separated in time by a major overhaul of the trace element XRF apparatus. Therefore, the statistics were determined on the two different sets of rocks and compared. Significant differences (at the 3σ level) exist between the two means for all the elements except Nb (Table 2.2). Rb, Sr, Ga and Y abundances were also determined by XRF (Mo tube) in a single batch at the University of Massachusetts with a precision based on replicate analyses of BHVO (Table 2.3). Mo tube and Au tube XRF analysis for Sr are associated with a similar precision (Table 2.2 and 2.3) and yield very close results. We arbitrarily chose to report Sr values from Au tube analyses. A comparaison between sample ML4–10 and sample ML4–10* analyses is presented in Table 2.4 in order to evaluate the possibility of contamination during the grinding process in a tungsten carbide shatterbox. Co and Ta abundances are significantly affected and vary by 18 and 79 σ-units respectively from one analysis to the other. The variation in Sr concentrations gives an estimate of the agreement between isotope dilution (ML4–10) and XRF Au tube (ML4–10*) measurements. The discrepancies in Eu and Ce values expressed in σ-units can be interpreted by the fact that our analytical σ for Eu (.78% relative error in the mean; Table 2.1) may be underestimated;

also, Ce values are the poorest of all rare earth elements analysed by INAA. The duplicates agree within less than one σ-unit for all remaining elements except Zr, Hf and Nb for which the variation is of the order of 1.7σ-unit (*i. e.* the 91% confidence level).

Finally, abundance of Rb and Sr were determined on a subset of unleached samples (mainly Mauna Loa) by isotope dilution, and the ratios of $^{87}Sr/^{86}Sr$ and $^{143}Nd/^{144}Nd$ by mass spectrometry at MIT following the techniques described by Hart and Brooks, 1977, for Rb-Sr and Zindler, 1980, for Sm-Nd. Within run statistics (2σ) are usually better than 0.005% for isotope ratios. All reported values are corrected to the Eimer and Amend SrCO3 standard (87/86=.70800) and BCR-1 (143/144=.51264). Error bars, when present in our diagrams, always refer to $\pm 1\sigma$ for trace element concentrations or ratios, and $\pm 2\sigma$ for isotopic ratios.

TABLE 2.1

INAA PRECISION. SAMPLE ML1–1

	anal. 1	anal. 2	anal. 3	σ	$\sigma/\sqrt{N}$	% error
Na_2O	1.55	1.54	1.50	.026	.015	1.0
Hf	2.29	2.28	2.16	.072	.042	1.8
Ta	2.20	2.25	2.20	.029	.017	.76
Sc	22.85	22.55	21.98	.442	.255	1.16
Co	105.2	105.5	101.8	2.06	1.19	1.18
Cr	1006	1005	985	11.85	6.84	.68
La	5.73	5.61	5.48	.125	.072	1.29
Ce	16.0	16.8	15.5	.656	.379	2.37
Nd	10.9	10.4	10.1	.404	.233	2.22
Sm	3.19	3.25	3.00	.13	.075	2.43
Eu	1.126	1.148	1.119	.015	.009	.78
Yb	1.41	1.44	1.49	.044	.023	1.61
Lu	.203	.189	.183	.010	.006	3.12

TABLE 2.2

XRF ANALYSES (AU TUBE) FOR BHVO

	April 1986 (8 values)			May 1987 (7 values)		
	mean	$\sigma/\sqrt{N}$	% error	mean	$\sigma/\sqrt{N}$	% error
Nb	18.90	.19	1.00	18.87	.11	.59
Zr	182.70	.69	.38	180.37	.40	.22
Sr	408.33	.76	.19	402.44	.85	.21
Ni	115.47	.59	.51	133.04	2.44	1.89
V	289.61	.79	.27	284.73	1.82	.64
Ba	140.11	1.87	1.34	129.94	3.75	2.88

TABLE 2.3

XRF ANALYSES (MO TUBE) FOR BHVO

	mean	σ	$\sigma/\sqrt{N}$	% error
Rb	8.85	.31	.09	.97
Sr	391.29	1.66	.46	.12
Ga	21.19	.56	.16	.74
Y	24.86	.23	.06	.26

TABLE 2.4

VARIATIONS BETWEEN DUPLICATE

ML4–10 AND ML4–10*

	abs.Δ	rel.Δ (%)	σ	Δ/σ
Ni	4.4	.30	6.46	.68
Cr	11.0	.56	11.85	.93
Sc	.26	.51	.44	.59
V	4.7	1.11	4.81	.98
Co	36.9	21.12	2.06	17.91
Rb	.04	.51	.31	.13
Sr	6.27	1.43	1.66	3.78
Ba	5.00	4.85	9.92	.50
Zr	1.70	.87	1.05	1.61
Nb	.90	6.29	.54	1.67
Hf	.14	3.00	.08	1.75
Ta	2.36	72.84	.03	78.67
La	.02	.16	.12	.16
Ce	.9	2.55	.66	1.36
Nd	.1	.42	.40	.25
Sm	.04	.58	.13	.31
Eu	.04	1.60	.015	2.67
Yb	.01	.32	.044	.23
Lu	.01	2.22	.01	1.0

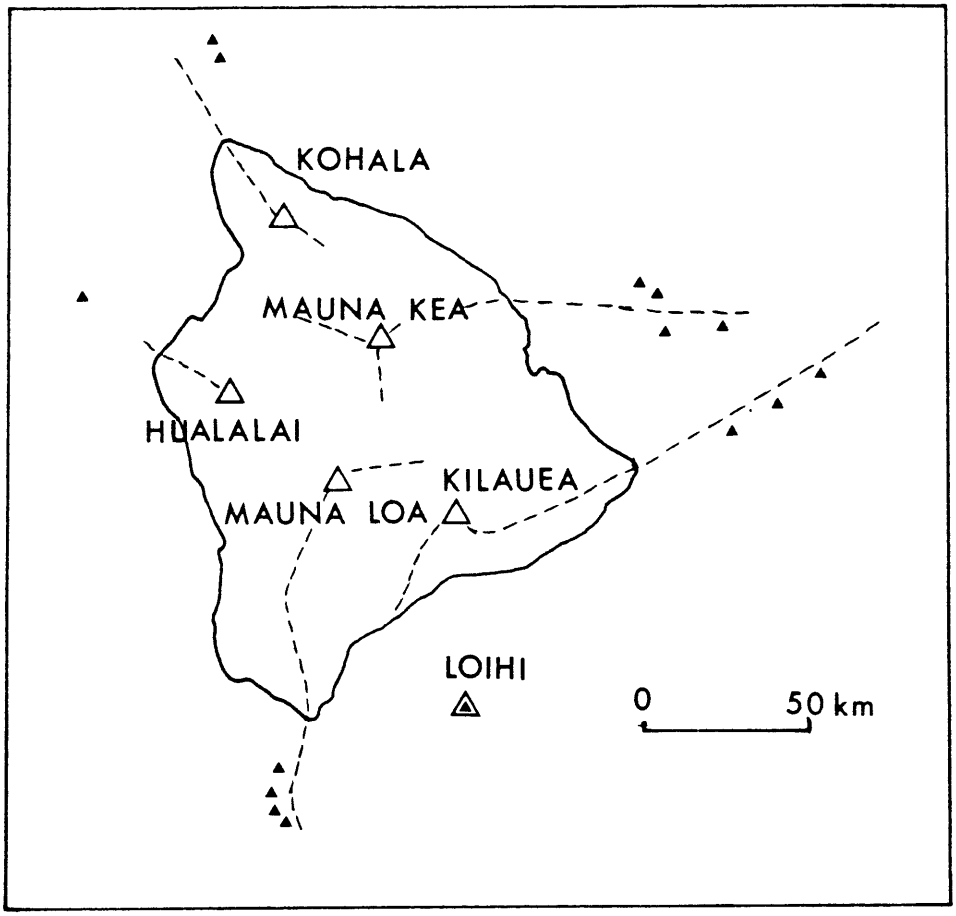

Figure 2.1. Location of the dredging sites (small filled triangles). They are usually located along the main rifts (dashed lines) associated with each volcano.

3. PETROGENESIS BASED ON MAJOR AND COMPATIBLE TRACE ELEMENT GEOCHEMISTRY

3.1. Mineralogy

Phenocryst assemblages were determined at the University of Hawaii by modal analyses of thin sections. Olivine is the dominant phenocryst in all the samples (5-40 vol.%) and is sometimes the only phenocryst phase. It often appears as large euhedral crystals up to several mm. in size, normally zoned with cores of Fo85 or greater and Cr-rich spinel inclusions. A less abundant population of reversely zoned olivine phenocrysts and microphenocrysts with Fo79 to Fo83 cores is also represented. Olivine xenocrysts are commonly found in Kilauea samples and more sparsely distributed in the other sets of rocks.

Plagioclase is the second most abundant phenocryst phase. It occurs almost exclusively in the form of microphenocrysts ($< 500\mu$) with cores ranging from An62 to An72. Plagioclase abundance can reach 20 vol.%, typically in Kohala samples where it is very abundant.

Finally, clinopyroxene is occasionaly found in small amounts (< 7 vol.%) in the form of microphenocrysts or phenocrysts with hour-glass zoning in some instances.

3.2. Variability in major element content

The major element compositions for the 40 samples analysed are presented in Table 3.1. Mg-numbers were calculated assuming a molar ratio of $Fe^{3+}/(Fe^{3+} + Fe^{2+}) = 0.1$ which is the smallest ratio reported in the literature (Wright, 1971). In an $Na_2O + K_2O$ versus SiO_2 plot, all samples lie in the tholeiite field defined by Macdonald and Katsura, 1964, for Hawaiian lavas (Figure 3.1). Intervolcano differences are present in Figure 3.1 where Kilauea, Kohala and Mauna Kea are higher in total alkalis than Mauna Loa and Hualalai, at the same SiO_2 wt%. Variations in major element abundances with MgO concentration are presented in Figures 3.2(a) to 3.9(a) for the whole rock data. The glass data is also plotted in Figures 3.2(a) to 3.9(a) with no distinction of sample origin for the sake of clarity. Expanded scale plots of the glass data are presented in Figures 3.2(b) to 3.9(b).

The major element data for the whole rocks typically plot along strong olivine control lines over a wide range of MgO values (5% to 25%). This feature is a common characteristic of Hawaiian tholeiites (*e.g.* Wright *et al.*, 1975) and is usually interpreted as the result of significant olivine accumulation in the rocks. In figures 3.2(a) to 3.9(a), the glass data seem to fall along well defined liquid lines of descent involving at least one mafic phase (olivine or clinopyroxene) *and* plagioclase. However, a more detailed examination of the glass data (Figures 3.2(b) to 3.9(b)) indicates that the spread in data points is the result of systematic compositional differences between volcanoes rather than the superposition of consistent liquid lines

of descent for each individual volcano. For instance, at the same MgO%, Mauna Loa is higher in SiO_2, lower in TiO_2 and K_2O than Kilauea. Also, a systematic grouping of Mauna Loa glasses in two separate fields can be observed, particularly in TiO_2, K_2O and P_2O_5 content. The overall systematics of Mauna Loa lavas on a large geographical length scale is illustrated in Figure 3.10, where K_2O is plotted against MgO for our Mauna Loa glasses as well as five dredged glasses collected by J. Moore at different locations and six historical Mauna Loa lavas analysed by Rhodes and Hart (unpublished data). Nevertheless, the complete data set does not define a single liquid line of descent over the range in MgO (5% to 7.5%).

There is no simple and systematic relationship between Mauna Kea lavas and lavas from other volcanoes. Sample MK1–8 appears to be highly evolved and invariably plots away from the main Mauna Kea group (lowest MgO, CaO, highest TiO_2, K_2O, P_2O_5 and Na_2O). Our only Loihi sample is also distinctive by its low SiO_2, high FeO and CaO. However, it neither appears like a higly evolved rock because of its relatively low K_2O and P_2O_5, nor departs from the compositionnal range of Loihi tholeiites (Frey and Clague, 1983). These fundamental differences are also illustrated in Figure 3.11 where individual volcano glass data sets are projected on an Ol–Cpx–Qtz pseudoternary. The data fall along the 1-atmosphere phase boundary with, however, a major discrepancy: the MgO content of the glass (or any indicator of differentiation like $1/K_2O$) does *not* decrease continuously from Loihi (the closest to the olivine-cpx joint with 5–6.5 wt% MgO in the glasses) to Mauna Loa (6.2–7.6 wt% MgO in the glasses and the most distant from the olivine-cpx joint). The most

straightforward explanation for these chemical differences is that the parental melts were derived from different mantle sources, or are mixtures of melts of different origin. This approach was proposed to account for the chemical variability of Kilauea through time (Wright *et al.*, 1975), and the systematic differences between Kilauea and Mauna Loa (Wright, 1971) through time. Indeed, significant differences in isotope ratios between Mauna Loa and Kilauea (to be discussed) give considerable strength to this argument.

There is a strong correlation between the characteristics of the glass data described above and whole rock compositions. In all cases, singularities in the distribution of whole rock data points mimic the singularities in the glass distribution but transposed to a higher MgO content as a result of olivine accumulation. Indeed, all tie lines drawn between glass-whole rock pairs (sample MK1–8 in particular) tend to parallel an olivine control line. As a result, the systematic composition differences between Mauna Loa and Kilauea lavas still hold true in the whole rock data sets and are consistent with the relationships between historical Mauna Loa samples (Rhodes, 1983) and samples from the 1969 eruption of Kilauea (Wright *et al.*, 1975). Moreover, the best fit lines through the above data sets often fit the present data as well, in most oxide-MgO plots with the exception of FeO* where tie lines tend to scatter in direction. Unlike most of the oxides, FeO* is very sensitive to olivine composition. The scatter in Figure 3.5(a) may reflect accumulation of olivines with variable fayalite content. Electron probe analyses of olivine crystals were performed by M. Garcia at the University of Hawaii on a subset of Mauna

Loa samples and presented in Table 3.2. Compositions vary from Fo80 to Fo90. Accumulation lines of olivines in the above compositional range are represented in Figure 3.5(a) and are consistent with the observed variability in the slope of tie lines.

3.3. Importance of low pressure crystal fractionation

A problem in studying the behaviour of crystal-melt batches is that the observed phenocryst assemblage may not reflect equilibrium phase proportions. If this was the case, the evaluation of post melting crystal melt segregation would simply consist in comparing glass and whole rock compositions for each sample. In more complex situations however, it may be necessary to examine the trend of all the whole rocks and identify what additional process this trend reflects. For example, Hawaiian tholeiites sampled at the surface are probably derived from more primitive melts by moderate pressure olivine fractionation. The extent of this first stage of crystal fractionation remains an open problem in Hawaiian research. However, the consecutive accumulation of xenocrystic olivines in sampled lavas can be identified on oxide-MgO variation plots as suggested before, and separated from late stage, low pressure crystal fractionation within a flow, by testing the olivine-liquid equilibrium hypothesis (Roeder and Emslie, 1970).

In the following approach we proceed backward, from the easy task of assessing the extent of low pressure crystal fractionation within the lava flows toward the more complicated problem of understanding the strong olivine control in the major element data set. For each individual volcano, a parent is selected by choosing the highest MgO% glass. Relatively low P_2O_5 and K_2O are also required as a confirmation that extensive fractionation did not take place. On this basis, samples ML2–8, KIL1–6 and MK5–5 are chosen as most primitive glasses for Mauna Loa, Kilauea

and Mauna Kea respectively. These "parent" lavas are identified on Al_2O_3/CaO versus MgO plots of both glass and whole rock data (Figures 3.12, 3.13 and 3.14) from which several inferences can be made.

(1) Mauna Loa and Kilauea whole rock Al_2O_3/CaO ratios are independent of MgO content and tend to cluster around the corresponding value of their parent glass. Therefore, the chemical variability within the whole rocks is related to addition of a mafic phase that does not affect the Al_2O_3/CaO ratios, *e.g.* olivine. Also, these rocks must preserve the plagioclase/clinopyroxene proportions inherited during low pressure crystal fractionation. This result is common among submarine basalts (Bryan, 1983). The majority of Mauna Kea rocks and two Kilauea rocks do not follow this simple trend (Figures 3.13 and 3.14). Whole rock Al_2O_3/CaO ratios can plot significantly higher than the chosen parent glass as in samples MK1–3, MK1–8, MK1–10, KIL1–5 and KIL3–8. These differences may be interpreted by low pressure fractionation of clinopyroxene. Indeed, samples plotting above the main trend are systematically associated with highly evolved, phenocryst rich glasses, as shown by the glass-whole rock tie lines in Figures 3.13 and 3.14. Also, the significant clinopyroxene fractionation that could account for the high Al_2O_3/CaO in sample MK1–8 is confirmed by an abnormally low Sc value for MK1–8 (Figure 3.25). Sample MK2–1 is a unique occurence of lower than normal Al_2O_3/CaO ratio that can be explained by clinopyroxene accumulation or/and plagioclase fractionation. No significant Sr depletion or Sc enrichment is observed in MK2–1 that would favour either hypothesis. However, a slight overall incompatible element enrichment

in this sample as exemplified by its plotting slightly above "normal" Mauna Kea trend in a La *vs.* MgO plot (Figure 4.32) tends to support the hypothesis of crystal (plagioclase) fractionation.

(2) In the Kilauea data set, all the glasses have Al_2O_3/CaO ratios greater than their parent whereas both the Mauna Loa and Mauna Kea data sets extend to higher and lower Al_2O_3/CaO values. Since the net effect of clinopyroxene removal is to increase Al_2O_3/CaO, an interpretation is that Kilauea is the only volcano where the parent lava has actually reached clinopyroxene saturation. In contrast, at Mauna Loa and Mauna Kea, some samples more evolved than the parental glass, highest in MgO, may have only experienced olivine and/or plagioclase fractionation before clinopyroxene saturation was achieved. In Figure 3.15, clinopyroxene and plagioclase volume % (mode) in the rocks are plotted against the MgO content of the corresponding glasses for Mauna Loa samples. We observe a group of high MgO glasses with very little ($\leq$ 2 vol.%) modal abundance of cpx or modal abundance of plagioclase greater than clinopyroxene. The glass ML1–11 which has the lowest Al_2O_3/CaO of all Mauna Loa glasses is also the lowest MgO glass in this group. The lower MgO glasses are systematically associated with a greater abundance of clinopyroxene crystals except for samples ML1–7 and ML4–44. This feature could be the likely result of clinopyroxene fractionation in a phenocryst rich rock. It is not understood, however, why Al_2O_3/CaO ratios in the corresponding whole rocks remain undisturbed. In view of Figure 3.15, the most likely explanation to the differences in Figures 3.12, 3.13 and 3.14 is therefore that Kilauea is the only

volcano where the parent lava corresponds to a stage where clinopyroxene exceeds plagioclase in the crystallising assemblage.

The liquid line of descent from the parent glass through the glass data set can be modeled by simple mass balance using typical equilibrium plagioclase, olivine and clinopyroxene. In the results presented hereafter, the olivine composition was calculated with an iron-magnesium distribution coefficient

$$K_d^{\mathrm{Fe-Mg}} = X_{\mathrm{FeO}}^{\mathrm{Ol}} X_{\mathrm{MgO}}^{\mathrm{Gl}} / X_{\mathrm{FeO}}^{\mathrm{Gl}} X_{\mathrm{MgO}}^{\mathrm{Ol}} \tag{1}$$

equal to 0.30 (Roeder and Emslie, 1970). The plagioclase composition was inferred using a calcium-sodium distribution coefficient equal to 1.0 (Baker, 1988). Finally, the clinopyroxene composition was determined using $K_d^{\mathrm{Fe-Mg}} = 0.25$ (Grove and Bryan, 1983). In the latter case however, the K_d is not sufficient to completely determine the composition. Therefore, SiO_2, TiO_2, Al_2O_3, FeO+MgO, CaO and Na_2O were arbitrarily fixed to 52.8%, 0.9%, 2.9%, 24%, 19% and .25% respectively by analogy with an average of typical Hawaiian clinopyroxene phenocryst compositions (Fodor *et al.*, 1975).

For each glass composition, the mass balance equation

$$[\text{Parental Glass}] = a\,[\text{Glass}] + b\,[\text{Ol}] + c\,[\text{Plag}] + d\,[\text{Cpx}] \tag{2}$$

was solved for a, b, c and d on the basis of a constrained ($a + b + c + d = 1$) unweighted least square solution using the oxides SiO_2, TiO_2, Al_2O_3, FeO, MgO, CaO and Na_2O. The fit of the glass data to such a simple model is good for Mauna Loa and Kilauea for which the sum of squared residuals is consistently less than

0.8 wt%, and only fair for Mauna Kea with sums of squared residuals less than 1.7 wt%. Figure 3.16 is a plot of the melt fraction (coefficient a) versus mineral abundances of olivine, plagioclase and clinopyroxene (coefficients b, c and d respectively) throughout differentiation. The behaviour of the fractionating assemblage in Figure 3.16 is consistent with a situation where clinopyroxene saturation is about to be reached. Indeed, clinopyroxene appears to "lift-off" after a few percent of crystallisation whereas the abundance of plagioclase grows steadily throughout the sequence. These lavas follow a typical Ol–Ol+Plag–Ol+Plag+Cpx paragenesis commonly found in submarine tholeiites (Shido *et al.*, 1974). Low amounts of removed olivine values should not be misunderstood since they only reflect fractionation from a relatively low MgO% parent, itself probably evolved from a higher MgO% liquid by significant olivine fractionation. Furthermore, the tendency for olivine abundance to level-off as the melt fraction decreases is consistent with the expected behaviour of a phase which gets closer to a resorption stage as the orthopyroxene stability field is approached (Grove and Baker, 1984). Similar characteristic features are found when experimental data are plotted in the same fashion (Figure 3.17: MORB sample AII-32-12-6, Grove and Bryan, 1983).

3.4. Contrasted glass and whole rock compositions

The relationships between whole rock and their associated glasses can be further clarified when the data are projected on an Ol–Qtz-Cpx pseudoternary (Figures 3.18, 3.19 and 3.20). In these projections, the glasses consistently plot along or near the 1-atmosphere, plagioclase-saturated, olivine-clinopyroxene phase boundary defined by the experiments of Tormey *et al.*, 1987, for basaltic melts of MORB composition. However, there are systematic differences in the grouping of glass data points for the three volcanoes. Some of Mauna Loa and Mauna Kea glasses clearly plot in the olivine phase volume and have probably not achieved clinopyroxene saturation yet, as was suggested earlier. In contrast, Kilauea glasses follow a well defined multiple saturation Ol-Plag-Cpx phase boundary slightly displaced from the MORB phase boundary, away from the olivine corner. This displacement could reflect the dependence of the phase boundaries in the Ol-Qtz-Plag-Cpx pseudo-quaternary system on bulk composition (Grove and Baker, 1984).

In the pseudoternary diagrams, whole rock data typically strike from the cluster of glass data points directly toward the olivine corner. This feature can have two different explanations:

(1) The whole rock data represent more primitive melts formed at higher pressures.

(2) The spread of whole rock data points reflects varying amounts of olivine accumulation in evolved melts plotting near the low pressure cotectic boundary.

The underlying assumption in the first hypothesis is that significant high pressure clinopyroxene (or orthopyroxene if the depth of origin is sufficient) fractionation took place in order to generate a spread of data points in a direction perpendicular to an olivine tie line as is the case for Mauna Kea, and to a lesser extent Kilauea (Figures 3.19 and 3.20). The modal mineralogy however, does not support this hypothesis. Clinopyroxene crystals are sparsely distributed in the form of microphenocrysts in most cases, and orthopyroxene is virtually absent from all samples. Moreover, the striking tendency of all glass-whole rock tie lines to point directly toward olivine would be fortuitous after a high pressure crystal fractionation stage. It is therefore believed that hypothesis no. 2 is the most plausible explanation for the major element variability of these rocks. A very definite answer could be found by adressing the problem of clinopyroxene Fe-Mg equilibrium with the melt providing the data were available.

Some of the compositional variability between volcanoes seen in Figures 3.18 to 3.20 may be related to crystal-melt segregation during magma ascent. For example, it may be argued that the Mauna Loa lavas experienced an early stage of olivine accumulation followed by low pressure crystal fractionation hence generating a quasi-straight array of data points in Figure 3.18. On the other hand, Mauna Kea lavas may have undergone significant low pressure clinopyroxene fractionation before olivine crystals are randomly added to the evolved liquids hence creating a spread in the data distribution in a direction perpendicular to an olivine control line (Figure 3.20).

In Figure 3.21, the total fraction of olivine in the rock (mode) is plotted against the amount of olivine that must crystallise from the parental glass composition to create the corresponding glass composition for each Mauna Loa sample. Undoubtely, the olivine amount that crystallised from a parent reflects the cooling time for a particular flow. The inverse correlation in Figure 3.21 could therefore indicate:

(1) A single massive olivine accumulation stage followed by the gravitational settling of the crystals. In this case, the settling, i.e. the decrease in modal olivine is proportional to the cooling time as measured by the calculated amount of crystallised olivine, hence an inverse relationship. It comes as a surprise however that olivine rich cumulates were never sampled.

(2) A late stage, pillow emplacement related dynamic phenomenon whereby the rapidly quenched margins become the most olivine enriched parts of the pillow.

The same plot for Mauna Kea exhibits a completely different, inverted U-shaped pattern (Figure 3.22) that may again be related to a different, yet not deciphered, sequence of accumulation/fractionation events between the two volcanoes.

3.5. First series transition element analysis: further evidence for significant olivine accumulation

First series transition element concentrations in our dredged samples are displayed in Table 3.1, and variations in these elements abundance with MgO are presented in Figures 3.23 to 3.26. In the case of Ni and Sc, the path of olivine fractionation from the highest MgO sample is also represented using a general equation derived in Appendix 1. These curves provide a poor match to the data. Following the approach of Hart and Davis, 1978, Ni-MgO correlation plots (Figure 3.23) can be used to assess the MgO content of a liquid in equilibrium with accumulative olivines. Assuming a partition coefficient for Ni in olivine in the form $D = a + b/\mathrm{MgO}$, the problem consists in matching the Ni-MgO mixing line between a melt of given MgO% and its equilibrium olivine with the best fit line through the data points. Setting x and y as the MgO% and FeO% of the melt, the MgO content of the equilibrium olivine is given by

$$\mathrm{MgO_{Ol}} = 100\lambda \frac{66.67w(\mathrm{MgO})}{66.67\left[\lambda w(\mathrm{MgO}) + (1-\lambda)w(\mathrm{FeO})\right] + 33.33w(\mathrm{SiO_2})} \qquad (3)$$

with

$$\lambda = \left(1 + K_d\left[\frac{yw(\mathrm{MgO})}{xw(\mathrm{FeO})}\right]\right)^{-1} \qquad (4)$$

and where the acronym "$w(..)$" stands for the molar weight of the corresponding oxide. After some tedious but straightforward algebra, the above formula simplifies into

$$\mathrm{MgO_{Ol}} = \frac{A}{B + C/x} \qquad (5)$$

where A, B and C are constants given by

$$A = 268709.4 \tag{6a}$$

$$B = 4689.7 \tag{6b}$$

$$C = 3810.5\, y\, K_d \tag{6c}$$

Setting the Ni-MgO regression line in the form Ni $= \alpha$MgO $+ \beta$, the analytical formulation of the problem is to solve the following equation for x

$$(\alpha x + \beta)\,(a + b/x - 1)\left(\frac{A}{B + C/x} - x\right)^{-1} = \alpha \tag{7}$$

After simplification, a third order polynomial is to be solved for the MgO content of the melt in equilibrium with the olivine crystals. All the following results were derived assuming a mean FeO content (y) of 10 wt% and a K_d of 0.3. In order to test the sensitivity of the method, the calculations were also carried out with an arbitrarily fixed MgO value in the olivine. The justification for this approach is that accumulative olivine can be significantly Fo-richer (Table 3.2), having fractionated at a much earlier stage, than the olivine in equilibrium with the melt. The results are presented in Table 3.3.

The results are stable and vary by less than half a percent in MgO over a wide range of olivine compositions (Fo 84 to Fo 92). If the whole data set is to be used regardless of the volcano of origin with an "equilibrium" olivine composition, the MgO content of the melt is of the order of 9.2 wt%. On the basis of individual volcanoes, typical values for the melt MgO concentration are of the order of 9.4 wt%, 9.1 wt% and 6.9 wt% for Mauna Loa, Kilauea and Mauna Kea respectively.

These values are consistently higher than the reported MgO concentrations in the glasses, suggesting that the stage of olivine accumulation took place before low pressure fractionation was completed. Also, the MgO content of the equilibrium melt is always lower for Mauna Kea compared to Mauna Loa and Kilauea which tends to indicate that olivine accumulation may have taken place at a much later stage in the case of Mauna Kea as was also suggested earlier.

Other transition elements such as Cr, Sc and V, also correlate well with MgO (Figures 3.24, 3.25 and 3.26). The mineral-melt partition coefficient required to fit an "accumulative" model to the data can be calculated by simply dividing the trace element concentration read on the best fit line for an equilibrium olivine (Fo82=44 wt% MgO) by the concentration of a 9.2 wt% MgO-rich melt (also given by the best fit line through the data points). The inferred bulk solid/liquid distribution coefficients are displayed in Table 3.4. These number are in good agreement with the values reported by Frey *et al.*, 1977 for Sc and V. The slightly high value that was calculated for Cr partition coefficient can be related to the fact that olivine crystals often bear Cr-rich spinel inclusions (Garcia, personnal communication).

3.6. Conclusions

The major and first series transition element analysis developped in this chapter allows the following conclusions to be made:

(1) Based on the study of the glass data alone, it appears that these rocks follow a typical Ol–Ol+Plag–Ol+Plag+Cpx paragenesis, characteristic of Hawaiian tholeiites. Volcanoes have experienced various amounts of low pressure crystal fractionation ranging from none at all (Mauna Loa) to noticeable (in Al_2O_3/CaO for instance) amounts of clinopyroxene and plagioclase fractionation (Mauna Kea).

(2) Comparing glass and corresponding whole rock compositions, we conclude that the whole rocks are affected by massive amounts of olivine accumulation. This hypothesis is confirmed by the observation that most of the olivine crystals in the rocks are not in Fe-Mg equilibrium with the glass. Also the study of compatible elements (Ni, Cr, Sc, V) in these rocks strongly supports the "accumulative" model.

(3) Based on the comparison of glass and whole rock data, we infer that there are variations in the relationships between low pressure fractionation stage and olivine accumulation stage (*e.g.* relative timing) from one volcano to the other.

(4) There are intervolcano compositional differences in our data set that are not explained by either one of the processes mentionned above. These differences exist in both the glass and whole rock data and seem to require differences in the source material of the corresponding volcanoes.

TABLE 3.1

MAJOR AND TRANSITION ELEMENT ANALYSES

	MAUNA LOA							
	1–1	1–7	1–9	1–10	1–11	1–14	2–1	2–3
SiO_2	47.94	51.37	50.59	49.38	48.93	48.37	50.09	50.16
TiO_2	1.45	2.18	1.85	1.85	1.64	1.53	2.10	1.78
Al_2O_3	9.34	13.41	12.32	10.62	10.46	9.78	11.81	12.00
Fe_2O_3	12.11	12.19	11.93	12.22	12.06	12.09	12.32	11.87
MnO	0.17	0.17	0.17	0.17	0.17	0.17	0.17	0.17
MgO	19.50	7.73	11.40	15.22	16.13	18.27	11.82	12.21
CaO	7.31	10.52	9.62	8.42	8.22	7.66	9.35	9.34
Na_2O	1.53	2.20	1.99	1.78	1.74	1.61	1.99	1.92
K_2O	0.23	0.34	0.31	0.34	0.31	0.26	0.38	0.28
P_2O_5	0.14	0.21	0.18	0.19	0.16	0.15	0.21	0.17
Sum	99.72	100.32	100.36	100.19	99.82	99.89	100.24	99.90
FeO*	10.90	10.97	10.73	11.00	10.85	10.88	11.09	10.68
Mg#	78.0	58.3	67.8	73.3	74.6	76.9	67.9	69.4
Ni	1102	142	401	684	784	976	413	484
Cr	1002	346	698	892	1001	980	671	708
Sc	22.5	31.0	28.1	25.5	24.7	23.3	28.2	27.3
V	192.8	275.9	243.1	219.7	215.4	201.3	244.0	235.7

TABLE 3.1

MAJOR AND TRANSITION ELEMENT ANALYSES (CONT.)

	MAUNA LOA							
	2–8	3–30	4–3*	4–9*	4–10	4–10*	4–11	4–11*
SiO_2	48.50	48.39	50.13	50.31	49.21	49.24	50.35	50.21
TiO_2	1.51	1.54	2.07	2.13	1.62	1.60	2.14	2.11
Al_2O_3	10.20	9.74	11.84	12.19	10.77	10.81	11.93	11.90
Fe_2O_3	11.92	11.96	12.21	12.16	11.97	11.98	12.28	12.29
MnO	0.17	0.16	0.18	0.18	0.17	0.17	0.17	0.18
MgO	17.01	18.85	11.79	10.65	15.64	15.70	11.33	11.57
CaO	8.01	7.55	9.32	9.58	8.50	8.49	9.40	9.33
Na_2O	1.68	1.61	1.98	2.03	1.74	1.75	2.01	1.99
K_2O	0.24	0.28	0.39	0.40	0.27	0.27	0.38	0.39
P_2O_5	0.15	0.15	0.21	0.22	0.16	0.16	0.22	0.22
Sum	99.39	100.23	100.12	99.85	100.05	100.17	100.21	100.19
FeO*	10.73	10.76	10.99	10.94	10.77	10.78	11.05	11.06
Mg#	75.8	77.6	68.0	65.8	74.2	74.3	67.0	67.4
Ni	879	962	427	349	740	744	403	415
Cr	980	1007	621	631	968	979	638	629
Sc	24.3	22.9	27.9	28.7	25.3	25.6	28.2	28.1
V	202.1	199.6	250.6	254.8	213.7	209.0	251.5	251.1

TABLE 3.1

MAJOR AND TRANSITION ELEMENT ANALYSES (CONT.)

	MAUNA LOA			KILAUEA				
	4–22*	4–44	4–59	1–BR	1–4	1–5	1–7	2–1
SiO_2	50.48	50.93	49.27	49.68	49.99	50.28	48.23	46.97
TiO_2	2.17	2.12	1.46	2.29	2.29	2.70	1.89	1.64
Al_2O_3	12.31	12.98	11.28	12.43	12.50	13.60	10.44	8.52
Fe_2O_3	12.17	11.82	11.05	12.45	12.37	12.28	12.13	12.24
MnO	0.18	0.17	0.16	0.18	0.18	0.17	0.17	0.17
MgO	10.45	9.05	15.72	9.98	9.97	7.14	15.93	21.42
CaO	9.65	10.08	8.75	10.20	10.26	10.84	8.62	7.01
Na_2O	2.05	2.19	1.73	2.04	2.02	2.23	1.68	1.37
K_2O	0.41	0.33	0.23	0.44	0.42	0.54	0.34	0.29
P_2O_5	0.22	0.20	0.14	0.22	0.22	0.27	0.18	0.16
Sum	100.09	99.87	99.79	99.91	100.22	100.05	99.61	99.79
FeO*	10.95	10.64	9.94	11.20	11.13	11.05	10.91	11.01
Mg#	65.4	62.8	75.8	63.8	64.0	56.1	74.3	79.4
Ni	336	233	723	258	275	116	784	1207
Cr	592	461	902	527	553	314	806	1120
Sc	28.7	29.8	24.7	29.6	29.7	30.3	25.6	21.1
V	258.1	269.4	195.0	265.7	273.9	284.1	225.6	187.0

TABLE 3.1

MAJOR AND TRANSITION ELEMENT ANALYSES (CONT.)

	KILAUEA		MAUNA KEA					
	2–8	2–9	3–8	1–3	1–8	1–10	2–1	5–13
SiO_2	46.30	46.63	47.82	48.76	50.76	48.99	48.68	49.33
TiO_2	1.57	1.65	2.02	2.11	2.70	2.14	2.01	1.97
Al_2O_3	8.01	8.62	9.68	10.10	11.34	10.27	10.86	11.67
Fe_2O_3	12.50	12.31	12.59	12.42	12.86	12.44	12.18	11.94
MnO	0.17	0.17	0.17	0.17	0.17	0.17	0.17	0.16
MgO	22.48	20.83	17.92	15.76	10.93	15.43	14.61	13.23
CaO	6.62	7.19	7.62	7.68	7.95	7.77	9.12	9.32
Na_2O	1.33	1.45	1.60	1.86	2.29	1.90	1.69	1.92
K_2O	0.28	0.29	0.39	0.42	0.63	0.43	0.32	0.31
P_2O_5	0.16	0.16	0.21	0.24	0.34	0.24	0.18	0.19
Sum	99.42	99.30	100.02	99.52	99.97	99.78	99.82	100.04
FeO*	11.25	11.08	11.33	11.18	11.57	11.19	10.96	10.74
Mg#	79.8	78.8	75.8	73.6	65.2	73.2	72.5	70.9
Ni	1217	1135	888	729	441	716	619	533
Cr	1375	1156	1003	927	593	939	846	705
Sc	20.4	22.0	22.4	24.0	25.4	24.3	27.4	27.6
V	181.2	193.7	224.3	231.6	276.2	235.8	231.1	240.0

TABLE 3.1

MAJOR AND TRANSITION ELEMENT ANALYSES (CONT.)

	MAUNA KEA		KOHALA			HUALALAI		LOIHI
	6–6	6–18	1–17	2	2–8	5	7	6
SiO_2	47.98	49.70	48.69	50.05	50.47	49.48	50.21	48.14
TiO_2	1.76	2.06	1.89	2.28	2.36	1.71	1.86	2.43
Al_2O_3	10.28	12.28	11.44	12.97	13.30	11.21	12.18	12.18
Fe_2O_3	12.29	11.83	12.30	11.87	11.91	12.04	11.93	13.33
MnO	0.17	0.17	0.17	0.16	0.17	0.17	0.17	0.18
MgO	16.85	11.33	13.89	9.52	8.92	14.30	11.23	10.07
CaO	8.11	9.76	9.27	10.16	10.29	8.96	9.76	11.11
Na_2O	1.69	2.04	1.83	2.21	2.25	1.74	1.92	2.14
K_2O	0.28	0.33	0.33	0.43	0.45	0.28	0.30	0.39
P_2O_5	0.18	0.20	0.20	0.26	0.27	0.16	0.17	0.23
Sum	99.59	99.70	100.01	99.91	100.39	100.05	99.73	100.20
FeO*	11.06	10.64	11.07	10.68	10.72	10.83	10.73	11.99
Mg#	75.1	67.8	71.3	63.8	62.2	72.3	67.5	62.5
Ni	804	415	494	261	225	671	421	229
Cr	1015	585	865	456	390	773	626	620
Sc	24.7	28.9	27.4	29.0	29.5	26.0	28.4	32.7
V	217.0	245.5	235.3	260.4	264.3	229.6	254.0	322.2

TABLE 3.2

OLIVINE CORES ANALYSES FOR MAUNA LOA SAMPLES

ML1–10	Zoning	N	—	N	N	N	—
	Fo	86	82	86	85	83	82
	K_d	.16	.22	.16	.17	.20	.22
	Size	0.3	1.0	0.3	1.2	0.1	0.1
ML–11	Zoning	N	N	R	N	N	—
	Fo	87	90	84	86	90	81
	K_d	.17	.14	.22	.19	.13	.26
	Size	0.8	0.5	0.2	0.2	0.9	0.5
ML2–3	Zoning	R	R	R	R	—	—
	Fo	82	82	82	80	82	83
	K_d	.27	.27	.27	.31	.27	.25
	Size	0.2	0.8	0.2	0.9	0.2	0.2
ML2–8	Zoning	—	N	—	N	R	—
	Fo	83	89	82	87	82	86
	K_d	.27	.18	.30	.21	.30	.23
	Size	0.6	0.5	0.1	1.0	0.7	0.2
ML4–10	Zoning	—	N	N	N	—	N
	Fo	83	87	83	83	82	81
	K_d	.27	.19	.27	.28	.28	.30
	Size	0.3	1.2	0.4	1.3	0.4	0.6
ML4–11	Zoning	N	N	R	—	N	—
	Fo	89	88	84	85	89	83
	K_d	.12	.13	.19	.17	.12	.19
	Size	0.9	0.5	0.7	0.2	1.2	0.1
ML4–44	Zoning	N	N	N	N	N	—
	Fo	83	82	85	83	84	80
	K_d	.18	.20	.16	.19	.17	.22
	Size	0.2	0.1	0.6	0.2	0.4	0.1

TABLE 3.3

MgO CONTENT IN THE LIQUID AFTER Ni-MgO MODELLING (SEE TEXT)

	Mauna Loa	Mauna Kea	Kilauea	Whole set
Equilibrium olivine	9.40	6.88	9.10	9.20
Fo76 olivine	8.86	6.77	8.61	8.68
Fo84 olivine	9.45	7.22	9.19	9.26
Fo92 olivine	10.14	7.74	9.86	9.94

TABLE 3.4

INFERRED BULK PARTITION COEFFICIENT

FROM TRACE ELEMENT-MgO PLOTS

	conc. in glass	conc. in solid	bulk $D^{s/l}$
Cr	495.55	2615.53	5.28
Sc	29.79	4.84	0.16
V	266.3	26.6	0.10

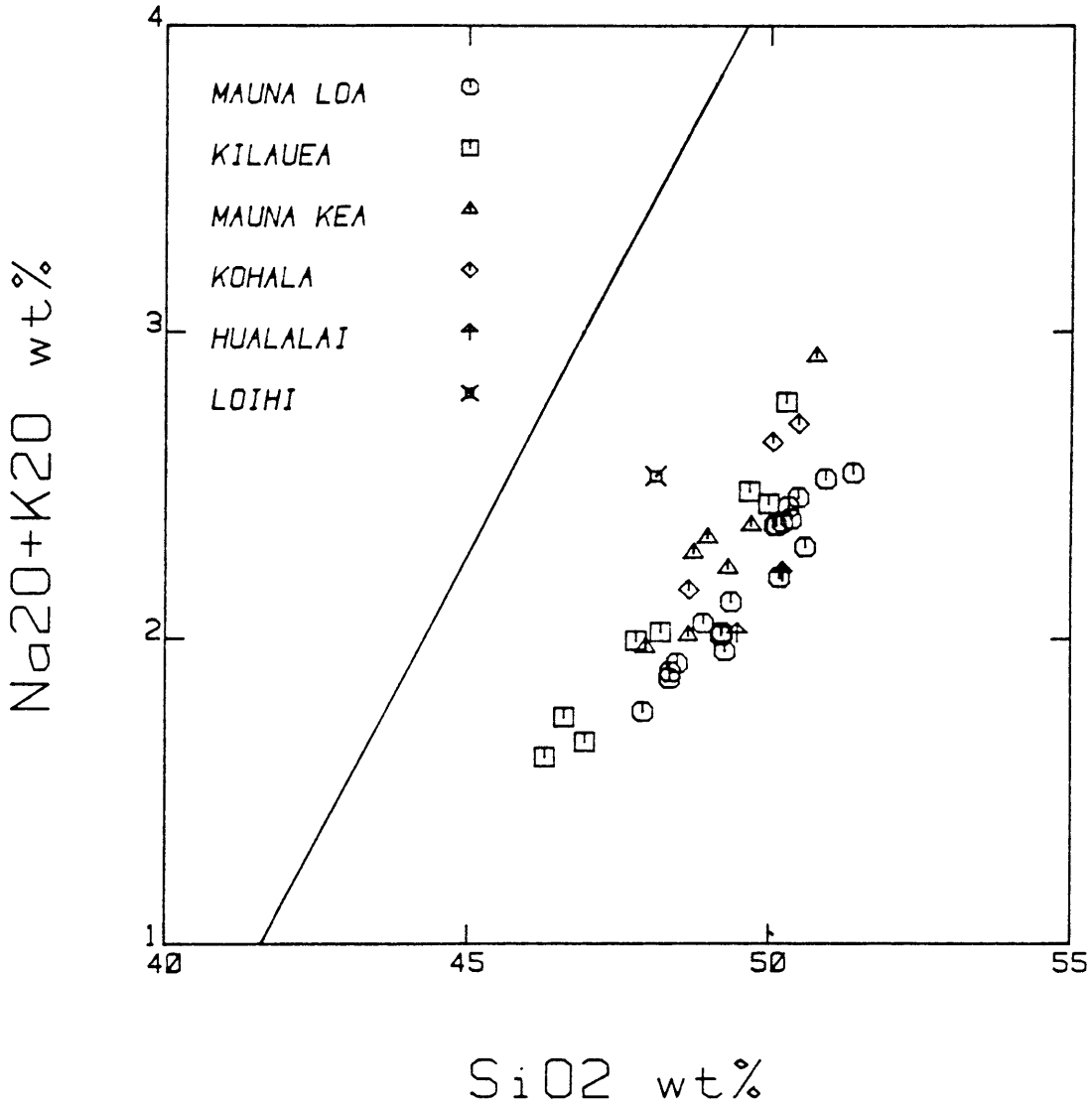

Figure 3.1. Total alkalis versus silica plot of the complete data set. All the lavas plot in the tholeiite field defined by Macdonald and Katsura, 1964, for Hawaiian basalts.

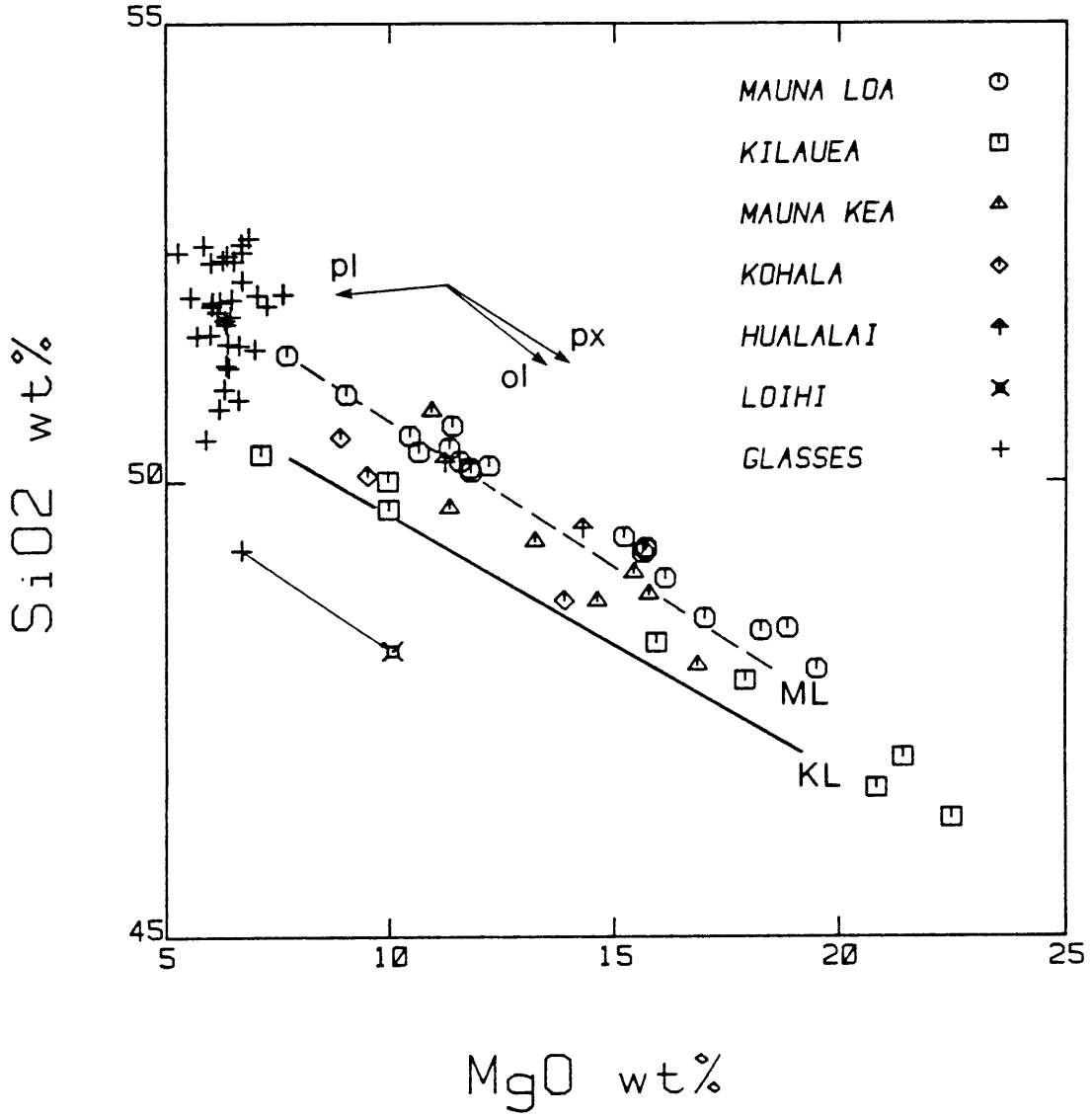

Figures 3.2(a)–3.9(a). Oxide-MgO plots for the glasses (crosses) and whole rocks (symbols). The solid and dashed lines labeled KL and ML respectively are the best fit lines to the 1969 Kilauea eruption (Wright *et al.*, 1974) and historical Mauna Loa (Rhodes, 1983) data sets. The vectors indicate the effect of crystal accumulation based on typical Hawaiian minerals analyses (Keil *et al.*, 1972, Fodor *et al.*, 1975). Glass-whole rock tie lines are also drawn for pertinent samples (see text).

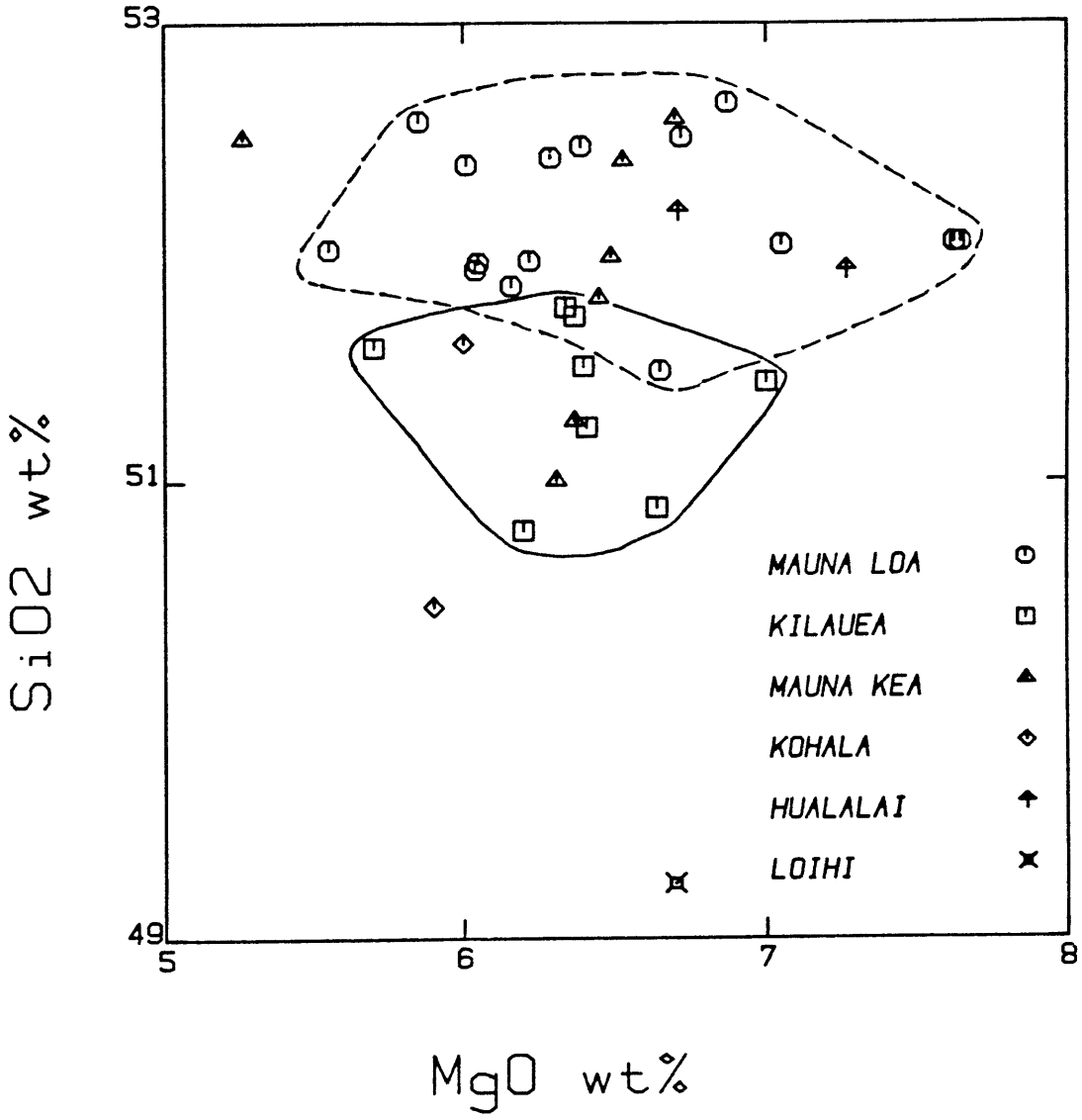

Figures 3.2(b)–3.9(b). Enlarged view of the glass data plotted in Figures 3.2(a) to 3.9(a). Mauna Loa and Kilauea fields are contoured with a dashed and a solid curve, respectively.

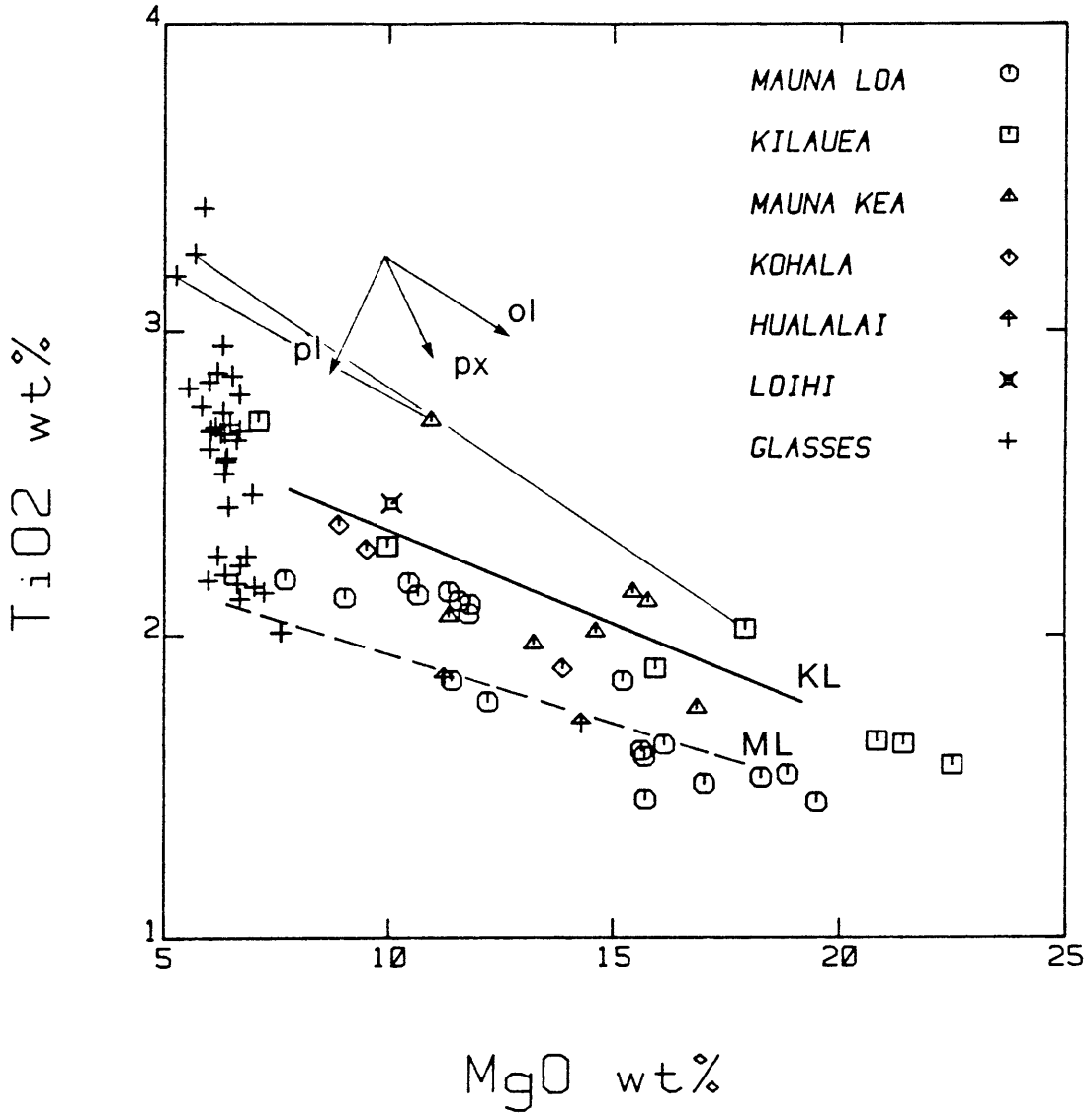

Figure 3.3(a). Same as 3.2(a).

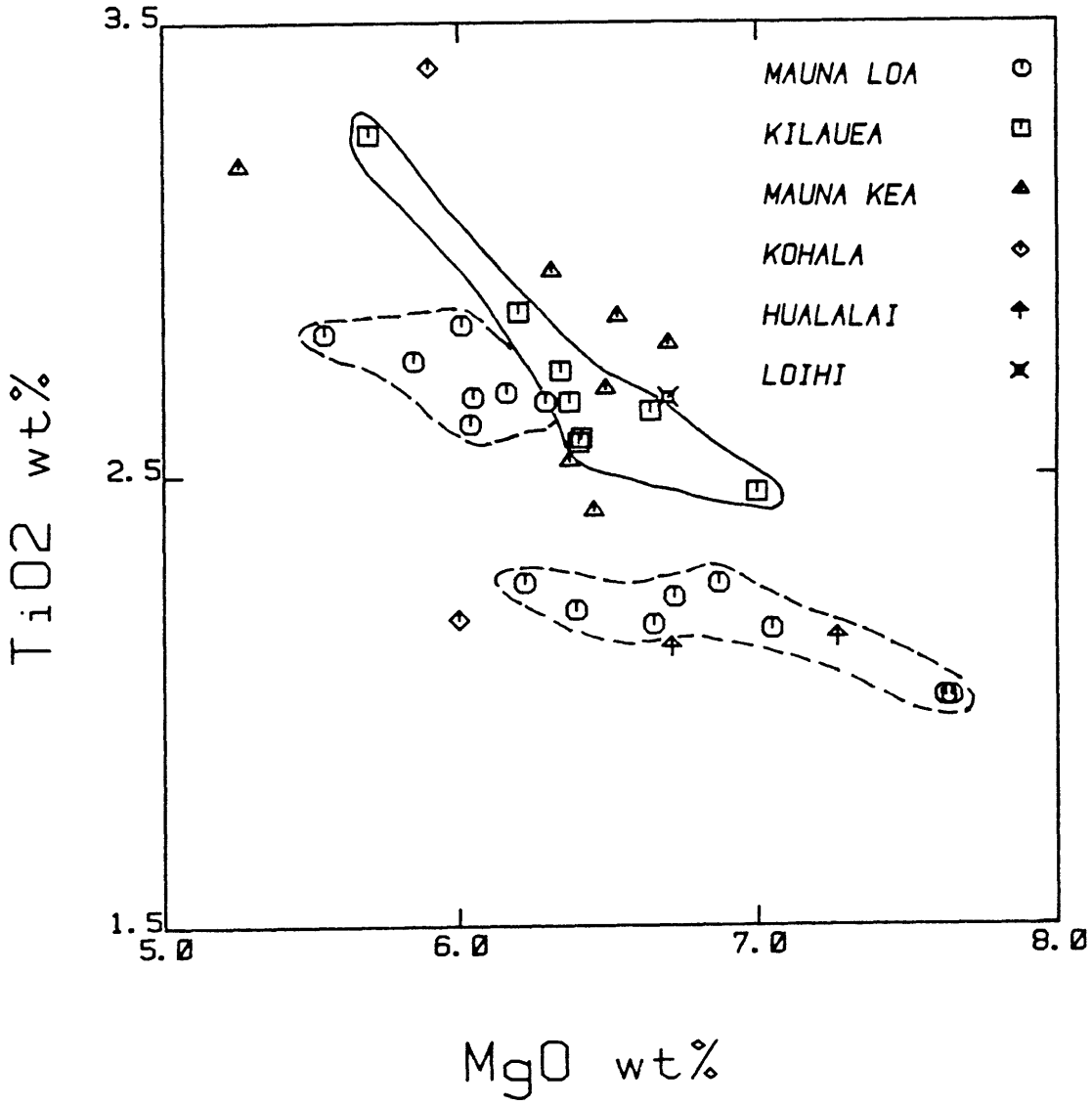

Figure 3.3(b). Same as 3.2(b).

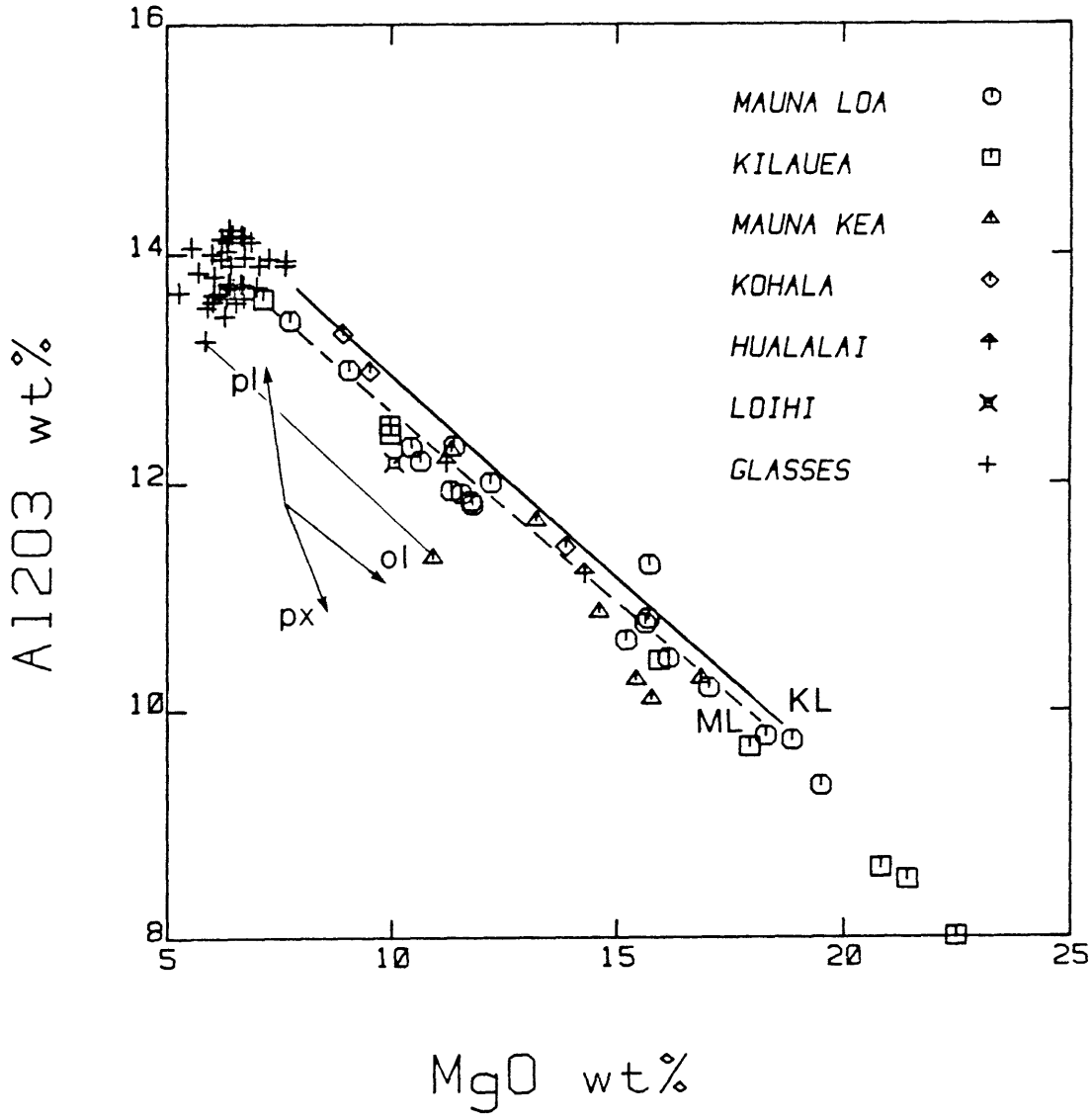

Figure 3.4(a). Same as 3.2(a).

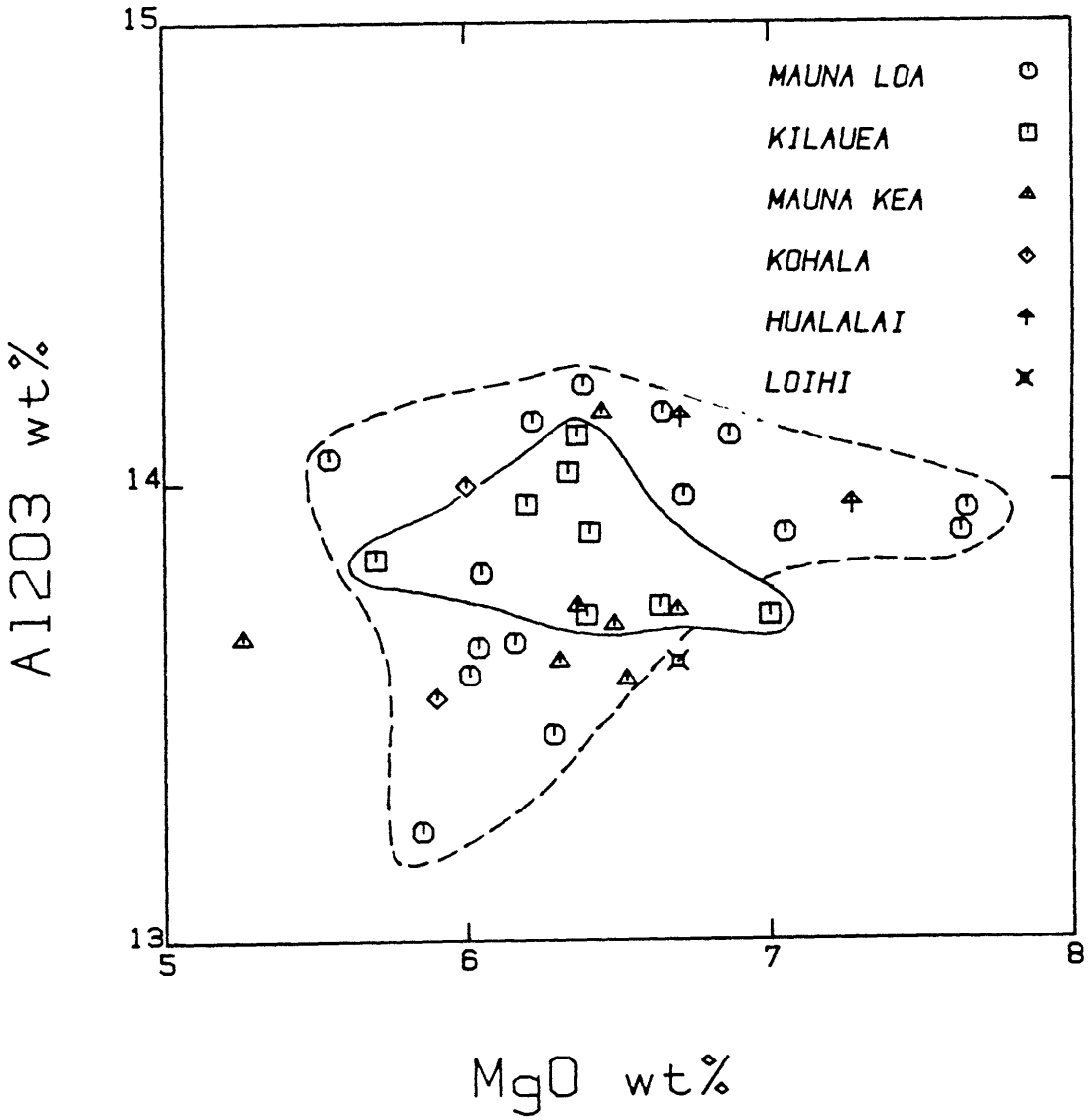

Figure 3.4(b). Same as 3.2(b).

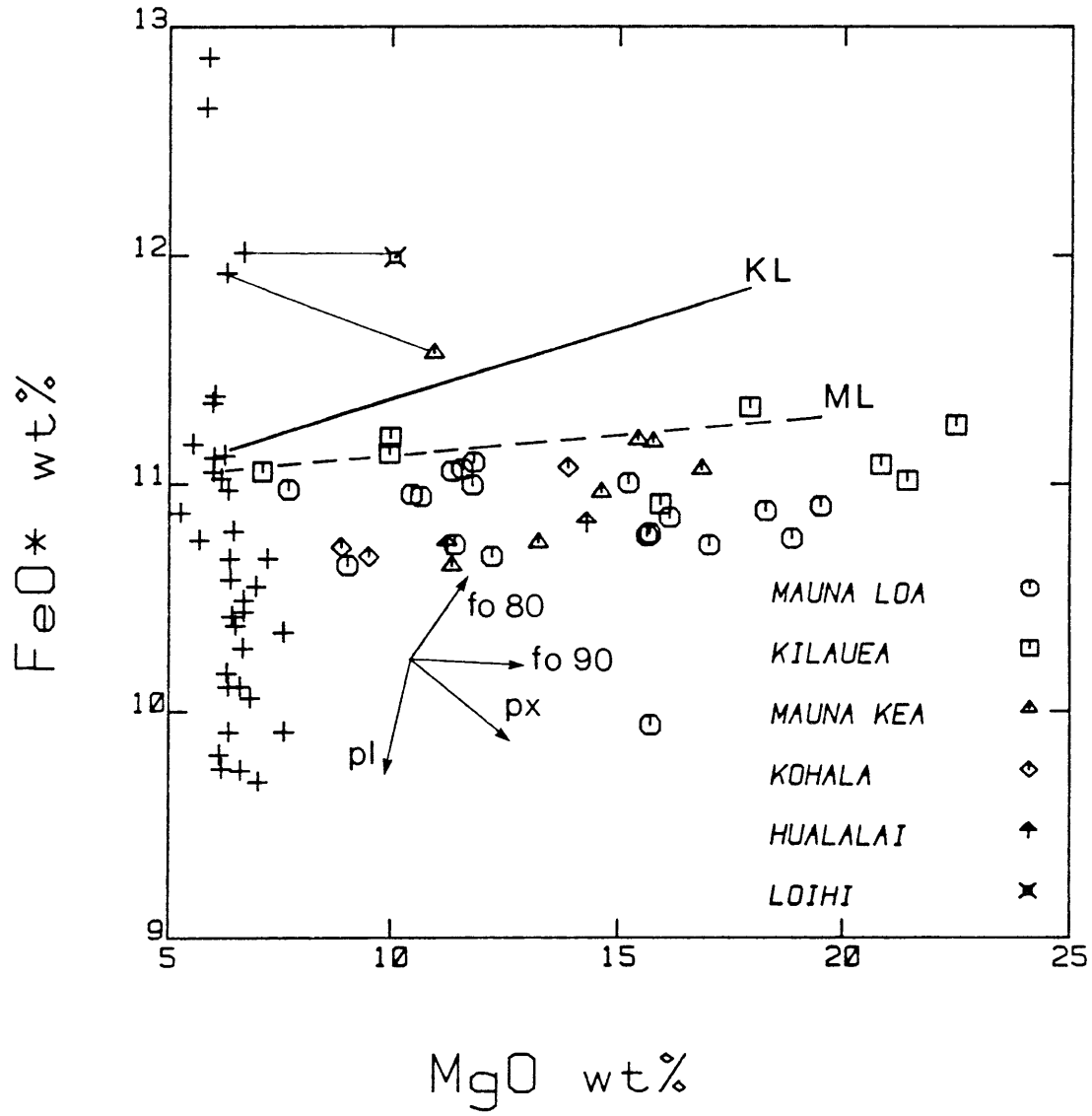

Figure 3.5(a). Same as 3.2(a).

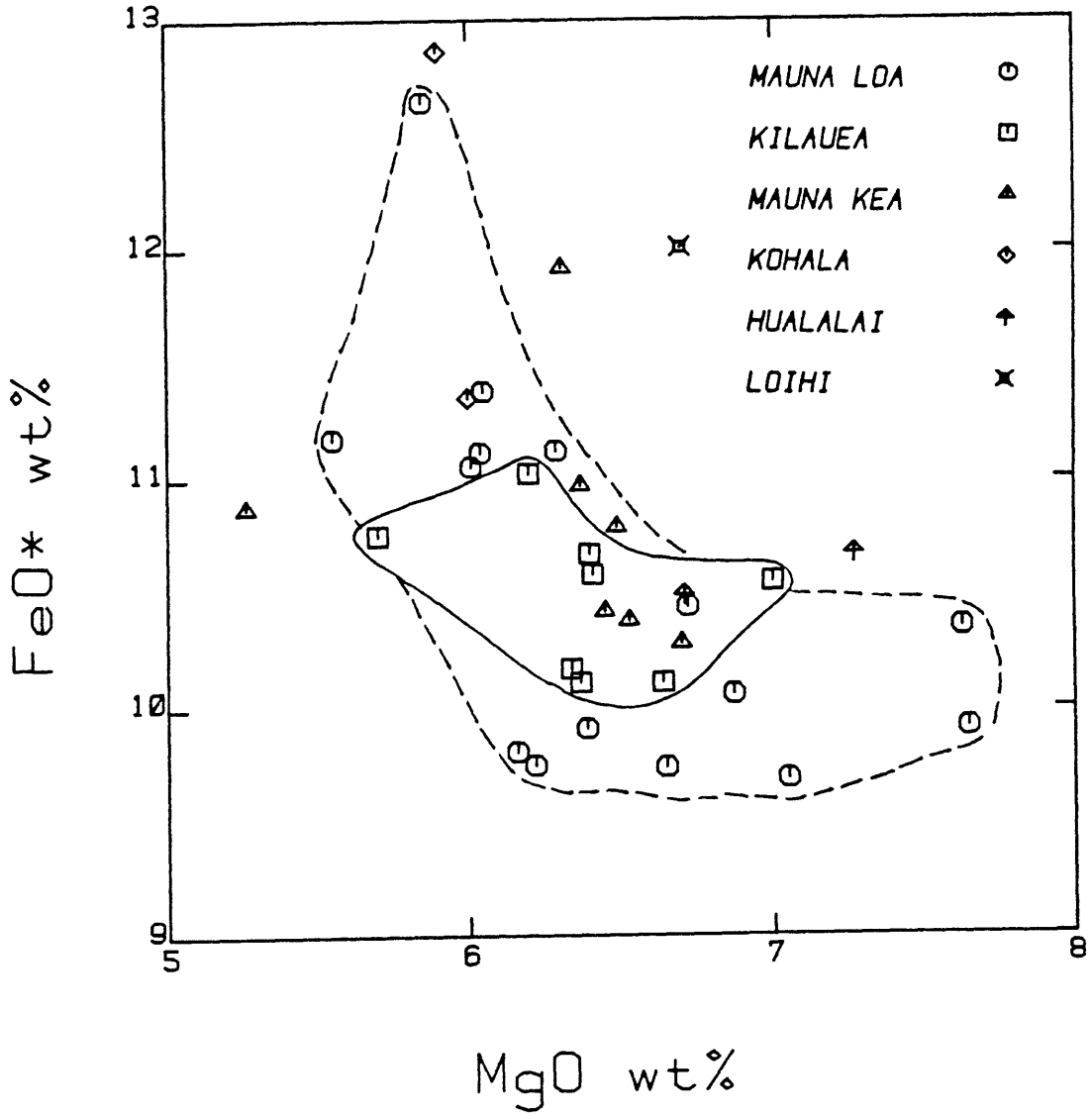

Figure 3.5(b). Same as 3.2(b).

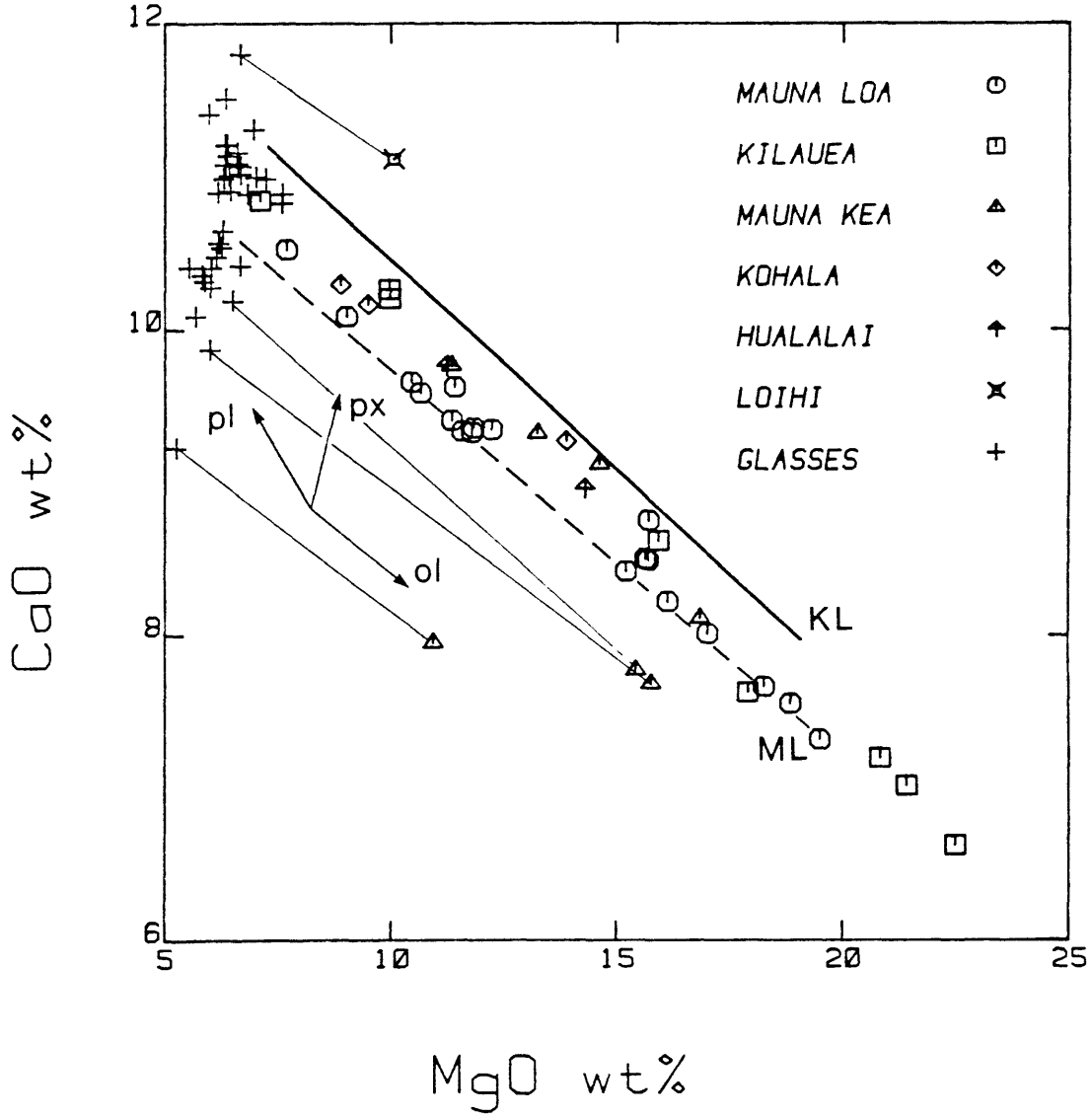

Figure 3.6(a). Same as 3.2(a).

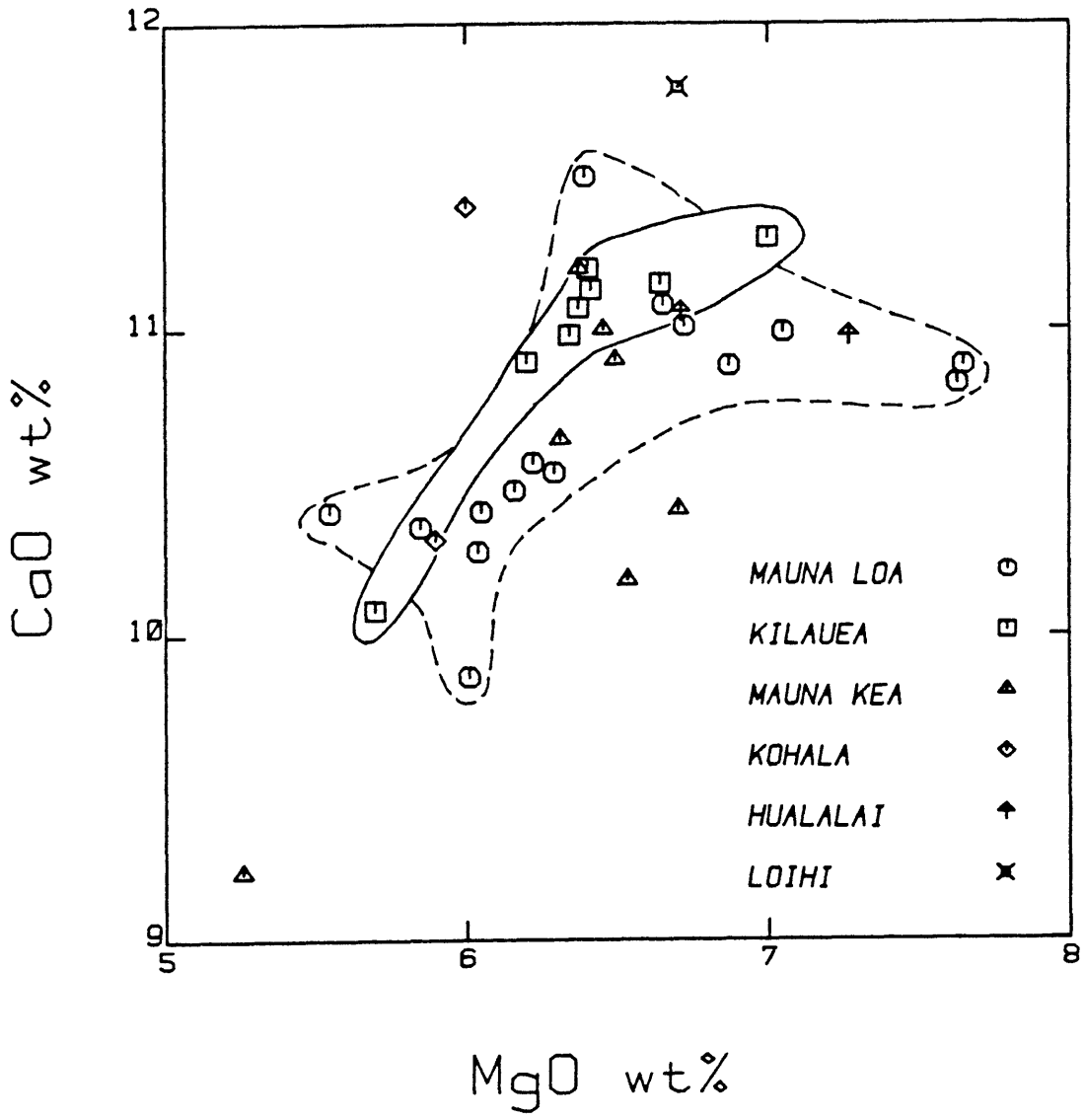

Figure 3.6(b). Same as 3.2(b).

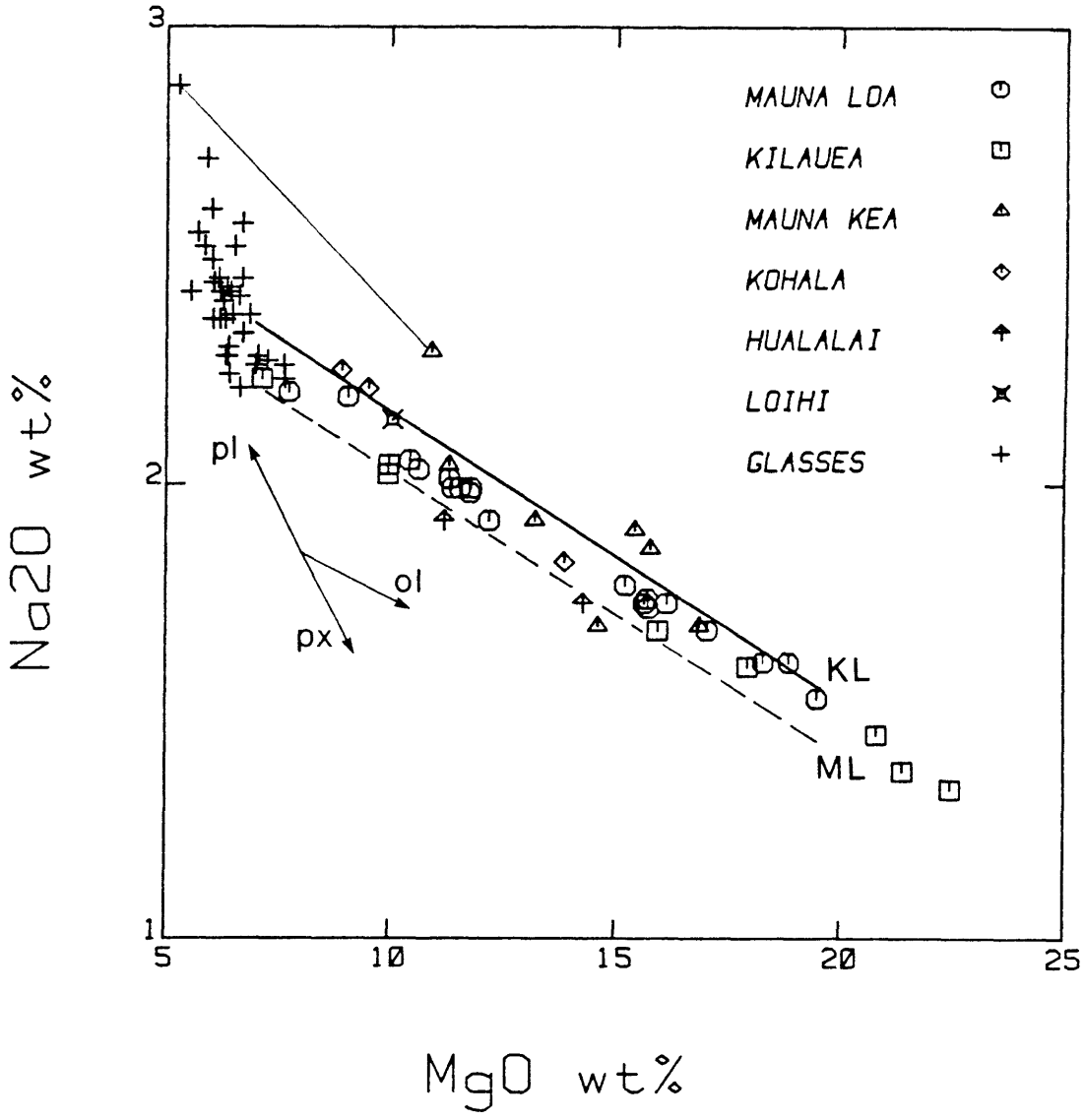

Figure 3.7(a). Same as 3.2(a).

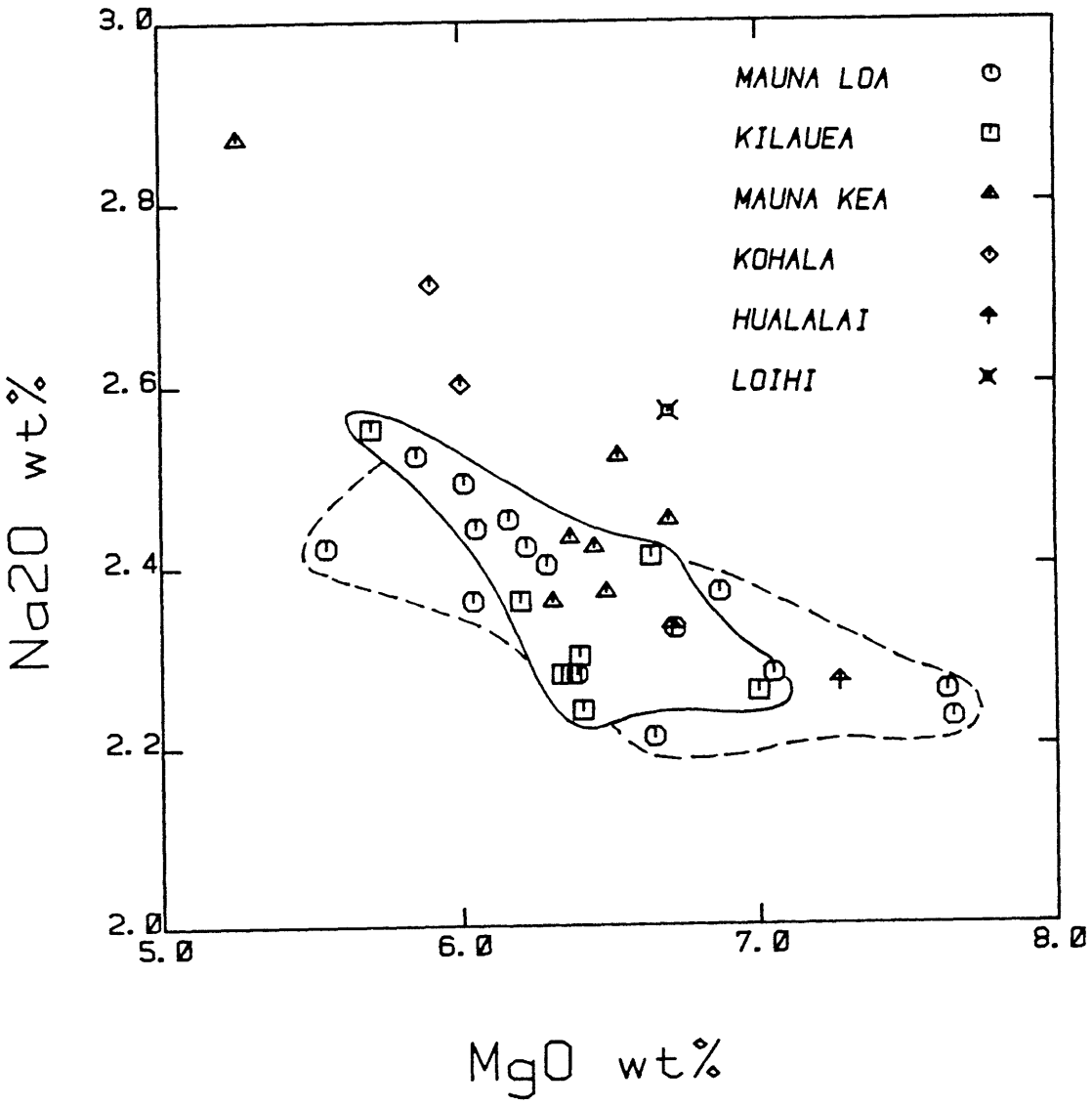

Figure 3.7(b). Same as 3.2(b).

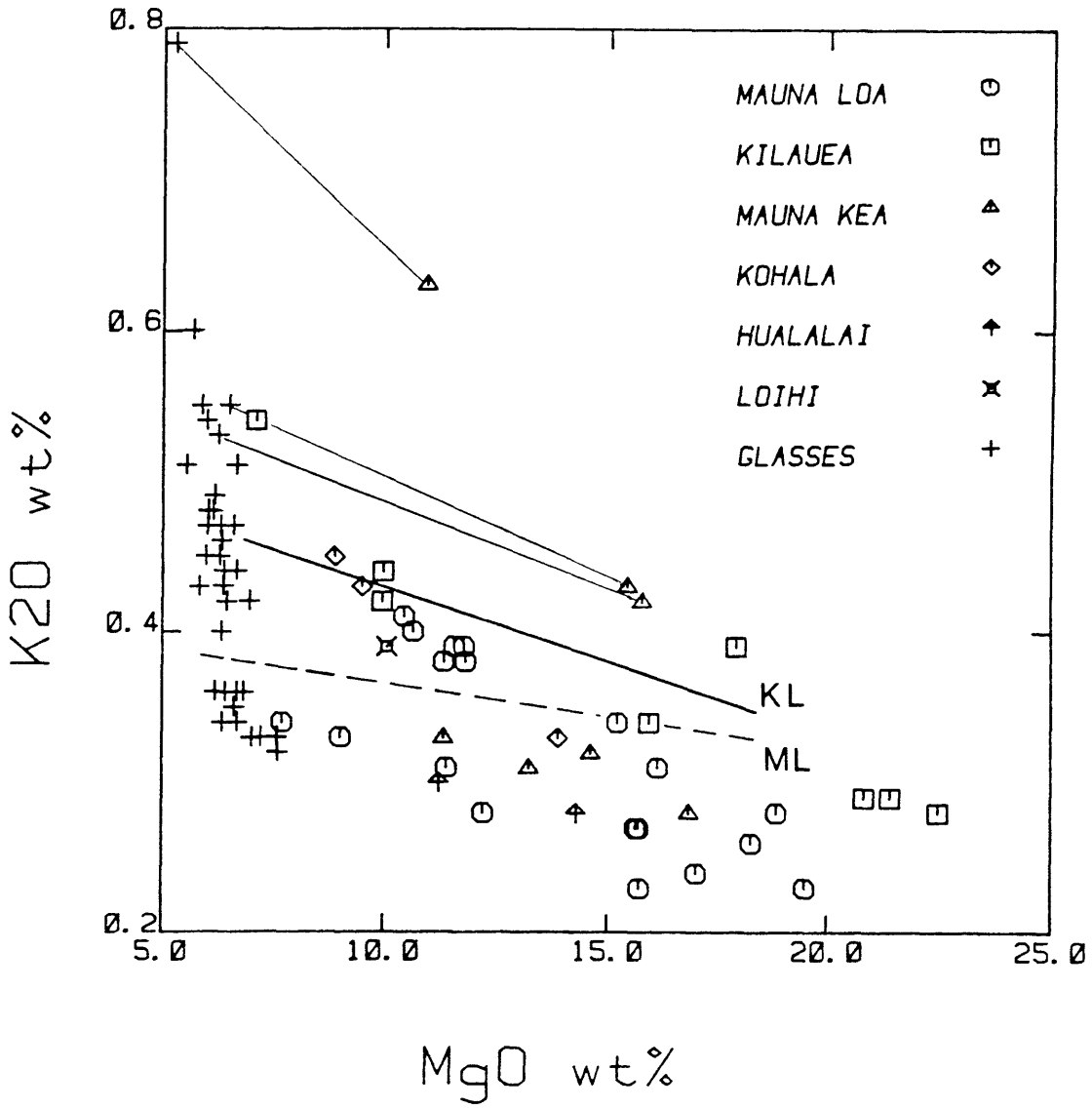

Figure 3.8(a). Same as 3.2(a).

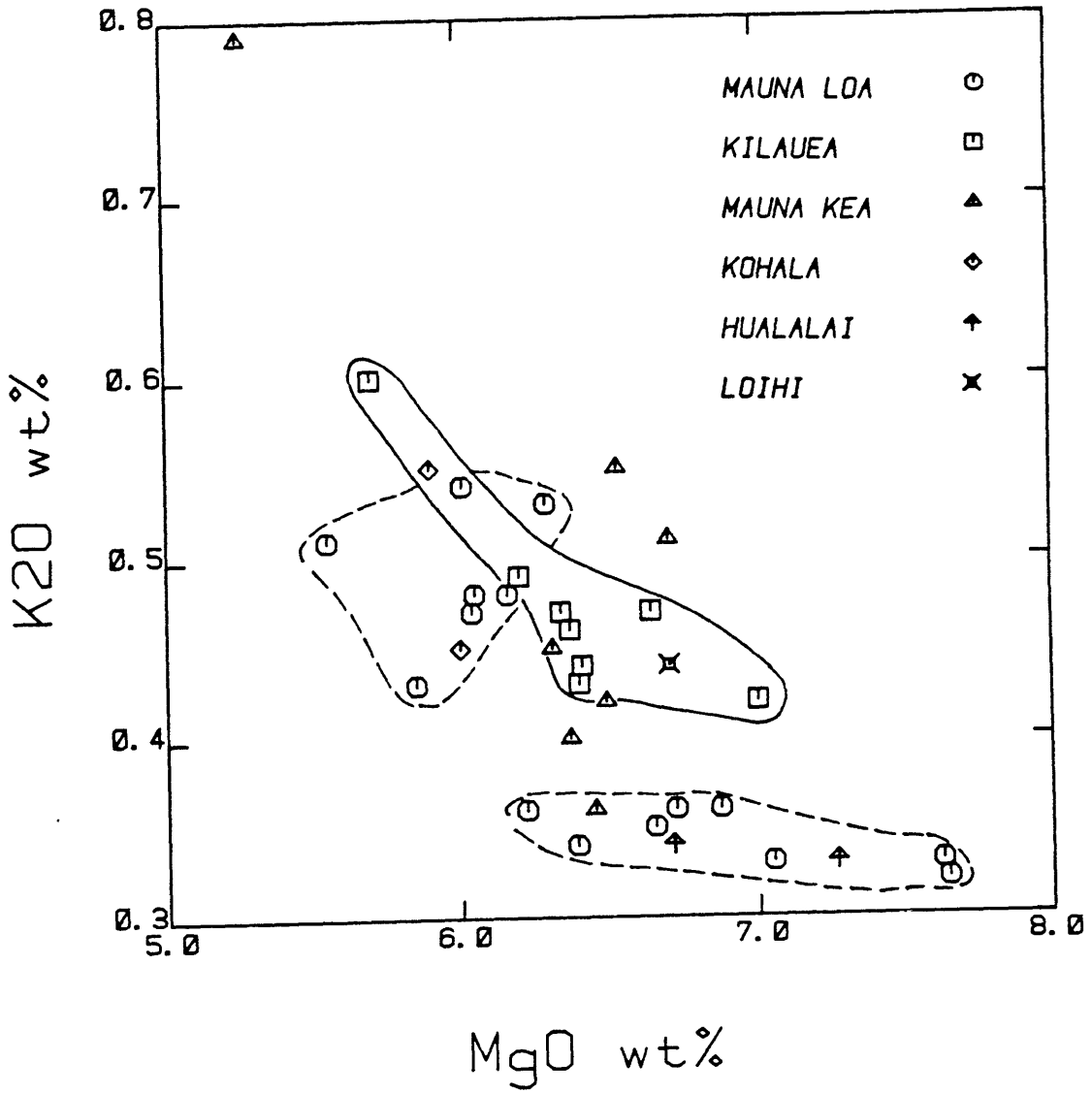

Figure 3.8(b). Same as 3.2(b).

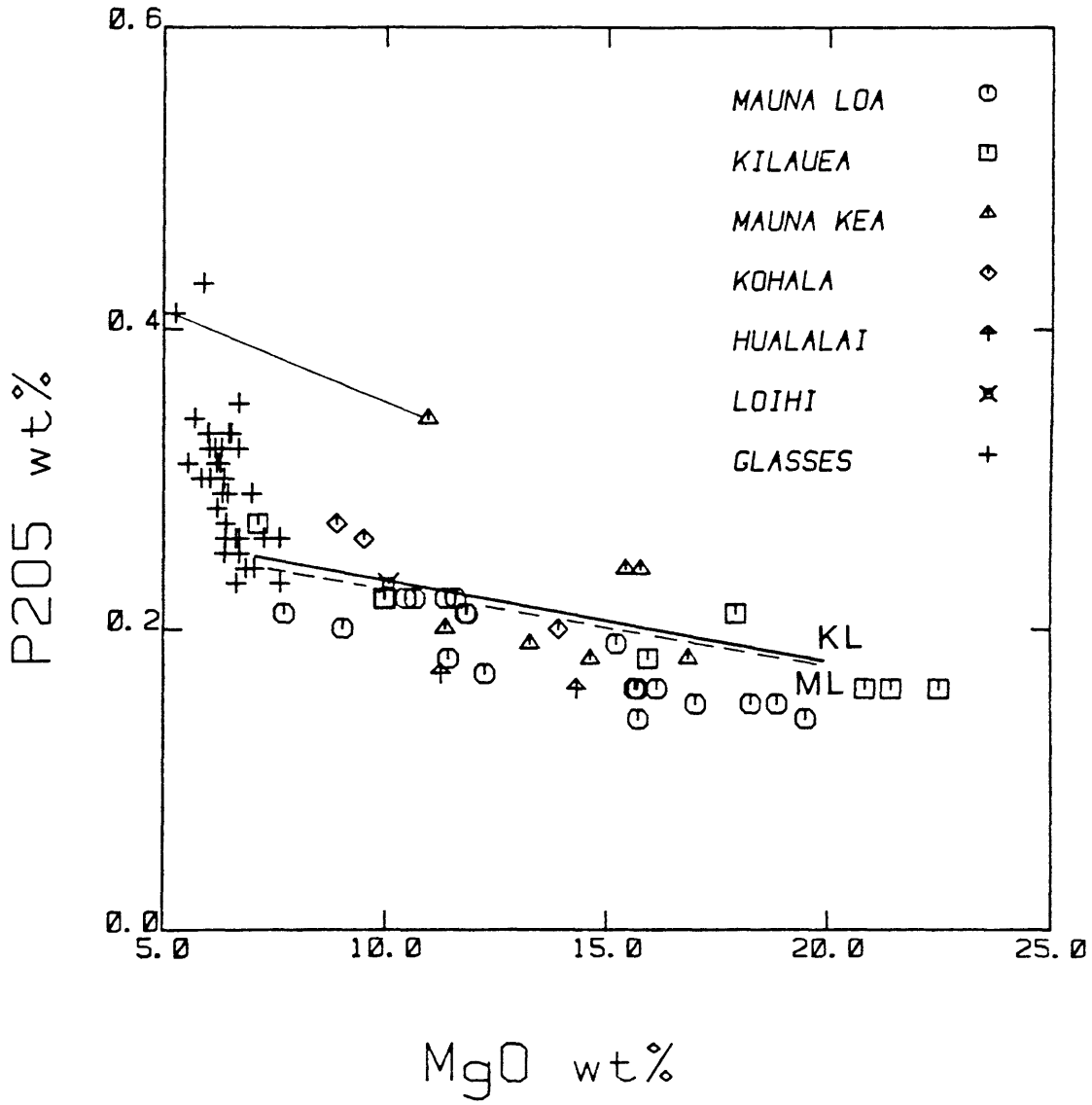

Figure 3.9(a). Same as 3.2(a).

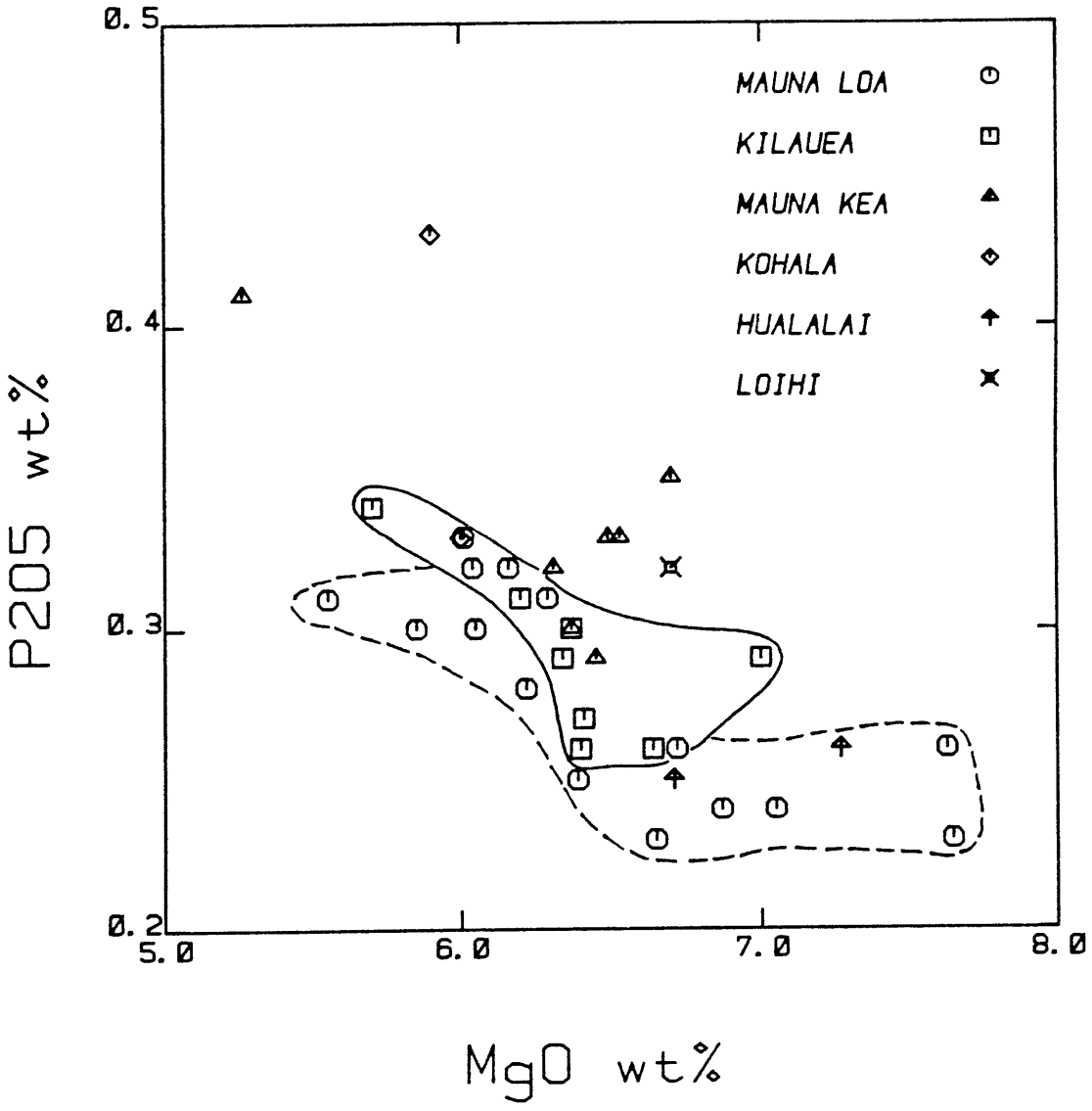

Figure 3.9(b). Same as 3.2(b).

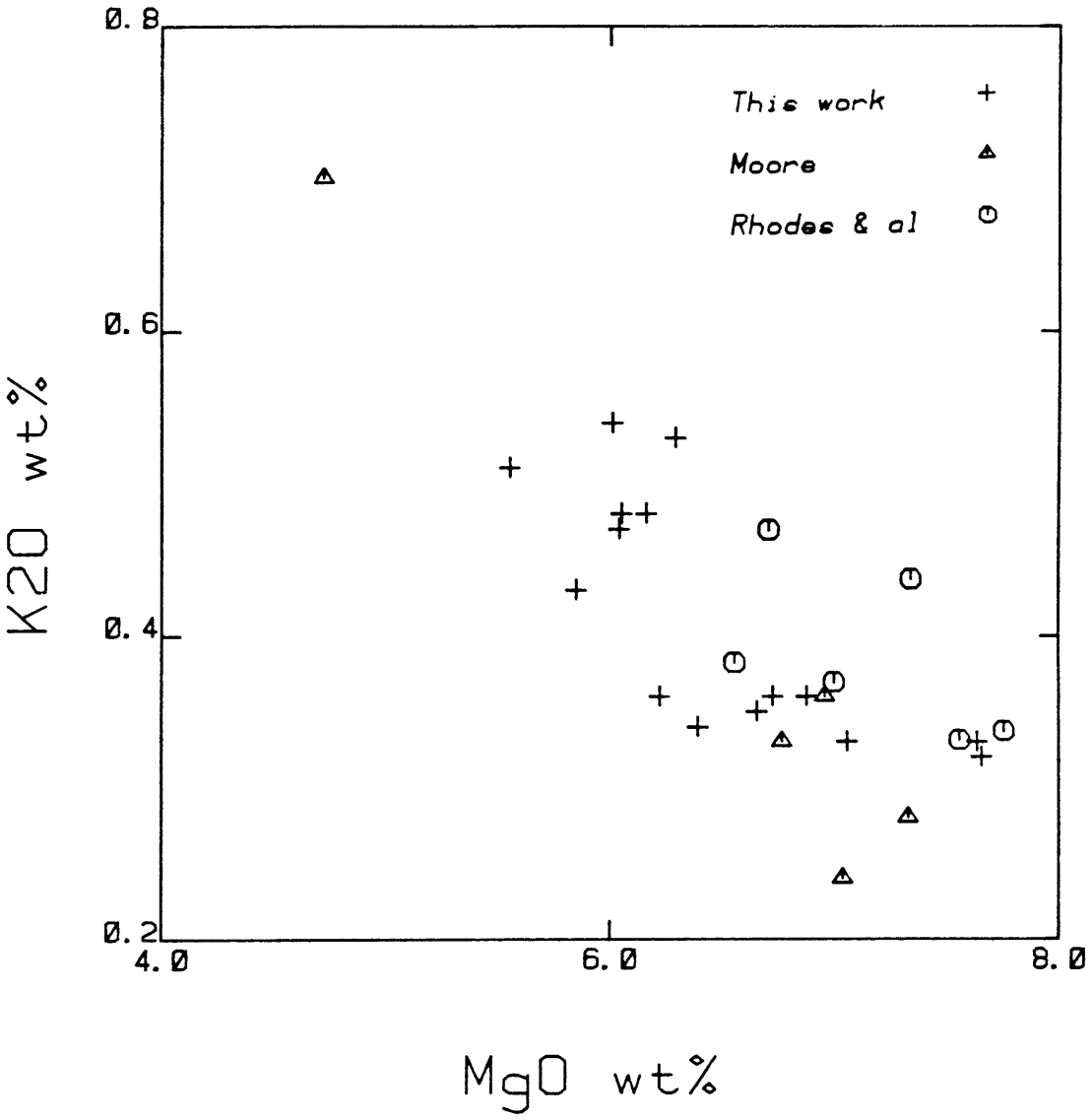

Figure 3.10. Abundance variation diagram of K_2O versus MgO for the glasses from Mauna Loa. Also plotted are five glasses collected by J. Moore and six historical samples analysed by Rhodes and Hart (unpublished data).

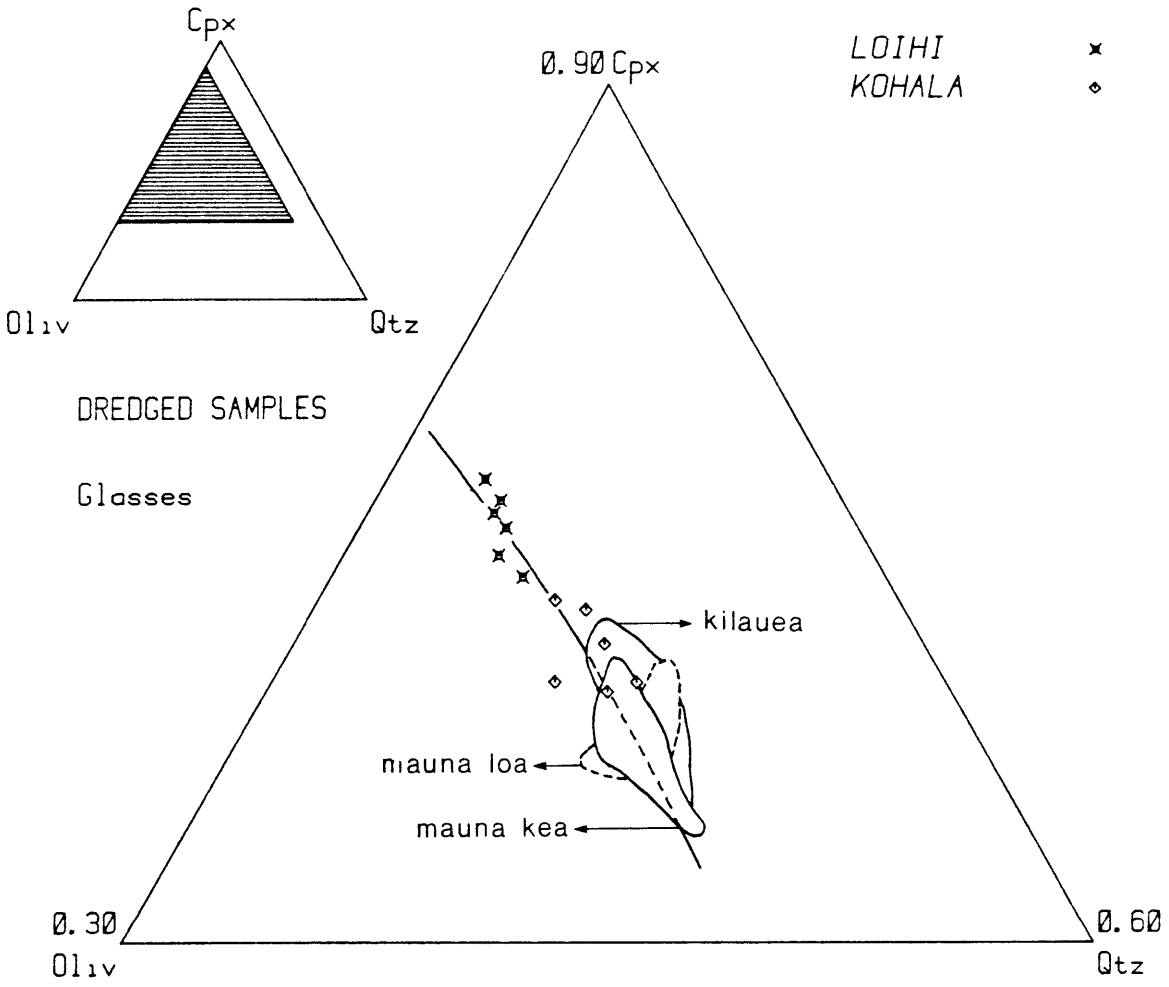

Figure 3.11. Projection of the complete glass data set on the ol-cpx-qtz pseudoternary.

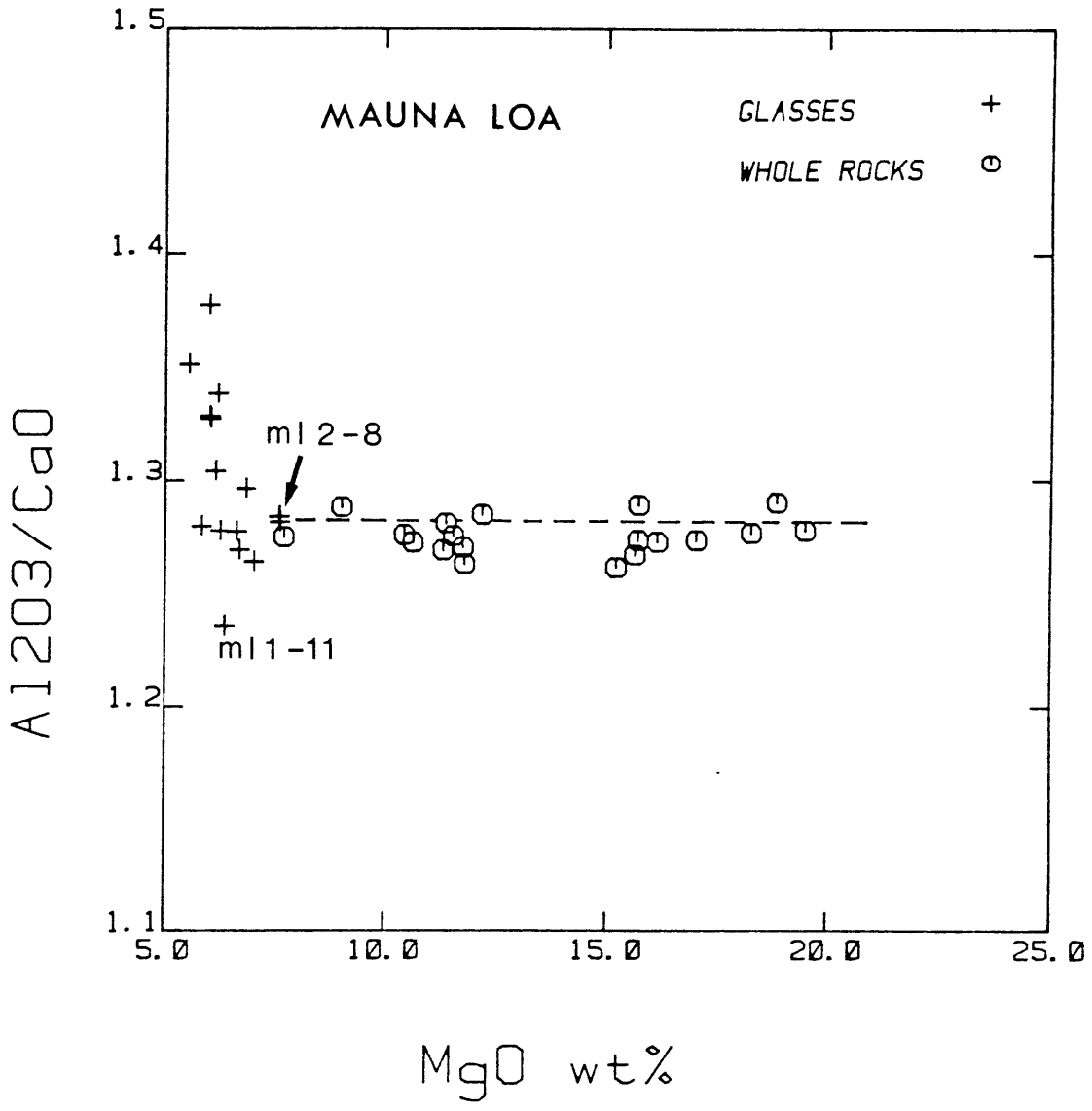

Figures 3.12. Plot of Al_2O_3/CaO *vs.* MgO in the glasses and associated whole rocks for Mauna Loa. The arrow points to the "parent" glass identified for each volcano.

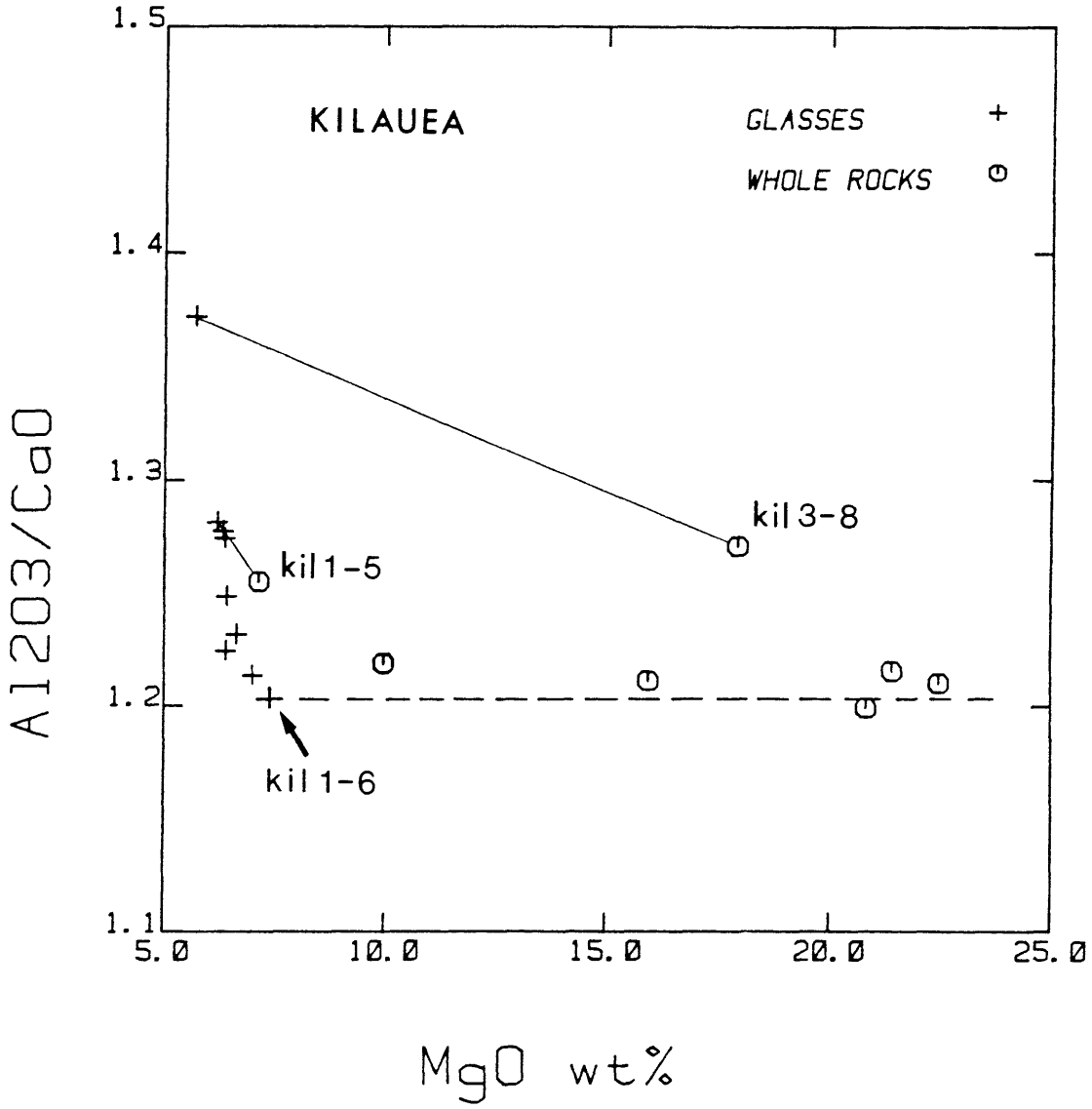

Figure 3.13. Same as 3.12 for Kilauea.

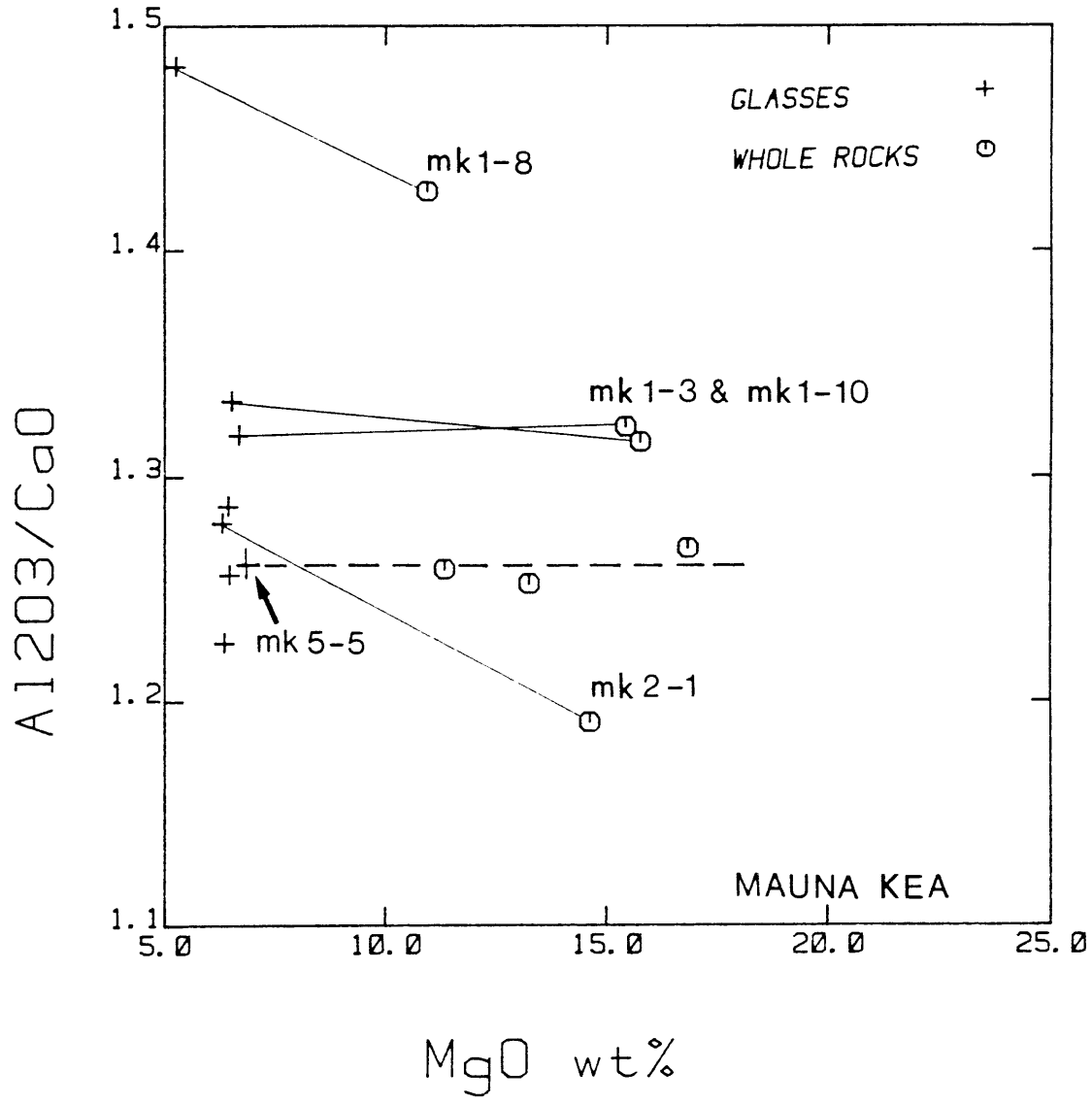

Figure 3.14. Same as 3.12 for Mauna Kea.

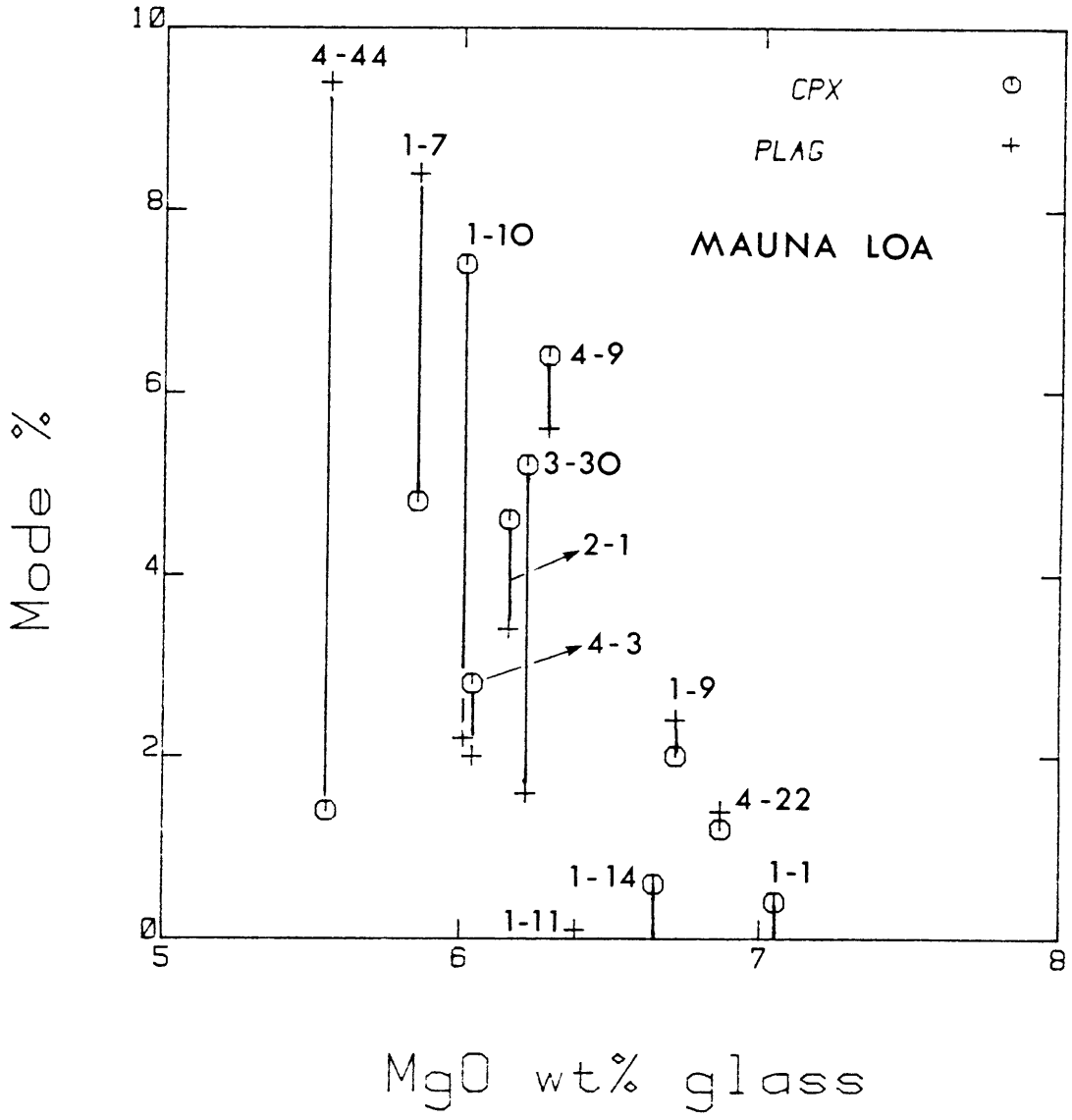

Figure 3.15. Modal abundances of clinopyroxene and plagioclase plotted against MgO content in the corresponding glasses, for Mauna Loa samples. Vertical lines join the two symbols corresponding to the same sample.

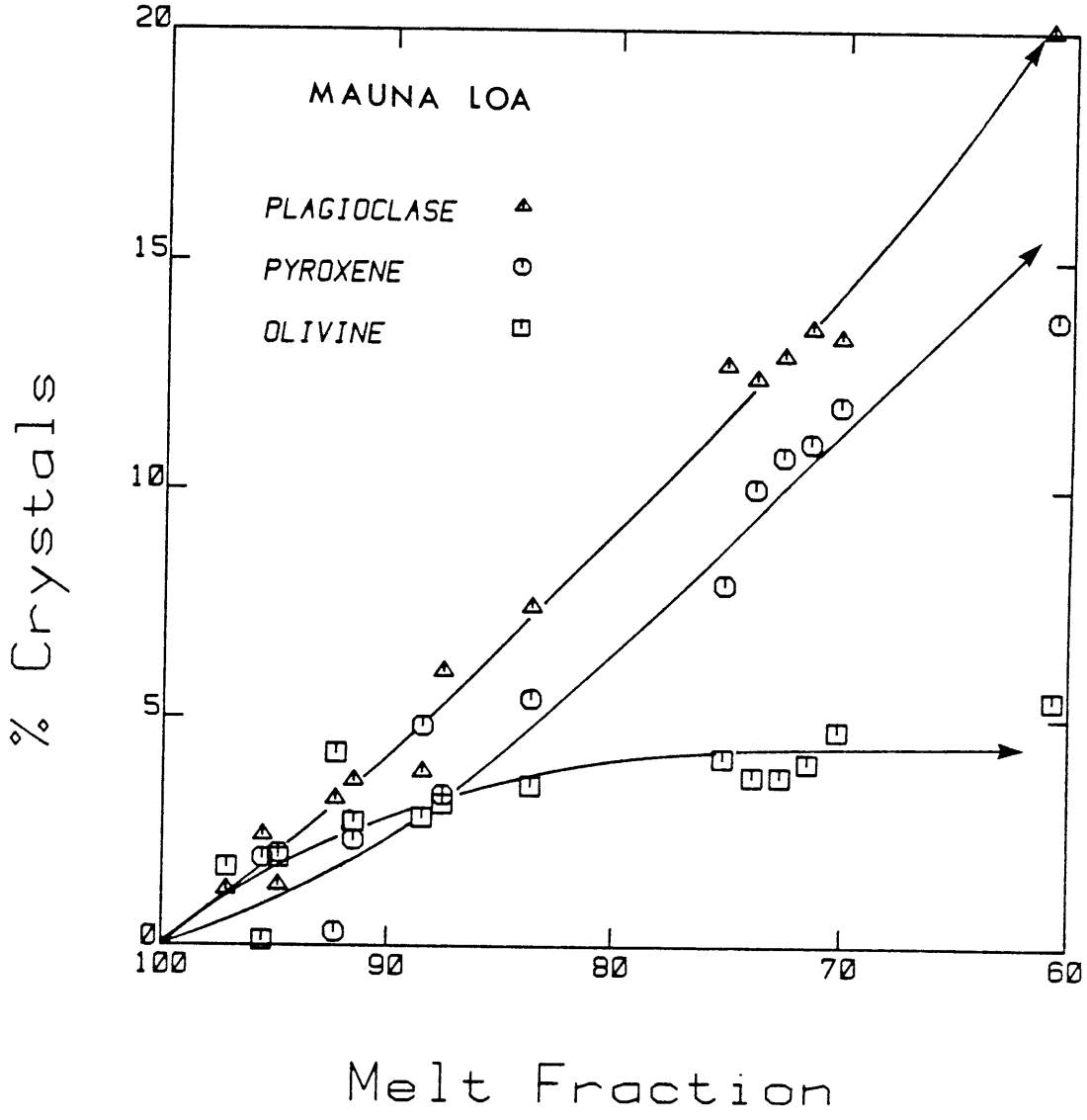

Figure 3.16. Abundances of fractionating phases (plagioclase, olivine and clinopyroxene) versus melt fraction as a result of low pressure crystal fractionation modelling (see text). The curves are eye fitted through the points and give qualitative insights on phase behaviour during differenciation.

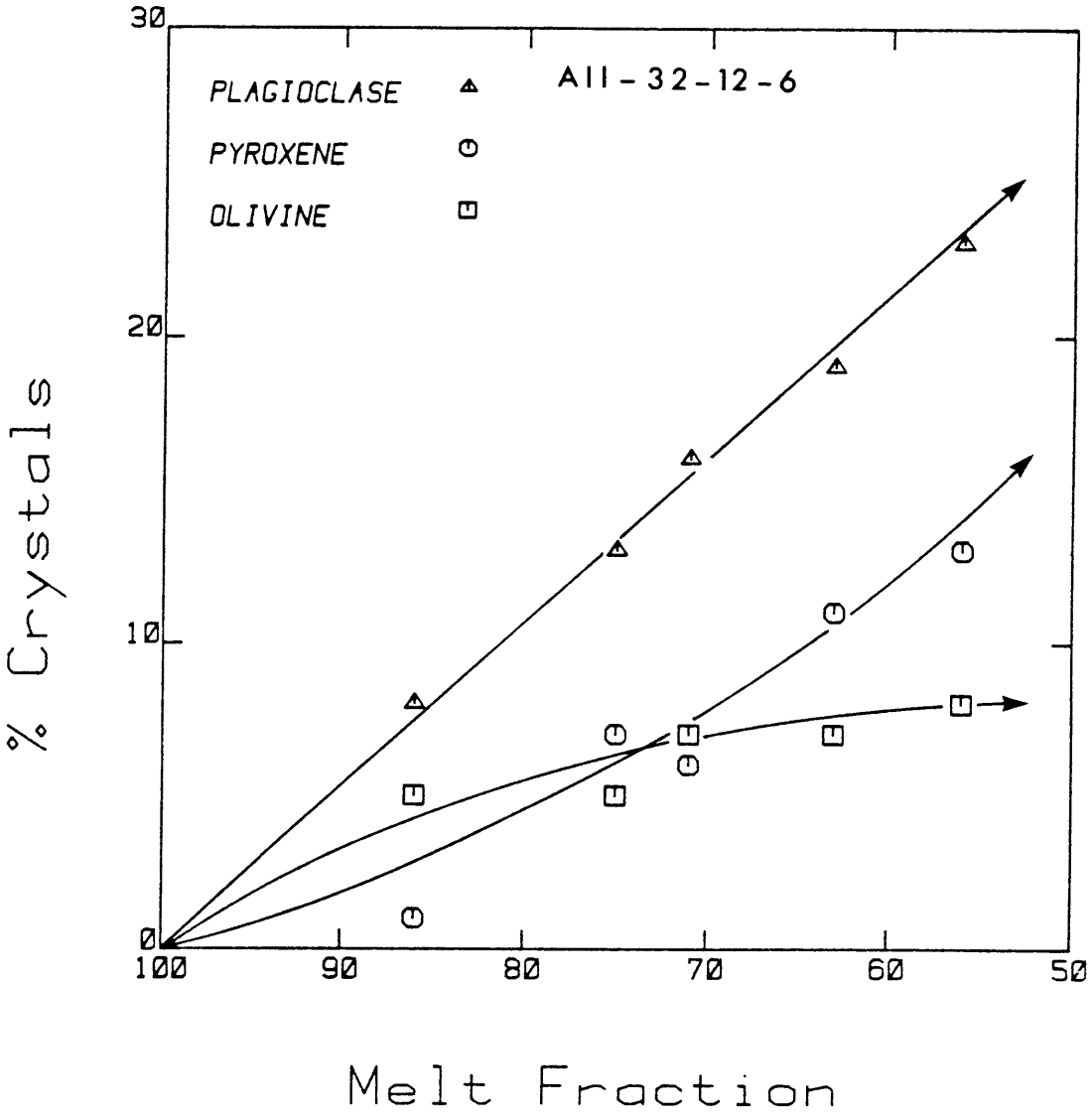

Figure 3.17. Abundances of fractionating phases versus melt fraction as a result of 1-atmosphere experiments on MORB sample AII-32-12-6 from Grove and Bryan, 1983.

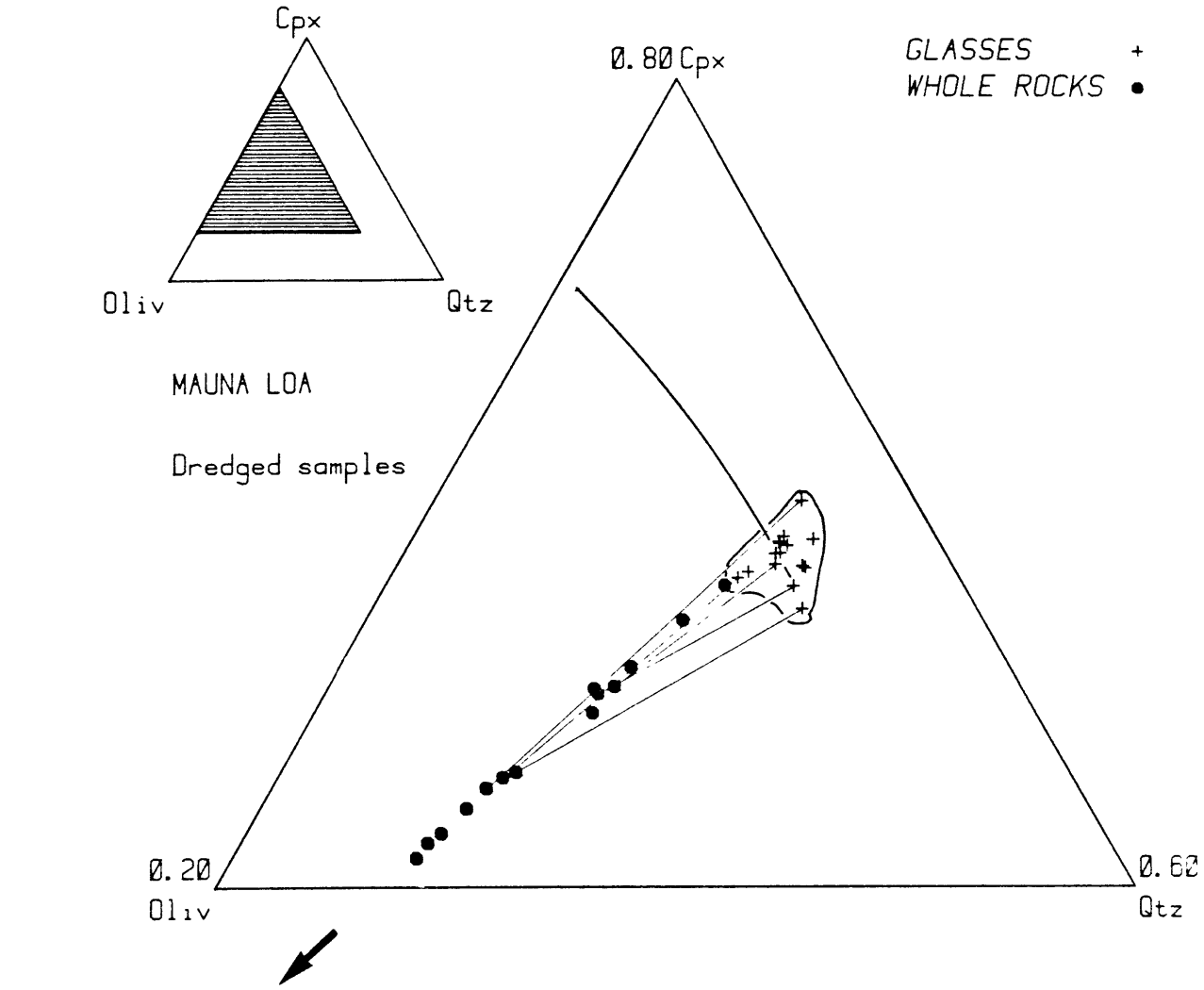

Figure 3.18. Glass and whole rock compositions projected on a portion of the Ol–Cpx–Qtz pseudoternary for Mauna Loa, Kilauea and Mauna Kea. The cotectic line was determined from the 1-atm. experiments of Tormey *et al.*, 1987. The solid arrow points directly to the olivine corner. The complete field of glass analyses made at the university of Hawaii is contoured.

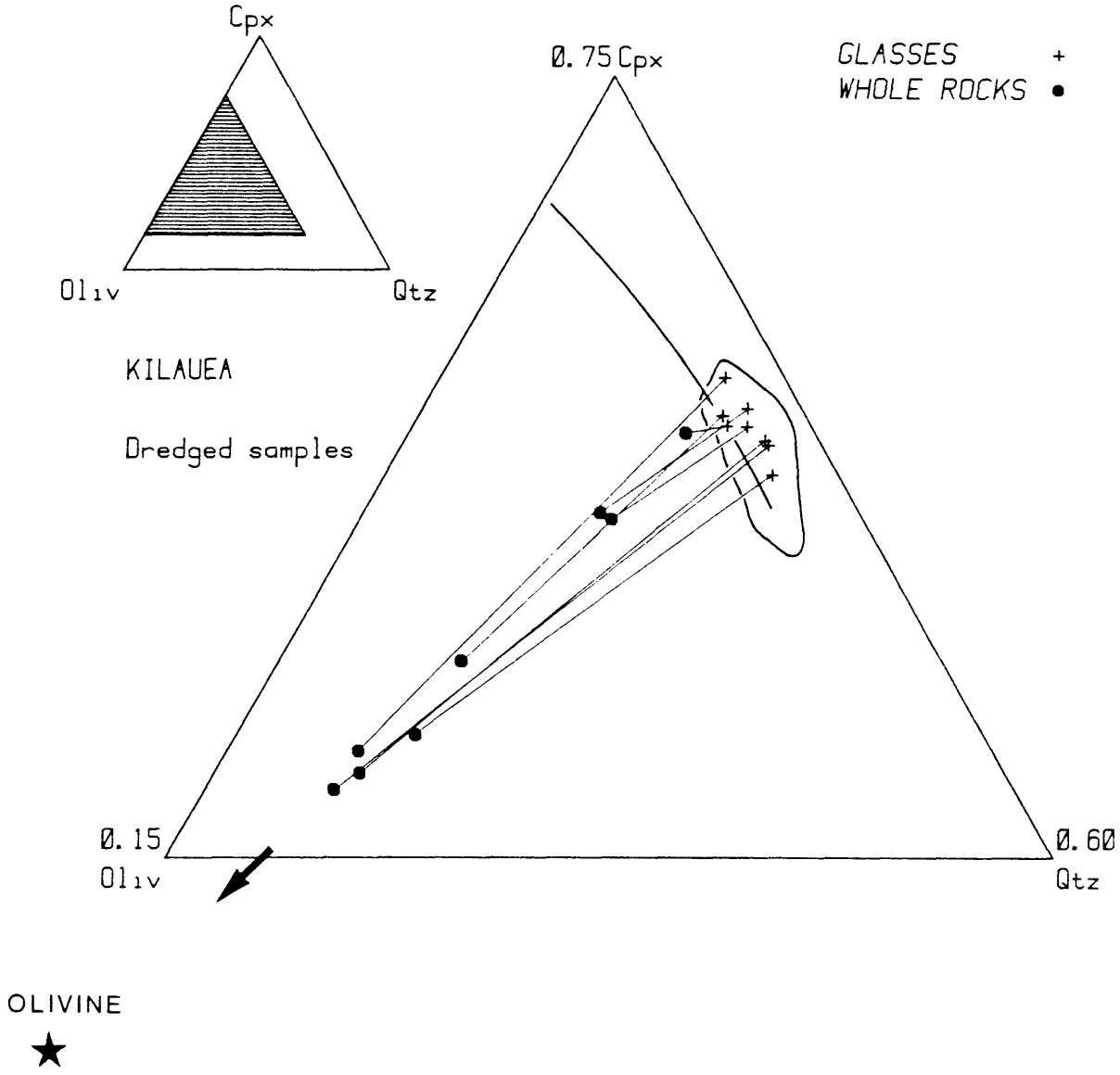

Figure 3.19. Same as 3.18 for Kilauea.

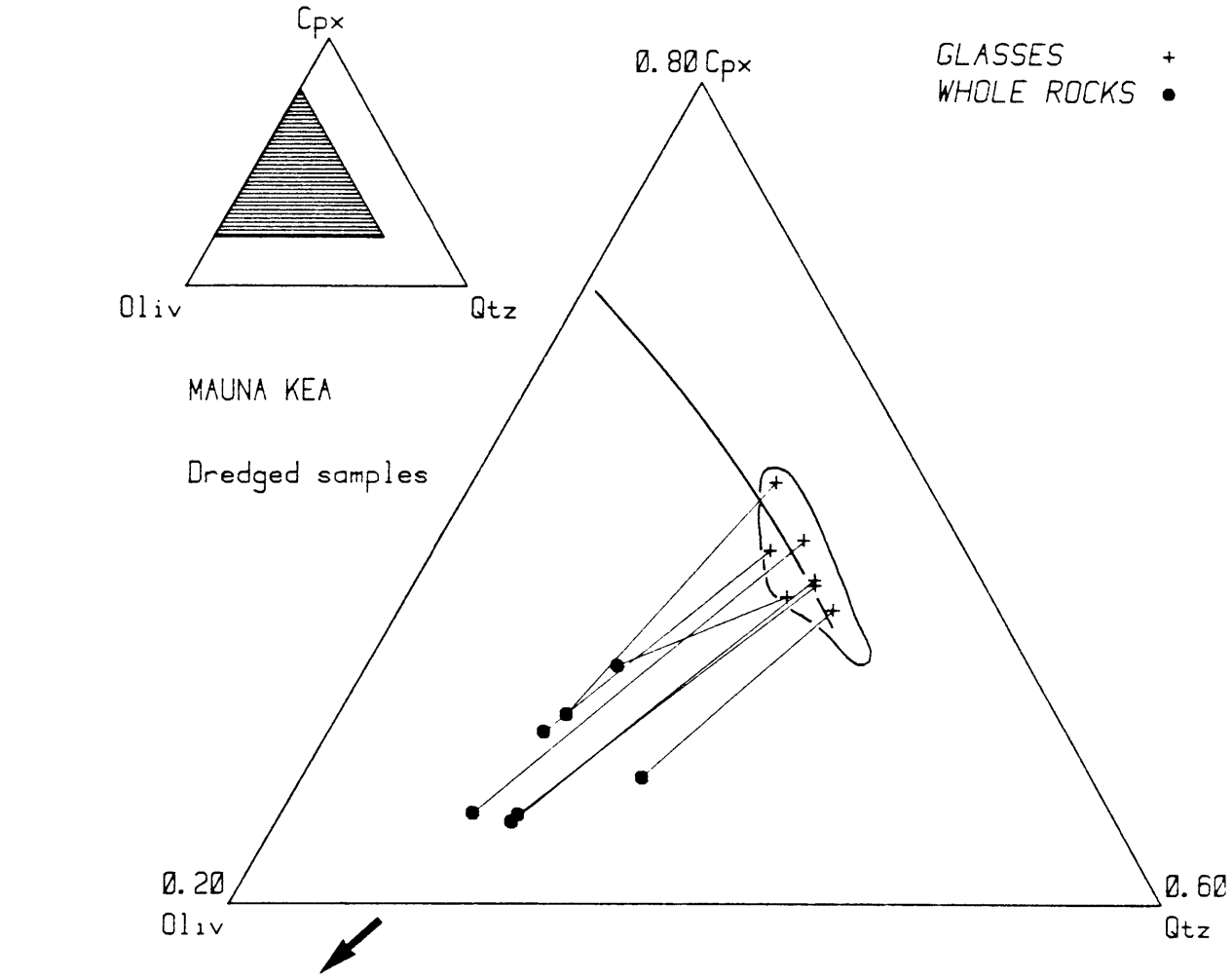

Figure 3.20. Same as 3.18 for Mauna Kea.

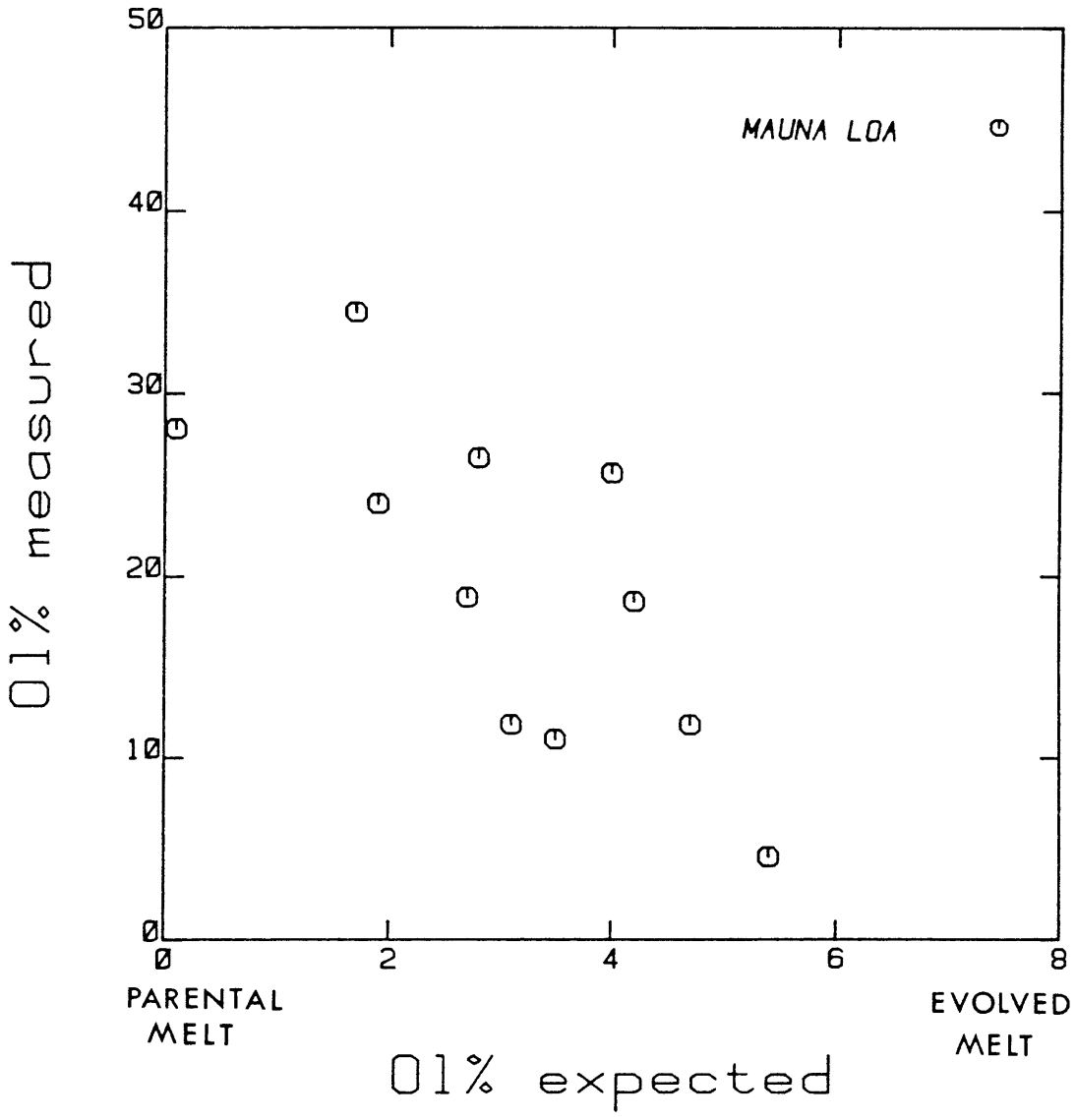

Figure 3.21. Plot of the olivine quantity that fractionated from the parental glass (see text) against the actual olivine content of the corresponding rocks for Mauna Loa.

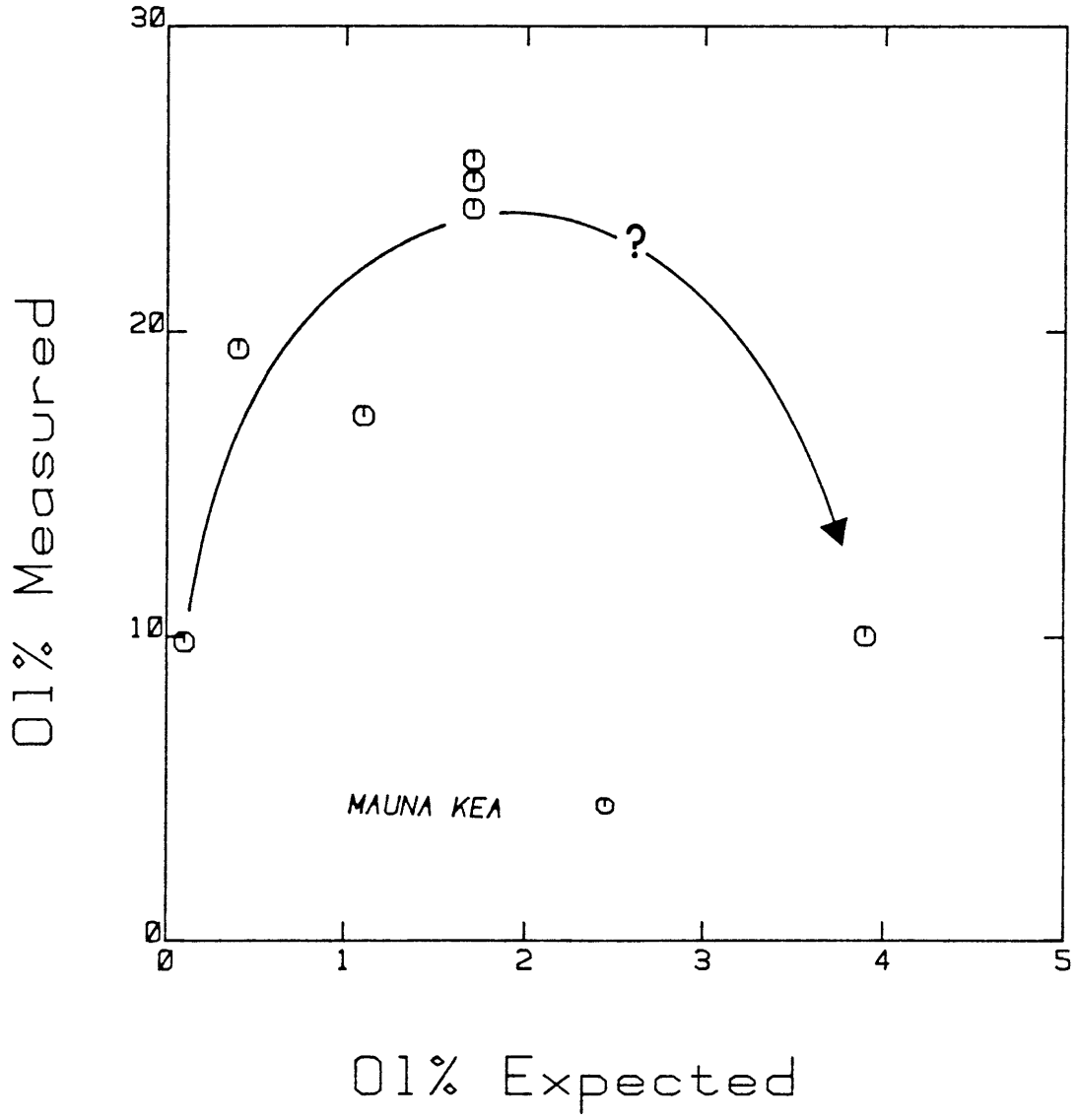

Figure 3.22. Same as 3.21 for Mauna Kea.

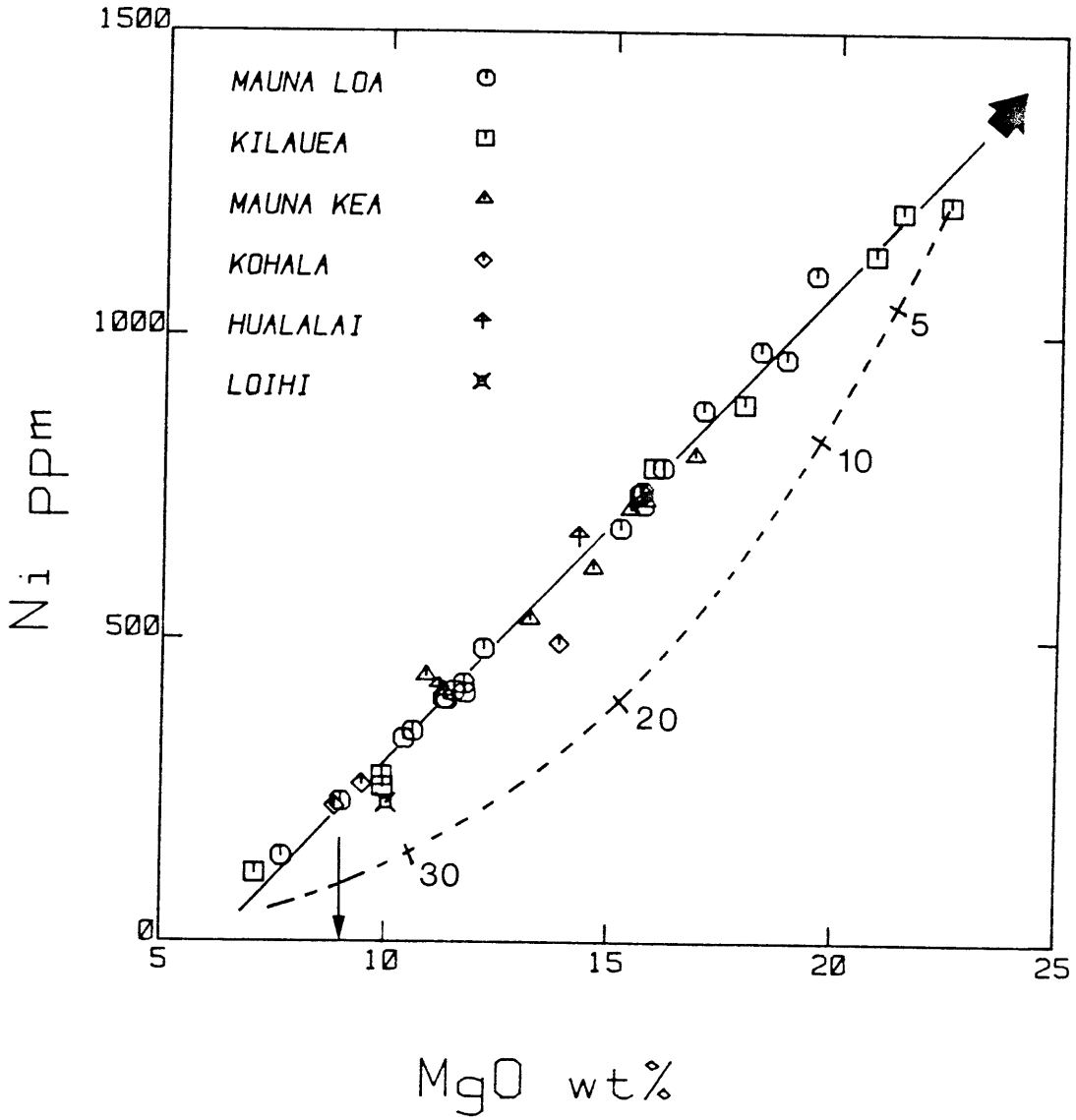

Figures 3.23–3.26. Transition element-MgO correlation plots for the complete data set. The solid line is the best fit line through the points. The vertical solid arrow points to an MgO content (9.2 wt%) corresponding to a liquid in equilibrium with accumulative olivines when the complete data set is regressed with no distinction of volcanoes. The dashed line, when present, gives the path of olivine fractionation from the highest MgO glass as explained in Appendix 1. Tick marks on this line indicate the amount of olivine that has fractionated from the highest MgO rock.

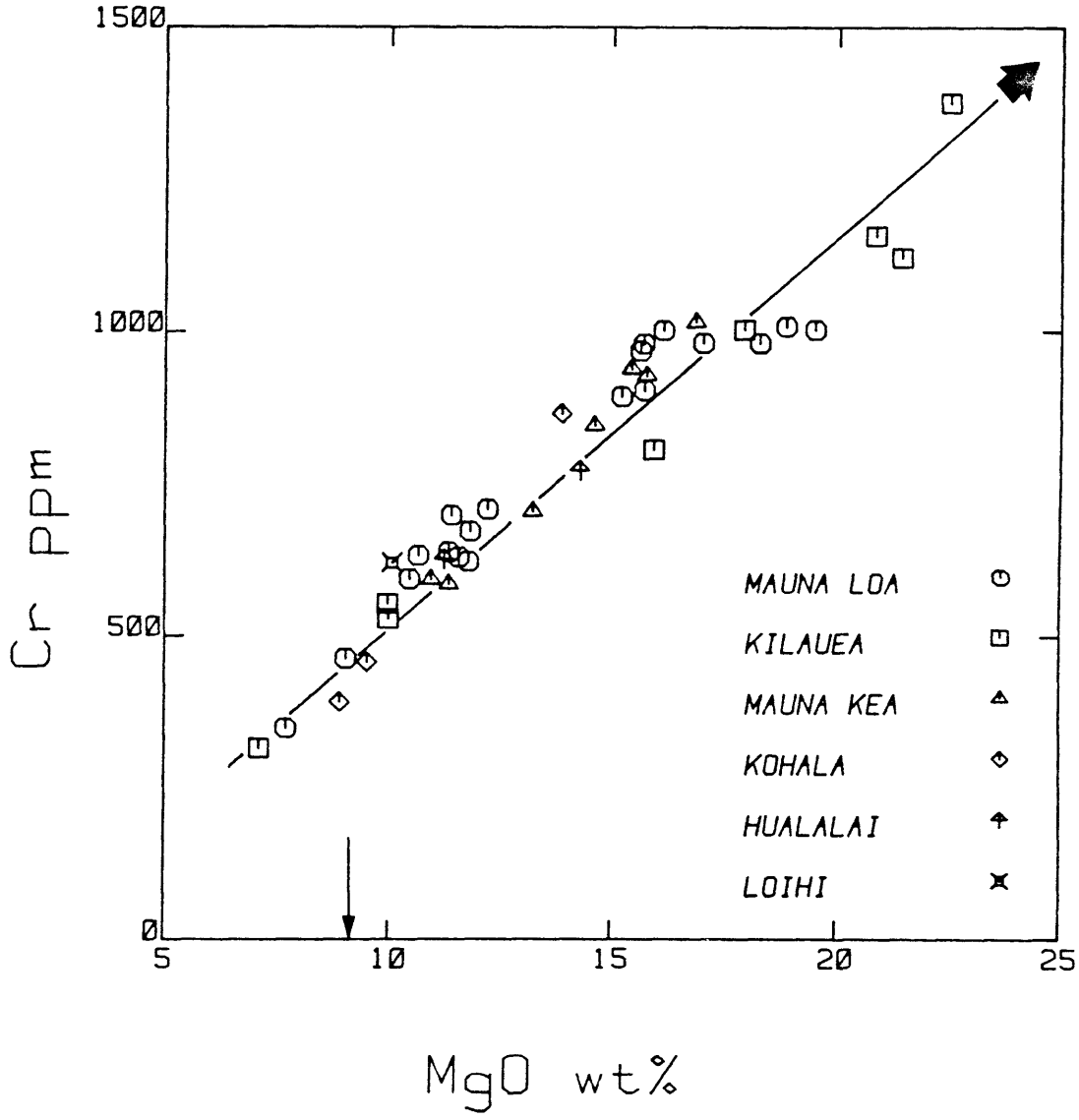

Figure 3.24. Same as 3.23.

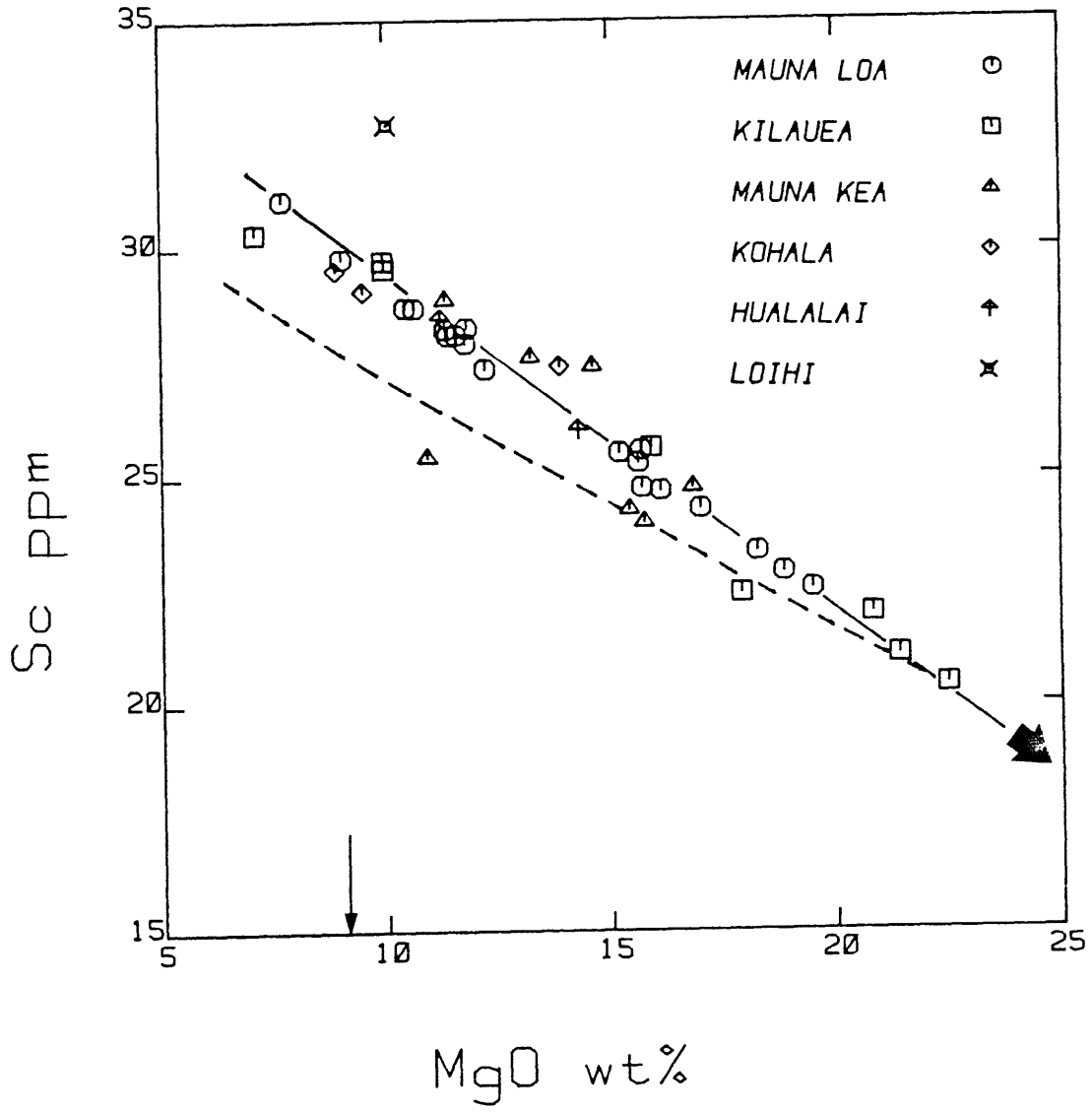

Figure 3.25. Same as 3.23.

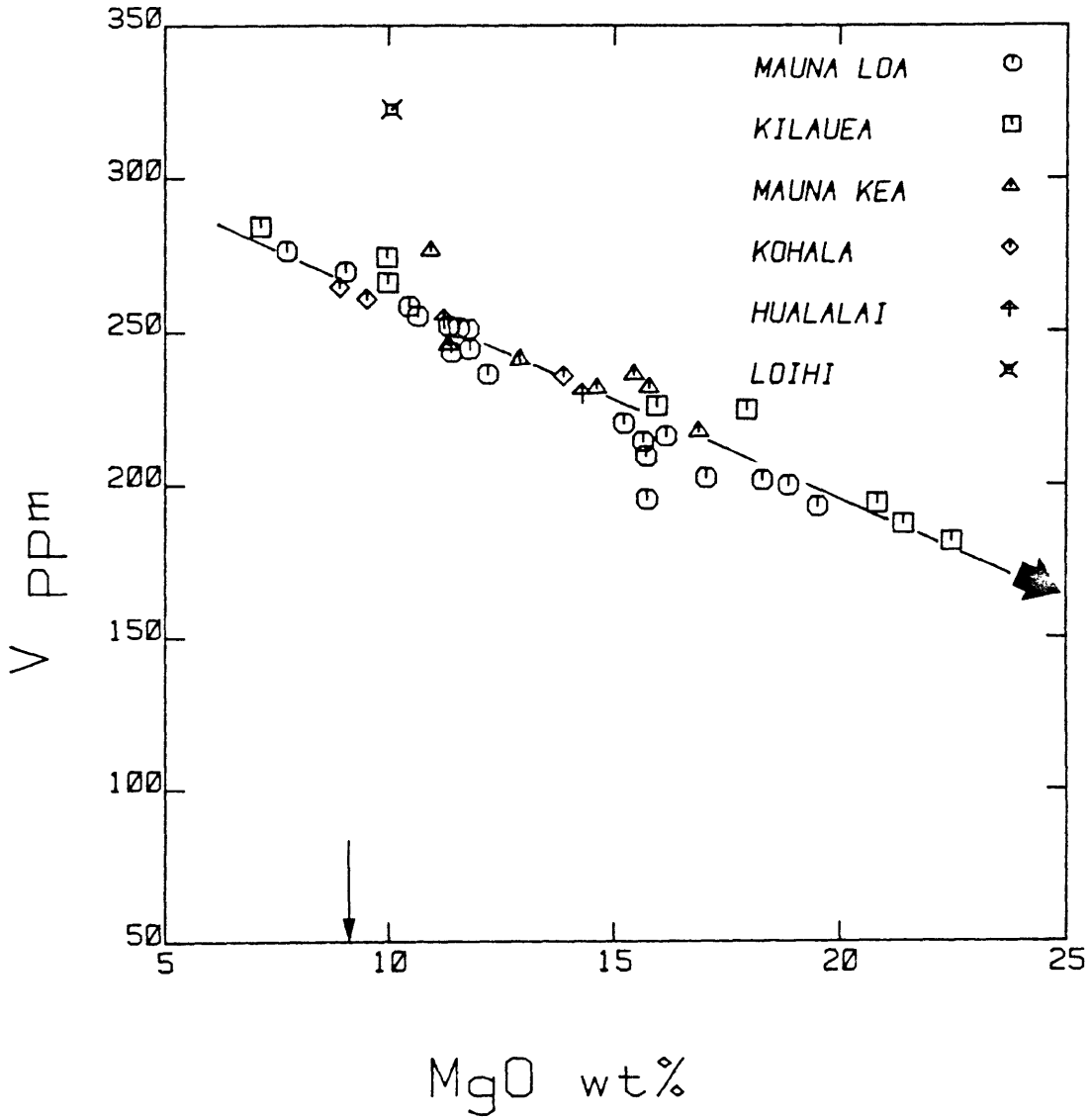

Figure 3.26. Same as 3.23.

4. ISOTOPE AND TRACE ELEMENT GEOCHEMISTRY

4.1. $^{87}Sr/^{86}Sr$ and $^{143}Nd/^{144}Nd$ Systematics

In this study, Sr isotopic compositions were determined on a subset of 16 samples, 9 coming from Mauna Loa dredges and the remaining 7 split between the other 5 volcanoes. Also, five of the the Mauna Loa samples with $^{87}Sr/^{86}Sr$ data were were analysed for Nd isotopic composition. Isotopic analyses focussed on Mauna Loa because this suite exhibits considerable heterogeneity in abundance ratios among incompatible elements.

Our new isotopic data are presented in Table 4.1 and agree to various degrees with existing data. Sample KIL2–9 has an $^{87}Sr/^{86}Sr$ ratio of .703605 which is well within the range of Kilauea tholeiites defined by the data of Stille *et al.*, 1987 (.70346–.70368) although clearly higher than any value reported for present day Kilauea by Hofmann *et al.*, 1984. Similarly, sample LO-6 has an $^{87}Sr/^{86}Sr$ ratio of .703488 which is within the range given by Lanphere, 1983 for tholeiites from Loihi (.70345–.70357) but lower than what was reported by Staudigel *et al.*, 1983 (.70353–.70370). Our two Mauna Kea samples differ markedly and range from the lower to the higher extreme of the data of Stille *et al.*, 1987 and Frey and Kennedy (unpublished). There is no systematic offset between our data and the values referenced

above that could indicate a major interlaboratory discrepancy or experimental flaw. Furthermore, all the references cited above, with the exception of Lanphere, 1983, provide $^{87}Sr/^{86}Sr$ ratios corrected to a value of .70800 for the Eimer and Amend $SrCO_3$ standard which is our procedure too. Seawater contamination may provide an explanation for the occurence of high $^{87}Sr/^{86}Sr$ values; this hypothesis could be tested by measuring the strontium isotopic composition of samples with high $^{87}Sr/^{86}Sr$ compared to the sub-aerial range (KO2–8 and MK1–8 for example), after acid-leaching, which was not done in this study. Also, the low $^{87}Sr/^{86}Sr$ values (samples LO6 and KIL2–9) do not depart from the existing subaerial range by more than two σ units. We therefore believe that the isotopic compositions measured do not differ systematically from previous data from Hualalai, Mauna Kea, Kilauea, Loihi and Kohala volcanoes. In contrast, our Mauna Loa data exhibits significant discrepancies with sub-aerial data sets. We observe a wide range of $^{87}Sr/^{86}Sr$ values (.703587–.703763) which is significantly lower than the range defined by the data of Stille *et al.*, 1987 (.70378–.70384) or Rhodes and Hart, 1987 (unpublished data for historical lavas from 1843 to 1975: .703773–.703971). Also, $^{143}Nd/^{144}Nd$ reported range (.512885–.512950) is higher than Rhodes and Hart's (.512818-.512887).

$^{87}Sr/^{86}Sr$ and $^{143}Nd/^{144}Nd$ ratios are inversely correlated in the five Mauna Loa samples we analysed (Figure 4.1). This feature characterizes samples from single volcanoes (Roden *et al.*, 1981) to oceanic basalts taken as a whole (DePaolo and Wasserburg, 1976) and has been described as the "mantle array". Although many models were put forth to explain the occurence of a negative correlation, the most

likely explanation, on a small scale at least, is that it represents the time integrated covariation of Sm/Nd and Rb/Sr ratios during major petrogenic processes. It is well established that mixing within the mantle array is an important process (Chen and Frey, 1985). However, the trend that is observed in Figure 4.1, although very suggestive of a mixing event between Kilauea and Mauna Loa is misleading as will be shown when trace element systematics are considered in the next section.

In the simplest model, because the spread in $^{87}Sr/^{86}Sr$ ratio is the time integrated result of parent/daughter ratio differences in the samples, a positive correlation in isochron plots is also expected and indeed observed in Figure 4.2. The correlation is not perfect and is mainly defined by the split of the data in two groups with distinct isotopic ratios. It will be later shown that trace element concentrations in Mauna Loa data set also separate into these same groups. A rough age can be derived by calculating a best fit line through the data in Figure 4.2. The calculations yield an age of 0.9 b.y. which is slightly lower than the age range proposed by Brooks *et al.*, 1976, for the development of oceanic mantle heterogeneities (1.6 b.y.). It should finally be stressed that a negative correlation in an $^{87}Sr/^{86}Sr$ versus $^{143}Nd/^{144}Nd$ plot associated with positive correlations in the corresponding isochron plots corresponds to the simplest case of isotope systematics. The occurence of recent mixing between incipient melts from a depleted source (high Rb/Sr and $^{143}Nd/^{144}Nd$, low Sm/Nd and $^{87}Sr/^{86}Sr$) and an enriched component (high Rb/Sr and $^{87}Sr/^{86}Sr$, low Sm/Nd and $^{143}Nd/^{144}Nd$) is a possible explanation for the occurence of negative correlations in isochron plots associated with

apparently undisturbed $^{87}Sr/^{86}Sr$ *vs.* $^{143}Nd/^{144}Nd$ arrays (Chen and Frey, 1985).

4.2. Trace element variability

4.2.1. Introduction

The use of trace elements in the identification and interpretation of petrological processes has significantly increased in the past twenty years. In the last decade, fundamental theoretical papers defined the systematics and limitations of trace element behaviour modelling (*e.g.* Allègre and Minster, 1978). However, the precision that can be expected from sophisticated techniques (*e.g.* inversion schemes, Albarède, 1982) is often compromised by the relatively poor knowledge of key parameters like partition coefficients or by the superposition of diverse petrological processes (*e.g.* mixing, crystal fractionation) affecting the data set. Therefore, simpler approaches have became popular (Hofmann et al., 1984). Our approach to explaining the data is mainly based on the use of incompatible trace element ratios. Among all the trace elements analysed for, it is common wisdom to distinguish Rb, Ba, Th, Nb and La as highly incompatible elements in most basaltic source materials and typical Hawaiian fractionating assemblages (Ol+Opx+Cpx+Gt+Sp). In this study, the use of Ba whose abundance approaches the lower limit of reliable measurement by XRF is avoided. It is also widely accepted that ratios of highly incompatible trace elements are insensitive to crystal fractionation and only affected by very small degrees of partial melting hence their use, along with isotopic ratios, for assessing source heterogeneities or the occurence of mixing. For this purpose, ratios of trace elements with very similar partition coeficients can be used too (*e.g.* La/Ce, Sr/Zr,

Nb/Ta). On the other hand, ratios of moderately incompatible elements or ratios of trace elements with noticeably different partition coefficients (*e.g.* La/Sm) are affected by these processes. Finally, specific element abundances and their variations can be used to assess the importance of particular processes (*e.g.* K and Rb as tracers of alteration).

The following discussion will be focused on the volcanoes Mauna Loa, Mauna Kea and Kilauea for which enough samples were analysed to constitute a representative set.

4.2.2. Variations in trace element abundances and ratios

The trace element data set is presented in Table 4.2.; abundances of Rb, Sr, Ba, K, Zr, Nb, Hf, Ce, Nd, Sm, Eu, Yb and Y are plotted against La in Figures 4.3 to 4.15 because of its high analytical precision and relatively high incompatibility in most minerals. All these elements are positively correlated with La. In the above plots, the goodness of the fit of the data points to a straight line running through the origin seems to be a function of the analytical precision associated with the element considered (*e.g.* Ba *vs.* La) and the difference in incompatibility between the element and La (*e.g.* Yb *vs.* La). Element abundances vary by a factor of 3 or less for each individual volcano, as well as when the complete data set is considered. The range of straight lines running through the data set and the origin is systematically determined by two distinct clusters of Mauna Loa points identified earlier, except in the case of Nb which is highest in Kilauea samples. In all the

element plots, Kilauea data points plot along a relatively well contrained straight line going through the origin suggesting a simple history for these rocks. Sample MK1–8 defines the upper end of the range of trace element abundances in all the plots except Sr *vs.* La (Figure 4.4) where it is associated with other abnormally low Sr Mauna Kea samples (MK1–3 and MK1–10). It should be noted that these samples are associated with evolved glasses which have probably lost a fraction of their equilibrium phenocryst phases (Figure 3.14).

Ratios of La over Rb, Sr, Ba, K, Zr, Nb, Ce, Nd, Sm, Eu, Yb and Y abundances are plotted against La abundance in Figures 4.16 to 4.27. The ratios typically vary by more than 3 σ units and are broadly correlated with La abundance. These overall correlations probably reflect the consistent differences in partition coefficients between the elements ratioed throughout all petrological process having affected the rocks in their history. They also integrate a spurious correlation component that arises from the use of the same variable (La) as the denominator of both coordinates, whose correlation coefficient is given by

$$R_{\mathrm{La/i-La}} = \frac{C_{\mathrm{La}} - R_{\mathrm{La-i}}\, C_{\mathrm{i}}}{(C_{\mathrm{La}}^2 + C_{\mathrm{i}}^2 - 2\, R_{\mathrm{La-i}} C_{\mathrm{La}} C_{\mathrm{i}})^{1/2}} \qquad (8)$$

where $R_{\mathrm{La-i}}$ is the correlation coefficient between La and the other variable and C_{La} and C_{i} the coefficients of variation (ratio of the standard deviation to the mean) of the two variables (Chayes, 1949). In Table 4.3, we present the value of the spurious correlation coefficient for most La-incompatible trace element pairs. Surprisingly, these values are grater than 0.5 for all elements except Rb which tends to indicate that a significant part of the observed correlations, if not all, is artificial.

Some scatter is introduced in Figures 4.16 to 4.27 as a result of the olivine dilution effect in the form of horizontal trends affecting La absolute abundances only. This effect is particularly visible for Kilauea where the data points typically strike across the main positive trend (e.g Figure 4.24). However, the distribution of trace element ratios among individual volcanoes follows general rules summarized hereafter:

(1) Individual volcanoes as well as the two different Mauna Loa groups are characterized by distinct trace element ratios. This is best illustrated by La/Zr ratios (Figure 4.20) separating into five different fields (Kilauea, Mauna Kea and Hualalai, Kohala and two Mauna Loa groups).

(2) The total range in these ratios is systematically defined by the two groups of Mauna Loa data points that do not overlap.

(3) Variations in trace element ratios are always smaller in Kilauea data set than in Mauna Kea or Mauna Loa, and are proportional to the difference in incompatibility between the elements ratioed (*e.g.* in Kilauea, La/Sm ratios vary by a factor of 4% whereas La/Yb vary by a factor of 10%).

(4) Mauna Kea samples trace element ratios typically span over the range separating the two above mentionned Mauna Loa groups, in a positively correlated trend (*e.g.* La/Sm).

There are obvious exceptions to these rules. For instance, variations in La/Rb ratio within the depleted (low La/Sm) Mauna Loa group encompass the total range

in La/Rb of the whole data set (Figure 4.16) with very little variation in La absolute abundance. This feature should be associated with a similar, near vertical trend in a La/K_2O versus La plot (Figure 4.19) and will be discussed as a possible effect of low temperature alteration (Section 4.3.1). Also, samples MK1–3, MK1–8 and MK1–10 have significantly higher La/Sr ratios than the enriched Mauna Loa group. As mentionned earlier, these samples are associated with highly evolved glass. The hypothesis that their abnormally high La/Sr could result from plagioclase fractionation will also be discussed later. It should also be noted that discrepancies are common when the overall variation of a particular ratio approaches the analytical precision limit (compare La/Ce and La/Sm variations). In contrast, there is no simple explanation for the fact that Kilauea lavas are lowest in La/Ba and La/Nb ratios (Figures 4.18 and 4.21).

4.3. Process identification in the data set

Olivine accumulation has proved to be one of the major processes responsible for the major element variability in our dredged rocks. Because all incompatible elements as defined earlier have olivine/liquid partition coefficients equal or very close to zero, the effect of olivine addition is simple dilution. In order to correct for this effect and compare the lavas at a given MgO*, it is necessary to apply to each incompatible element abundance, a correction factor of magnitude (MgO^{Ol}-MgO*)/(MgO^{Ol}-MgO) where MgO^{Ol} in the mean MgO content of the accumulative olivine phenocrysts and MgO the magnesium oxide content of the lava considered. Taking an Fo85 olivine (45wt% MgO) as commonly found in our Mauna Loa samples (Table 3.2), a target MgO* of 10% as suggested by Ni-MgO modelling of the data and the maximum MgO found in any any whole rock (22.48% in sample KIL2–8), the highest correction factor applied in the data set is of the order of 1.5. This estimate is significantly lower than the range of element abundances at any given volcano (of the order of 3). Therefore, at least half of the total compositional range *and* the complete range of trace element ratios is the result of other petrological processes that we try to unravel in the following sections.

4.3.1. The effect of alteration in Mauna Loa

In Figures 4.16 and 4.19, it can be noticed that a group of samples from the "depleted" Mauna Loa group tend to scatter significantly in La/K_2O and La/Rb

with very little variation in the absolute La content. These near vertical trends indicate that K_2O and Rb concentrations vary independantly of other trace elements in the samples considered. This characteristic can also be observed in La *vs.* Rb and La *vs.* K_2O plots (Figures 4.3 and 4.6) where the same samples depart slightly from the main trends toward high Rb and K_2O values. The two most affected samples are ML3–30 and ML1–11 (lowest in La/K_2O and La/Rb).

Although all the samples analysed appear pristine in thin section (Garcia, personnal communication), we tested the hypothesis that the above singularities could be the result of alteration in a marine environment by plotting K_2O/Rb ratios against La in Figure 4.28. All samples range between 600 and 800 in K_2O/Rb which is typical of fresh basalts (Hart and Nalwalk, 1970). However, samples with abnormally high La/Rb and La/K_2O from the depleted Mauna Loa group also tend to have slightly higher K/Rb than other Mauna Loa samples. Also, detailled thin section analysis of selected Mauna Loa rocks revealed slight brown alteration features in the glass of sample ML1–11 that may be related to the formation of clay particules. At this point, it is a satisfying explanation that clay formation within the glass may be responsible for the slightly high Rb and K_2O concentration observed in the rocks. However, microprobe study of the brown alteration features in the glass of sample ML1–11 are needed to confirm that these zones are indeed enriched in the above elements. There is no straightforward explanation however, for the abnormally high La/Rb ratio in sample ML1–9 (Figure 4.16).

Because Rb is decoupled from Sr during this alteration process, it is likely that

the Rb/Sr ratio of sample 3-30, the second most affected sample, is biased toward high values. Correcting the La/Rb ratio of sample 3-30 to 1.68 which is typical for unaltered samples from the depleted Mauna Loa group (ML1–1 and ML1–7 for example; see dotted line in Figure 4.16), the Rb value for ML3–30 becomes 3.56 ppm hence a Rb/Sr ratio of 0.018. This in turn amounts to shifting the original ML3–30 point to the black dot in Figure 4.2 which makes up for a better looking isochron. On the scale of Hawaii tholeiites as a whole, variations in K_2O/Rb between volcanoes are responsible for a very significant scatter in a strontium isochron plot (Figure 4.29) because of the strong negative correlation between K/Rb and Rb/Sr ratios that is found in these lavas (Figure 4.30).

4.3.2. Low pressure fractionation at Kilauea and Mauna Kea

As expected, Kilauea samples distribute along strong olivine control lines in a La *vs.* MgO plot (Figure 4.31). Samples KIL1–5 and KIL3–8 plot slightly above the trend. These two samples are also characterized by higher Al_2O_3/CaO ratios than the other Kilauea samples (Figure 3.13) which is consistent with the occurence of low pressure clinopyroxene fractionation. In Figure 4.32, a similar plot for Mauna Kea samples exhibits significant departures from a straight line. By analogy with Figure 3.14, we choose to define the reference olivine control line by samples MK5–13, MK6–6 and MK6–18 whose Al_2O_3/CaO ratios are similar to Mauna Kea parental glass. Samples MK1–3, MK1–10 and MK1–8 plot significantly above this trend and are also characterized by higher than normal Al_2O_3/CaO ratios. In order to

test if clinopyroxene fractionation can account for the difference between the most discrepant point (sample MK1–8) and a "regular" Mauna Kea sample (*e.g.* MK6–6), the following approach can be taken.

Fractionation is usually formulated in the form of a Rayleigh distillation equation

$$\frac{C}{C^0} = F^{D-1} \tag{9}$$

where C, C^0, F and D stand for the melt concentration, source concentration, melt fraction and partition coefficient in the fractionating assemblage respectively. Hence the variation in a ratio of two trace elements i and j in terms of the melt fraction

$$\frac{C_\mathrm{i}}{C_\mathrm{j}} = \frac{C_\mathrm{i}^0}{C_\mathrm{j}^0} F^{(D_\mathrm{i}-D_\mathrm{j})} \tag{10}$$

Taking the logarithm and differenciating, we get

$$d\left(\frac{C_\mathrm{i}}{C_\mathrm{j}}\right) / \frac{C_\mathrm{i}}{C_\mathrm{j}} = (D_\mathrm{i} - D_\mathrm{j}) \frac{dF}{F} \tag{11}$$

Since variations in rare earth concentration ratios are small compared to the absolute magnitude of the ratios themselves ($\leq$15%, see Figures 4.16 to 4.27), differentials can be replaced by differences. Equation 11 may be rewritten

$$\Delta\left(\frac{C_\mathrm{i}}{C_\mathrm{j}}\right) / \frac{C_\mathrm{i}}{C_\mathrm{j}} = (D_\mathrm{i} - D_\mathrm{j}) \frac{\Delta F}{F} \tag{12}$$

Therefore, for any two samples related by fractional crystallisation, all pairs of trace elements should lie on a straight line going through the origin when the difference in their respective partition coefficients in the fractionating assemblage is plotted against the relative variation in the ratio of their abundances between the two rocks

considered. Moreover, the slope of the line provides an estimate of the relative variation in melt fraction from one sample to the other. It is important to realize that one plot only accounts for the genetic relationship between two samples. For a complete suite of rocks presumably related by fractionation, a plot must be contructed for any pair of rocks. In the present case, we choose to construct a plot for the most different samples only (MK1–8 and MK6–6) and make the assumption that the same petrogenetic process may also be responsible for similar but smaller variations between the other Mauna Kea samples. Finally, in order to place a limit on interlaboratory biases, we restrict this treatment to rare earth elements for which coherent sets of partition coefficients are available (see Frey *et al.*, 1978, for review).

The results of the calculations are plotted in Figure 4.33 using clinopyroxene partition coefficients determined by Onuma *et al.*, 1968. The fit of the data points to a straight line through the origin is surprisingly good, although error propagation treatment was omitted. The slope of the best fit line is equal to 0.28 hence indicating a *relative* variation in melt fraction from MK6–6 to MK1–8 of approximately 30% which is reasonable. Olivine fractionation or accumulation does not disturb this result since REE partition coefficients in olivine are near zero; hence, the difference between the partition coefficients of any two elements is undisturbed. The fact that La/Zr ratios only remain within analytical error for all Mauna Kea samples (Figure 4.20) also suggests that clinopyroxene fractionation is a viable explanation for the chemical variability in Mauna Kea data set: partition coefficients of La and Zr between clinopyroxene and melts of tholeiitic composition are indeed very similar

Fujimaki *et al.*, 1984). The occurrence of clinopyroxene fractionation in samples MK1–8, MK1–3, MK1–10, KIL1–5 and KIL3–8 is confirmed by low Sc concentrations in these rocks as illustrated by Figure 4.34 where samples MK1–3, MK1–8 and MK1–10 plot significantly off trend. However, comparing Figures 4.34 and 4.4, it can be noticed that Sr behaviour closely mimics Sc behaviour in these samples. Indeed, none of the above mentionned samples plots off-trend in a Sr versus Sc plot (Figure 4.35). This characteristic is an indication that what was considered as simple clinopyroxene fractionation is actually the result of simultaneous clinopyroxene *and* plagioclase fractionation as was suggested in the preceeding chapter when sample MK2–1 low Al_2O_3/CaO ratio was discussed. The question may then be asked why the strong correlation in Figure 4.33 was not affected by plagioclase removal. Theoretically, a sufficient condition is that the differences in partition coefficients between La and the remaining REE in clinopyroxene and plagioclase are linearly correlated. This amounts to changing the x-axis scale in Figure 4.33 and preserving a linear relationship. Partition coefficient differences in plagioclase and clinopyroxene are plotted against each other in Figure 4.36 for two different data sets (Drake and Weill, 1975, at 1150°C and 1400°C). The observed correlations are not very well defined and it appears that the linearity of the curve in Figure 4.33 is more the result of plagioclase partition coefficient being significantly smaller ($\leq$ 20% except for Ce in the 1150°C set) than clinopyroxene partition coefficients.

4.3.3. Development of source heterogeneities at Mauna Loa and comparison with subaerial data

In the previous sections, it was suggested that Mauna Loa data separate into two distinct groups with different major element content (*e.g.* K_2O, Na_2O), trace element ratios (*e.g.* La/Yb, Zr/Nb)and isotope ratios. In an isochron plot of the Rb/Sr system, Mauna Loa rocks define a broad correlation (Figure 4.2) associated with an age of 0.9 b.y.. Also, incompatible element ratios in these two groups vary by factors up to 1.4 (La/Zr) while absolute abundances of La do not vary by more than a factor of 2. In particular, La/Ce ratio varies by a factor of 1.14 between the two Mauna Loa groups, while La abundance varies by a factor of 2. As showed by Chen, 1982, these values are not consistent with any petrogenetic process like partial melting where La and Ce behave similarly; it would require a 50 fold increase in La absolute abundance to match the increase in La/Ce due to 0.5% melting of a peridotitic source. It is therefore believed that the two Mauna Loa groups (labeled Mauna Loa "E" for enriched, high abundances of REE, high La/REE, and Mauna Loa "D" for depleted) come from different souces that have evolved in separate systems since their formation, a billion year ago. Abundances of incompatible elements in these two sub groups define two distinct olivine control lines when plotted against MgO (Figure 4.37), as could be anticipated. These two batches seem to have evolved in different ways. In Figures 4.38, 4.39 and 4.40, we plotted various trace element ratios (Sr/Zr, Sr/Sm and La/Yb) versus La/Sm for our Mauna Loa samples. La/Sm was chosen because of its relative

sensitivity to differences in degrees of partial melting in a peridotitic source. It can be observed that the "enriched" group forms broad positive correlations while the "depleted" group generally clusters within a few sigma units with very little tendency to spread out along any direction. Sample ML4–59 plotting out of the main cluster of "depleted" Mauna Loa samples has no genetic significance: this particularity is confined to the plots involving Sr and is the result of a not yet understood high Sr value in this particular sample. Because the Mauna Loa data set is free of low pressure crystal fractionation effects except for olivine (consistent Al_2O_3/CaO, no Sc anomalies), it is believed that the variability in trace element ratios within the "enriched" group reflects variations in the generation process such as small scale variations in the degree of melting of the source. Indeed, $^{87}Sr/^{86}Sr$ ratios remain within experimental uncertainties in each Mauna Loa group which tends to indicate a homogeneous source for each group.

In Figures 4.38 to 4.40, we also plotted the data of Rhodes and Hart (unpublished) on subaerial Mauna Loa samples. This set of data overlaps our depleted group. Also, the most enriched of the subaerial samples defines a vector subparallel to the trend of our enriched group. In order to test for possible mixing components, Figures 4.41 to 4.43 were constructed where Sr/Zr, La/Sm and La/Yb ratios are plotted against $^{87}Sr/^{86}Sr$. Companion plots as defined by Langmuir *et al.*, 1978, are also presented. It should be stressed that this type of approach can only identify mixing between melts since source mixing is obscured by the melting process itself, unless the the area sampled by the melting is small compared to the scale of

source heterogeneities. If mixing takes place between Rhodes and Hart's data and our depleted group, any curve suggestive of melting in the upper plots must be accompanied by a straight line in the corresponding lower plot. Although satisfactory trends are observed in Figure 4.41 and 4.42, Figure 4.43 demonstrates that there is actually no interaction in the form of mixing between any of the three different groups. It also illustrates the point that poorly chosen plots can provide misleading pictures of the data. In Figure 4.42 for instance, the companion plot displays a very good trend for the only reason that Sm and Sr behave very similarly in major petrogenetic processes in a basaltic environment. Hence, meaningful plots involving an isotopic ratio must not have an element with partition coefficients similar to the daughter element as denominator of the second variable.

4.4. Characterisation of source differences between Hawaiian volcanoes

Chondrite-normalized plots of rare earth element abundances in lavas from individual volcanoes are presented in Figures 4.44 to 4.49. Much of the variations attributed to olivine accumulation and low pressure fractionation in the preceeding sections can be identified in these figures. Kilauea and Hualalai exhibit near parallel REE profiles. In contrast, some lavas from Mauna Kea and Kohala are fractionated, particularly in Eu/Tb. Finally, the split of Mauna Loa lavas in two groups is visible in Figure 4.44.

In order to evaluate intervolcano differences that are *not* the result of low pressure fractionation and accumulation processes, we corrected all lavas from Kilauea and the two groups of Mauna Loa that were not affected by clinopyroxene fractionation (KIL1–5 and KIL3–8 were excluded) to 10%MgO by addition/substraction of olivine in equilibrium with the corresponding glasses. The corrected lavas are presented on chondrite-normalized plots in Figures 4.50 to 4.52. Remaining variations are small and integrate subtle petrological processes (e.g. small variation in degrees of melting of a homogeneous source for individual volcanoes) as well as analytical variability. The observation that tholeiites from individual volcanoes are remarkably uniform after correcting for olivine dilution has been made previously (e.g. Leeman *et al.*, 1980). However, intervolcano differences remain after these simple corrections are made. In Figure 4.53, average compositions for the corrected lavas from Kilauea and the two Mauna Loa groups (Table 4.4) are presented in a

chondrite-normalized REE plot. Kilauea and Mauna Loa enriched group averages are similar in composition except for La and Ce, higher in Mauna Loa "E". These two group averages are significantly LREE enriched compared to the average for Mauna Loa depleted group lavas.

Other caracteristic differences between Mauna Loa and Kilauea can be found in preceeding sections. Overall, Kilauea is higher than both Mauna Loa groups in TiO_2 and K_2O (Figures 3.3(b) and 3.8(b)). Also, Kilauea is the highest of all volcanoes represented in Rb, Ba and Nb (Figures 4.3, 4.5 and 4.8) and consecutively the lowest in La/Rb, La/Ba and La/Nb (Figures 4.16, 4.18 and 4.21). It is common wisdom that these elements are more incompatible than La in a peridotitic assemblage (*e.g.* Sun *et al.*, 1979) hence the concept that somewhere in their history, Kilauea lavas or their source material were associated with smaller degrees of melting than their Mauna Loa equivalents. This hypothesis is consistent with the observation that Kilauea lavas are also highest in La/Yb (Figure 4.26): in a simple model, with a source composition intermediate between the two Mauna Loa groups, melts associated with small degrees of melting evolve toward the "depleted" group in all ratios of La over a more incompatible element (*e.g.* La/Ba), and toward the "enriched" group in all ratios of La over a less incompatible element (*e.g.* La/Yb). Unfortunately, many aspects of the data are not consistent with the idea that Kilauea and Mauna Loa lavas originated from a common source by different degrees of melting.

(1) Al_2O_3/CaO ratios are higher in Mauna Loa (1.28) than in Kilauea (1.20) as

illustrated in Figures 3.12 and 3.13. Based on spinel peridotite melting experiments, Klein and Langmuir, 1987, inferred that this ratio decreases in the melt as the degree of melting increases. Nevertheless, it is a possibility that the melting of garnet peridotite, more consistent with Hawaiian lavas HREE abundance constancy, produces the opposite trend because of the residual character of garnet during melting.

(2) Hawaiian volcanoes are characterized by significant isotopic differences. Moreover, these differences can not be completely explained by the close-system evolution of an aged heterogeneous mantle: Kilauea tholeiites are lower than Mauna Loa tholeiites in Sm/Nd, yet they are higher in $^{143}Nd/^{144}Nd$ (Figure 4.54).

This latter characteristic is the most intriguing feature of Hawaiian lavas and is also present when tholeiites and alkalic pre- and post-erosional basalts from a single volcano are compared (Chen and Frey, 1985). A two component mixing model between undepleted mantle and incipient melts from the lithosphere proposed by Chen and Frey, 1985, succesfully explains the observed $^{87}Sr/^{86}Sr$ ratios and trace element abundances and ratios. This model however suffers a major shortcoming: the non-radiogenic component must be derived by extremely small degrees (0.1-1.0%) of melting of the lithosphere in order to reproduce the trace element ratios and abundances observed in the lavas. Consequently, the mass ratio of lithospheric component to plume component reaches unrealistic values (2:1 to 17:1) considering that melts from the lithosphere are generated by simple conductive heat transfer from the uprising plume. Furthermore, the incorporation of lead data (West *et al.*,

1987) shows that an "enriched component", highly fractionated, lead-radiogenic and trace-element enriched, but non radiogenic in Sr, is needed to explain the observed array of tholeiites in a $^{206}Pb/^{204}Pb$ *vs.* $^{87}Sr/^{86}Sr$ plot. At this point, is seems that justifying the existence of this component is the key to explaining Hawaiian volcanism as a whole, which is beyond the scope of this work. Rather, we present the following remarks.

In preceeding sections, it was established that Mauna Loa data defines a rough isochron of age 0.9 b.y.. Also, some individual volcanoes (Koolau, Loihi and Mauna Loa "Rhodes"), define Nd isochrons (Figure 4.54) of age 0.6 to 0.8 b.y.. These ages are in broad agreement and are consistently lower than the age for the development of oceanic mantle heterogeneities derived by Brooks and Hart, 1976. This may indicate that the scale of differenciation within the mantle is decreasing with time. The concept that the positive correlations in Figure 4.54 are meaningful isochrons is all the more plausible that a mixing model for individual volcanoes would require a set of low Sm/Nd end-members with very different Nd isotopic compositions that is hard to justify. However, it is hard to reconcile this approach with the overall negative correlation observed between the upper part of individual volcano fields suggested by the solid line in Figure 4.54. It is not understood why within-volcano isochrons remain undisturbed after a mixing stage with the hypothetical "enriched component".

TABLE 4.1

ISOTOPIC DATA

	$^{87}Sr/^{86}Sr$	$^{143}Nd/^{144}Nd$
ML1–7	.703587	—
ML1–10	.703725	.512885
ML1–14	.703662	.512906
ML2–1	.703673	.512906
ML3–30	.703623	.512950
ML4–9*	.703748	—
ML4–10	.703660	.512906
ML4–11*	.703727	—
ML4–22*	.703728	—
KIL2–9	.703605	—
MK1–8	.703652	—
MK6–6	.703496	—
KO2	.703761	—
H5	.703775	—
H7	.703719	—
LO6	.703488	—

TABLE 4.2

TRACE ELEMENT ANALYSES

	MAUNA LOA							
	1–1	1–7	1–9	1–10	1–11	1–14	2–1	2–3
Rb	3.35	5.08	3.95	5.61	4.22	3.77	6.38	4.00
Sr	194.1	286.0	249.1	251.8	216.4	198.2	293.2	245.4
Ba	38.8	68.1	64.6	74.3	44.1	54.9	84.0	69.4
Zn	111.8	118.3	113.1	124.3	110.9	111.6	115.0	112.5
Ga	13.22	18.65	17.41	14.37	15.86	14.34	16.62	17.28
Y	16.83	24.43	21.26	20.84	18.69	17.58	23.40	20.26
Zr	92.4	135.6	114.7	126.8	101.6	93.2	139.8	110.7
Nb	7.0	9.6	9.0	11.9	8.0	8.0	13.0	8.3
Hf	2.24	3.19	2.91	3.08	2.40	2.42	3.31	2.72
La	5.62	8.58	7.56	10.09	6.28	5.98	12.16	6.85
Ce	16.0	23.6	20.3	26.3	17.1	16.8	30.7	19.0
Nd	10.4	16.2	13.8	15.3	11.6	11.2	18.1	13.4
Sm	3.15	4.62	4.03	4.43	3.51	3.25	4.76	3.79
Eu	1.13	1.64	1.46	1.50	1.25	1.22	1.64	1.43
Tb	0.53	0.78	0.68	0.64	0.55	0.60	0.73	0.62
Yb	1.44	2.08	1.75	1.78	1.62	1.49	1.91	1.71
Lu	0.19	0.29	0.26	0.24	0.23	0.21	0.25	0.24

TABLE 4.2

TRACE ELEMENT ANALYSES (CONT.)

	MAUNA LOA							
	2–8	3–30	4–3*	4–9*	4–10	4–10*	4–11	4–11*
Rb	3.53	4.07	6.37	6.63	3.92	3.88	—	6.50
Sr	207.7	198.8	302.1	299.6	216.2	222.4	298.1	303.4
Ba	38.1	51.2	91.3	98.3	54.0	49.0	88.8	85.5
Zn	110.3	107.5	113.1	116.2	117.8	113.0	116.0	116.8
Ga	14.17	14.55	17.78	18.14	—	15.37	—	17.92
Y	18.01	18.10	23.08	24.15	—	18.24	—	23.62
Zr	93.4	95.9	139.8	143.8	99.0	97.3	141.7	143.1
Nb	7.4	6.7	12.5	12.9	7.6	6.7	14.2	13.1
Hf	2.28	2.46	3.29	3.50	2.40	2.26	3.44	3.47
La	5.83	5.98	11.82	12.24	6.09	6.07	12.11	11.91
Ce	16.4	16.8	30.3	30.2	18.1	17.2	32.1	30.1
Nd	11.4	11.6	18.0	18.2	11.8	11.9	19.0	18.3
Sm	3.37	3.35	4.72	4.94	3.45	3.49	5.03	4.64
Eu	1.21	1.18	1.59	1.66	1.27	1.23	1.71	1.61
Tb	0.47	0.66	0.76	0.79	0.62	0.65	0.85	0.75
Yb	1.49	1.55	1.93	2.13	1.57	1.56	1.89	1.97
Lu	0.20	0.21	0.26	0.27	0.22	0.23	0.28	0.26

TABLE 4.2

TRACE ELEMENT ANALYSES (CONT.)

	MAUNA LOA			KILAUEA				
	4–22*	4–44	4–59	1–BR	1–4	1–5	1–7	2–1
Rb	6.71	4.97	3.48	6.45	6.87	8.22	5.66	4.84
Sr	306.2	278.0	227.8	319.1	312.6	354.1	257.1	213.9
Ba	95.1	55.3	46.1	97.9	101.3	113.1	80.4	71.9
Zn	115.4	112.3	100.7	113.5	115.3	117.9	116.3	111.5
Ga	18.89	18.78	15.57	19.45	18.71	21.25	15.14	13.38
Y	24.14	24.34	16.76	23.64	23.82	27.60	19.44	16.38
Zr	144.9	130.8	88.5	145.6	147.2	176.4	120.6	102.3
Nb	13.7	9.6	6.1	13.2	14.8	17.6	13.0	10.9
Hf	3.46	3.17	2.09	3.54	3.56	4.20	3.12	2.47
La	12.50	8.36	5.58	10.96	11.15	13.10	9.10	7.39
Ce	31.0	24.0	15.6	28.8	28.8	35.2	25.2	19.8
Nd	18.7	16.5	11.3	18.8	18.9	21.9	16.1	12.4
Sm	4.91	4.48	3.12	4.97	4.96	5.83	4.17	3.30
Eu	1.66	1.63	1.12	1.66	1.74	2.10	1.47	1.17
Tb	0.77	0.88	0.52	0.69	0.70	0.89	0.64	0.53
Yb	2.02	1.94	1.46	1.79	1.94	1.10	1.60	1.34
Lu	0.28	0.25	0.20	0.28	0.24	0.27	0.21	0.18

TABLE 4.2

TRACE ELEMENT ANALYSES (CONT.)

	KILAUEA		MAUNA KEA					
	2–8	2–9	3–8	1–3	1–8	1–10	2–1	5–13
Rb	4.56	5.00	6.39	6.98	11.12	6.77	5.24	4.88
Sr	200.5	216.4	257.5	241.1	273.3	242.1	248.7	259.9
Ba	58.8	65.3	88.6	90.0	133.2	87.2	75.5	63.1
Zn	129.5	112.2	116.9	121.8	145.0	120.9	113.1	111.4
Ga	12.51	12.13	16.08	16.65	19.36	16.88	16.99	17.66
Y	16.05	16.74	20.32	25.41	34.64	25.66	21.38	21.79
Zr	100.9	105.9	133.8	159.4	233.7	160.4	125.5	122.2
Nb	10.4	10.7	14.1	13.2	18.8	13.4	11.4	9.6
Hf	2.51	2.47	3.19	3.76	5.55	3.69	2.98	3.13
La	7.22	7.76	9.99	10.79	16.20	10.93	8.48	8.12
Ce	20.0	20.5	25.6	29.6	41.1	30.0	23.3	22.2
Nd	13.0	13.9	16.7	19.0	27.5	19.6	16.1	15.1
Sm	3.31	3.56	4.42	5.02	7.22	4.99	4.17	4.20
Eu	1.18	1.23	1.53	1.71	2.44	1.72	1.50	1.48
Tb	0.48	0.51	0.61	0.78	0.98	0.84	0.78	0.78
Yb	1.24	1.37	1.59	1.99	2.83	2.04	1.72	1.75
Lu	0.19	0.20	0.23	0.26	0.40	0.27	0.25	0.25

TABLE 4.2

TRACE ELEMENT ANALYSES (CONT.)

	MAUNA KEA		KOHALA			HUALALAI		LOIHI
	6–6	6–18	1–17	2	2–8	5	7	6
Rb	4.58	4.90	5.21	6.40	6.51	4.20	4.62	6.89
Sr	225.0	273.7	289.1	339.8	356.4	231.8	251.7	314.2
Ba	60.8	63.4	75.7	94.4	91.9	53.8	56.7	97.5
Zn	114.2	110.4	113.2	113.0	110.5	111.3	111.0	126.7
Ga	15.74	17.86	16.50	19.03	19.94	16.16	16.43	19.05
Y	19.77	22.85	20.00	24.29	24.61	19.02	20.24	23.30
Zr	110.2	128.8	123.4	156.3	158.8	99.7	109.4	137.3
Nb	9.7	10.2	10.4	12.2	11.9	9.1	10.5	14.1
Hf	2.78	3.18	3.00	3.58	3.80	2.32	2.74	3.19
La	7.47	8.66	8.70	10.91	11.34	6.54	7.41	11.00
Ce	19.8	23.2	24.8	30.3	31.5	17.7	19.7	29.1
Nd	13.4	16.3	15.5	20.0	21.1	11.5	14.3	18.4
Sm	3.98	4.42	4.12	5.16	5.33	3.47	3.84	4.81
Eu	1.36	1.57	1.46	1.77	1.86	1.24	1.38	1.60
Tb	0.72	0.79	0.72	0.77	0.82	0.59	0.65	0.72
Yb	1.73	1.92	1.61	1.91	1.97	1.56	1.76	1.99
Lu	0.22	0.27	0.21	0.27	0.26	0.22	0.22	0.29

TABLE 4.3

SPURIOUS CORRELATIONS IN LA/REE VERSUS LA PLOTS (SEE TEXT)

Element(i)	C_i	R_{La-i}	Spurious R
La	.2829	1.0	—
Rb	.2826	.9589	.15
K_2O	.2402	.9334	.56
Sr	.1702	.7750	.81
Y	.1728	.8715	.84
Ce	.2553	.9909	.66
Zr	.2253	.9310	.66
Nd	.2313	.9568	.68
Sm	.1972	.9423	.83
Eu	.1788	.9090	.85
Yb	.1629	.8337	.85

TABLE 4.4

REE CONTENT IN LAVAS CORRECTED TO 10% MgO

	Mauna Loa (D)	Mauna Loa (E)	Kilauea
La	7.61	12.46	11.08
Ce	21.35	31.48	29.67
Nd	14.57	18.78	19.30
Sm	4.21	5.01	5.02
Eu	1.53	1.70	1.75
Yb	1.91	2.07	1.93
Lu	.26	.28	.28

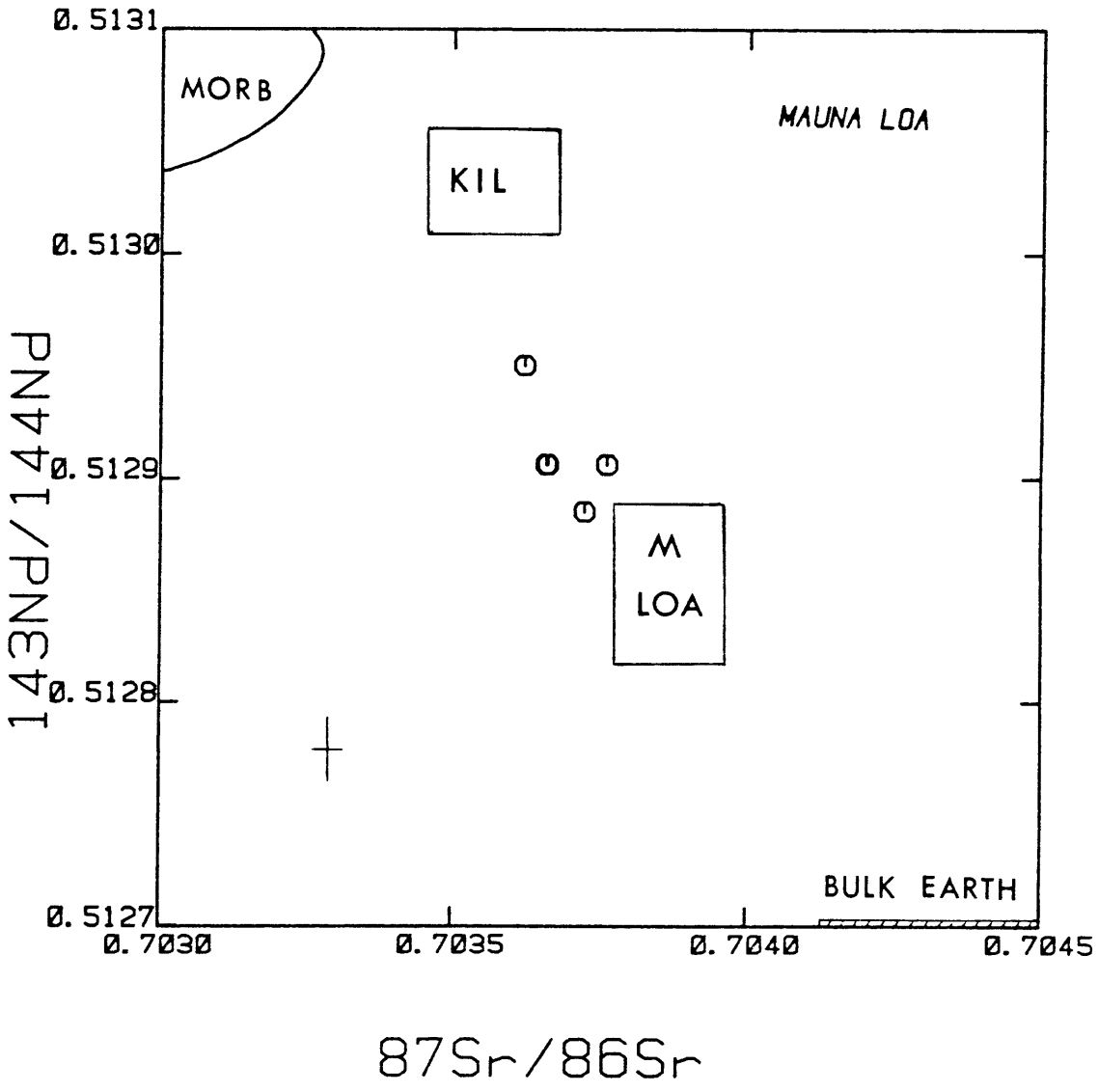

Figure 4.1. Plot of $^{143}Nd/^{144}Nd$ versus $^{87}Sr/^{86}Sr$ for the 4 Mauna Loa samples analysed for Nd isotopes. The fields labeled "M LOA" and "KIL" correspond to the data of Stille *et al.*, 1987, and Rhodes and Hart, 1987.

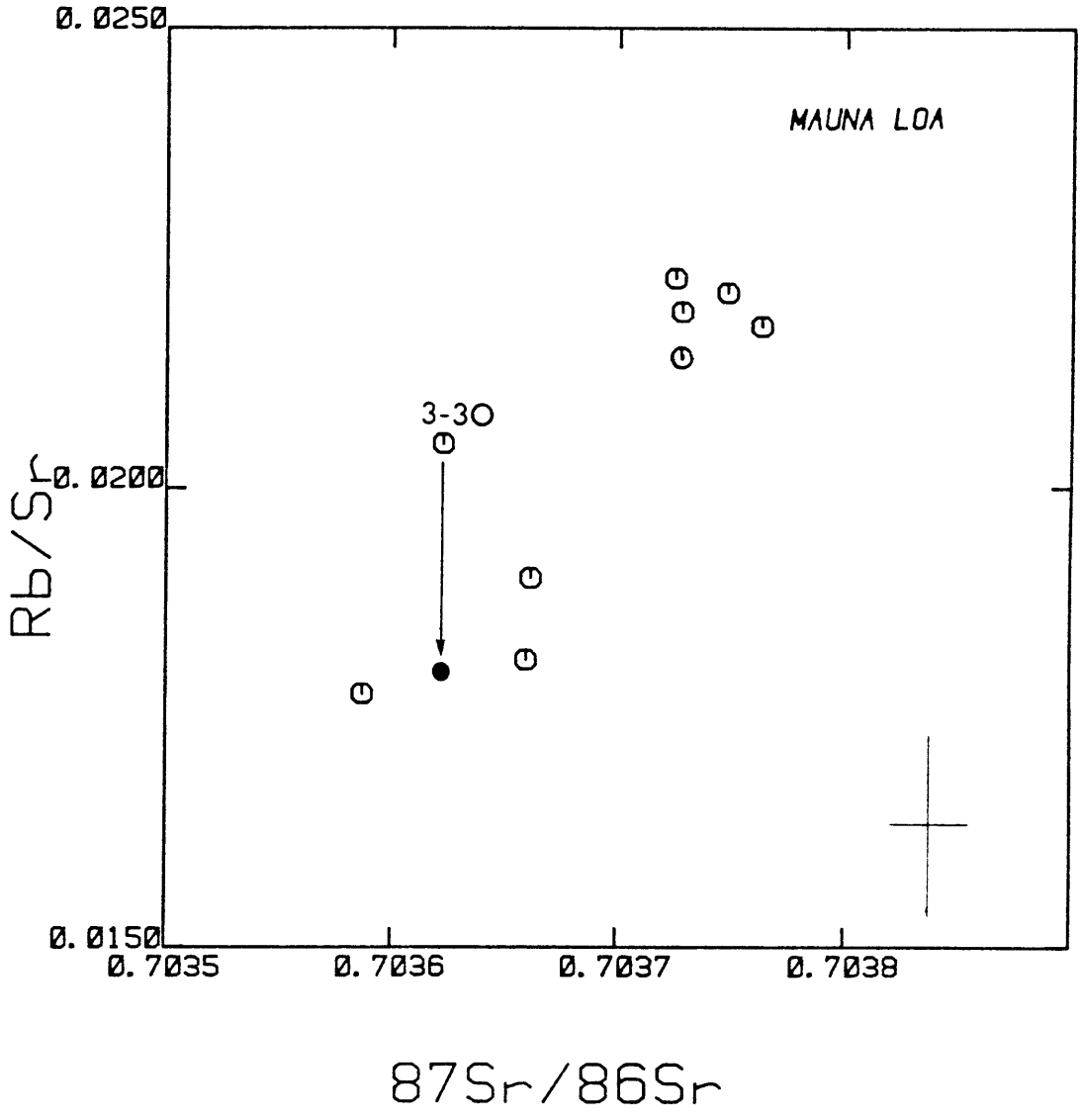

Figure 4.2. Isochron plot of the Mauna Loa data. The Rb/Sr value in sample 3-30 is corrected as explained in section 4.3.1.

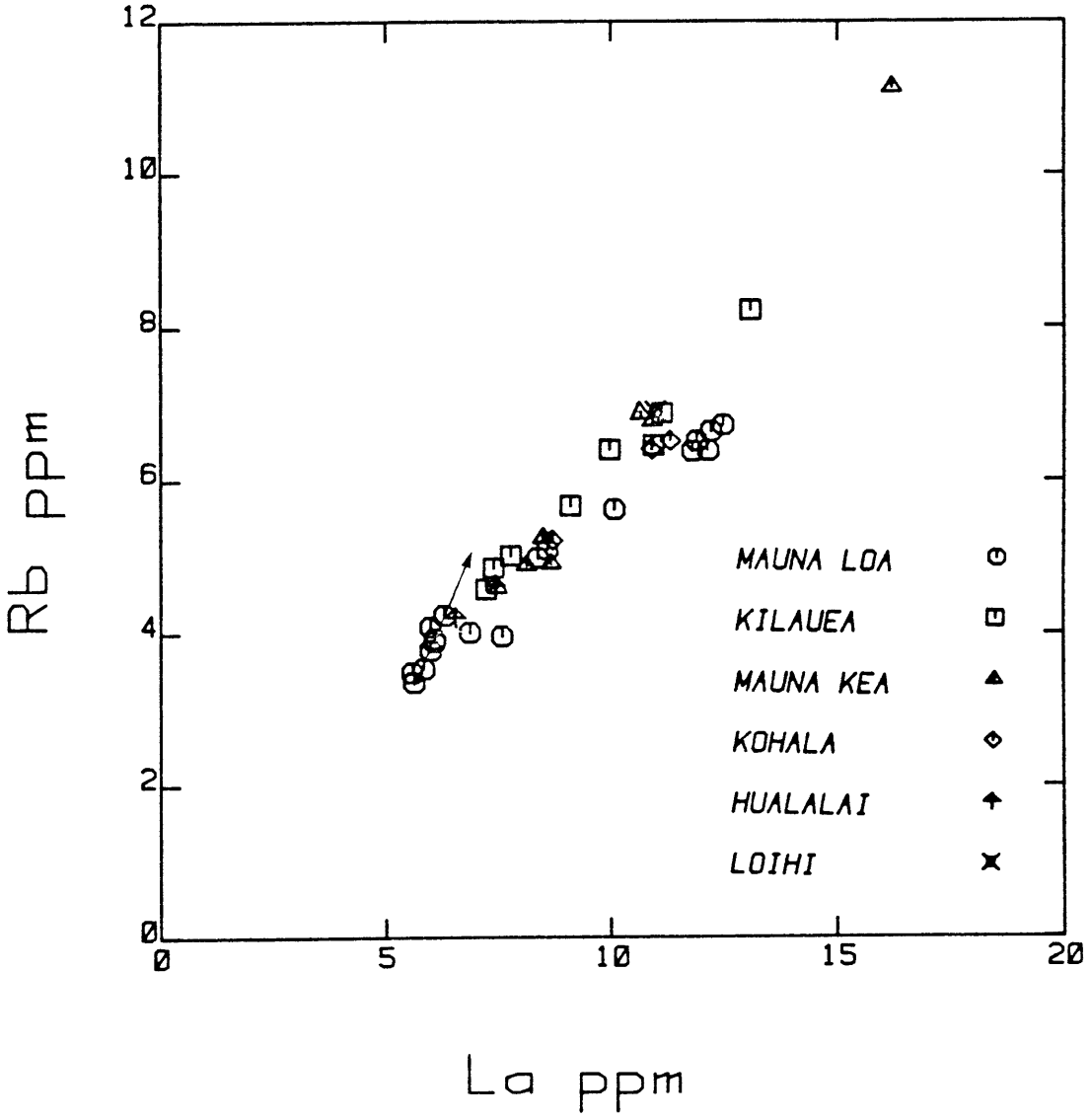

Figures 4.3–4.15. Plots of Rb, Sr, Ba, K_2O, Zr, Nb, Hf, Ce, Nd, Sm, Eu, Yb, and Y abundances versus La abundance in the complete data set. The two lines running through the origin, when present, give the range in the ratio of the element considered and La. In the case of Rb and K_2O, the small arrow through Mauna Loa low-La group indicates departures from the main trend and are discussed in section 4.3.1.

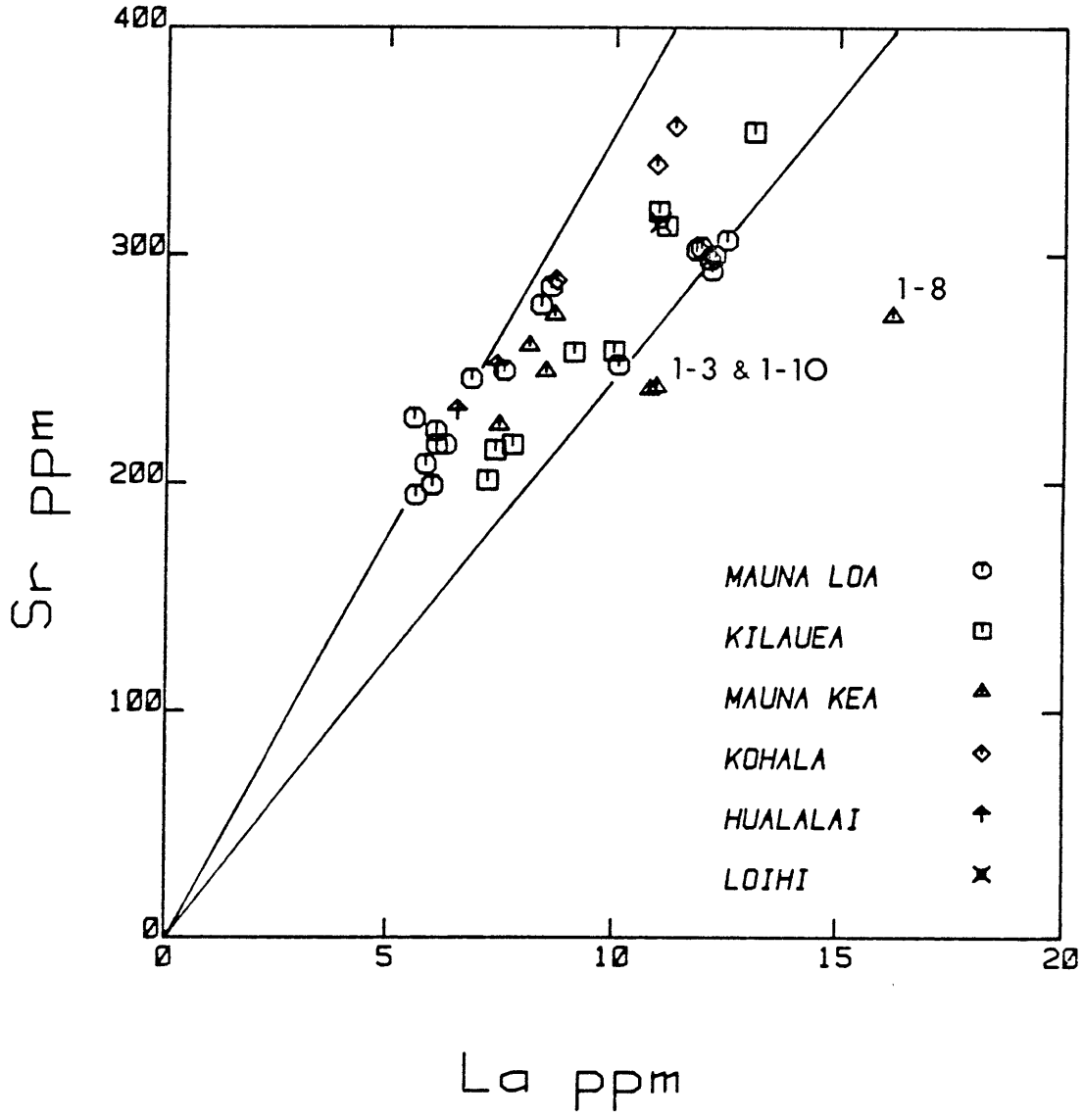

Figure 4.4. Same as 4.3

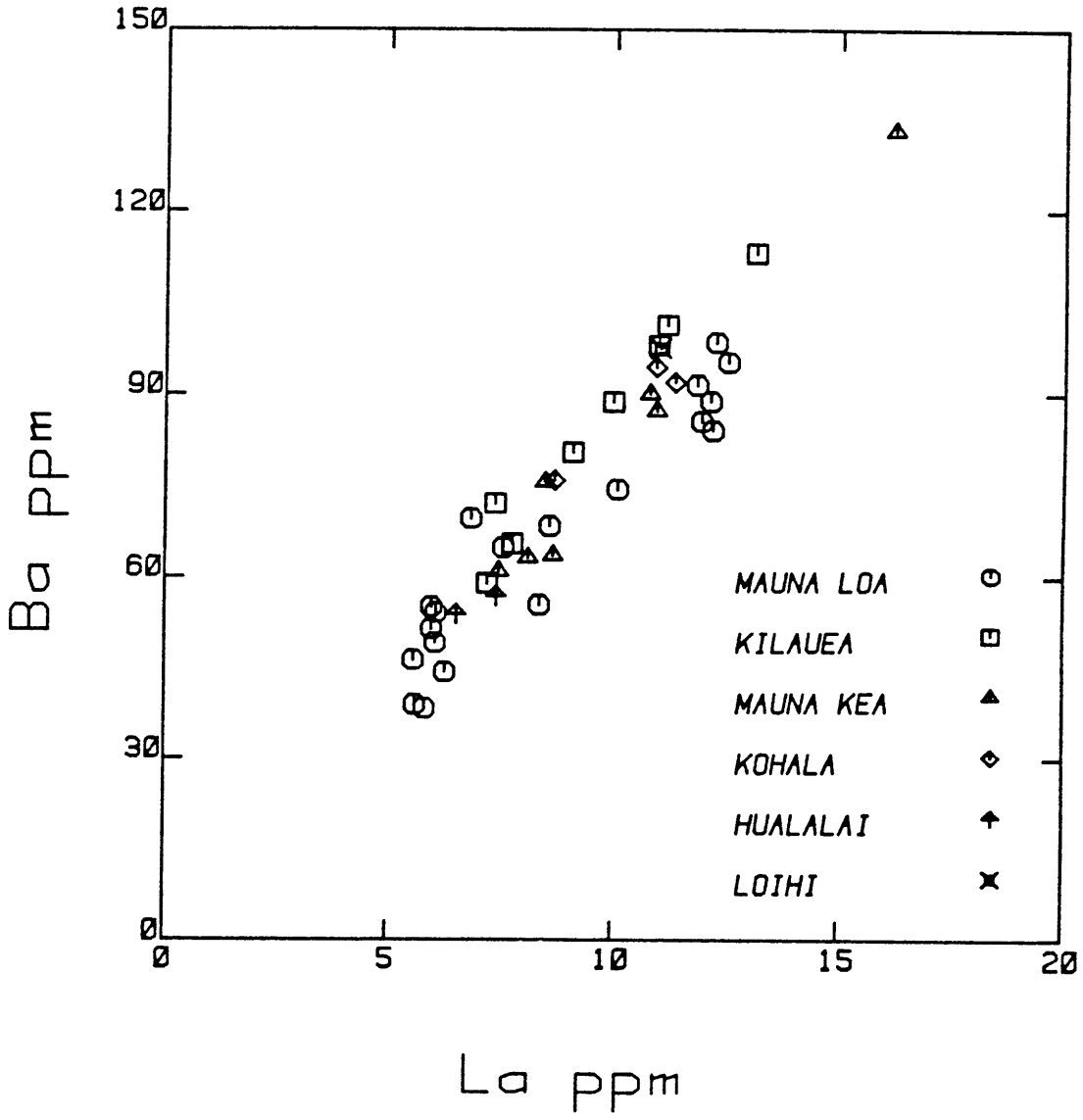

Figure 4.5. Same as 4.3

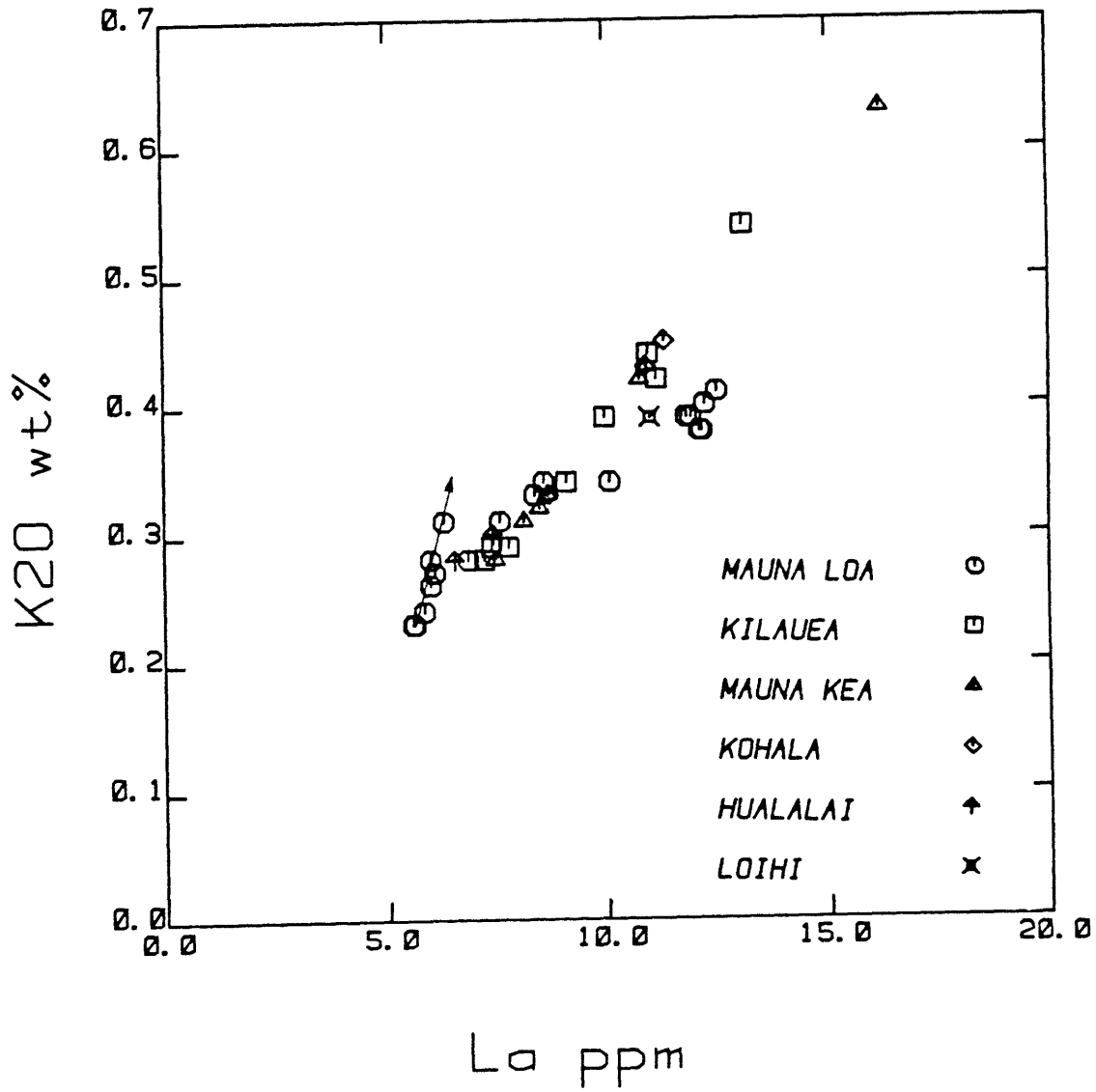

Figure 4.6. Same as 4.3

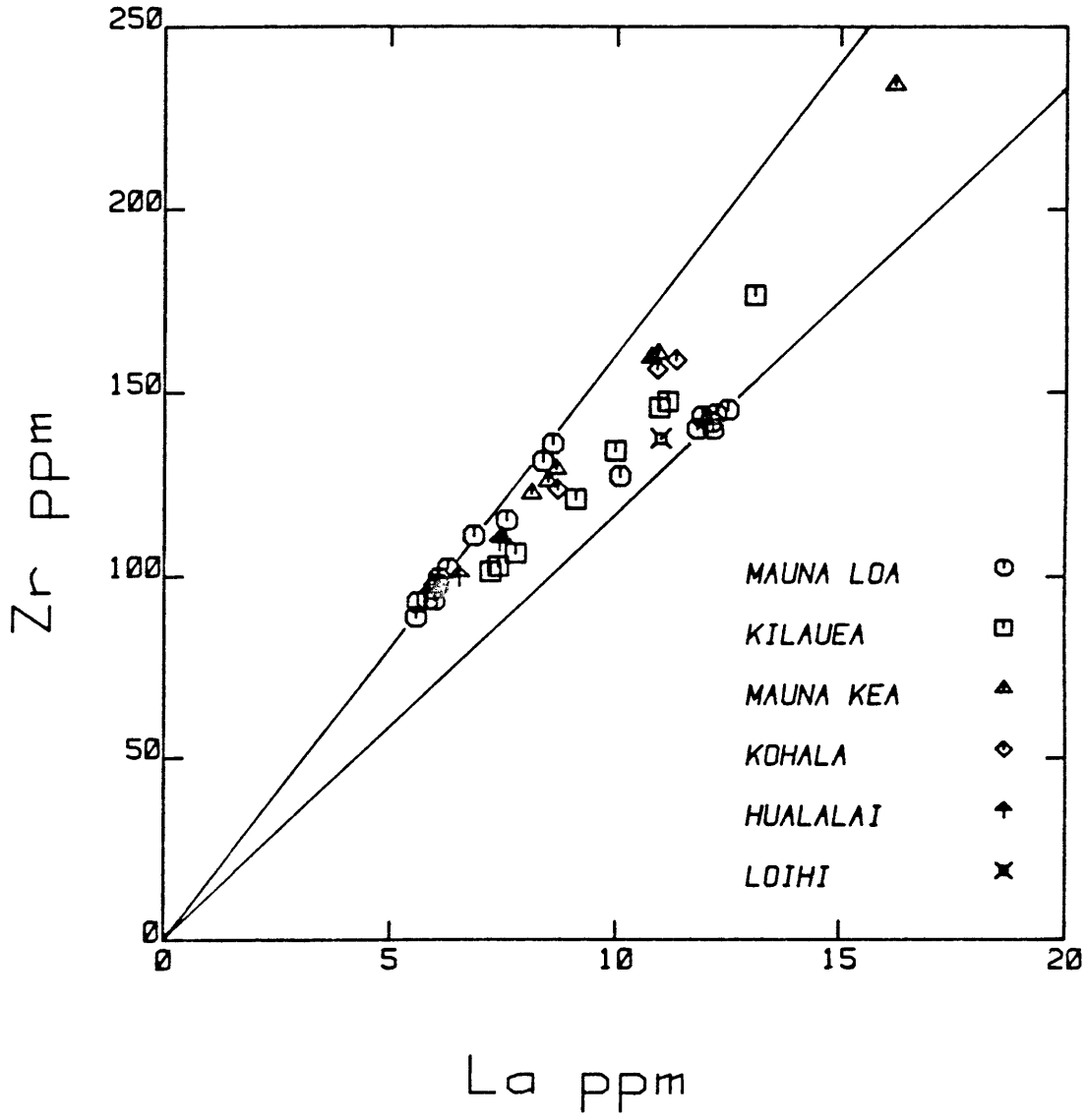

Figure 4.7. Same as 4.3

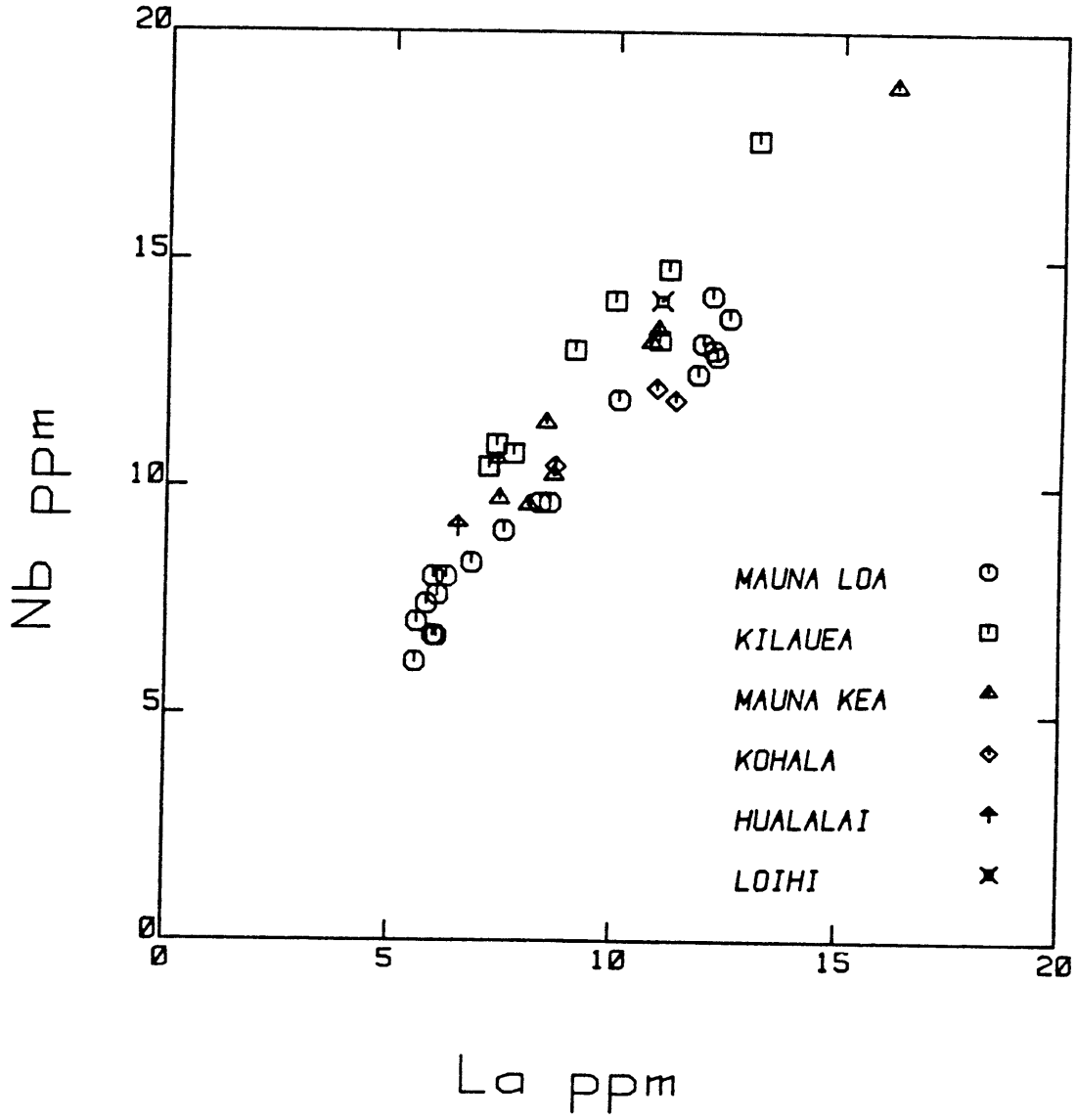

Figure 4.8. Same as 4.3

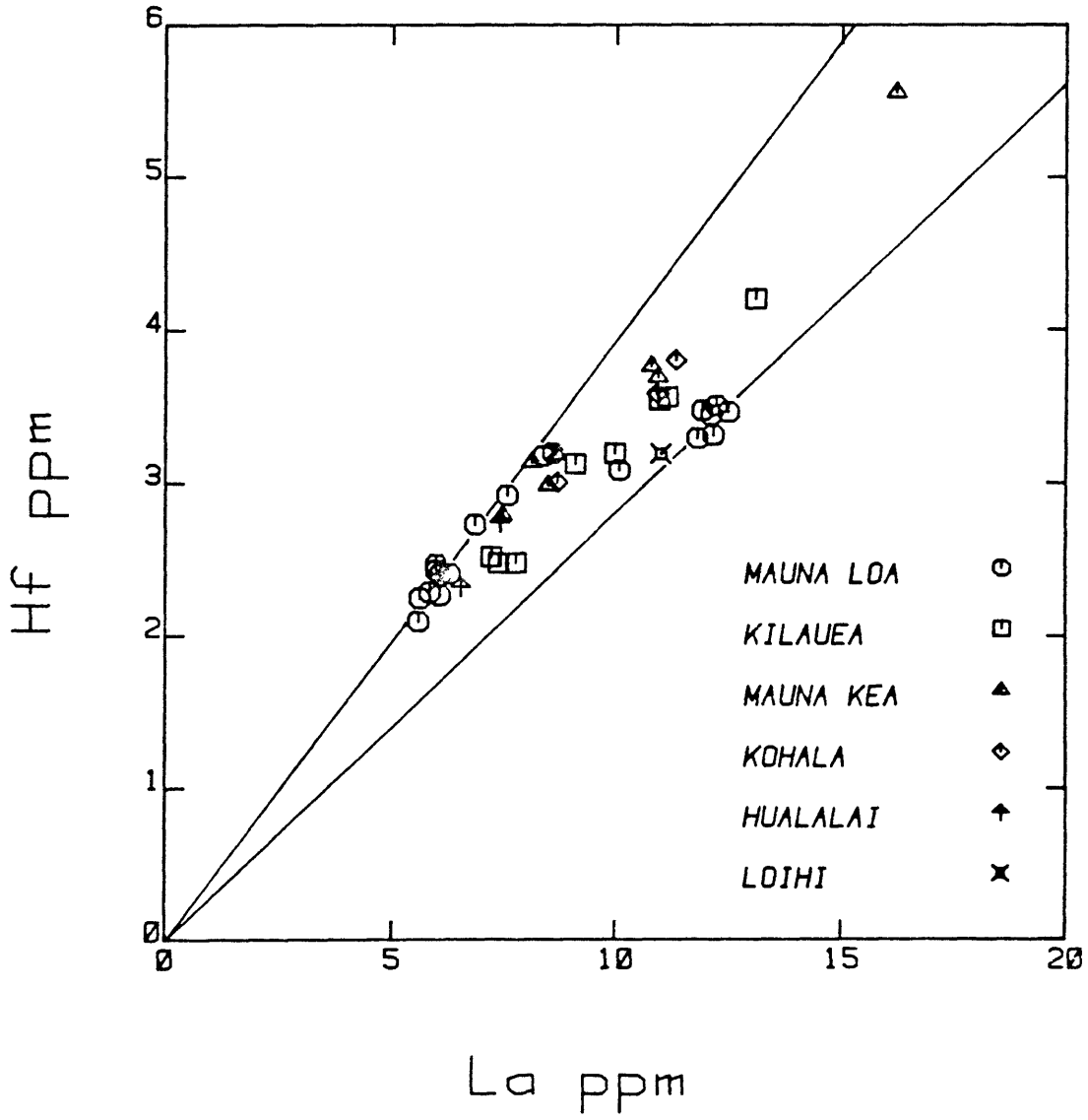

Figure 4.9. Same as 4.3

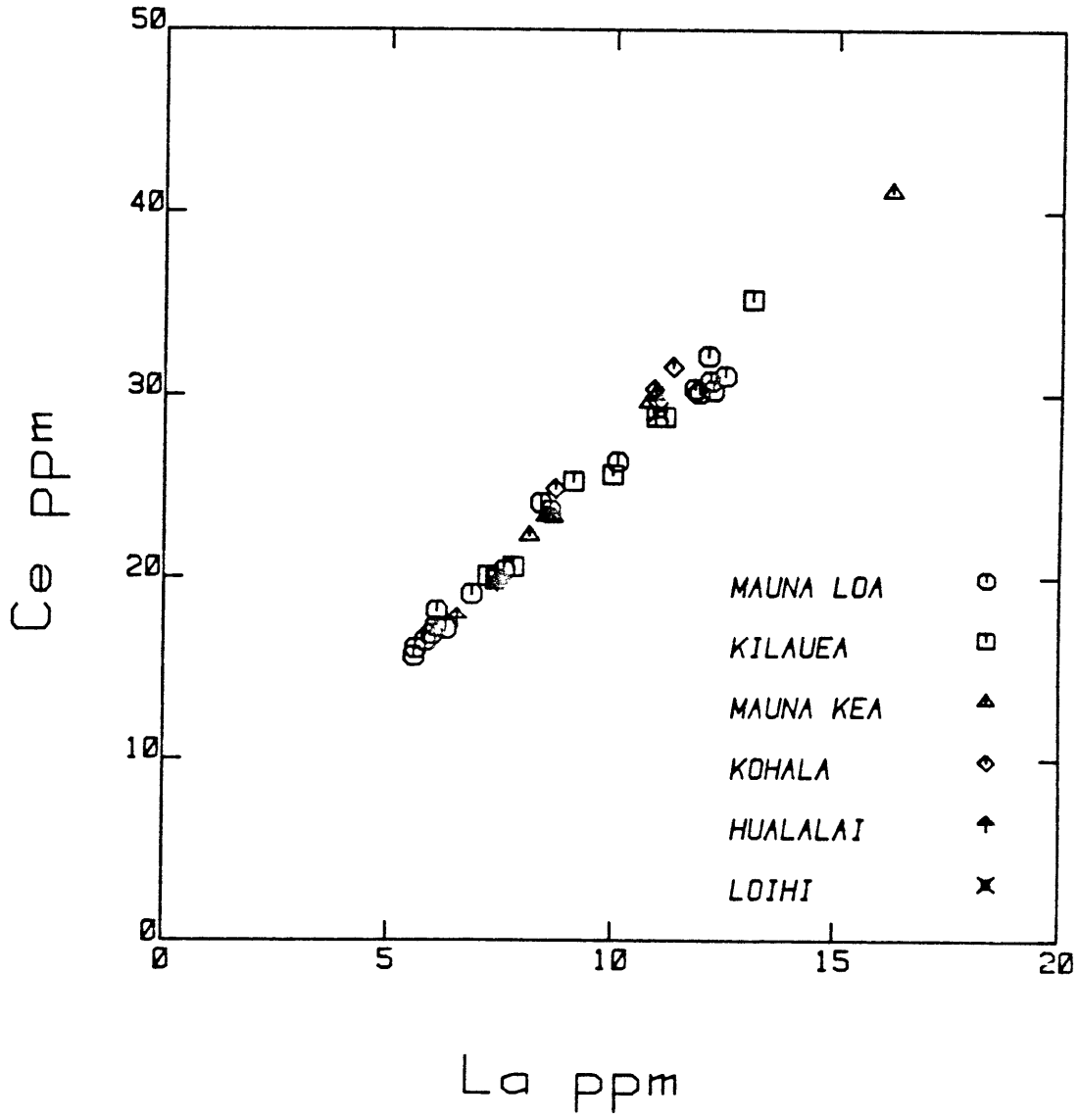

Figure 4.10. Same as 4.3

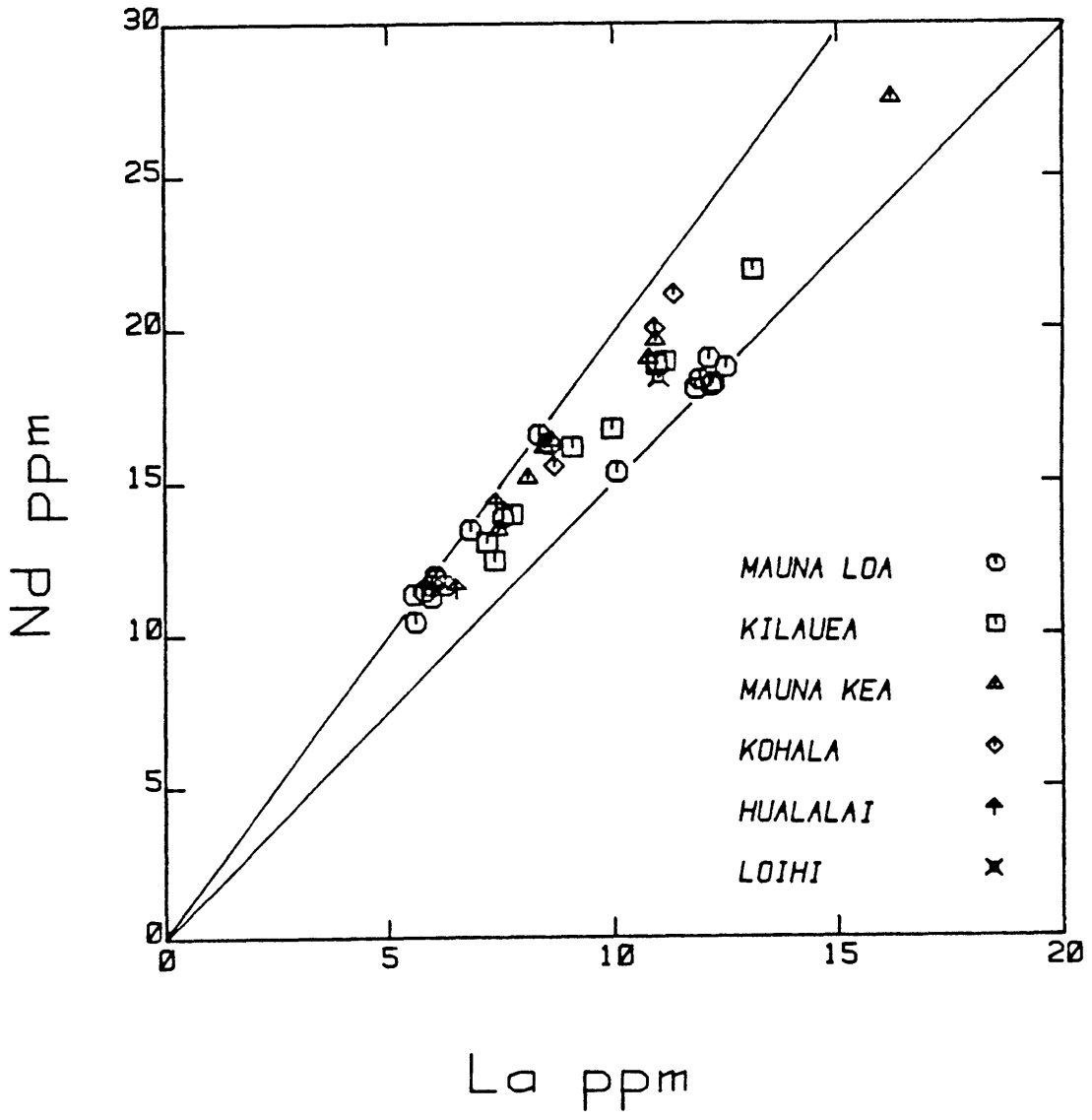

Figure 4.11. Same as 4.3

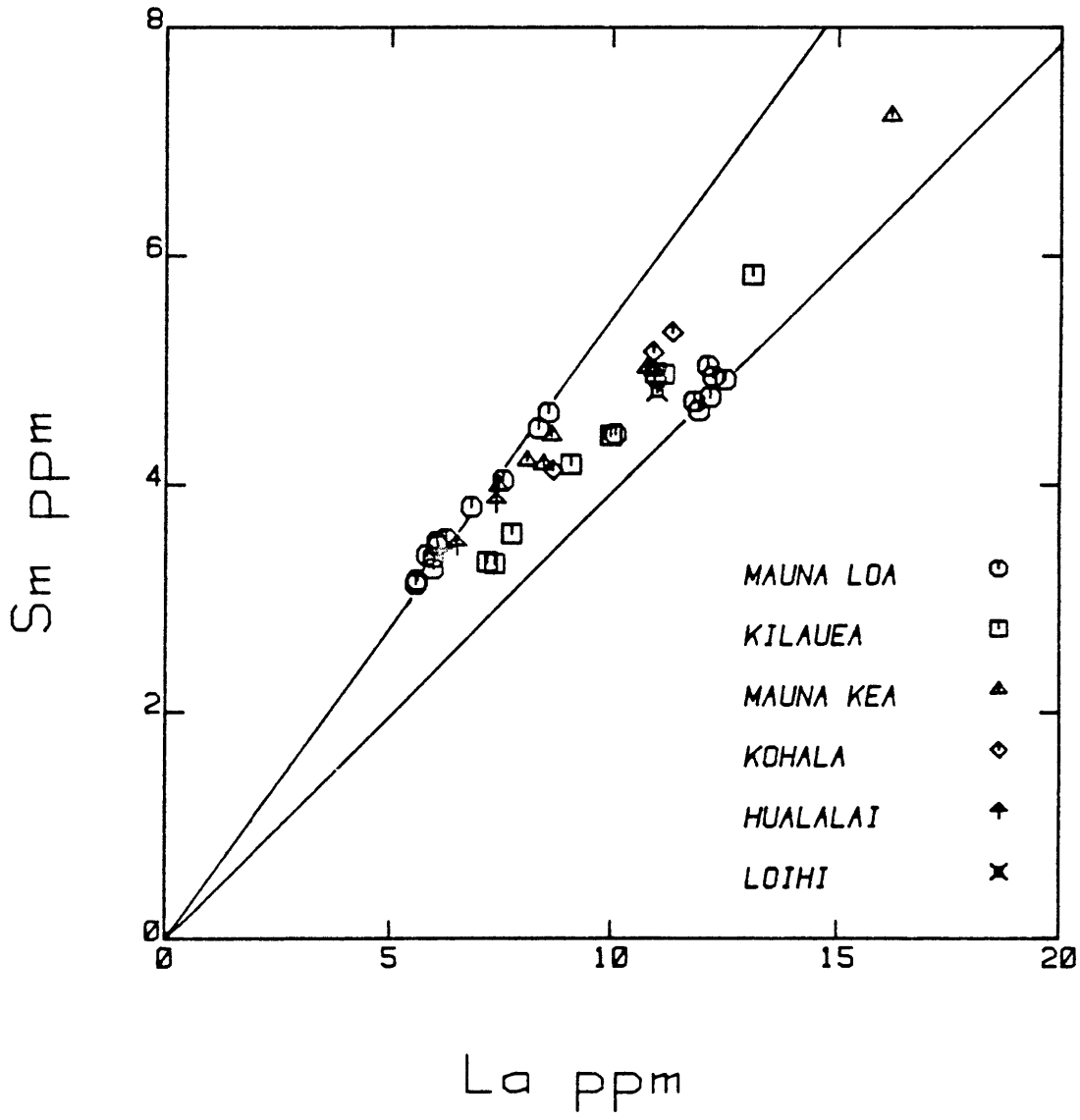

Figure 4.12. Same as 4.3

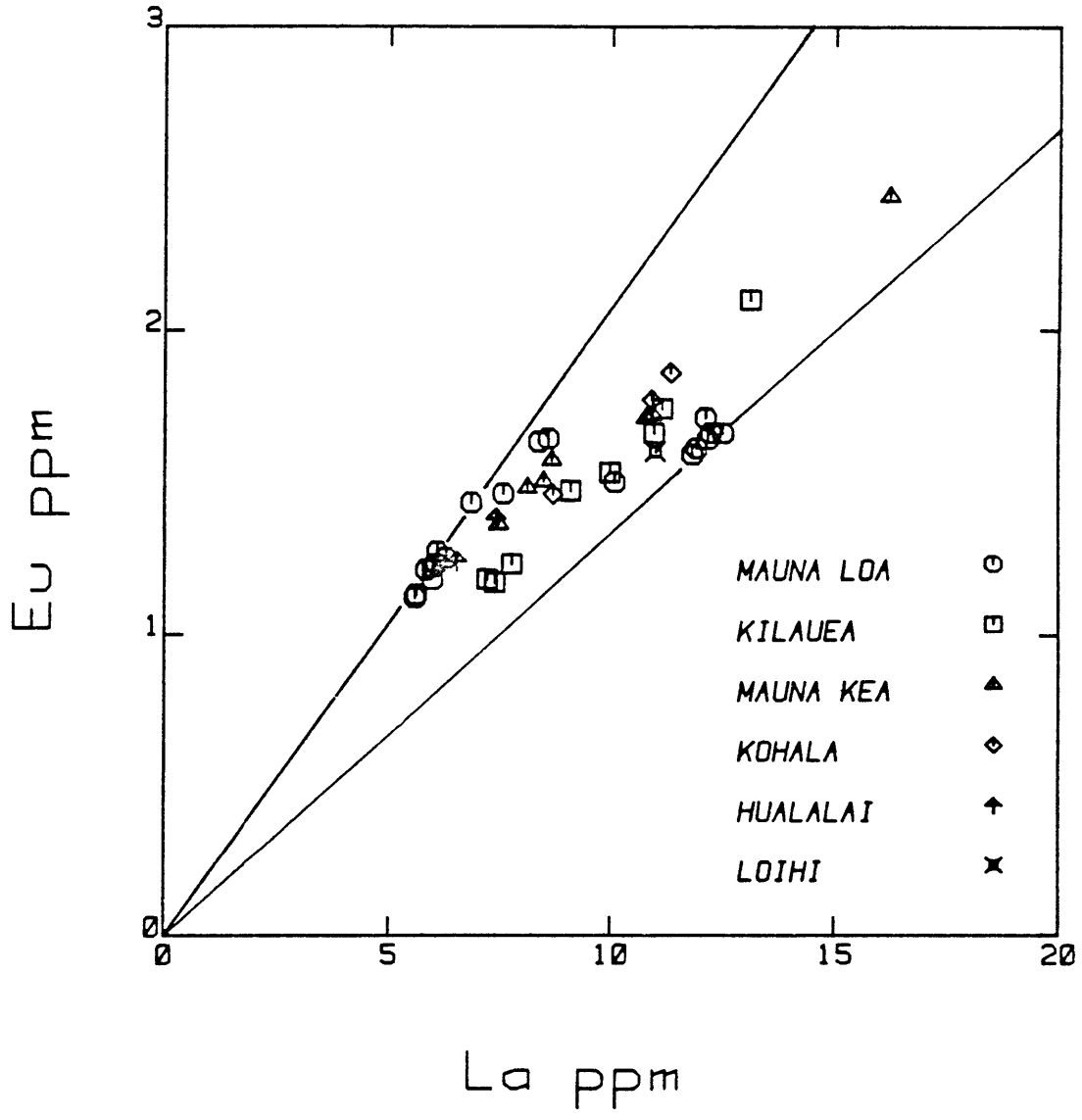

Figure 4.13. Same as 4.3

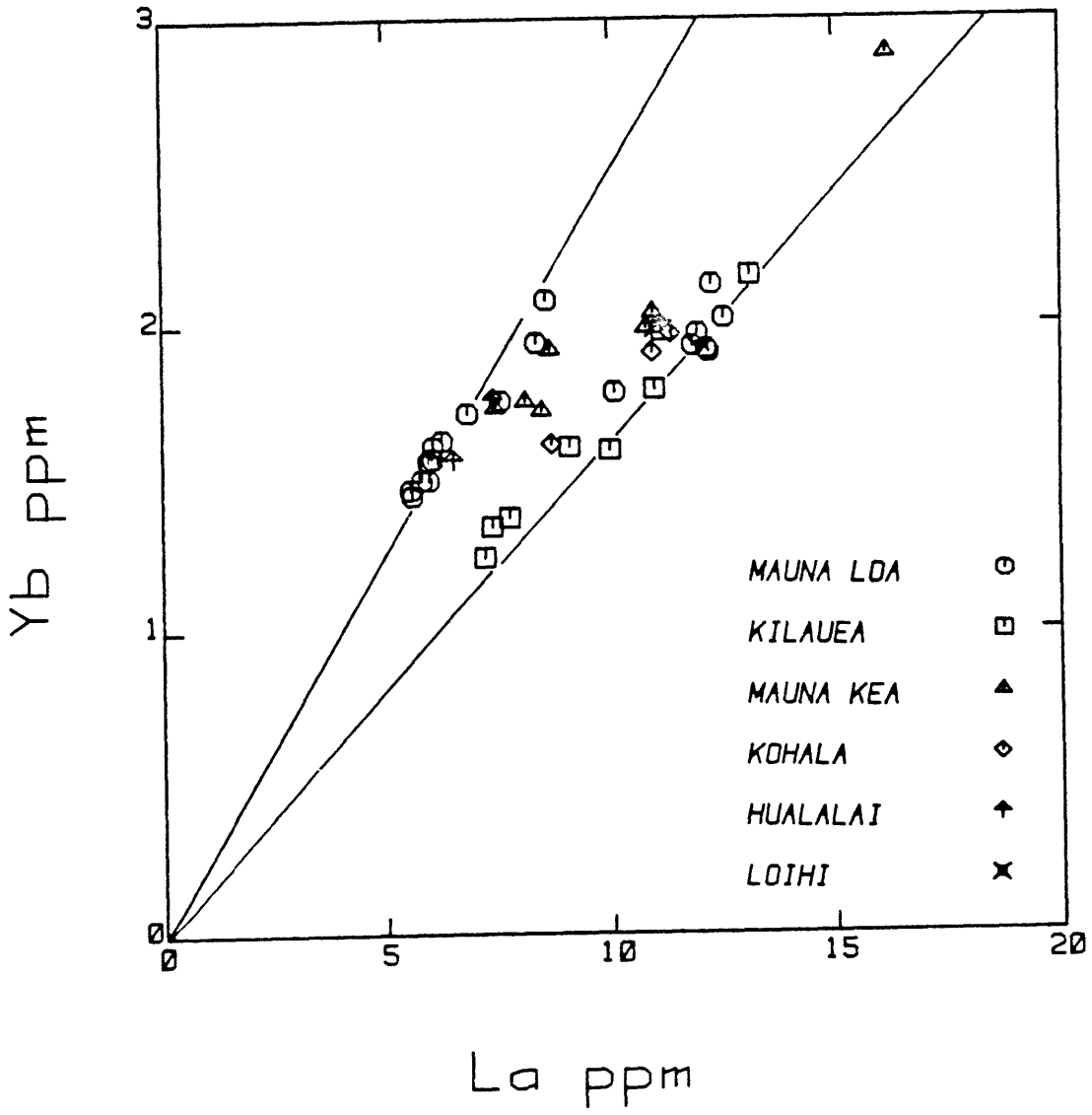

Figure 4.14. Same as 4.3

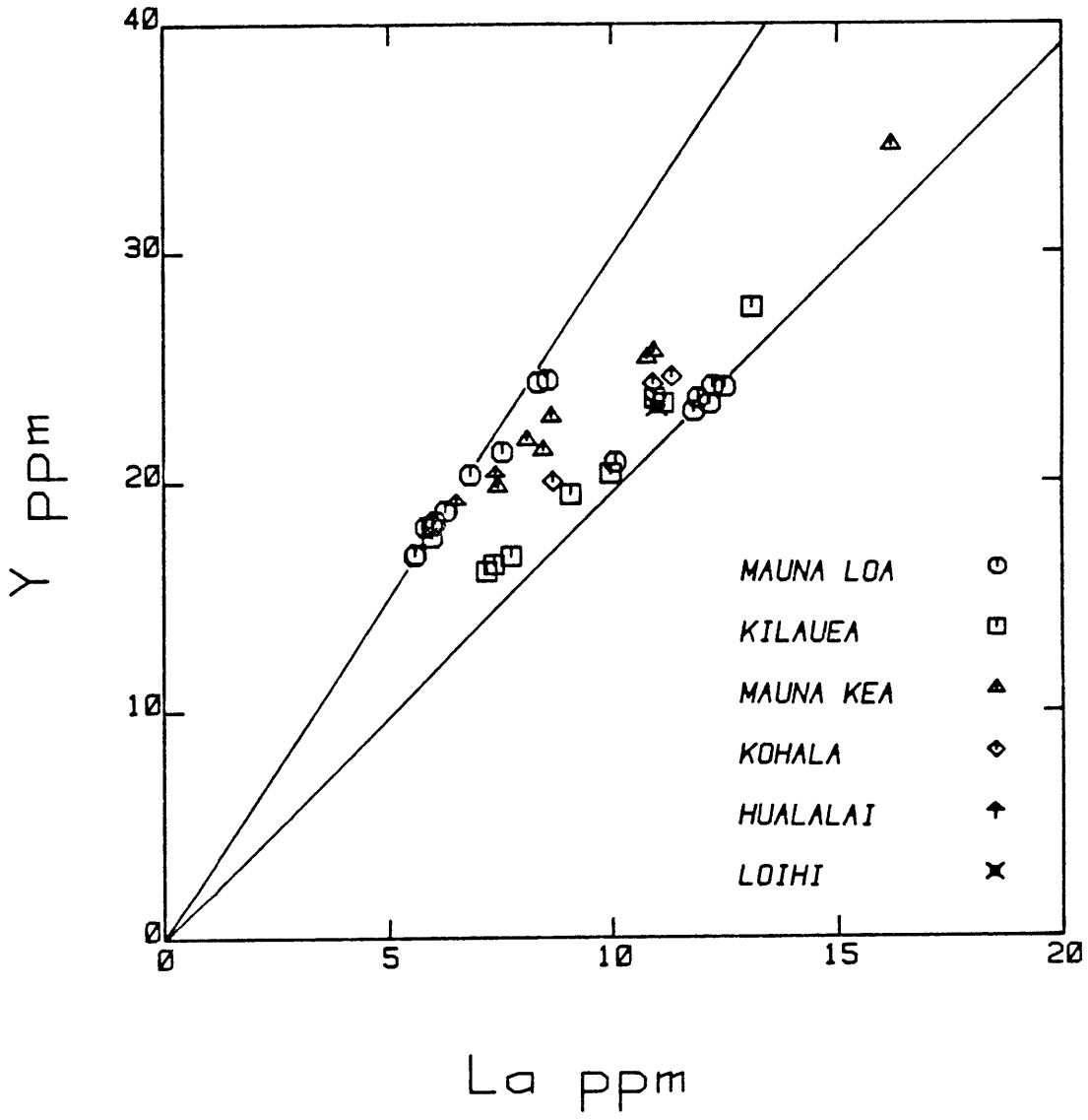

Figure 4.15. Same as 4.3

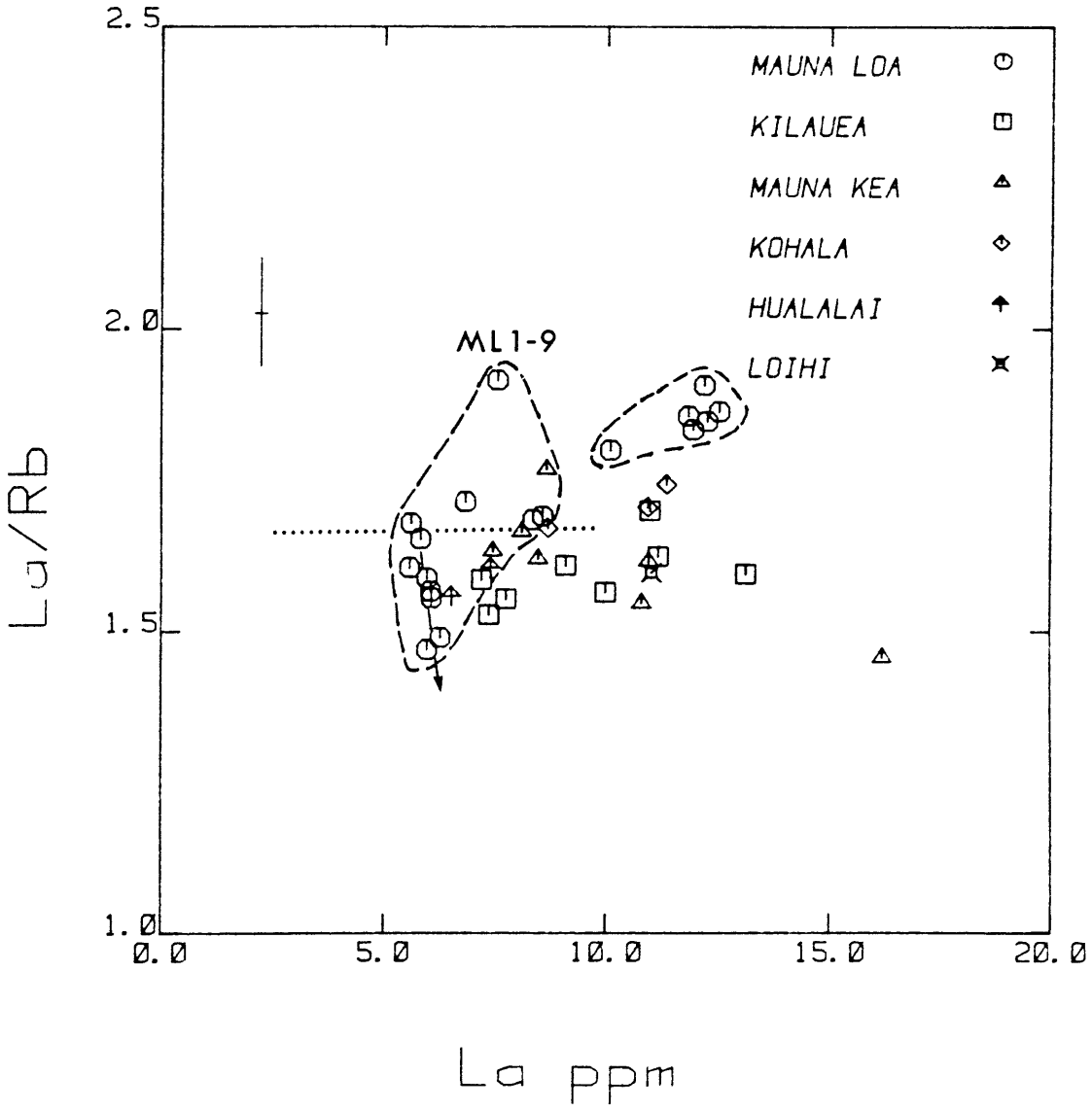

Figures 4.16–4.28. Plots of La/Rb, La/Sr, La/Ba, La/K_2O, La/Zr, La/Nb, La/Ce, La/Nd, La/Sm, La/Eu, La/Yb, La/Y and K_2O/Rb ratios versus La abundance. The two different Mauna Loa groups are circled with dashed curves. The arrows in La/Rb *vs.* La, K_2O/Rb *vs.* La and La/K_2O *vs.* La indicate a possible effect of low temperature alteration as discussed in section 4.3.1.

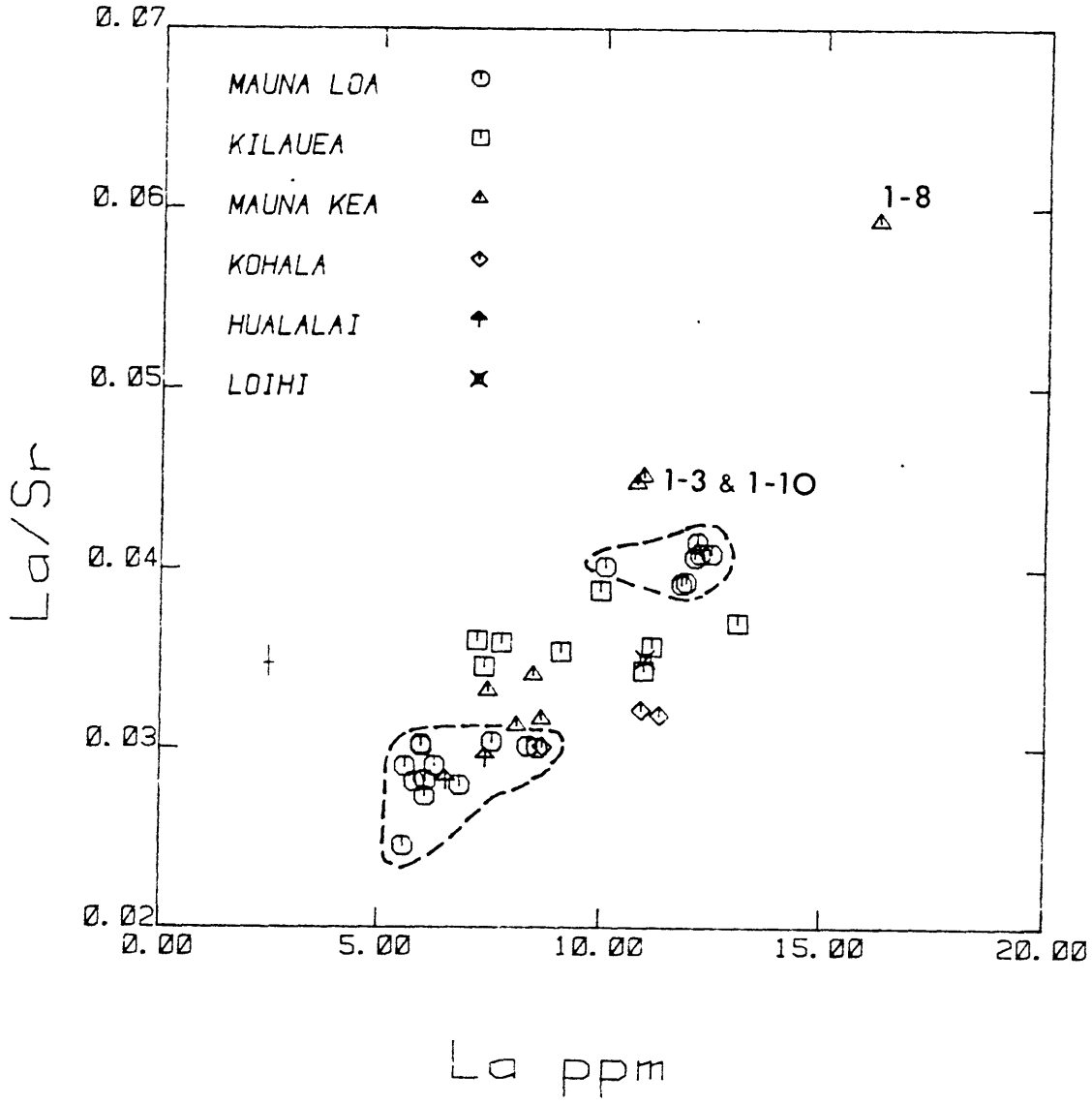

Figure 4.17. Same as 4.16

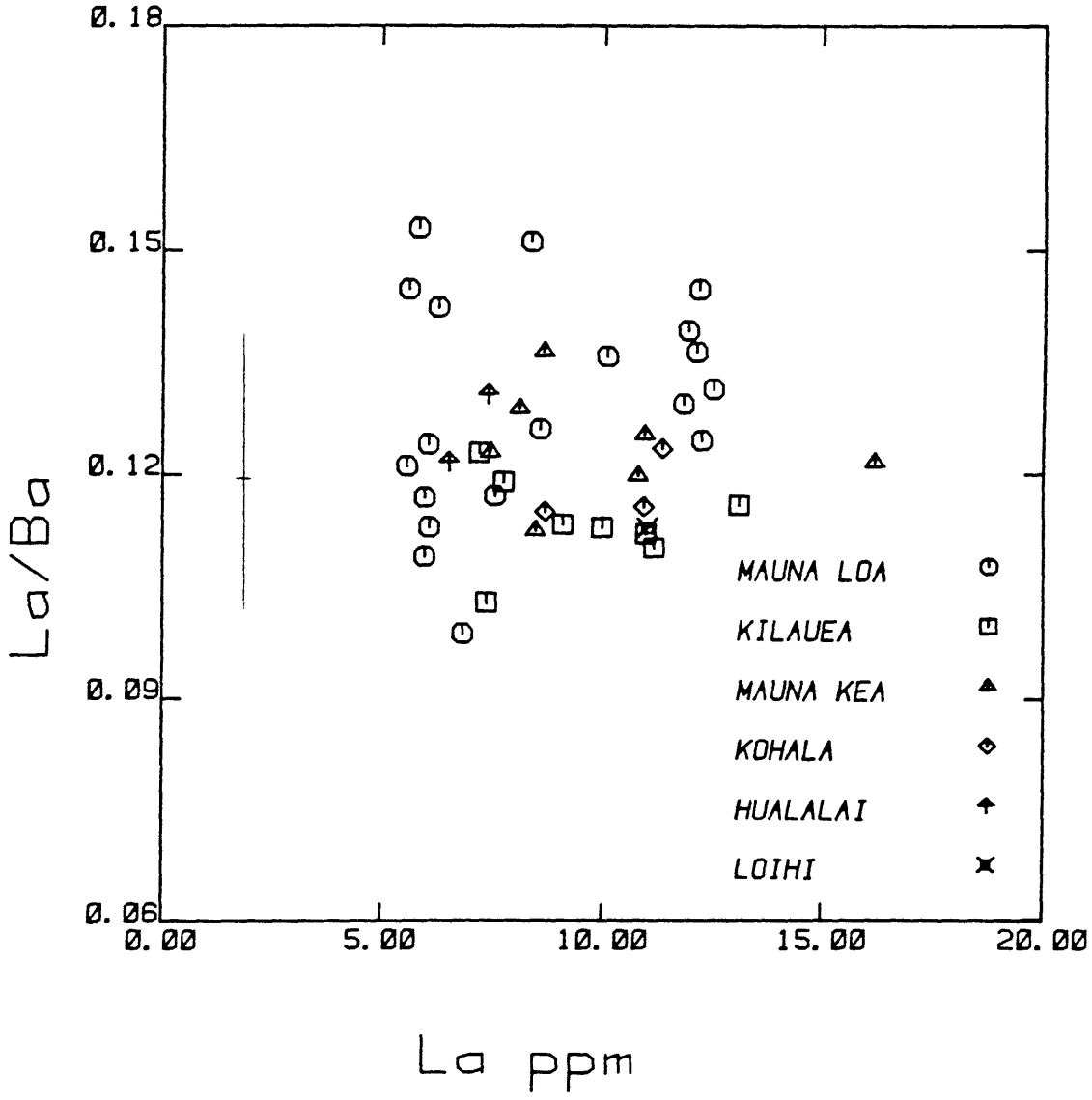

Figure 4.18. Same as 4.16

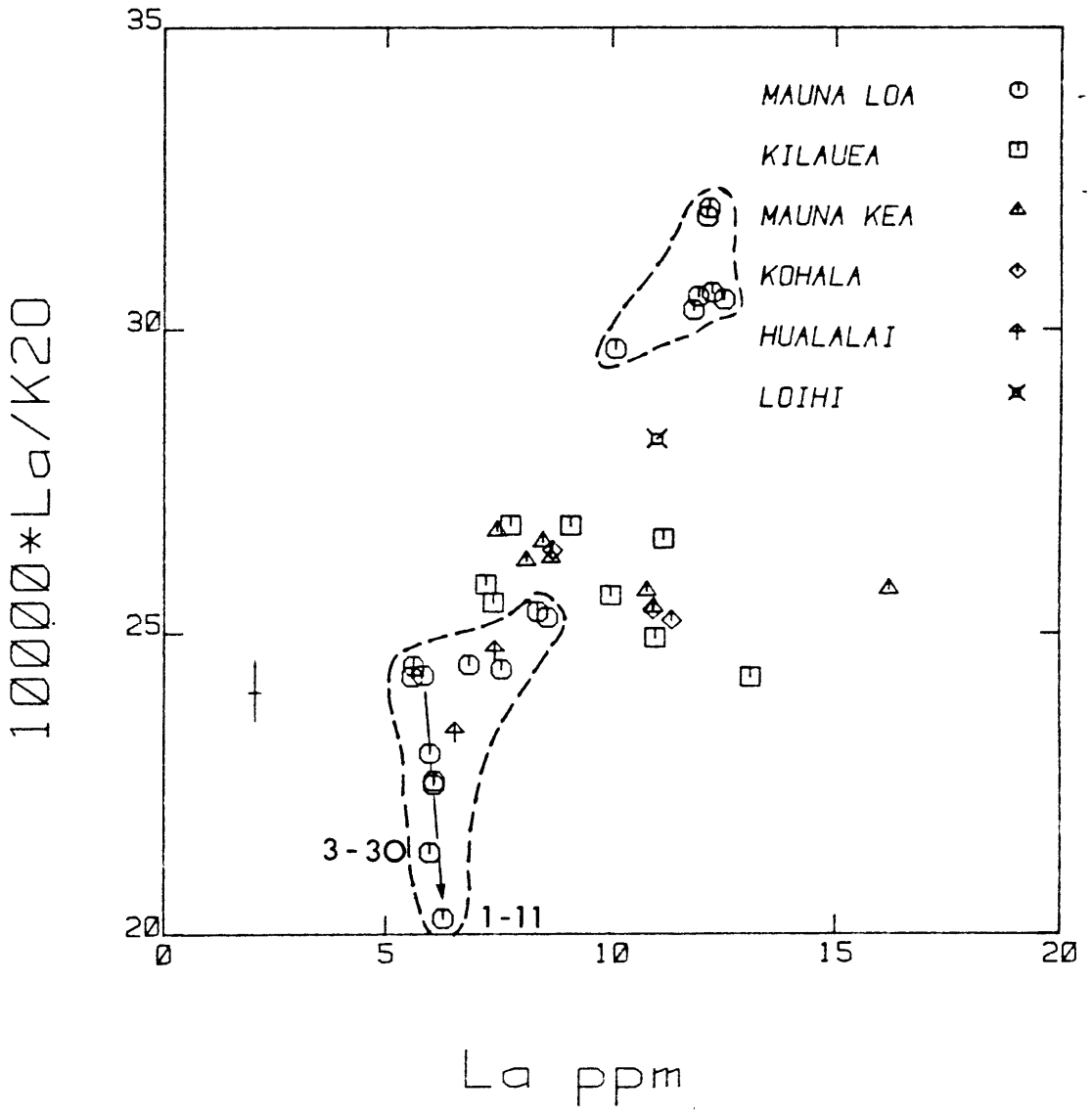

Figure 4.19. Same as 4.16

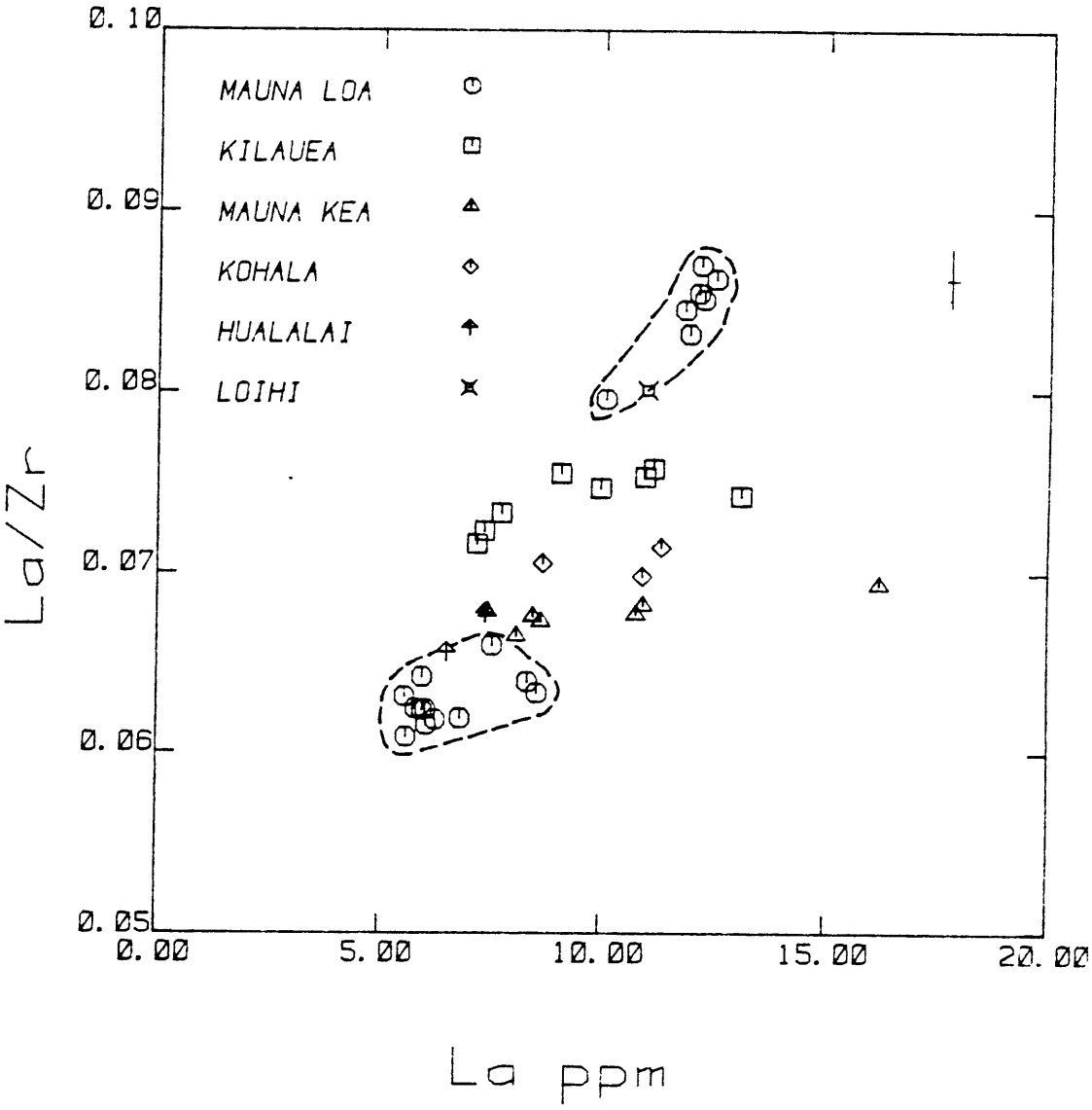

Figure 4.20. Same as 4.16

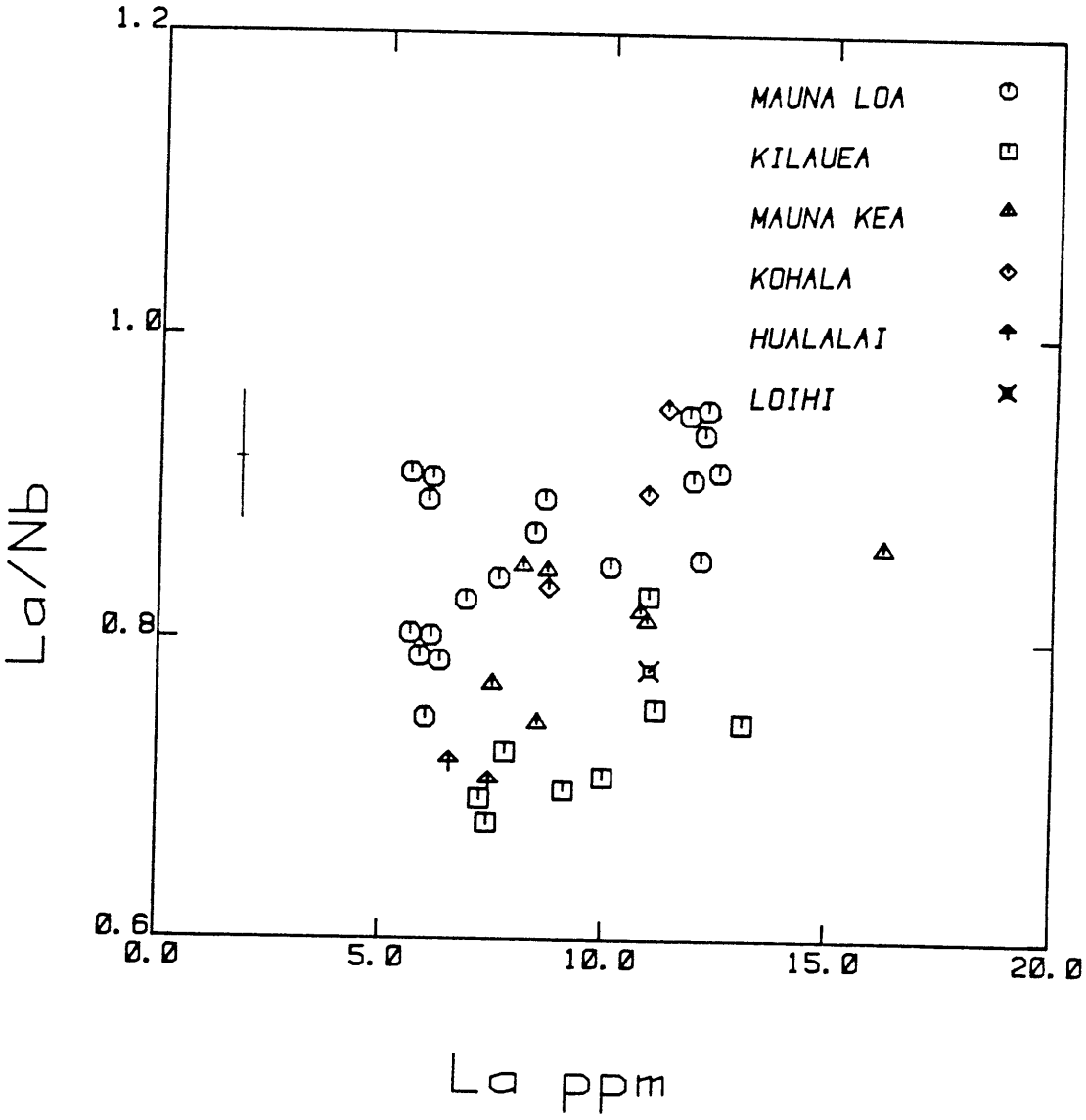

Figure 4.21. Same as 4.16

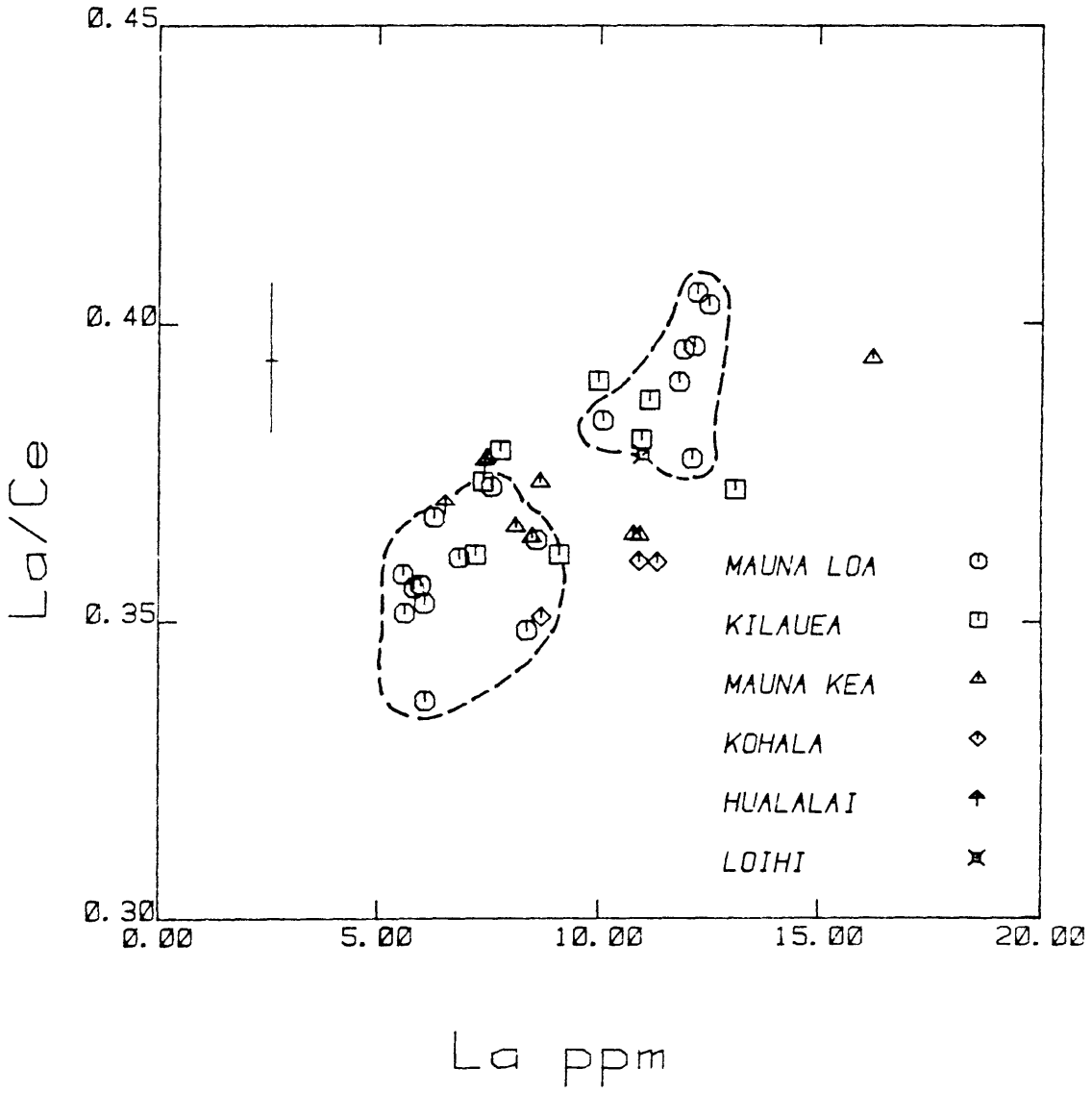

Figure 4.22. Same as 4.16

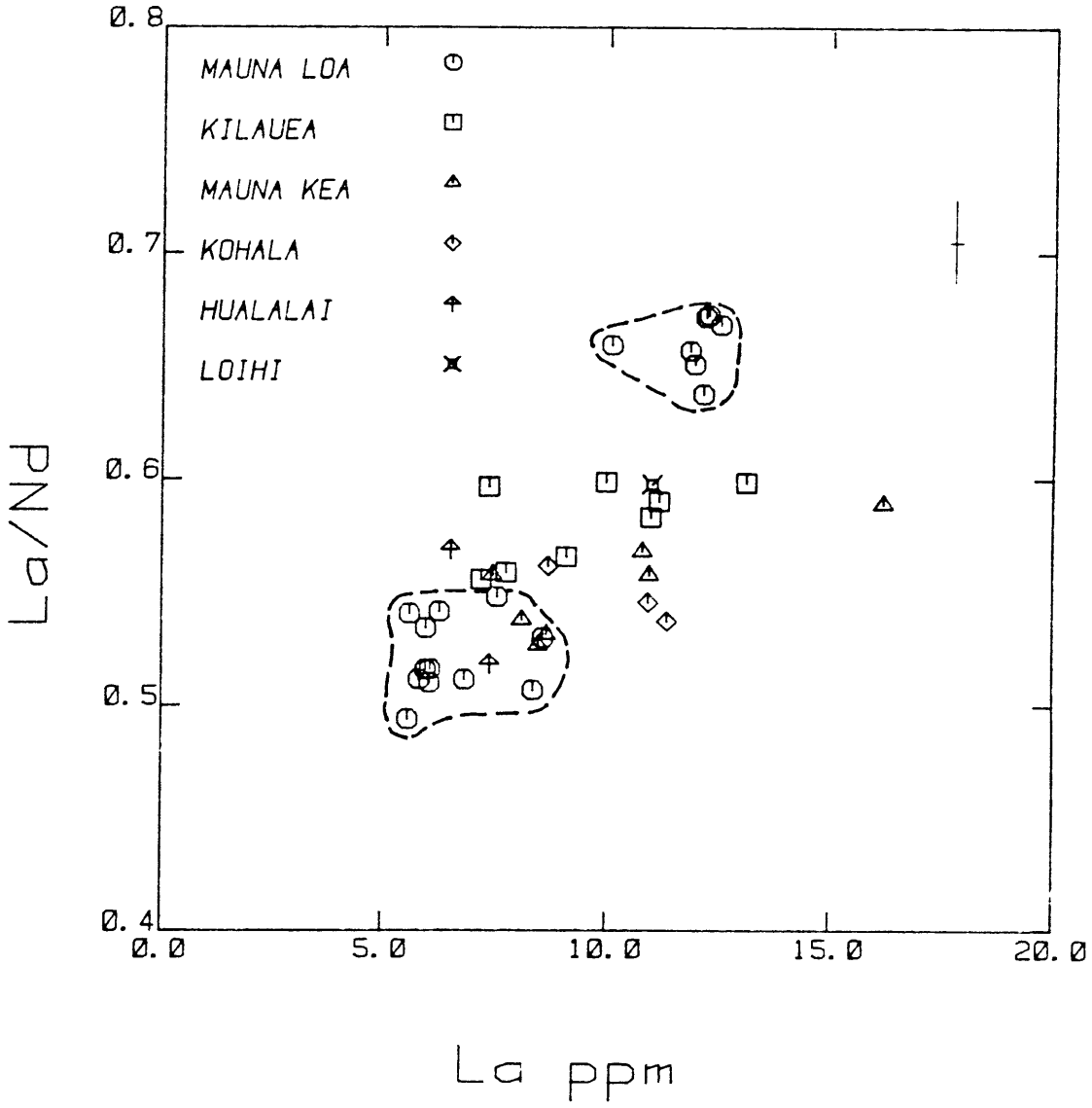

Figure 4.23. Same as 4.16

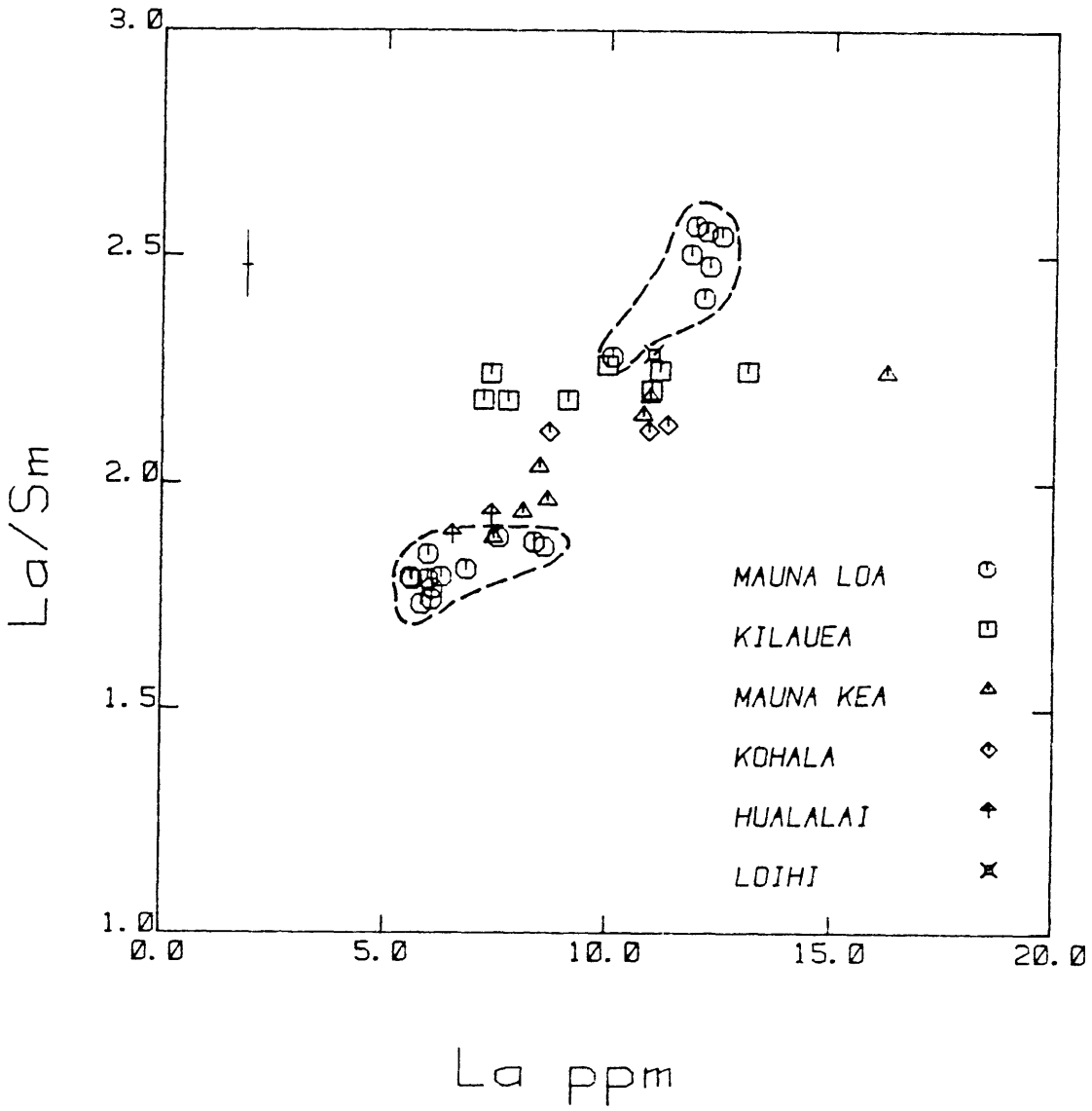

Figure 4.24. Same as 4.16

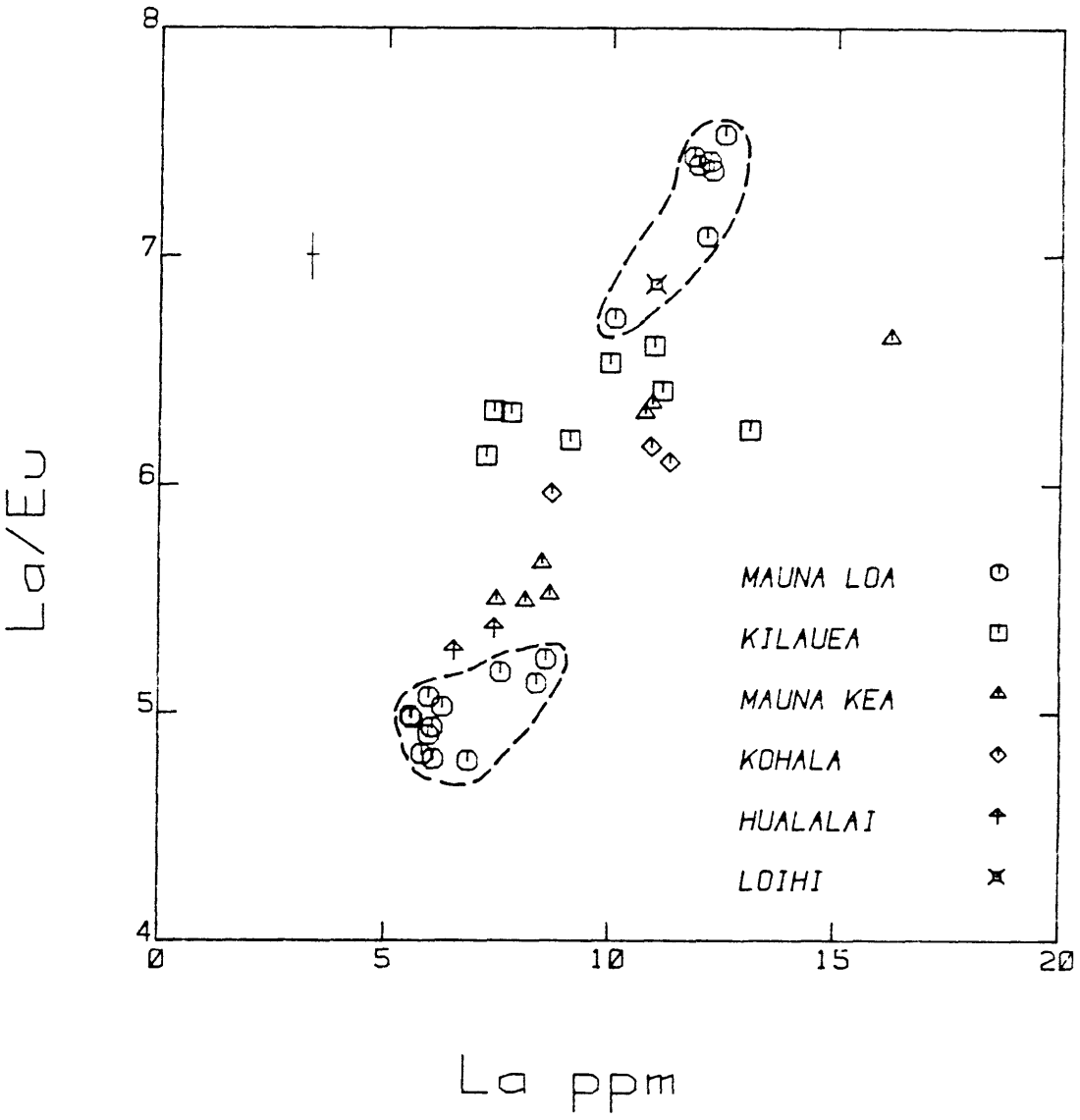

Figure 4.25. Same as 4.16

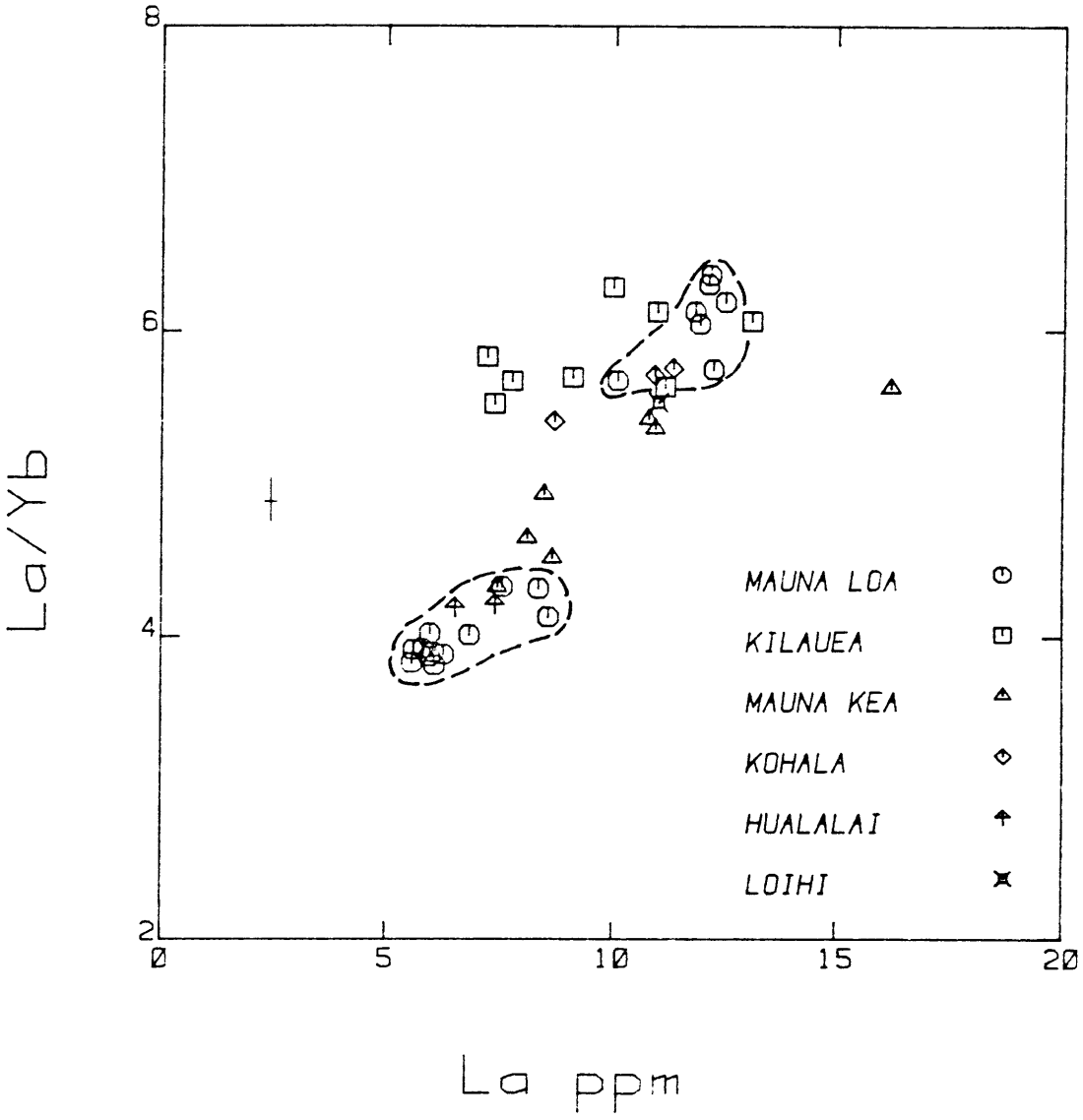

Figure 4.26. Same as 4.16

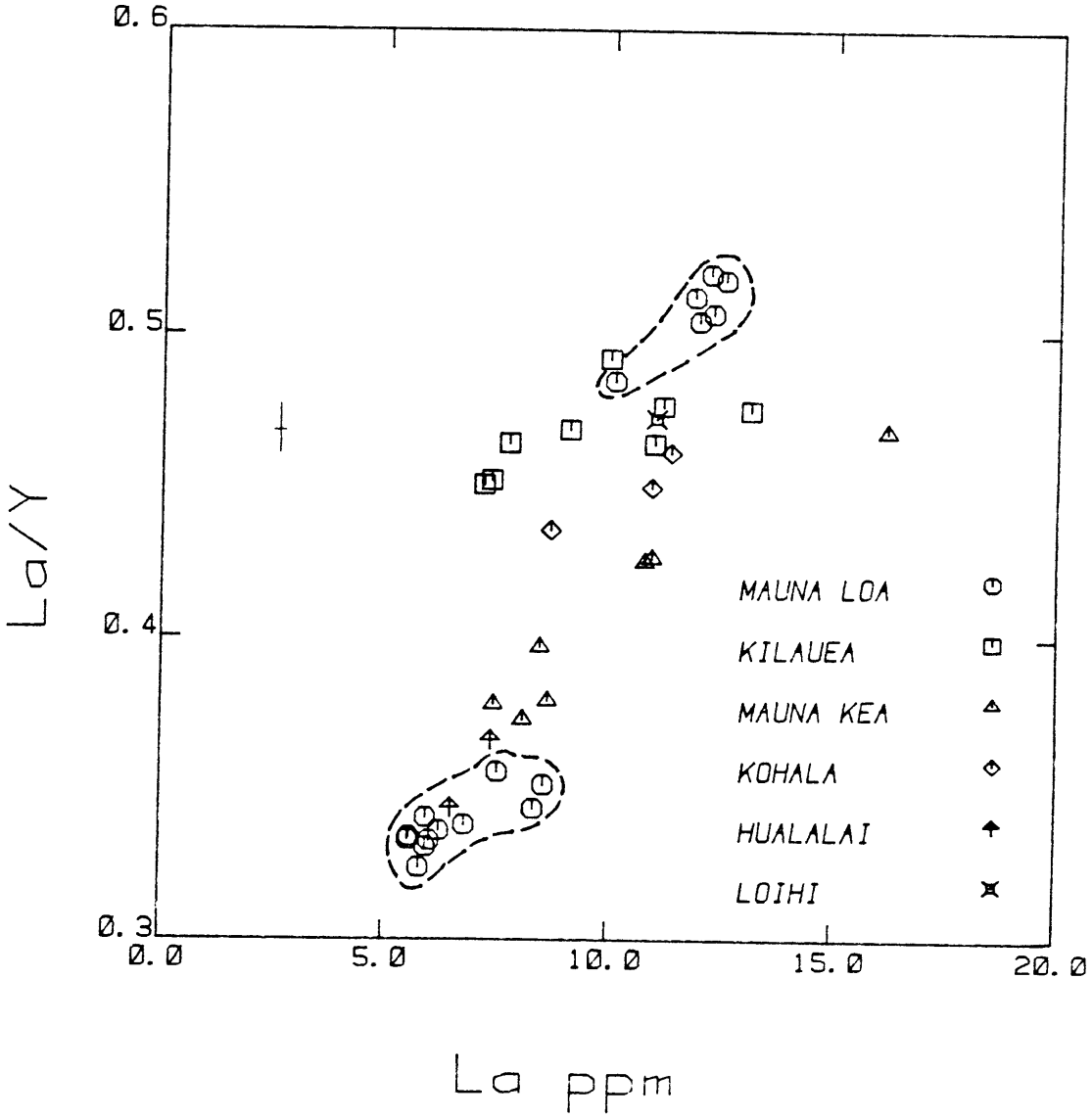

Figure 4.27. Same as 4.16

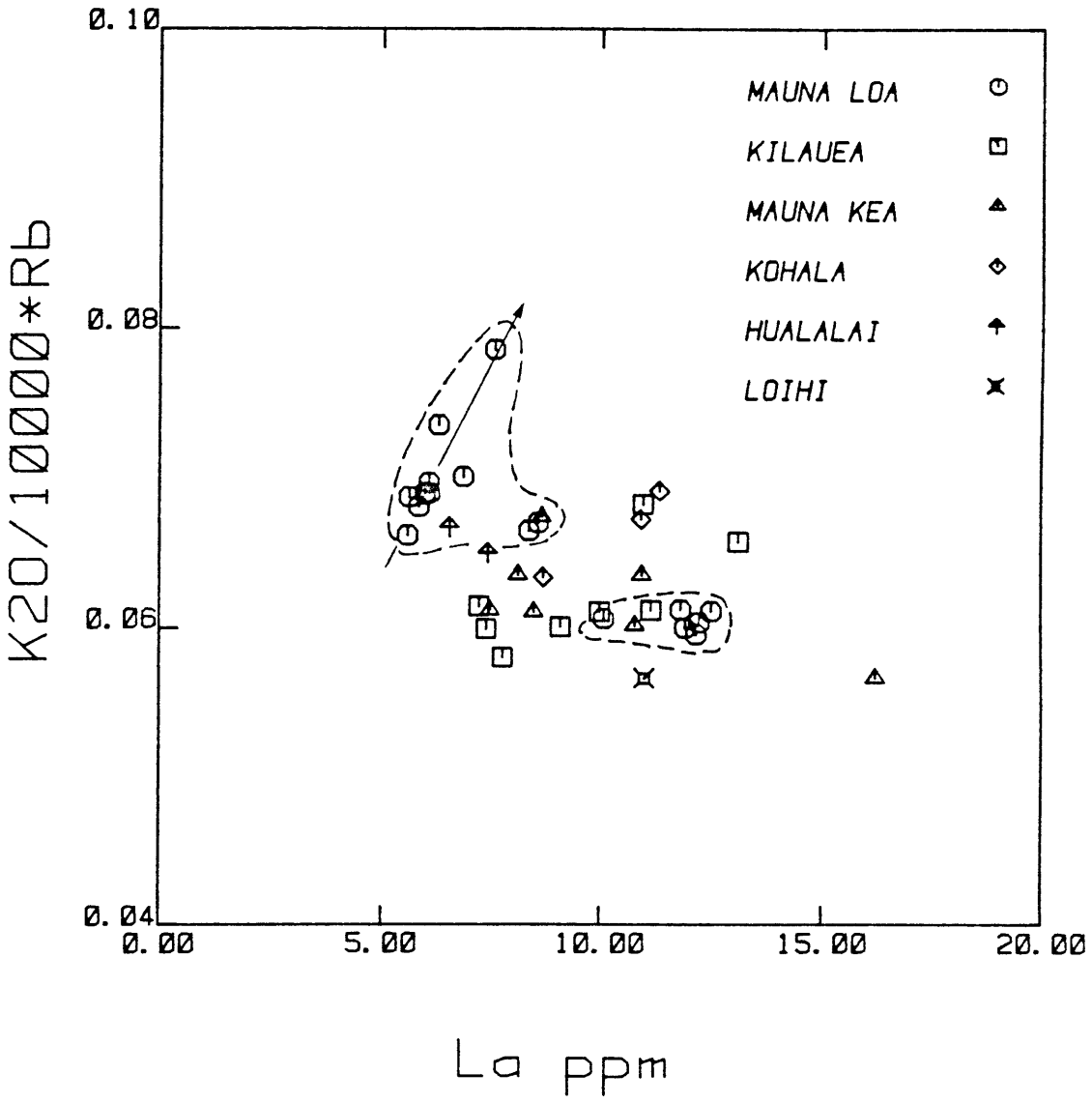

Figure 4.28. Same as 4.16

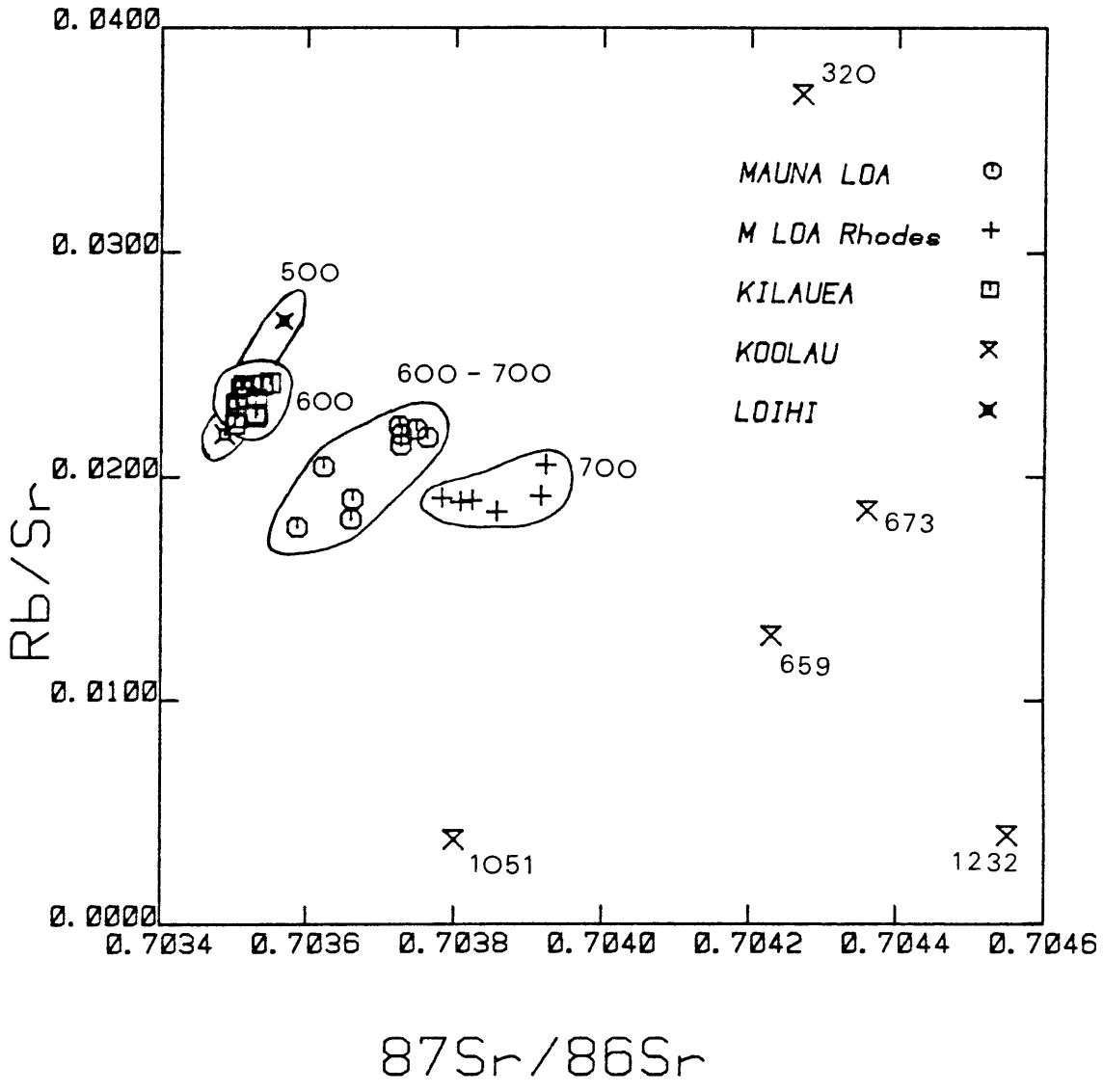

Figure 4.29. Strontium isochron plot of Hawaiian tholeiites. The data lableled "M LOA Rhodes" are from Rhodes and Hart, 1987. Kilauea, Koolau and Loihi data are from Hofmann *et al.*, 1984, Roden *et al.*, 1984 and Staudigel et al., 1984, respectively. The numbers adjacent to individual fields give the average K_2O/Rb value in lavas from the corresponding volcano.

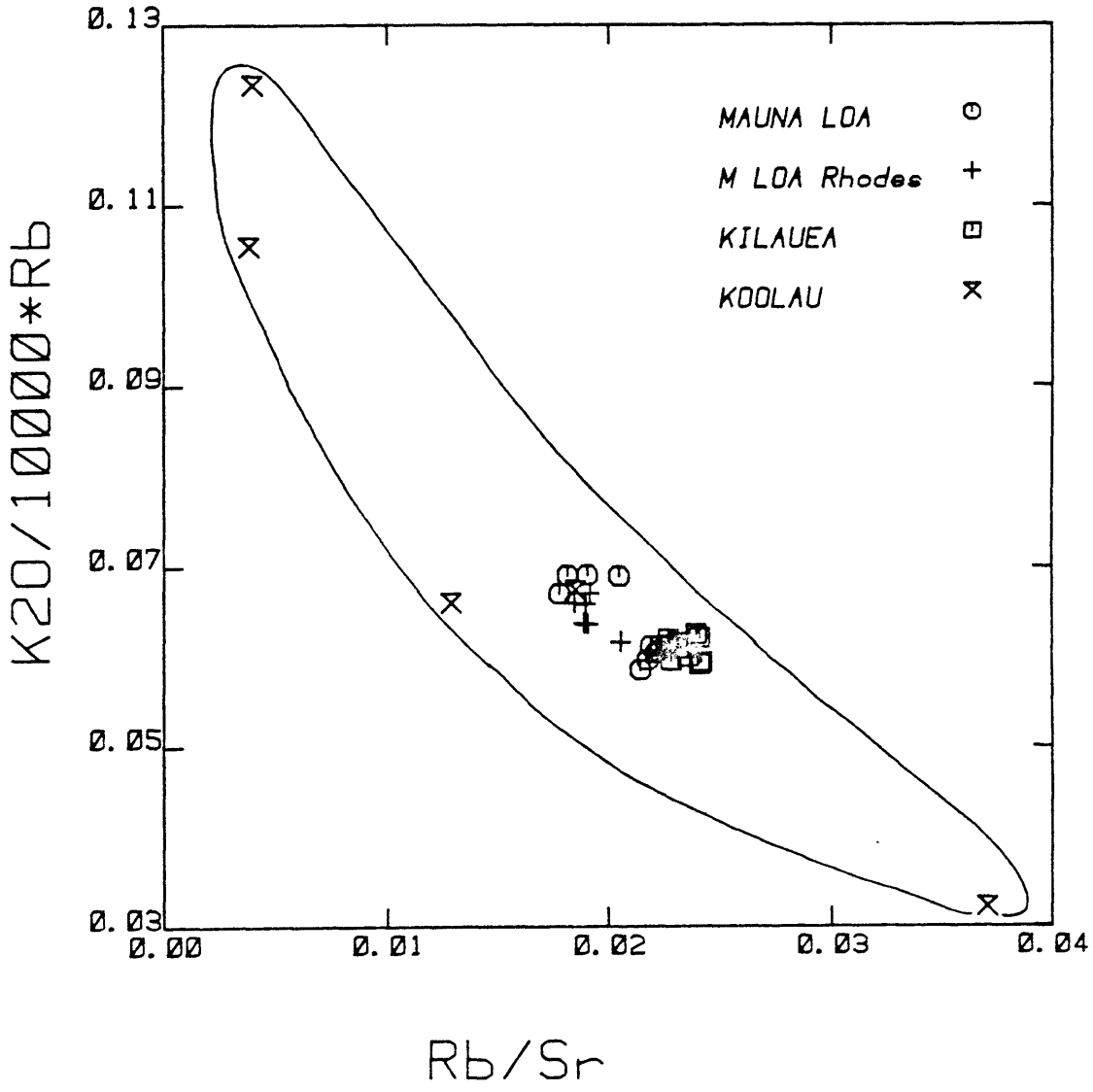

Figure 4.30. Correlation of K_2O/Rb and Rb/Sr ratios in Hawaiian tholeiites. References are same as in Figure 4.28.

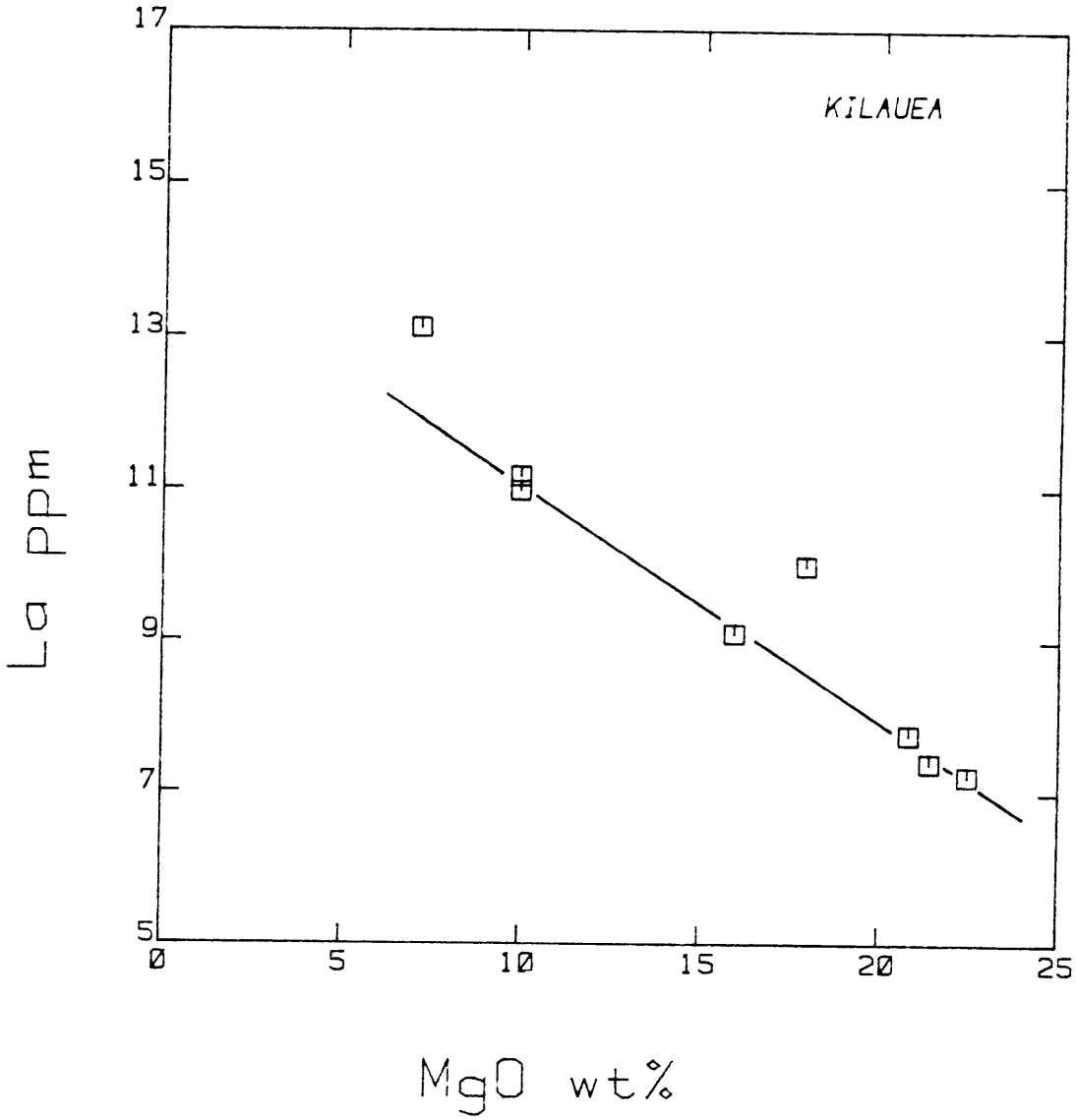

Figure 4.31. Abundance of La versus MgO concentration in Kilauea data set.

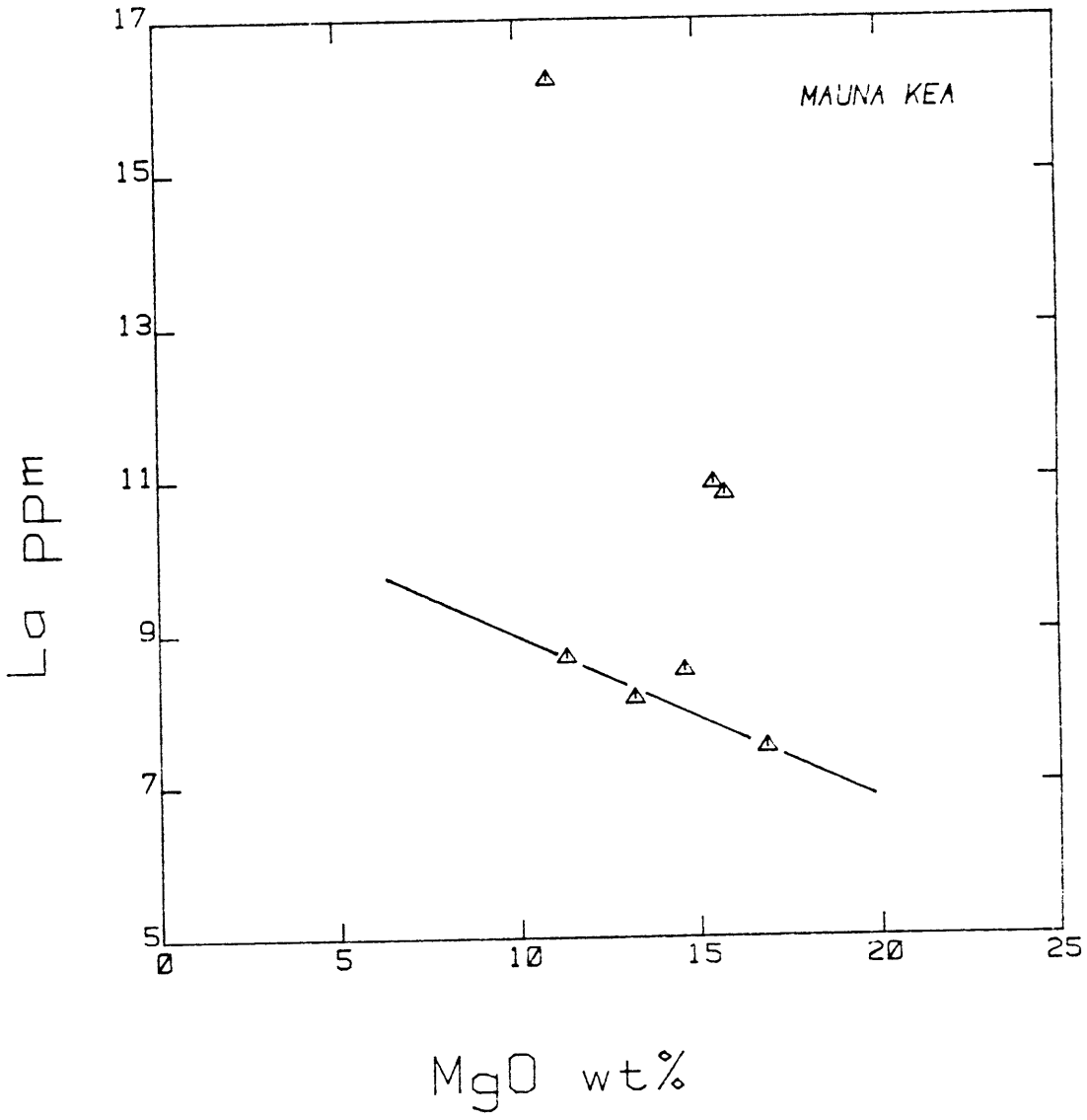

Figure 4.32. Abundance of La versus MgO concentration in Mauna Kea data set.

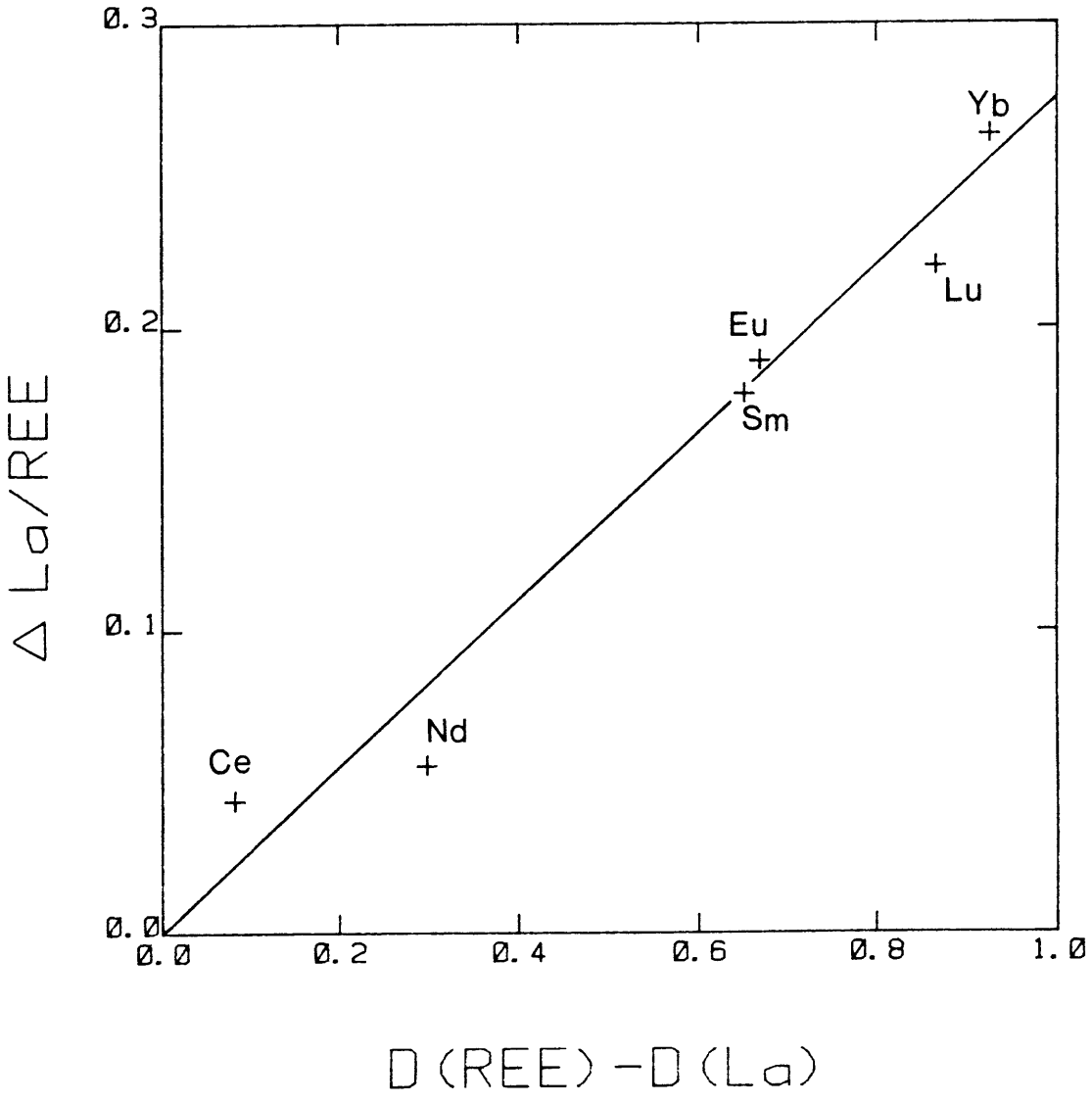

Figure 4.33. Plot of the relative variation in the ratio of La over other rare earth elements between samples MK1–8 and MK6–6, versus the difference in partition coefficient in clinopyroxene between the elements considered and La (see text). The set of partition coefficients used is from Onuma *et al.*, 1968 (0.084, 0.166, 0.382, 0.736, 0.753, 1.01 and 0.95 for La, Ce, Nd, Sm, Eu, Yb and Lu respectively).

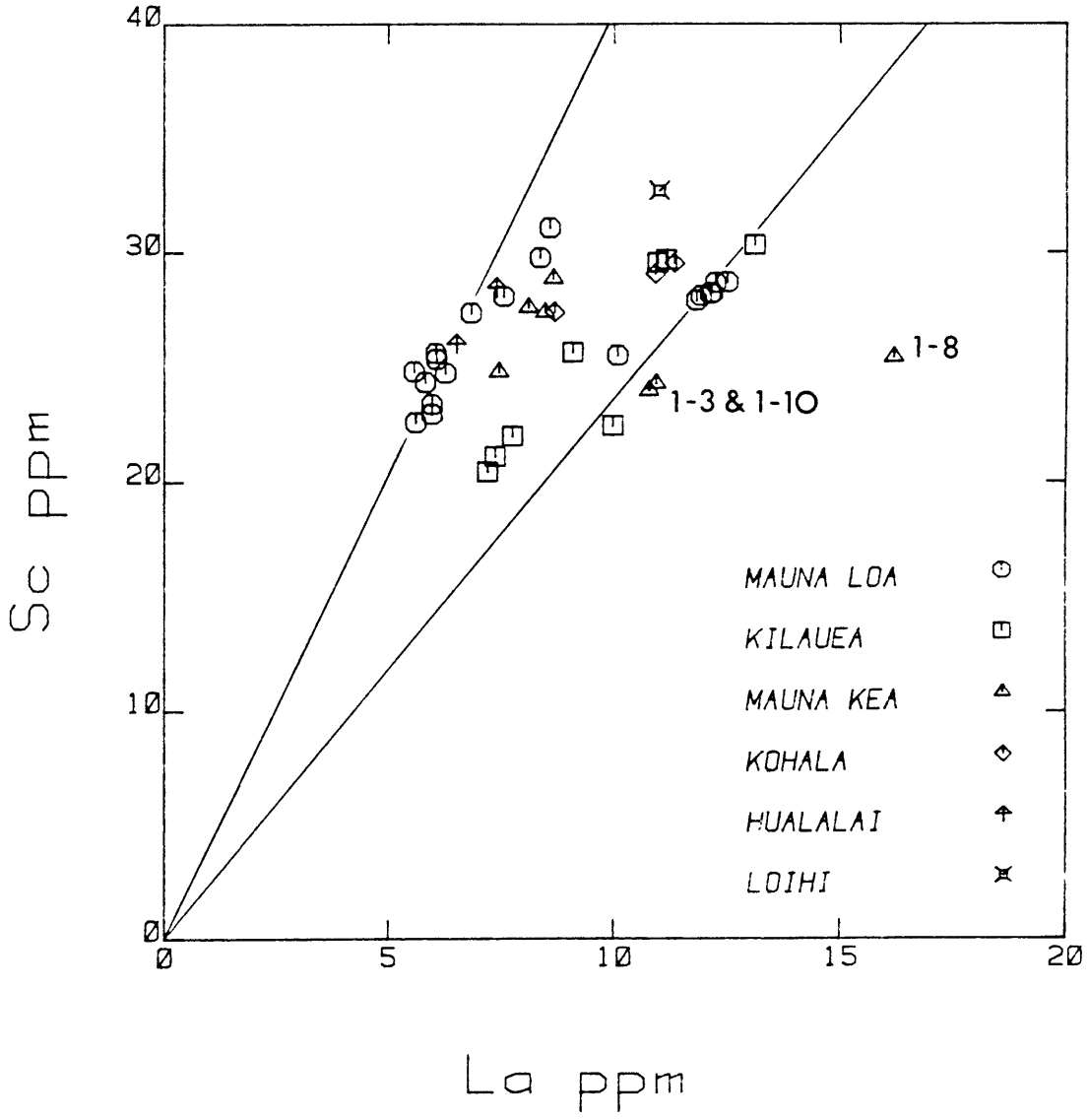

Figure 4.34. Plot of Sc versus La for the complete data set

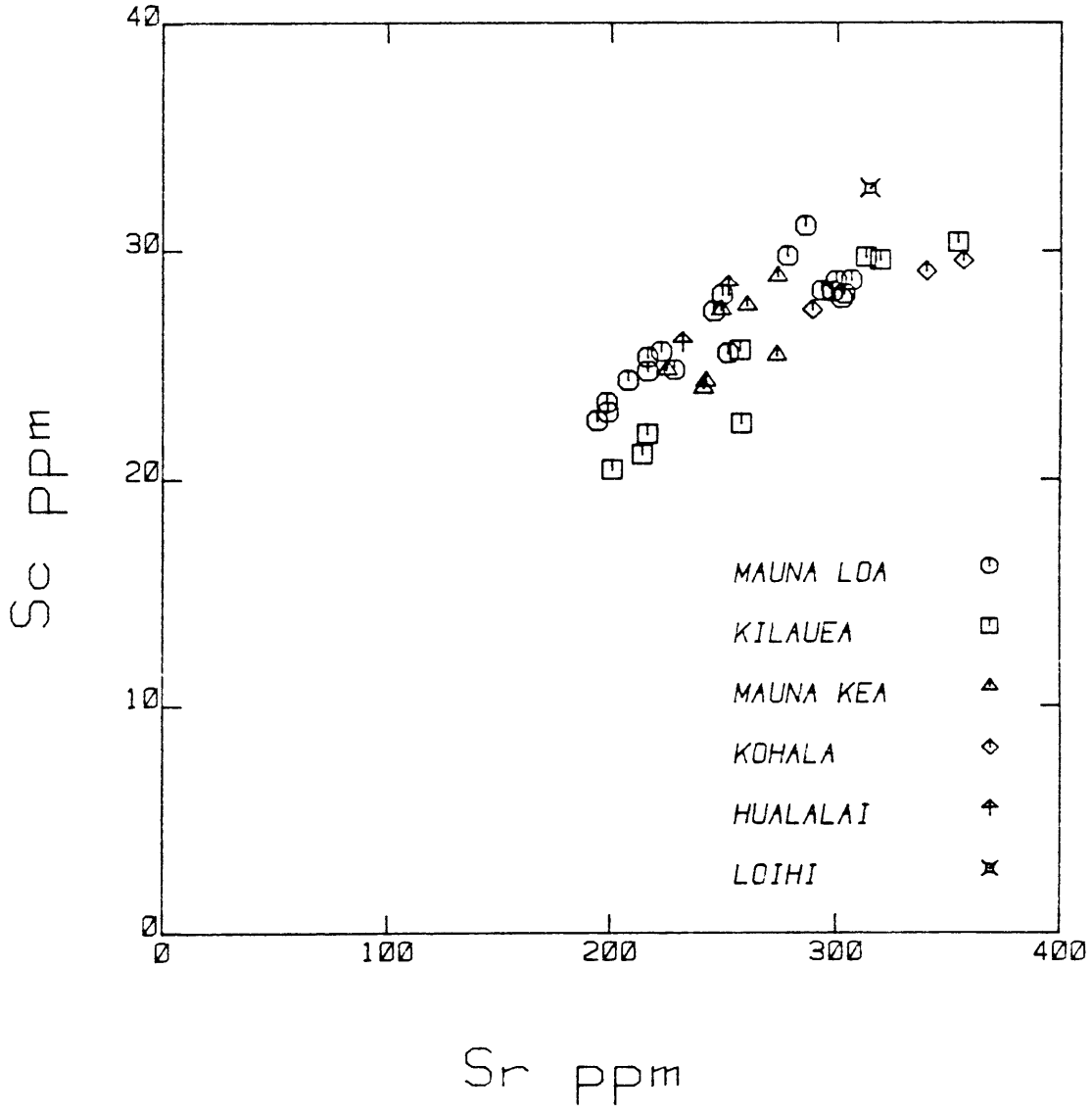

Figure 4.35. Plot of Sc versus Sr for the complete data set

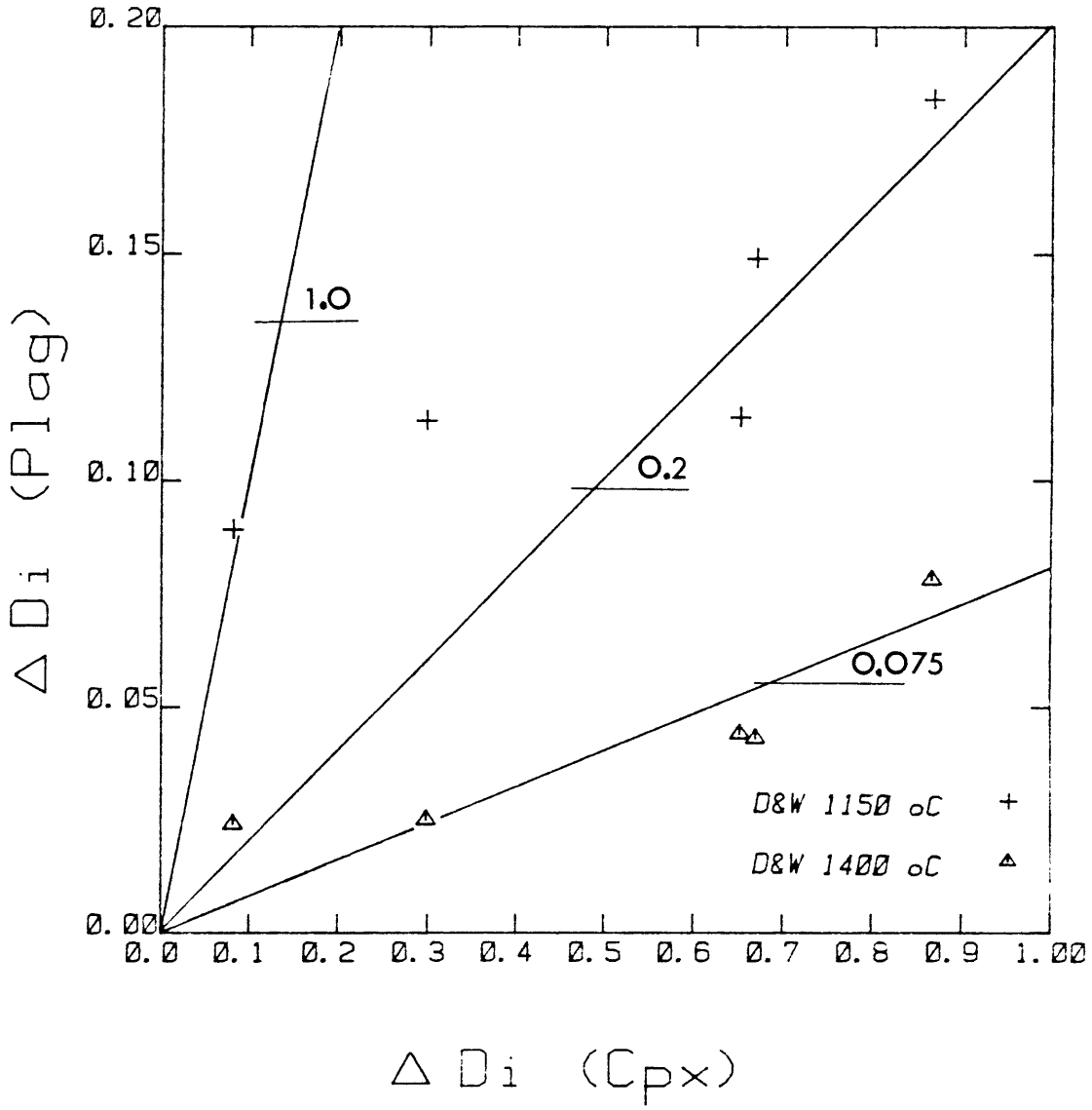

Figure 4.36. Plot of the difference in partition coefficients between La and other rare earth elements in plagioclase versus the same quantity in clinopyroxene. Clinopyroxene PC are from Onuma *et al.*, 1968. We used plagioclase PC from Drake and Weil, 1974, at 1150°C and 1400°C. Lines of slope 1.0, 0.2 and 0.075 are drawn for comparison of the two variables' magnitudes.

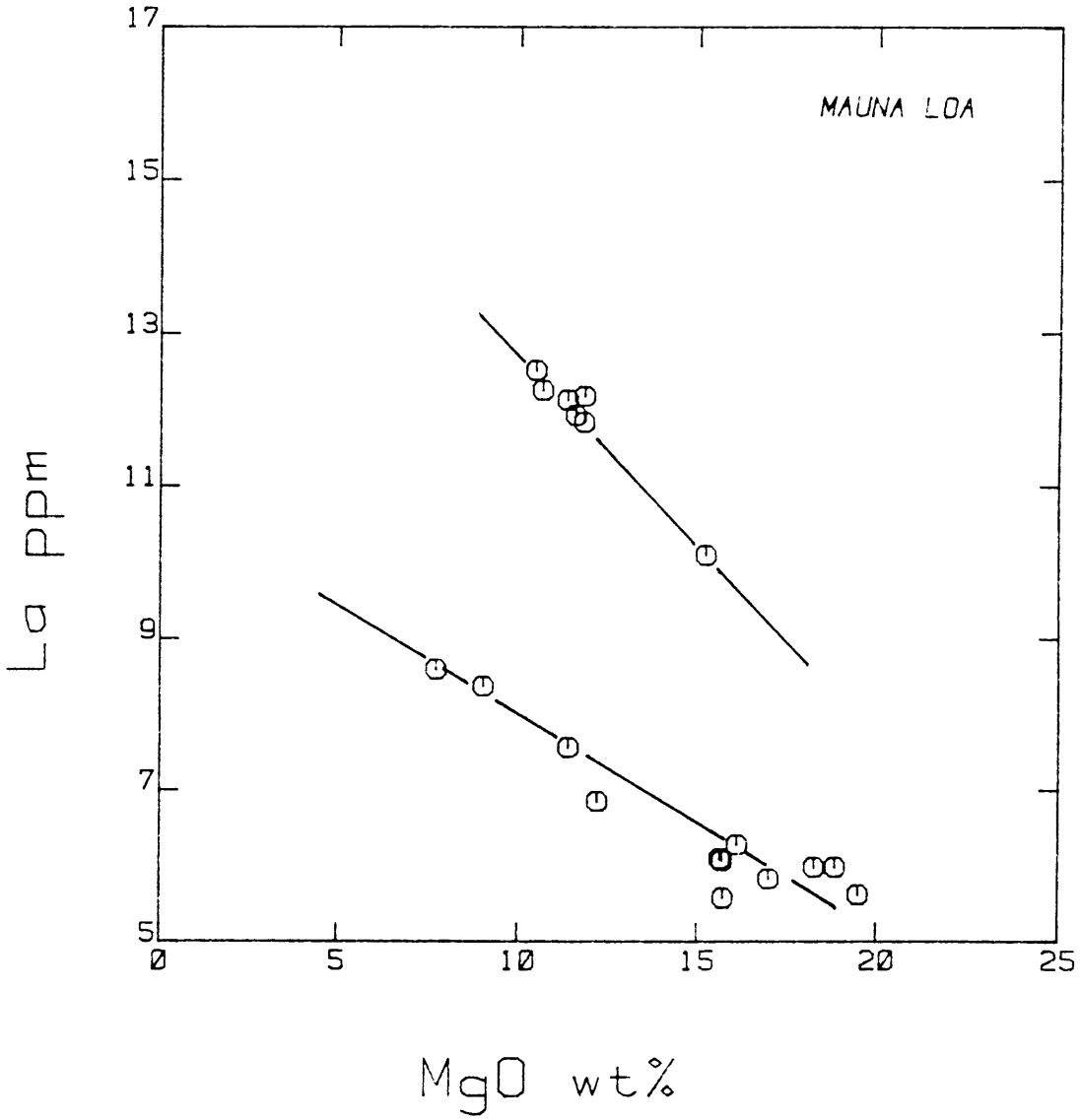

Figure 4.37. Abundance of La versus MgO concentration in Mauna Loa data set

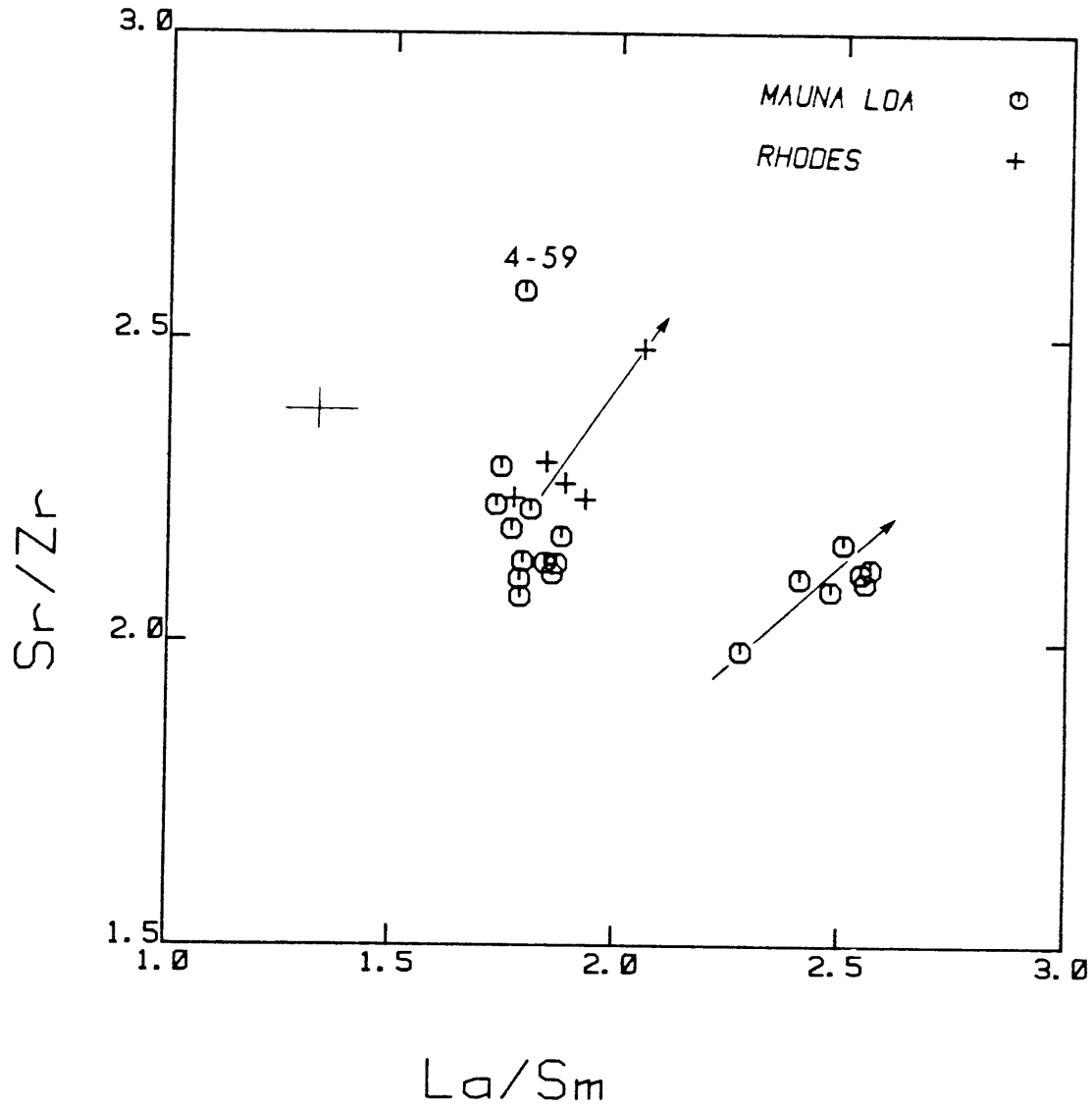

Figure 4.38. Sr/Zr ratios versus La/Sm ratios in our Mauna Loa samples. Also plotted are historical Mauna Loa lavas analysed by Rhodes and Hart.

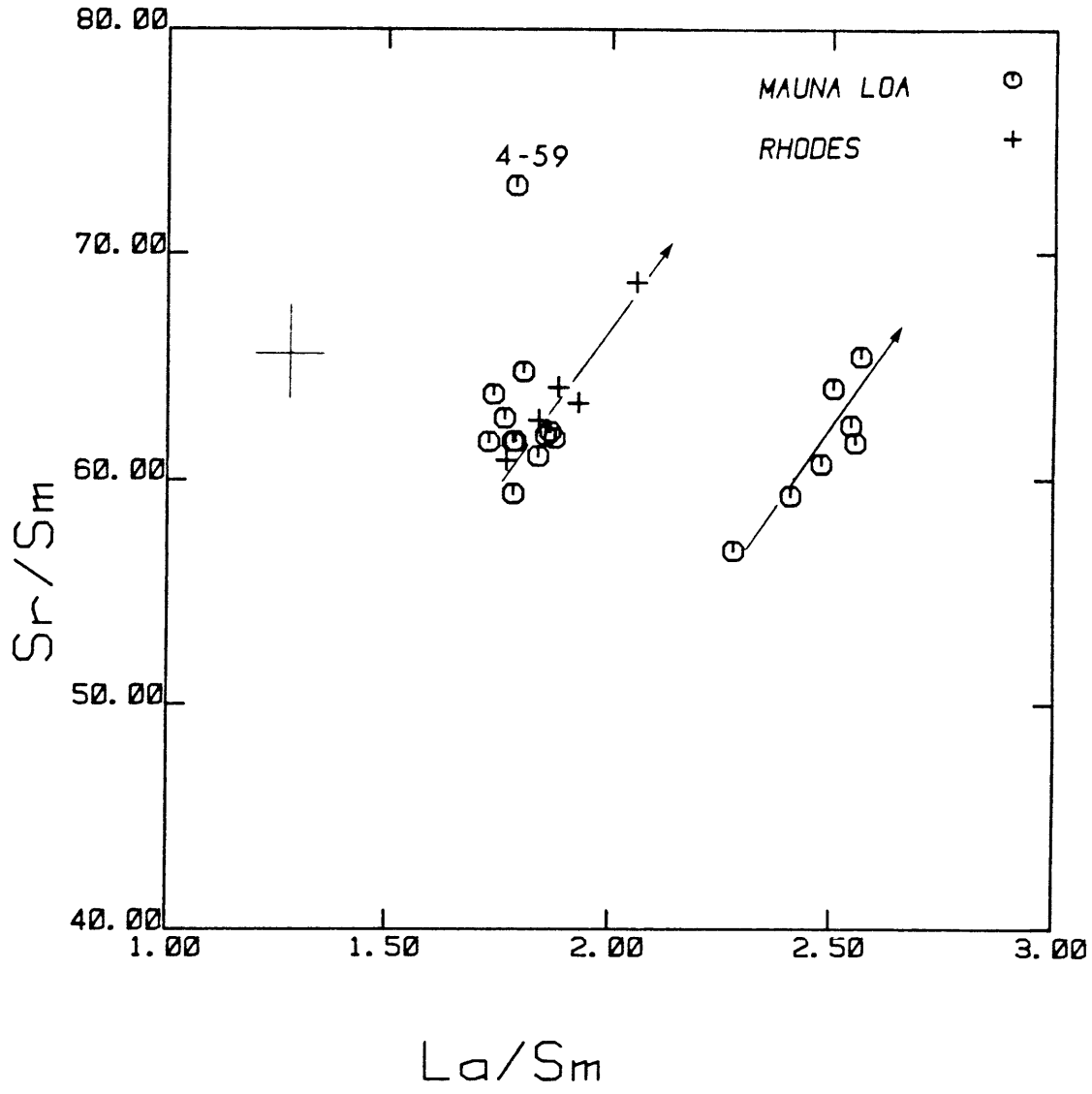

Figure 4.39. Sr/Sm ratios versus La/Sm ratios in our Mauna Loa samples. Also plotted are historical Mauna Loa lavas analysed by Rhodes and Hart.

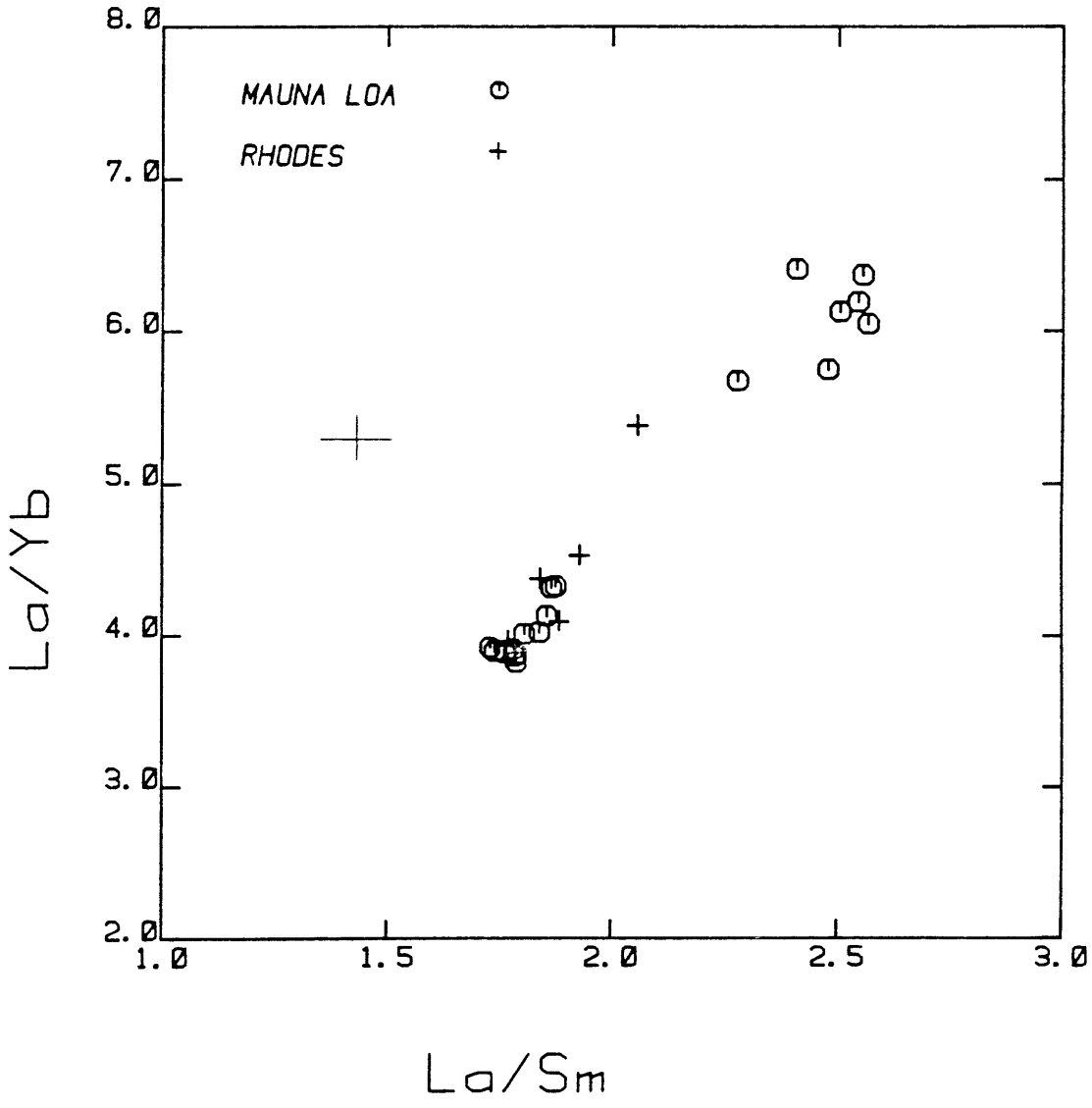

Figure 4.40. La/Yb ratios versus La/Sm ratios in our Mauna Loa samples. Also plotted are historical Mauna Loa lavas analysed by Rhodes and Hart.

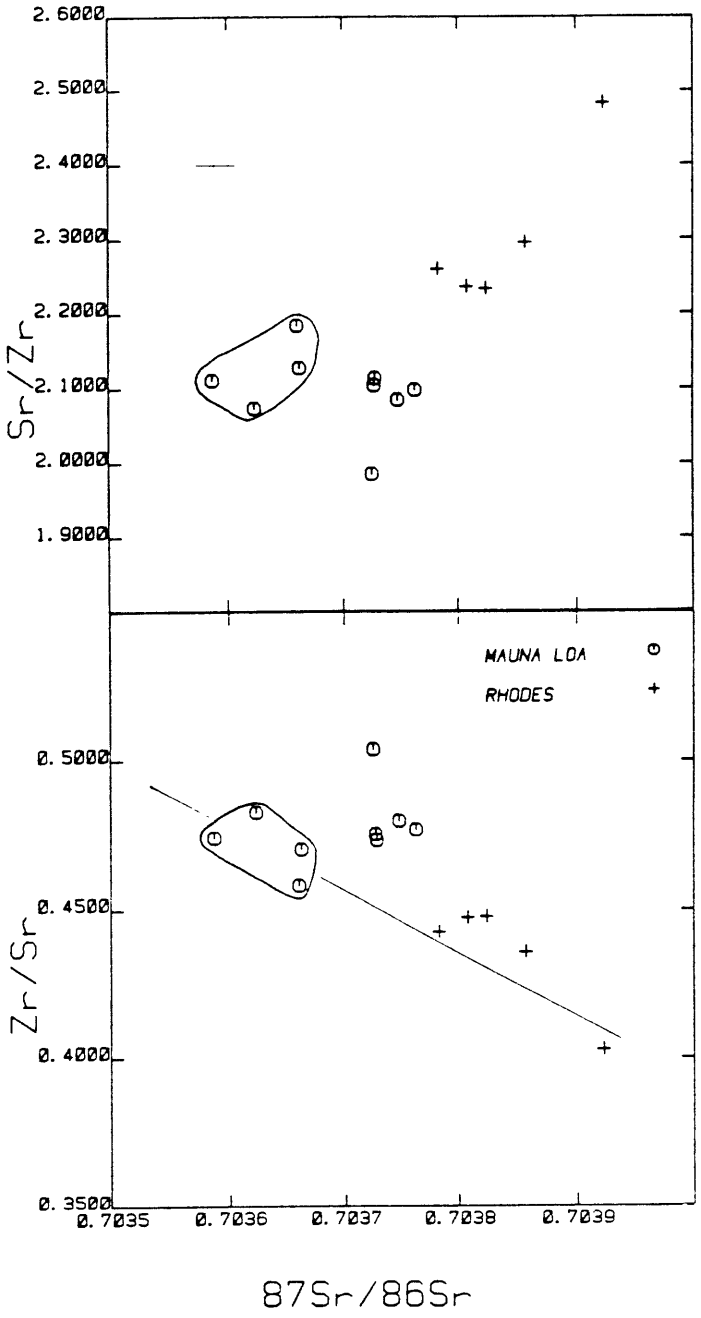

Figure 4.41. Plot of Sr/Zr ratio versus $^{87}Sr/^{86}Sr$ in our Mauna Loa samples and five historical Mauna Loa lavas analysed by Rhodes and Hart. The field of our "depleted" Mauna Loa samples is circled. A companion plot (Langmuir *et al.*, 1978) of the ratio of the two denominators versus one of the variables accompanies each plot. The dashed line provides an eye estimation of the fit of the data to a straight line in the companion plot, which would be consistent with mixing between our depleted group and Rhodes and Hart data.

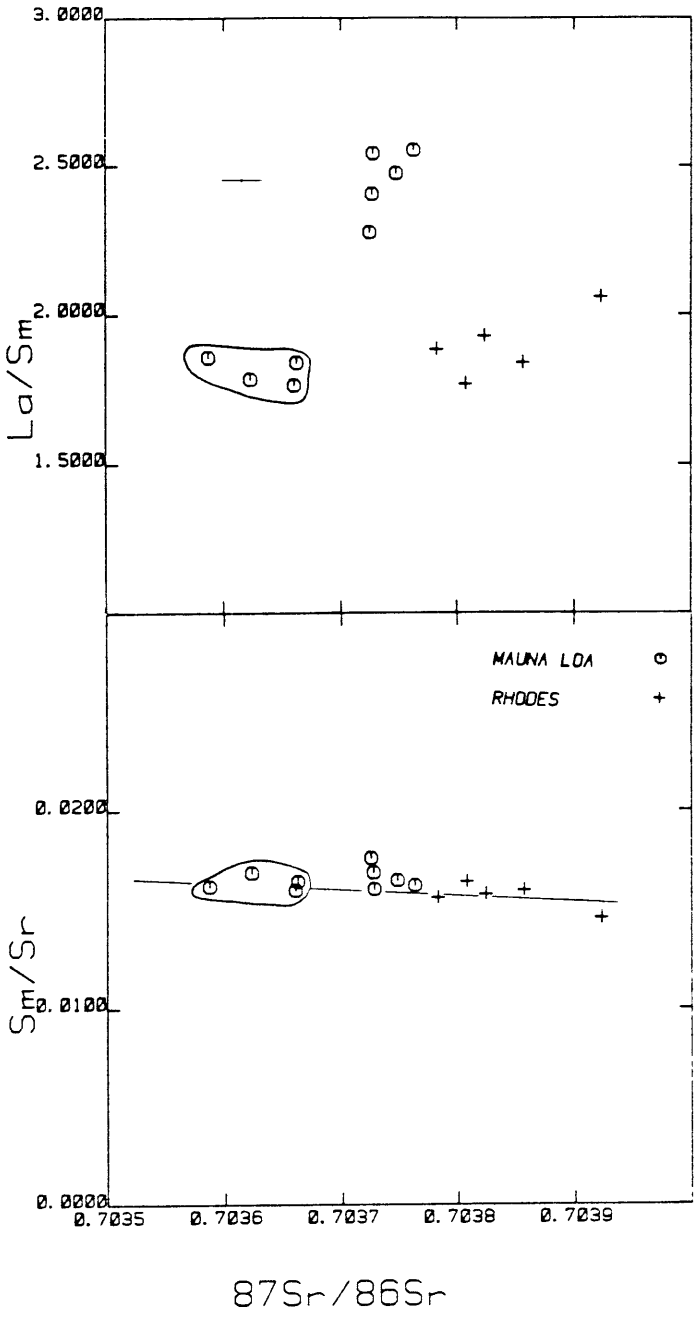

Figure 4.42. Same as 4.41 for La/Sm ratio versus $^{87}Sr/^{86}Sr$

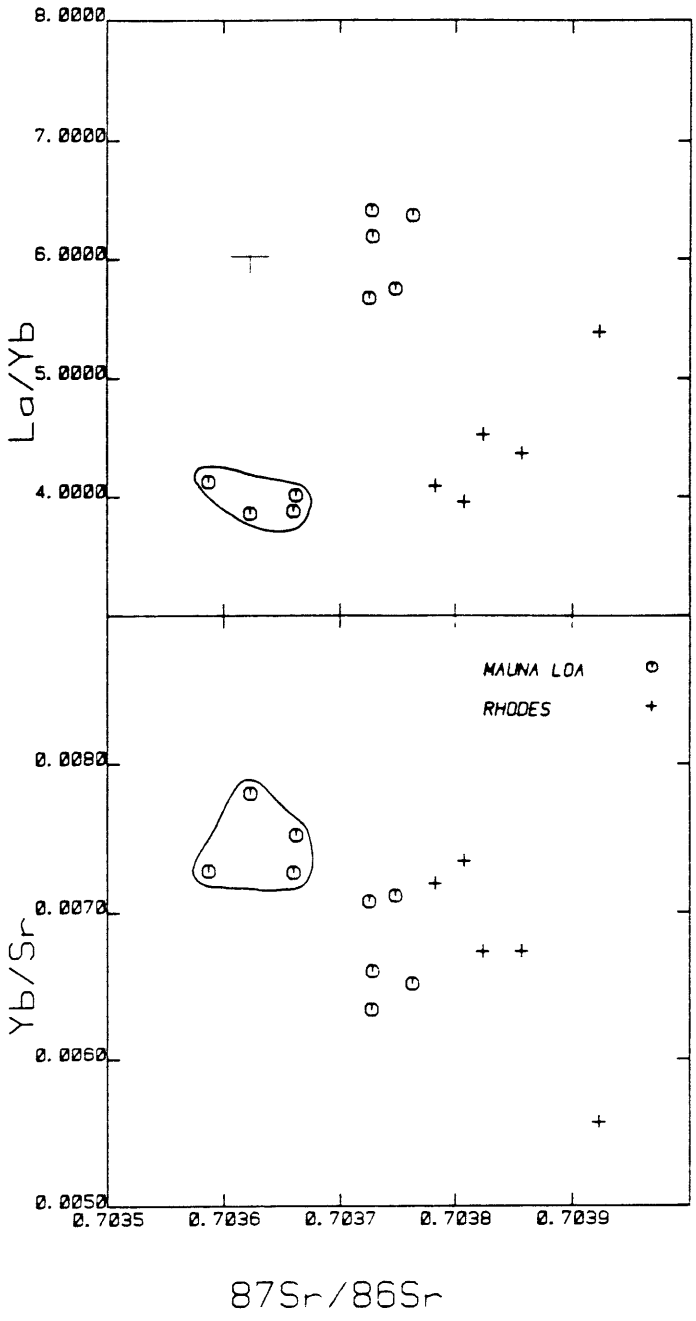

Figure 4.43. Same as 4.41 for La/Yb ratio versus $^{87}Sr/^{86}Sr$

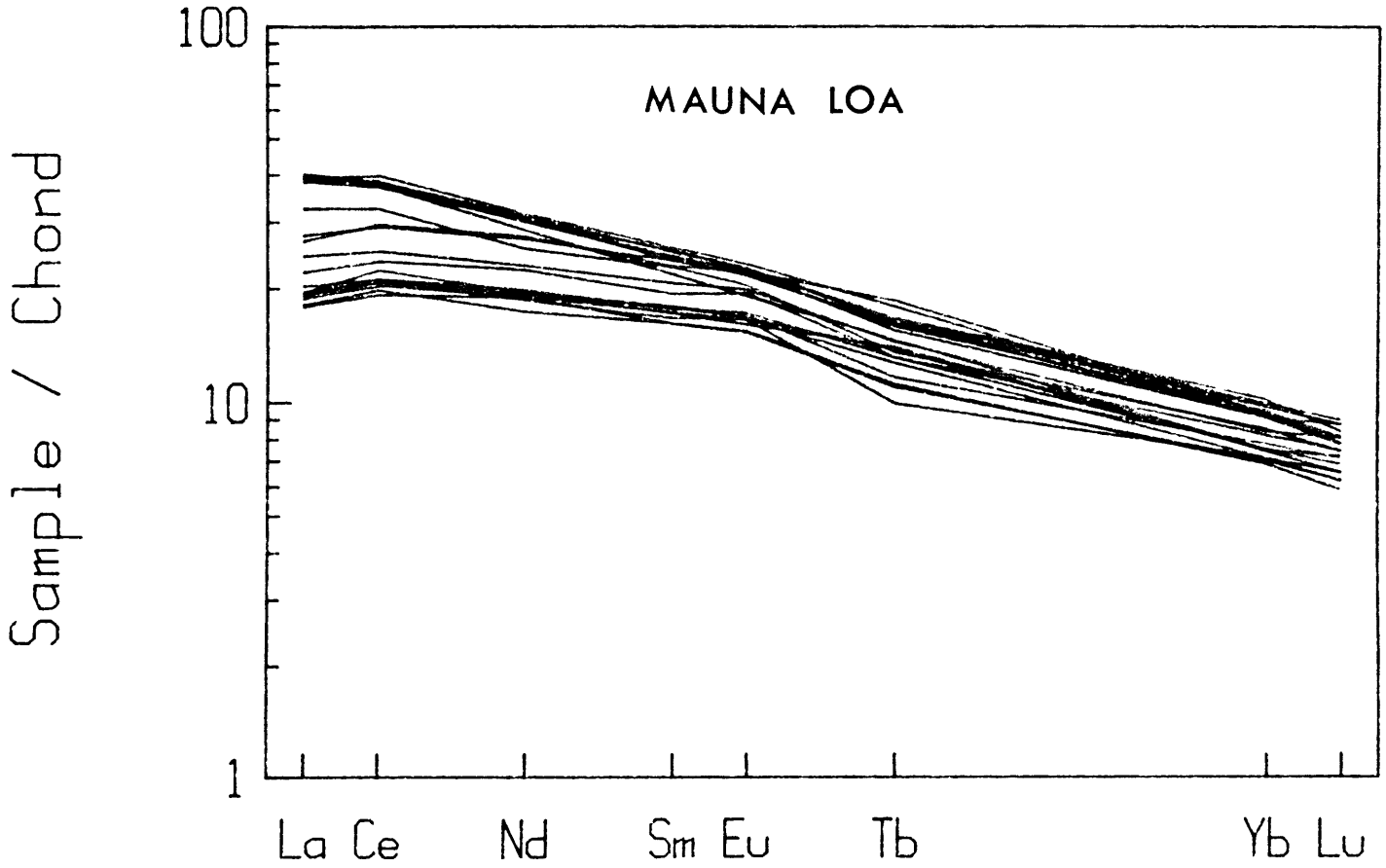

Figure 4.44–4.49. Chondrite normalized plots of REE data for individual volcanoes. The chondriric abundances used are from the "recommended chondrite" proposed by Boynton, 1984.

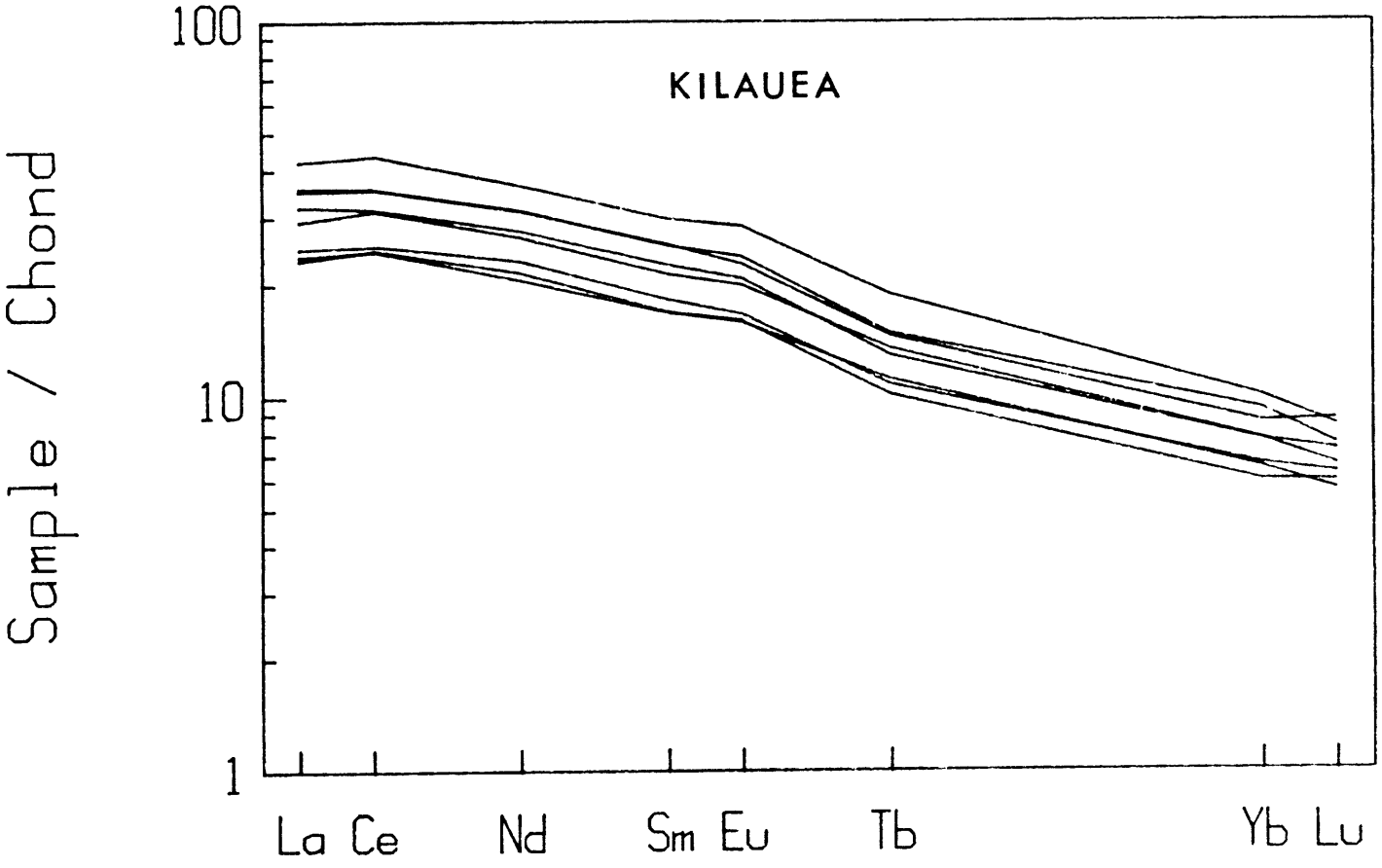

Figure 4.45. Same as 4.44

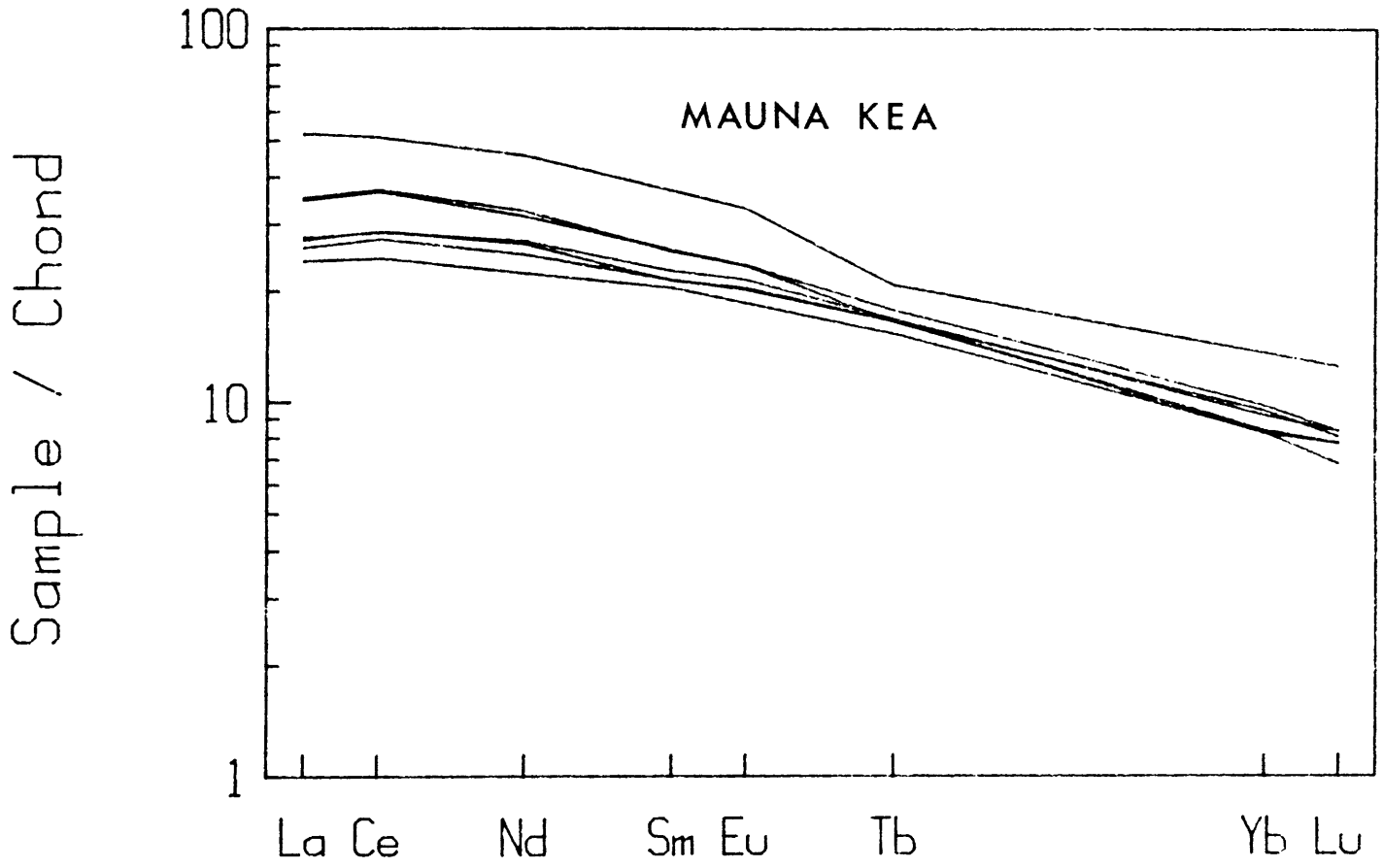

Figure 4.46. Same as 4.44

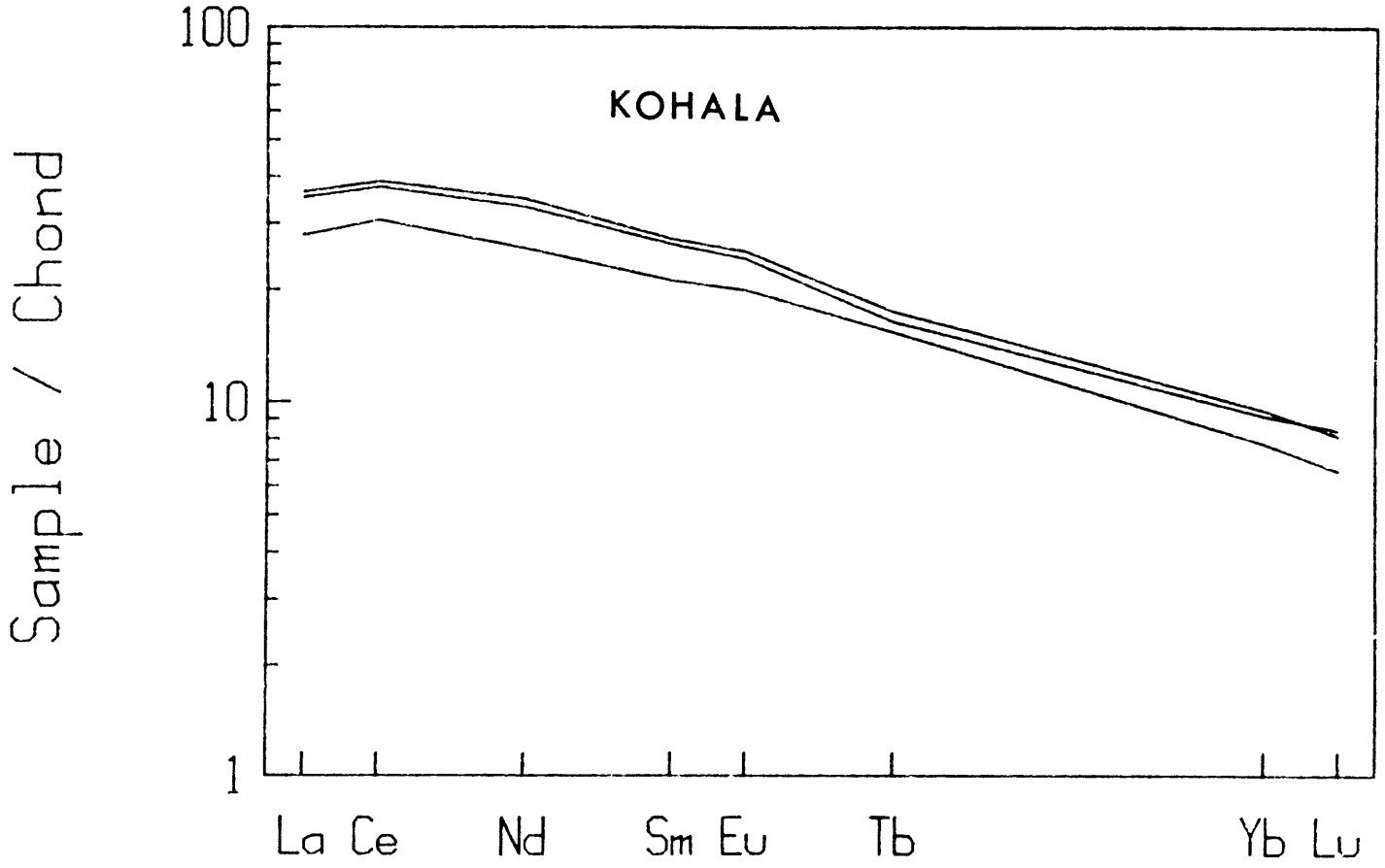

Figure 4.47. Same as 4.44

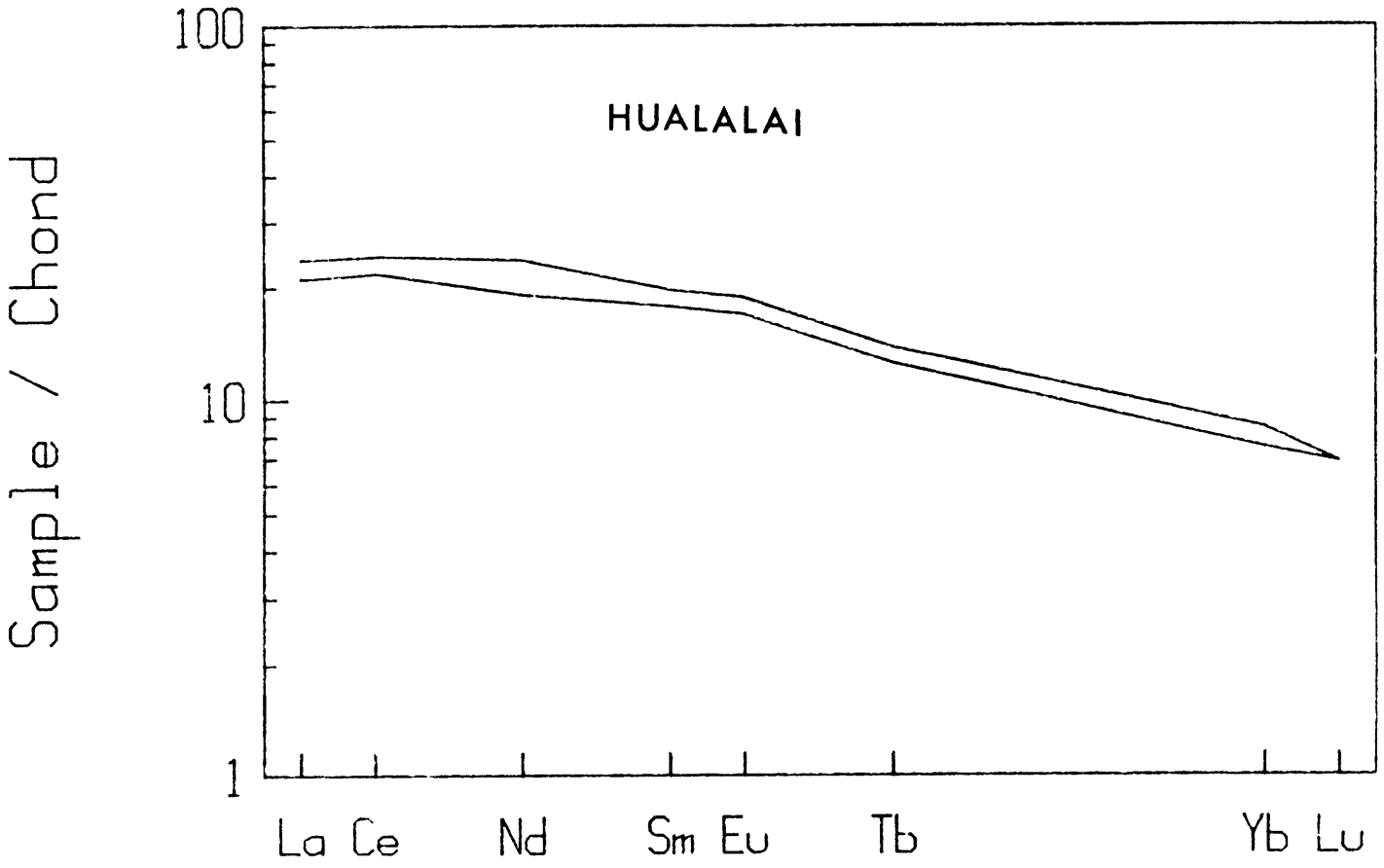

Figure 4.48. Same as 4.44

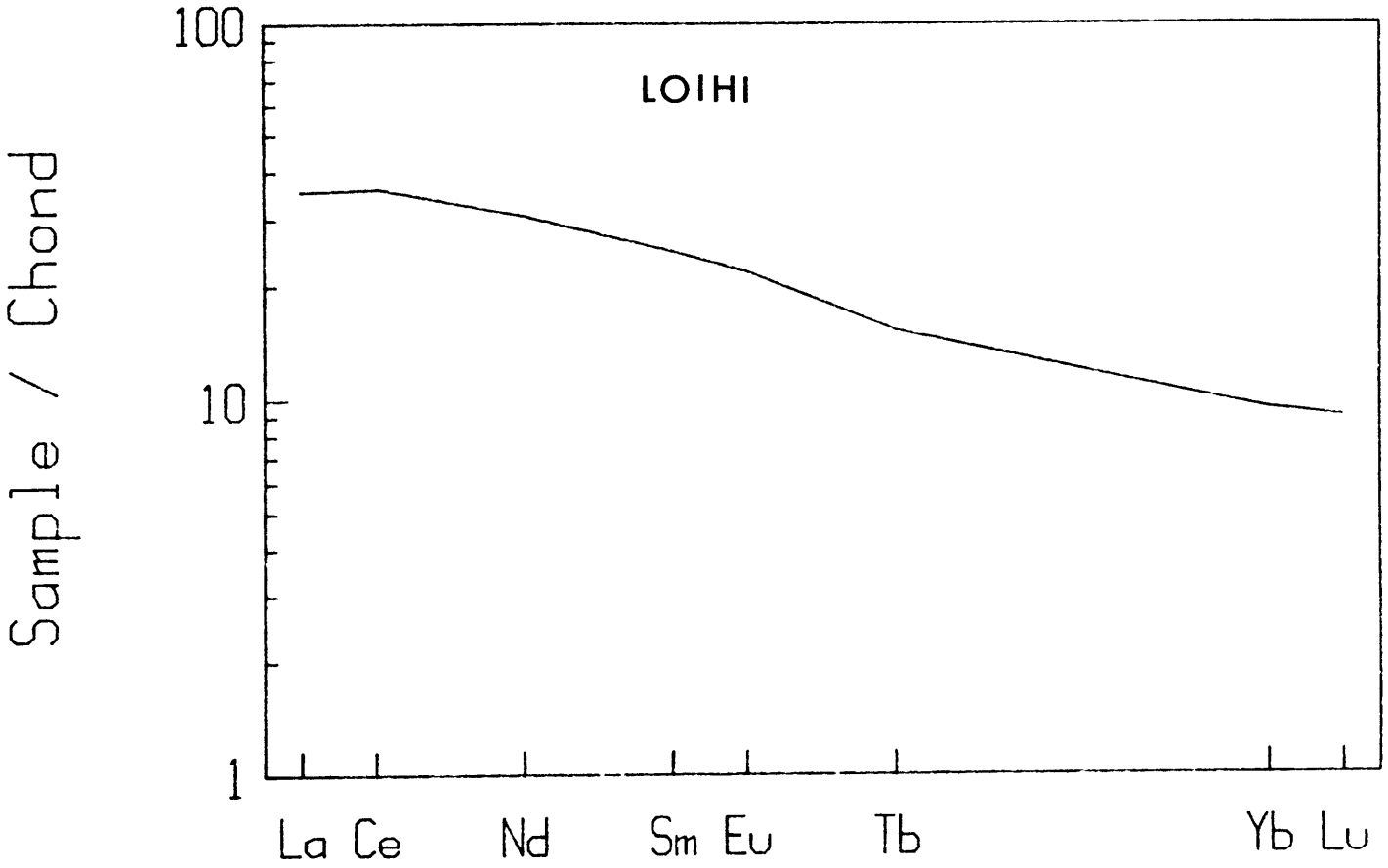

Figure 4.49. Same as 4.44

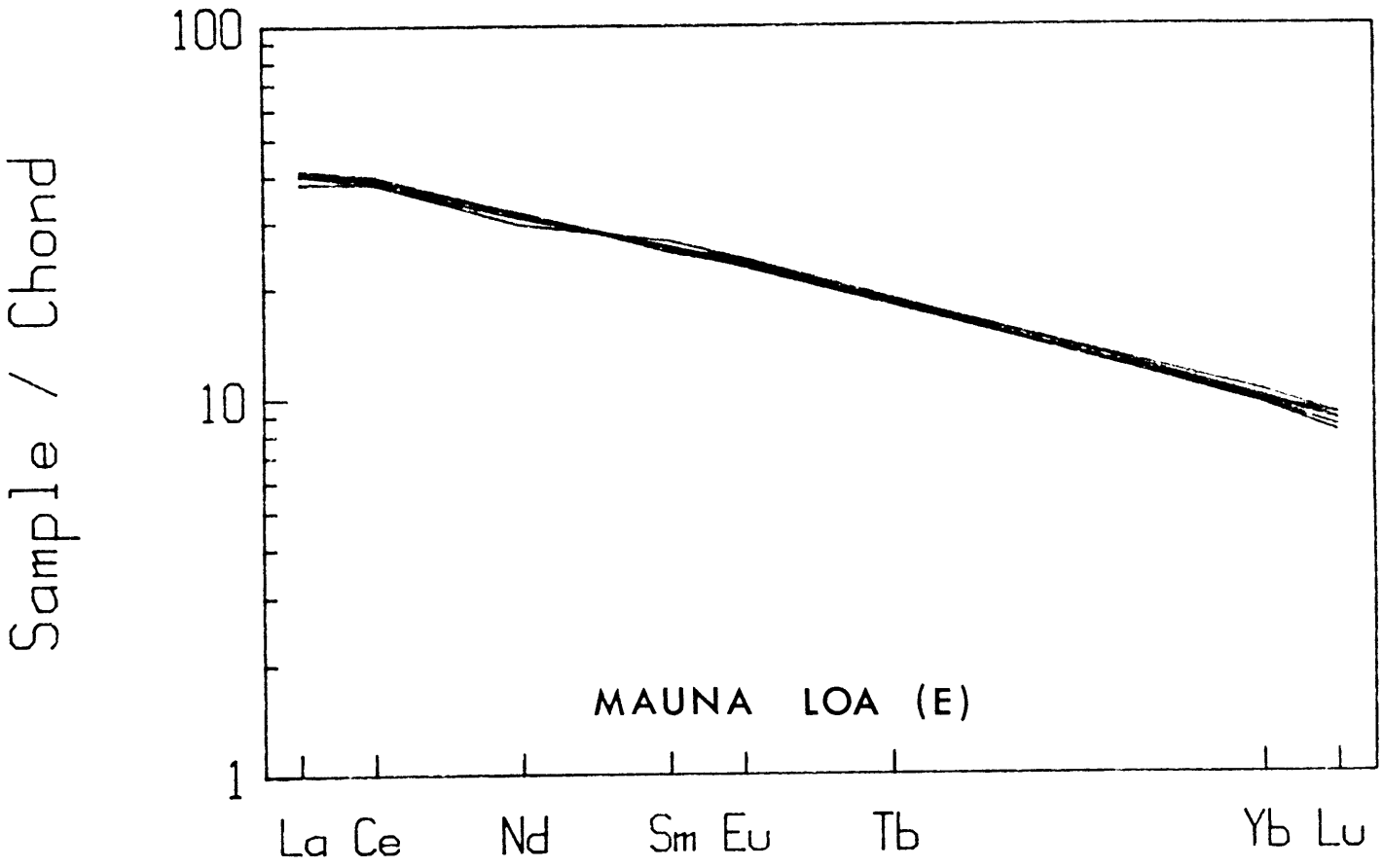

Figure 4.50–4.52. Chondrite normalizd plots of normalized (to 10 wt% MgO by olivine correction only) REE data for Mauna Loa enriched group.

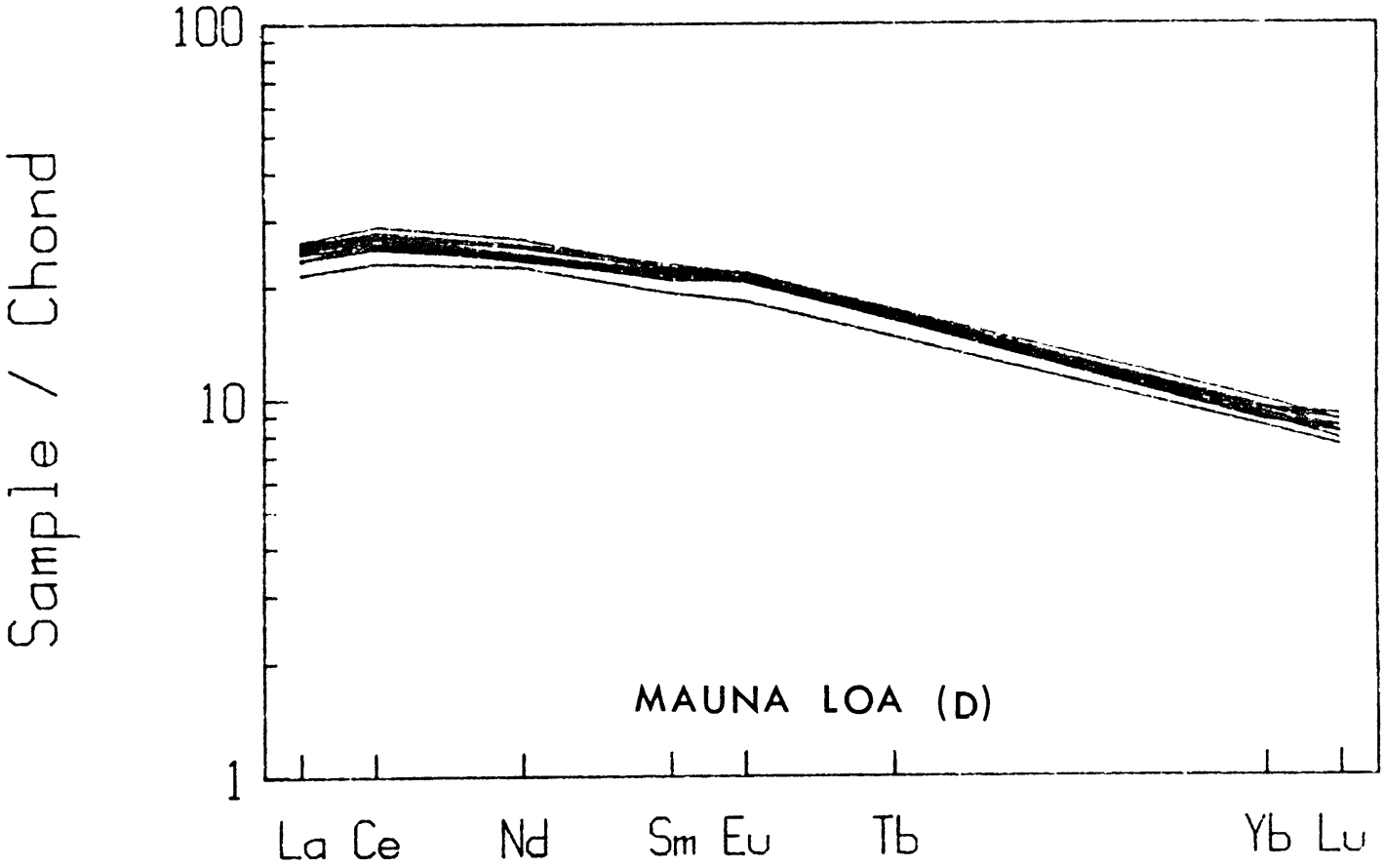

Figure 4.51. Same as 4.50 for Mauna Loa depleted group.

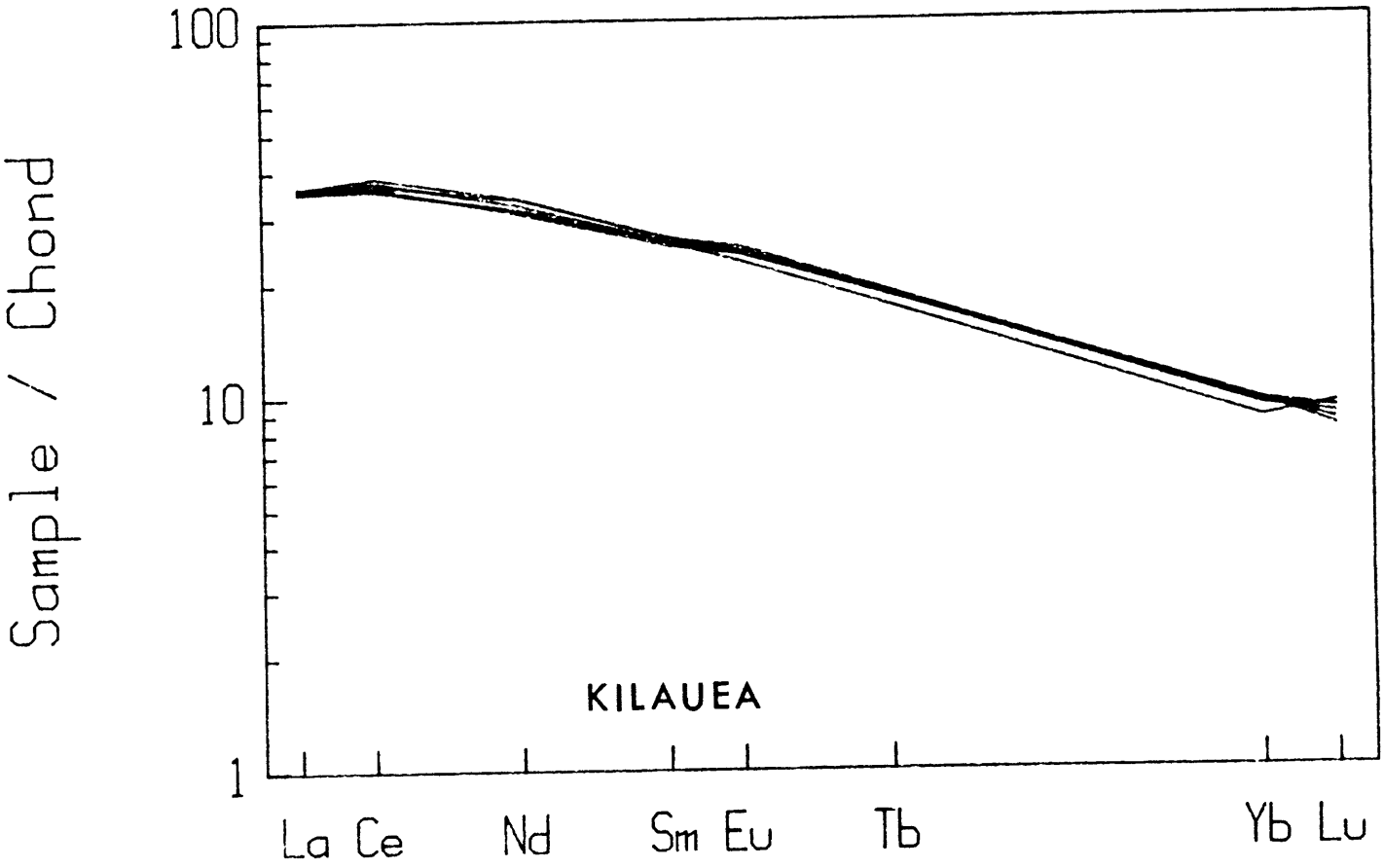

Figure 4.52. Same as 4.50 for Kilauea samples. Samples KIL1–5 and KIL3–8 may have experienced some amount of clinopyroxene fractionation and are not included.

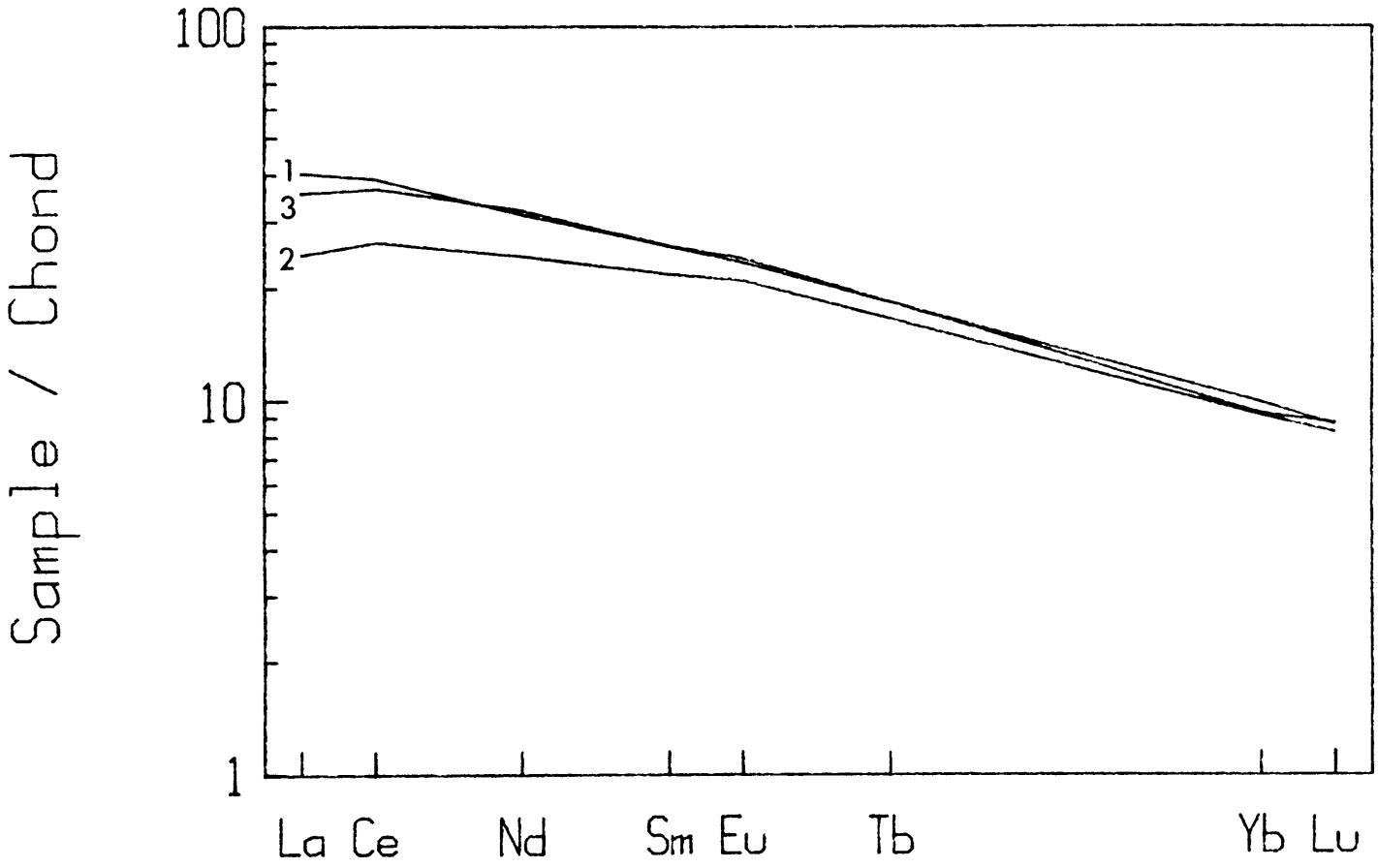

Figure 4.53. Chondrite normalized plot of REE abundances in the average of normalized (to 10 wt% MgO) lavas from the enriched (1) and depleted (2) Mauna Loa group, and Kilauea (3).

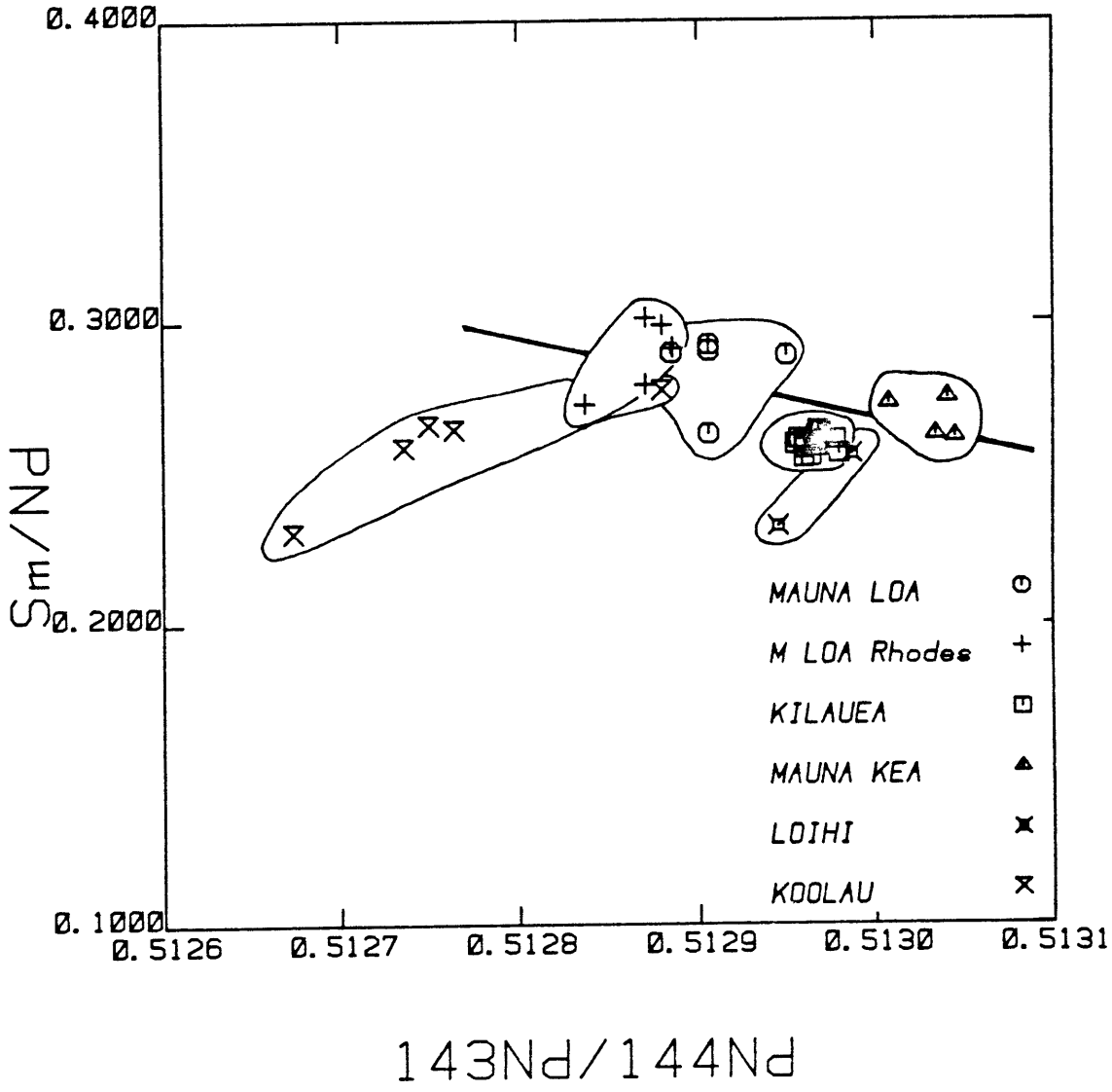

Figure 4.54. Neodymium isochron plot of Hawaiian tholeiites. The data lableled "M LOA Rhodes" are from Rhodes and Hart. Kilauea, Koolau and Loihi data are from Hofmann *et al.*, 1984, Roden *et al.*, 1984 and Staudigel et al., 1984, respectively. Mauna Kea data are from Frey and Kennedy, unpublished.

5. CONCLUSIONS

This work aims at presenting a comprehensive study on a wide selection of Hawaiian submarine tholeiites. Based on the major element compositions of associated glasses, we are able to infer that these lavas have undergone low pressure fractionation of plagioclase and, to a lesser extent, clinopyroxene. Yet, the whole rock data shows that they have preserved their equilibrium phase proportions in most cases with the exception of some Mauna Kea and Kilauea samples. Also, these lavas have experienced extensive non-equilibrium olivine accumulation that is expressed in the form of olivine control lines in major element concentrations and confirmed by the study of first series transition elements. Comparison of glass and whole rock compositions provides clues on the temporal relationships between these low pressure processes. However, the glass data exhibits intervolcano differences that can not be explained by simple petrological processes. For example, Kilauea is higher than other volcanoes in K_2O and TiO_2, at the same MgO%.

On the basis of trace elements, our most significant result is that unlike lavas from other volcanoes in this study, Mauna Loa samples differ markedly from subaerial tholeiites in trace element ratios and radiogenic isotope ratios. Moreover, they define two seperate groups that can not be explained by mixture with Kilauea volcano or simple petrogenetic processes in a homogeneous source. Also, we ob-

serve intervolcano differences that are consistent with the major elements: Kilauea is the highest in highly incompatible elements (Rb, Ba, Nb) and in ratios of highly incompatible elements over less incompatible ones (*e.g.* Rb/Sr). The fact that this characteristic is associated with low $^{87}Sr/^{86}Sr$ and high $^{143}Nd/^{144}Nd$ is a problem that is also present when tholeiites and alkali basalts from a particular volcano are compared, and that no current model completely explains yet.

APPENDIX 1

The fundamental relationship describing surface equilibrium states:

$$dX_s + dX_l = 0 \tag{A1}$$

where X_s and X_l stand for the absolute abundances of an element in the fractionating phase and the liquid. Setting M_s and M_l as the respective masses of solid and liquid ($dM_s = -dM_l$), and C_s and C_l the respective concentrations of the element in the solid and the liquid, Equation (A1) can be written

$$\frac{dX_s}{M_l C_l} + \frac{dF}{F} + \frac{dC_l}{C_l} = 0 \tag{A2}$$

where F stands for the total melt fraction.

In the case of a trace element following Henri's Law, we have

$$\begin{aligned} \frac{dX_s}{dM_s} &= C_s \\ &= D\, C_l \end{aligned} \tag{A3}$$

where D is the solid/liquid partition coefficient for the element in the particular phase involved. Substituting into Equation (A2) one gets the familiar equation of a Rayleigh distillation:

$$\frac{dC_l}{C_l} = (D-1)\frac{dF}{F} \tag{A4}$$

A few problems arise from this simple formalism. First, geochemists usually monitor the advancement of fractionation by the abundance of a particular element (MgO in the case of olivine) and not the degree of melting which is extremely difficult to assess directly. Moreover, in the case of a variable partition coefficient, the variations are usually given as a function of MgO too (*e.g.* Ni in olivine, Hart and Davis, 1978). Therefore, it is useful to obtain a differential equation relating MgO to the melt fraction in order to restrict the variables in Equation (A3) to the element considered and MgO only. Such an expression is available in the case of olivine fractionation for the unique reason that the olivine composition can be completely determined by the liquid FeO and MgO content. Similarly, an analytical relation between the melt fraction and CaO or Na_2O in the case of plagioclase fractionation could also be derived.

It is shown above [eq. (4)] that the MgO content of an olivine in equilibrium with a melt of known composition could be written in the form

$$\mathrm{MgO}_s = \frac{A}{B + C/\mathrm{MgO}_l} \tag{A5}$$

Therefore, in the case of olivine fractionation, we get

$$dX_s = -dM_l \left(\frac{A}{B + C/\mathrm{MgO}_l} \right) \tag{A6}$$

Substitution into Equation (A2) yields

$$\frac{d(\mathrm{MgO}_l)}{\mathrm{MgO}_l} = \frac{dF}{F} \left[\frac{A}{B\,\mathrm{MgO}_l + C} - 1 \right] \tag{A7}$$

Substituting dF/F from Equation (A7) into Equation (A4) yields a differential

equation where MgO_l and C_l are the only variables and which, after some staightforward algebra, can be written in the form

$$\frac{dC_l}{C_l} = (D-1)\left[\frac{\lambda}{MgO_l} + \frac{\mu}{(A-C) - B\ MgO_l}\right] d(MgO_l) \tag{A8}$$

where

$$\lambda = \frac{C}{(A-C)}, \tag{A9a}$$

$$\mu = \frac{A\ B}{(A-C)}. \tag{A9b}$$

In the simplest case where D is constant (*e.g.* Sc and V in olivine), the integration of Equation (A8) yields

$$\frac{C_l}{C_l^0} = \left[\frac{MgO_l}{MgO_l^0}\right]^{A_1} \left[\frac{(A-C) - B\ MgO_l}{(A-C) - B\ MgO_l^0}\right]^{A_2} \tag{A10}$$

where

$$A_1 = \frac{C(D-1)}{(A-C)}, \tag{A11a}$$

$$A_2 = \frac{A(1-D)}{(A-C)}. \tag{A11b}$$

In the particular case of Ni partitioning in olivine however, the partition coefficient dependence on MgO_l is of the form

$$D - 1 = \frac{\gamma}{MgO_l} + \delta, \tag{A12}$$

where γ and δ are constants. Integration of Equation (A8) is slighly more tedious and yields

$$\ln\left[\frac{C_l}{C_l^0}\right] = A_3\ \ln\left[\frac{MgO_l}{MgO_l^0}\right] + A_4\ \ln\left[\frac{(A-C) - B\ MgO_l}{(A-C) - B\ MgO_l^0}\right] + A_5\left[\frac{1}{MgO_l^0} - \frac{1}{MgO_l}\right] \tag{A13}$$

where

$$A_3 = \frac{\gamma A B}{(A-C)^2} + \frac{\delta C}{(A-C)}, \tag{A14a}$$

$$A_4 = \frac{\gamma A B^2}{(A-C)^2} + \frac{\delta A B}{(A-C)}, \tag{A14b}$$

$$A_5 = \frac{\gamma C}{(A-C)}. \tag{A14c}$$

APPENDIX 2

The following paper presents a physical model for the transition from tholeiitic to alkalic volcanism in Hawaii. Conductive heat transfer from the hot uprising plume, to the lower lithosphere, is reponsible for the greater involvement of a depleted component in the waning stages of Hawaiian volcanism. This paper resembles the geochemical approach of Chen and Frey, 1985 in its fundamentals. However, the degrees of melting generated within the lithosphere are far greater (a few percent) than what is needed by the simple two-component mixing model in order to reproduce the trace elements enrichment observed in the lavas.

Earth and Planetary Science Letters, 82 (1987) 153–158
Elsevier Science Publishers B.V., Amsterdam – Printed in The Netherlands

[5]

A thermal model for the origin of post-erosional alkalic lava, Hawaii

Philippe Gurriet

Department of Earth, Atmospheric and Planetary Sciences, Massachusetts Institute of Technology, Cambridge, MA 02139 (U.S.A.)

Received June 26, 1986, revised version received December 9, 1986

The model of lithospheric thinning and reheating for the origin of the Hawaiian swell assumes that the lower lithosphere (> 60 km) is rapidly reset to an asthenospheric temperature as it passes over the hot spot. It is shown that this heat input induces melting in a few kilometer thick layer of lithosphere just above the thermal anomaly. By solving the appropriate energy equation, the mean degree of melting in the molten layer was estimated to be 1–5% with a total melt thickness of 25–150 m. The minimum width of the thermal anomaly required to account for the observed rate of post-erosional eruptions is of the order of 10–40 km which is probably satisfied. The melt generated by this process matches the petrological and geochemical characteristics of Hawaiian post-erosional lava and their typical MORB-related isotopic signature. Because small degrees of melting are involved, the extraction time scale is long (a few million years) and is consistent with the time span of post-erosional eruptions. Also, the characteristic sequence of Hawaiian volcanism can be explained if the source for Hawaiian lava is considered as a molten layer with melt fraction decreasing upward.

1. Introduction

Hawaiian volcanism is characterized by a multi-stage eruption sequence [1,2]. A tholeiitic shield stage makes up > 98% of the total volume in less than 1 million years. It is followed by a post-shield alkalic stage, and after a period of volcanic quiescence of up to 2.5 m.y., by a post-erosional alkalic stage (Fig. 1). Also, an early shield alkalic stage has been identified recently at Loihi seamount [3]. It is now well established that the tholeiitic phase is the surface expression of upwelling currents within the upper mantle. However, the geological setting, geochemical characteristics and timing of post-erosional eruptions preclude simple genetic relationships with the main eruption stages. Post-erosional lava erupts in very small volumes, generally from satellite vents unrelated to the pre-existing shield. Their isotopic signature is systematically closer to MORB than lavas from other volcanic stages and sometimes overlaps with the MORB field, e.g., at Haleakala [4]. This characteristic suggests that the lithosphere plays an important role in the generation of post-erosional lava in Hawaii. In this paper, I propose that melt generated within the lithosphere by conductive heat transfer as a response to the perturbed thermal structure acquired over the hot spot is responsible for the delayed post-erosional volcanic stage at Hawaiian volcanoes.

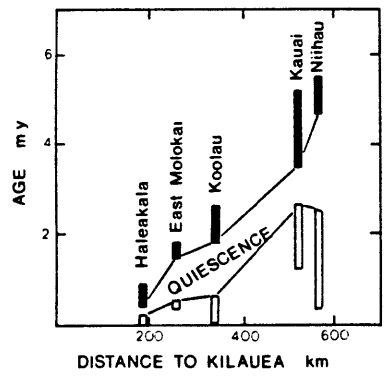

Fig. 1. Distribution of the different erupting stages along the Hawaiian Chain. A period of quiescence separates tholeiitic phase and post-shield alkalic phase (filled boxes) from post-erosional stage (empty boxes) (adapted from Clague et al. [2] and Garcia et al. [24]).

2. Governing equations

2.1. Thermal structure of the plate

Various models exist to explain the features related to mid-plate swells. Thermal models based on purely conductive mechanisms have been extensively developed in the literature [5,6] and pro-

0012-821X/87/$03.50

vide an acceptable explanation of the depth-age relation for swells. They are supported by Pratt-type compensation analysis of geoid-depth curves of which an apparent depth of compensation of 60–90 km can be inferred for the Hawaiian swell [7]. However, it has been shown that the observed heat flow, topography and geoid anomalies could result from the temperature structure of convection underneath the swell [8].

The approach developed in this paper is based on the lithospheric thinning and reheating model proposed by Crough [5]. Before passing over a hot spot, the lithosphere geotherm is assumed to be an error function:

$$T(z) = T_m \operatorname{erf}\left\{ z/2(Kt)^{1/2} \right\} \quad (1)$$

where T_m is the ambient asthenospheric temperature, K is the thermal diffusivity, z is the depth and t the age of the lithosphere. A reheating event is assumed to bring the lower lithosphere to a higher temperature T_a. The initial temperature profile immediately after reheating is thus given by:

$$T(z) = T_m \operatorname{erf}\left\{ z/2(Kt_0)^{1/2} \right\} \quad z < L \quad (2a)$$

$$T(z) = T_a \quad z > L \quad (2b)$$

where L is the lithospheric thickness after reheating and t_0 the age of the lithosphere at the time of reheating.

As this initial temperature profile evolves with time, it may cross the lithosphere solidus at some depth. This possibility must be taken into account by setting the appropriate energy equation.

2.2. Energy equation

The dynamics of magma generation and segregation have been intensively developed over the last few years [9–11]. The problem can be simplified by decoupling the generation of melt from the extraction process. The energy equation is thus solved assuming that the melt is stationary with respect to its source rock. In the reference frame of the moving plate, the system is at rest and the one-dimensional energy equation reduces to:

$$\frac{\partial T}{\partial t} = K\frac{\partial^2 T}{\partial z^2} \quad T < T_s(z) \quad (3a)$$

$$\frac{\partial T}{\partial t} + \frac{H}{C_p}\frac{df}{dt} = K\frac{\partial^2 T}{\partial z^2} \quad T > T_s(z) \quad (3b)$$

The temperature $T_s(z)$ is an expression for the lithosphere solidus, H is the heat of fusion, C_p is the heat capacity of the material and f the degree of melting whose variations with depth and temperature are discussed in the next section. Setting $f = f(T, z)$, we get:

$$\frac{df}{dt} = \frac{\partial f}{\partial T}\frac{dT}{dt} + \frac{\partial f}{\partial z}\frac{dz}{dt} \quad (4)$$

which further simplifies to:

$$\frac{df}{dt} = \frac{\partial f}{\partial T}\frac{\partial T}{\partial t} \quad (5)$$

Hence the final form of the energy equation:

$$\frac{\partial T}{\partial t}\left[1 + \frac{H}{C_p}\frac{\partial f}{\partial T}\right] = K\frac{\partial^2 T}{\partial z^2} \quad (6)$$

This formulation provides an intuitive explanation of the behaviour of the geotherm when melting is taking place. The temperature structure is governed by an apparent thermal diffusivity:

$$K' = K/\left[1 + \frac{H}{C_p}\frac{\partial f}{\partial T}\right] \quad (7)$$

which is always smaller than the effective one. The temperature increases and decreases slower in a molten material because of the latent heat absorption due to melting and the latent heat release due to crystallisation, respectively.

Equation (6) was solved by finite-differences with the perturbed geotherm as initial condition. All the physical parameters of the model are displayed in Table 1. A depth of the thermal anomaly

TABLE 1

Physical parameters

Variable	Description	Value
T_m	ambient asthenospheric temperature	1350°C
T_a	temperature of uprising materials	1550°C
K	thermal diffusivity	10^{-2} cm^2/s
L	thickness of lithosphere after reheating	60 km
C_p	heat capacity	900 J/kg K
H	latent heat of fusion	4×10^5 J/kg
a	mean grain radius	0.1 mm
$(\xi + \frac{4}{3}\eta)$	effective viscosity of the matrix	10^{18} Pa s
μ	viscosity of the melt	1 Pa s
$\Delta\rho$	density contrast between matrix and melt	0.5×10^3 kg/m^3

(L) of 60 km is adopted following McNutt and Shure [7]. The values of T_m and T_a were derived by McKenzie [9] to match the observed melt thicknesses at ridges and swells. The existence of molten material at anomalously shallow depths within the lithosphere tends to buffer heat propagation toward the surface. The magnitude of this effect however is small and can be assessed by estimating the ratio K'/K. Using the parameters of Table 1, equation (7) yields $K'/K = 0.8$ which is close to unity. The shape of the geotherm 2 m.y. after reheating is given in Fig. 2. While the source of tholeiites (below 60 km) remains at high temperature and high melt fraction, a thin molten layer with small degree of melting starts to develop within the lithosphere. I propose that the thin molten layer is responsible for late stage, post-erosional eruptions in Hawaii.

3. Magma generation and extraction

3.1. Choice of a solidus

As suggested by Fig. 2, both the thickness of the molten layer and the extent of melting are critically dependent on the solidus curve chosen. Hence, we need to estimate the water content of this possible source for post-erosional lava. The post-erosional suite studied in most detail is the Honolulu Volcanics at Oahu. Based on the petrology and geochemistry of the Honolulu Volcanics, Clague and Frey [12] concluded that the lavas were derived by varying degrees of melting of an enriched source. Moreover, this enrichment may have resulted from the interaction of an H_2O-CO_2-rich phase with a garnet peridotite. Because the enrichment occurred recently, it is not recorded in the isotopic signature of the Honolulu Volcanics [13]. This model is consistent with the idea expressed by McKenzie [10] that an H_2O-CO_2-rich phase could segregate from ascending materials at the onset of partial melting. In the present case, the volatile-rich phase may have been extracted from the upwelling source of tholeiitic lava whose pre-eruption water content was estimated as 0.5% by Byers et al. [14].

Two different "wet" solidi are presented in Fig. 3 for similar water content (0.2 H_2O%). The differences in shape illustrate the experimental variability associated with the determination of a melting curve. The calculations were run with each of the two solidi to account for these experimental uncertainties. Variations in the degree of melting with temperature were approximated to a linear relationship in the form:

$$f(z, T) = s[T - T_s(z)] \tag{8}$$

where the parameter s is chosen to fit the data of Ringwood [17] at depths of the order of 40–80 km and for degrees of melting in the range 0–20%. Fig. 4 provides a visual estimation of the goodness

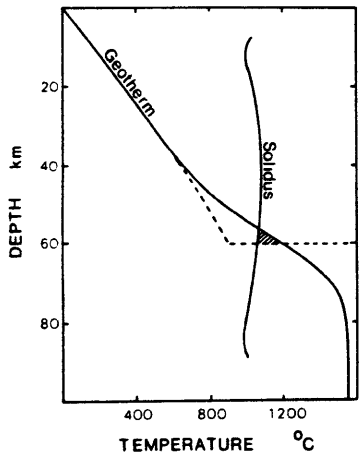

Fig. 2. Evolution of the lithosphere geotherm 2 m.y. after the reheating event. Melting takes place in the hatched zone above the thermal anomaly where temperature exceeds the peridotite solidus. The dashed curve indicates the initial conditions immediately after reheating. The solidus is from Millhollen et al. [16].

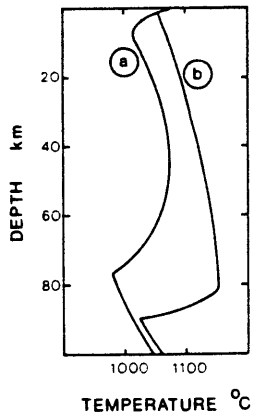

Fig. 3. Two different solidi used in the calculations: (*a*) Millhollen et al. [16] for 0.2% water and (*b*) Green [15] for 0.2% water.

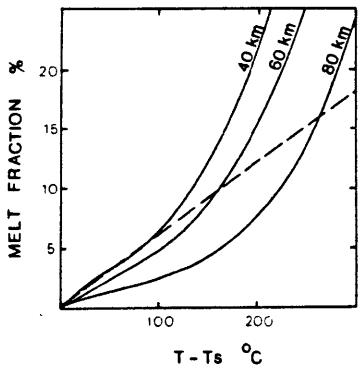

Fig. 4. The solid lines give the variations in degree of melting with temperature departure from the solidus at depths of 40, 60 and 80 km (adapted from Ringwood [17]). A linear relation (heavy dashed line) was used for the calculations.

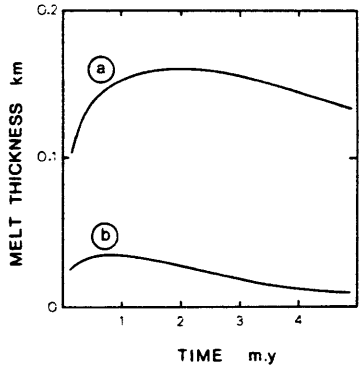

Fig. 6. Variations in the total melt thickness with time after reheating for two solidi: (*a*) Millhollen et al. [16] and (*b*) Green [15].

of the fit for the value of $s = 6.3 \times 10^{-4}$ °C^{-1} used in the calculations.

3.2. *Results*

The following results concern the behaviour of the molten layer in the lithosphere situated above the thermal anomaly. Fig. 5 gives the variations in the vertically averaged degree of melting across the layer with time after reheating. As expected from Fig. 2, the melt fraction is small (on the order of a few percent) and decreases systematically with time. The integration of the melt fraction over the layer thickness gives the total melt thickness whose variations with time since reheating are presented in Fig. 6. The melt thickness is brought almost instantaneously to a quasi-constant value which provides a stable melt supply for post-erosional lava over a few million year long period. The amount of melt, however, depends on the solidus chosen for the calculations and ranges from 0.02 to 0.12 km. A key question is whether this melt thickness is sufficient to account for the observed eruption rate of post-erosional lava. The latter has been estimated as less than 1% of the total volume of lava erupted at the hot spot and is probably of the order of 10^{-4} km^3/year (Clague, personal communication, 1986). If the extraction is complete, the melt thickness is related to the width of the thermal anomaly (w) by

$$wvm = M \tag{9}$$

where v is the plate velocity, m the melt thickness and M the flux of post-erosional eruptions. With a plate velocity of 100 mm/year, values of w inferred from (9) range from 10 to 40 km. These estimates are well within the hypothetical horizontal length scale of the Hawaiian "plume" [18] and suggest that only partial extraction occurs.

A typical degree of melting profile across the lithosphere is given in Fig. 7. The behaviour of this molten column with respect to compaction must lie between two end member models described in the literature. The first model considers the molten layer as a "chromatographic column" through which melt percolates as compaction proceeds [19,20]. In this case, erupted lava reflects reequilibration with the matrix at all depths in the column. On the contrary, the assumption can be made that melt is drained into an independent

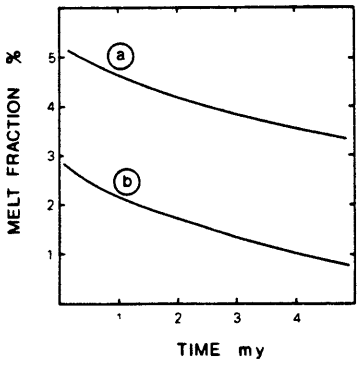

Fig. 5. Variations in the vertically averaged degree of melting across the molten layer of lithosphere with time after reheating for two different solidi: (*a*) Millhollen et al. [16] and (*b*) Green [15]

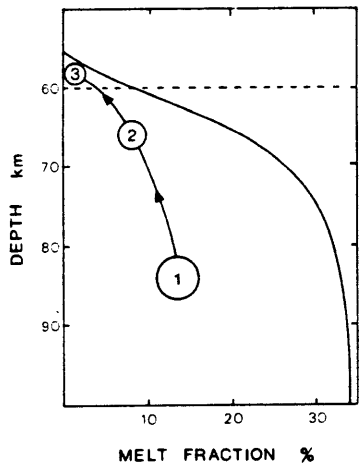

Fig. 7. Typical degree of melting profile (solid line) across the lower lithosphere 2 m.y. after reheating (the solidus is from Millhollen et al. [16]). The numbers *1*, *2* and *3* indicate a time sequence for the depths sampled by the compaction process (see text).

system of channels during compaction and that the erupted lava reflects its source rock composition. Such an approach is needed to account for U/Th disequilibrium beneath ridge axis, for instance [11]. In the present case where porosity decreases upward (Fig. 7), McKenzie [9] suggested that instabilities may develop in the molten layer. The existence of such instabilities makes intuitive sense when melts easily removed from high-porosity regions are forced upward into increasingly lower-porosity regions. It also favours the second model where chemical reequilibration through the molten column is limited. Hence, the progress of compaction can explain the succession of volcanic stages observed in Hawaii as follows:

(1) Rapid compaction of high-porosity regions (*1*, Fig. 7). Sudden eruption of tholeiitic lava with "plume-type" isotopic signature.

(2) As compaction reaches regions with lower melt fraction (*2*, Fig. 7), the surface eruption rate decreases. As a result, alkalic lava with isotopic signatures similar to the tholeiites are erupted in the waning stages of shield formation [21].

(3) Eventually, compaction reaches the molten layer in the lower lithosphere (*3*, Fig. 7). The lavas become highly SiO_2-unsaturated (alkalic) with typical MORB isotopic signature. The time span of eruptions is at its maximum because very small melt fractions are involved.

McKenzie [10] gave an empirical formulation for the characteristic time of extraction t_h taken to reduce the fluid content in a molten layer by a factor of e in the form:

$$t_h/\tau_0 = \delta_c/h + h/\delta_c \tag{10}$$

where h is the layer thickness, δ_c and τ_0 the compaction length and scaling factor for time respectively. Moreover we have:

$$\delta_c = \left[\frac{(\xi + 4\eta/3)k_\phi}{\mu}\right]^{1/2} \tag{11}$$

$$\tau_0 = \frac{\delta_c \mu \phi}{k_\phi (1-\phi)^2 \Delta\rho g} \tag{12}$$

where ξ and η are the effective bulk and shear viscosities of the matrix, μ the shear viscosity of the melt, ϕ the melt fraction and $\Delta\rho$ the density contrast between melt and matrix. The permeability k_ϕ is taken from Maaloe and Scheie [22] in the form:

$$k_\phi = a^2\phi^3/1000 \tag{13}$$

where a is the grain radius.

Equation (10) was applied to the postulated source of post-erosional lava for the period 0–5 m.y. after reheating (Fig. 8). The results should be considered as rough estimates of the extraction time scale, for equation (10) normally applies to a layer with uniform initial melt fraction. Nevertheless, the characteristic time of extraction appears to remain stable over a 5 m.y. long period in the range 2–10 m.y., which is compatible with the time span of post-erosional eruptions.

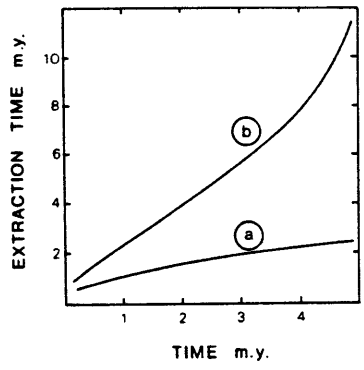

Fig. 8. Variations in the characteristic time of extraction of the molten layer of lithosphere with time since reheating, for two solidi: (*a*) Millhollen et al. [16] and (*b*) Green [15].

4. Concluding remarks

The above model provides a self-consistent picture of several aspects of Hawaiian volcanism. It is also in agreement with studies on He isotopes in Hawaiian lava [23] showing a decrease in $^3He/^4He$ with time at individual volcanoes. This variation in $^3He/^4He$ was interpreted as a decreasing participation of the most primitive component ("plume") in the late stages of Hawaiian volcanism.

Clague and Frey [12] expressed the need for garnet in the source of the Honolulu Volcanics to explain the heavy rare earth element patterns of erupted lava. Hence the proposed depth of origin for post-erosional lava (55–60 km) may be too shallow. However, it must be stressed that the depth of the thermal anomaly (L) is a poorly constrained variable in the range 60–90 km [7]. Moreover, because the differences between the two solidi increase with depth (Fig. 3), larger values of L would yield greater uncertainties on the extent of melting for a somewhat similar shape of the curves in Figs. 5, 6, 8.

Although the present model accounts for the time span of post-erosional eruptions, the existence of a quiescent period following the shield formation cannot be explained. It is plausible that because such small degrees of melting are involved, the melt remains trapped in the lower lithosphere until a triggering event allows eruption to the surface. Clague and Dalrymple [1] proposed that the overriding of the Hawaiian arch by the volcanic edifice would induce the generation of post-erosional lava. I suggest that melt already exists within the lithosphere at the time the overriding of the arch occurs and that the latter contributes only to its extraction.

Acknowledgement

This work was supported by NSF grant EAR-8419723 to Fred Frey.

References

1 D.A. Clague and G.B. Dalrymple, The geology of the Hawaiian-Emperor volcanic chain, U.S. Geol. Surv. Prof. Paper, in press, 1986.
2 D.A. Clague, C. Dao-Gong, R. Murnane, M.H. Beeson, M.A. Lanphere, G.B. Dalrymple, W. Friesen and R.T. Holcomb, Age and petrology of the Kalaupapa basalt, Molokai, Hawaii, Pac. Sci. 36, 411–420, 1982.
3 J.G. Moore, D.A. Clague and W.R. Normack, Diverse basalt types from Loihi Seamount, Hawaii, Geology 10, 88–92, 1982.
4 C.-Y. Chen and F.A. Frey, Trace element and isotopic geochemistry of lavas from Haleakala volcano, East Maui, Hawaii: implications for the origin of Hawaiian basalt, J. Geophys. Res. 90, 8743–8768, 1985.
5 S.T. Crough, Thermal origin of mid-plate hot spot swells, Geophys. J. R. Astron. Soc. 55, 451–469, 1978.
6 R.S. Detrick and S.T. Crough, Island subsidence, hot spots, and lithospheric thinning, J. Geophys. Res. 83, 1236–1244, 1978.
7 M. McNutt and L. Shure, Estimating the compensation depth of the Hawaiian swell with linear filters, J. Geophys. Res., in press, 1986.
8 B. Parsons and S. Daly, The relationship between surface topography, gravity anomalies, and temperature structure of convection, J. Geophys. Res. 88, 1129–1144, 1983.
9 D. McKenzie, The generation and compaction of partially molten rocks, J. Petrol. 25, 713–765, 1984.
10 D. McKenzie, The extraction of magma from the crust and mantle, Earth Planet Sci. Lett. 74, 81–91, 1985.
11 D. McKenzie, ^{230}Th-^{238}U disequilibrium and the melting process beneath ridge axes, Earth Planet. Sci. Lett 72, 149–157, 1985.
12 D.A. Clague and F.A. Frey, Petrology and trace element geochemistry of the Honolulu Volcanics, Oahu: implications for the oceanic mantle below Hawaii, J. Petrol. 23, 447–504, 1982.
13 M.F. Roden, F.A. Frey and D.A. Clague, Geochemistry of tholeiitic and alkalic lavas from the Koolau range, Oahu, Hawaii: implications for Hawaiian volcanism, Earth Planet. Sci. Lett. 69, 141–158, 1984.
14 C.D. Byers, M.O. Garcia and D.W. Muenow, Volatiles in pillow rim glasses from Loihi and Kilauea volcanoes, Hawaii, Geochim. Cosmochim. Acta 49, 1887–1896, 1985.
15 D.H Green, Experimental melting studies on a model upper mantle composition at high pressure under water-saturated and water-unsaturated conditions, Earth Planet. Sci. Lett. 19, 37–53, 1973.
16 G.L. Millhollen, A.J. Irving and P.J. Wyllie, Melting interval of peridotite with 5.7 percent water to 30 kilobars, J. Geol. 82, 575–587, 1974.
17 A.E. Ringwood, Composition and Petrology of the Earth's Mantle, McGraw-Hill, New York, N.Y., 1975.
18 P. Olson and I.S Nam, Formation of seafloor swells by mantle plumes, J. Geophys. Res. 91, 7181–7191, 1986.
19 F.M. Richter, Simple models for trace element fractionation during melt segregation, Earth Planet. Sci. Lett. 77, 333–344, 1986.
20 O. Navon and E. Stolper, Geochemical consequences of melt percolation: the upper mantle as a chromatographic column, J. Geol., submitted, 1986.
21 M.A. Lanphere and F.A. Frey, Geochemical evolution of Kohala volcano, Hawaii, Contrib. Mineral. Petrol., in press, 1986.
22 S. Maaloe and A. Scheie, The permeability controlled accumulation of primary magma, Contrib. Mineral. Petrol. 81, 350–357, 1982.
23 M.D. Kurz, M.O. Garcia, F.A. Frey and P.A. O'Brien, Temporal helium isotopic variations in Hawaiian volcanoes, preprint, 1986.
24 M.O. Garcia, F.A. Frey and D.G. Grooms, Petrology of volcanic rocks from Kaula Island, Hawaii, Contrib. Mineral. Petrol., in press, 1986.

REFERENCES

ALBARÈDE, F. 1983. Inversion of batch melting equations and the trace element pattern of the mantle. *J. Geophys. Res.*, **88**, 10573–10583.

ALLÈGRE, C. J., TREUIL, M., MINSTER, J. F., MINSTER, B. AND ALBARÈDE, F. 1977. Systematic use of trace element in igneous process. I Fractional crystallization processes in volcanic suites. *Contrib. Mineral. Petrol.*, **60**, 57–75.

ALLÈGRE, C. J. AND MINSTER, J. F. 1978. Quantitative models of trace element behaviour in magmatic processes. *Earth Planet. Sci. Lett.*, **38**, 1–25.

BAKER M. 1988. PhD Thesis, Massachusetts Institute of Technology.

BOYNTON W. V. 1984. In Rare Earth Element Geochemistry, Elsevier.

BROOKS, C., HART, S. R., HOFMANN, A., AND JAMES, D. E. 1976. Rb–Sr mantle isochrons form oceanic regions. *Earth Planet. Sci. Lett.*, **32**, 51–61.

BRYAN, W. B. 1983. Systematics of modal phenocryst assemblages in submarine basalts: Petrologic Implications. *Contrib. Mineral. Petrol.*, **83**, 62–74.

BUDAHN, J. R. AND SCHMITT, R .A. 1985. Petrogenetic modeling of Hawaiian tholeiitic basalts. *Geochim. Cosmochim. Acta*, **49**, 67–87.

CHAYES, F. 1949. On ratio correlation in petrography. *J. Geol.*, **57**, 239–254.

CHEN, C. Y. AND FREY, F. A. 1983. Origin of Hawaiian tholeiite and alkalic basalt. *Nature*, **302**, 785–789.

CHEN, C. Y. AND FREY, F. A. 1985. Trace element and isotopic geochemistry

of lavas from Haleakala volcano, East Maui, Hawaii: implications for the origin of Hawaiian basalts. *J. Geophys. Res.*, **90**, 8743–8768.

DRAKE, M. J. AND WEILL, D. F. 1975. Partition of Sr, Ba, Ca, Y, Eu^{2+}, Eu^{3+}, and other REE between plagioclase feldspar and magmatic liquid: an experimental study. *Geochim. Cosmochim. Acta*, **39**, 689–712.

FEIGENSON, M. D., HOFMANN, A. W. AND SPERA, F. J. 1983. Case studies on the origin of basalt. II The transition from tholeiitic to alkalic volcanism on Kohala volcano, Hawaii. *Contrib. Mineral. Petrol.*, **84**, 390–405.

FODOR, R. V., KEIL K. AND BUNCH T. E. 1975. Contributions to the mineral chemistry of Hawaiian rocks. IV Pyroxenes in rocks from Haleakala and West Maui volcanoes. *Contrib. Mineral. Petrol.*, **50**, 173–195.

FREY, F. A., GREEN, D. H. AND ROY, S. D. 1977. Integrated models of basalt petrogenesis: a study of quartz tholeiites to olivine melilitites from south eastern Australia utilizing geochemical and experimental petrological data, *J. Petrol.*, **19**, 463–513.

FREY, F. A. AND CLAGUE, D. A. 1983. Geochemistry of diverse basalt types from Loihi seamount, Hawaii: petrogenetic implications. *Earth Planet. Sci. Lett.*, **66**, 337–355.

FREY, F. A. AND RODEN, M. F. 1985. The mantle source for the Hawaiian islands: constraints from the lavas and ultramafic inclusions. In *Mantle Metasomatism*, Academic Press.

FUJIMAKI, H., TATSUMOTO, M. AND AOKI, K. I. 1984. Partition coefficients of Hf, Zr, and REE between phenocrysts and groundmasses. *J. Geophys. Res.*, **89**, B662–B672.

GREENLAND, L. P. 1970. An equation for trace element distribution during magmatic crystallization. *Amer. Mineral.*, **55**, 455–465.

GROVE, T. L. AND BRYAN, W. B. 1983. Fractionation of pyroxene-phyric MORB at low pressure: an experimental study. *Contrib. Mineral. Petrol.*, **84**,

293–309.

GROVE, T. L. AND BAKER, M. B. 1984. Phase equilibrium controls on the tholeiitic versus calc-alkaline differentiation trends. *J. Geophys. Res.*, **89**, 3253–3274.

GURRIET, P. 1987. A thermal model for the origin of post-erosional alkalic lavas, Hawaii. *Earth Planet. Sci. Lett.*, **82**, 153–158.

HART, S. R. AND NALWALK, A. J. 1970. K, Rb, Cs and Sr relationships in submarine basalts from the Puerto Rico trench. *Geochim. Cosmochim. Acta*, **34**, 145–155.

HART, S. R. AND BROOKS, C. 1977. The geochemistry of early precambrian mantle. *Contrib. Mineral. Petrol.*, **61**, 109–128.

HART, S. R. AND DAVIS, K. E. 1978. Nickel partitioning between olivine and silicate melt. *Earth Planet. Sci. Lett.*, **40**, 203–219.

HOFMANN, A. W. AND WHITE, W. M. 1982. Mantle plumes from ancient oceanic crust. *Earth Planet. Sci. Lett.*, **57**, 421–436.

HOFMANN, A. W. AND FEIGENSON, M. D. 1983. Case studies on the origin of basalts. I Theory and reassessment of Grenada basalts. *Contrib. Mineral. Petrol.*, **84**, 382–389.

HOFMANN, A. W., FEIGENSON, M. D. AND RACZEK, I. 1984. Case studies on the origin of basalts. III Petrogenesis of the Mauna Ulu eruption, Kilauea, 1969–1971. *Contrib. Mineral. Petrol.*, **88**, 24–35.

HOFMANN, A. W. 1986. Nb in Hawaiian magmas: constraints on source composition and evolution. *Chem. Geol.*, **57**, 17–30.

HOFMANN, A. W., JOCHUM, K. P., SEUFERT, M. AND WHITE, W. M. 1986. Nb and Pb in oceanic basalts: new constraints on mantle evolution. *Earth Planet. Sci. Lett.*, **79**, 33–45.

KEIL, K., FODOR, R. V. AND BUNCH, T. E. 1972. Contributions to the min-

eral chemistry of Hawaiian rocks. II Feldspars and interstitial material in rocks from Haleakala and West Maui volcanoes, Maui, Hawaii. *Contrib. Mineral. Petrol.*, **37**, 253–276.

KLEIN, E. M. AND LANGMUIR, C. H. 1987. Global correlations of ocean ridge basalt chemistry with axial depth and crustal thickness. *J. Geophys. Res.*, **92**, 8089–8115.

KURZ, M. D., GARCIA, M. O., FREY, F. A. AND O'BRIEN, P.,A. 1987. Temporal helium isotopic variations within Hawaiian volcanoes: basalts from Mauna Loa and Haleakala. *Geochim. Cosmochim. Acta*, **51**, 2905–2914.

LANGMUIR, C. H., VOCKE, R. D., HANSON, G. N. AND HART, S. R. 1978. A general mixing equation with applications to Icelandic basalts. *Earth Planet. Sci. Lett.*, **37**, 380–392.

LANPHERE, M. 1983. $^{87}Sr/^{86}Sr$ ratios for basalt from Loihi seamount, Hawaii. *Earth Planet. Sci. Lett.*, **66**, 380–387.

LEEMAN, W. P., BUDAHN, J. R., GERLACH, D. C., SMITH, D. R. AND POWELL, B.N. 1980. Origin of Hawaiian tholeiites: trace element constraints. *Am. J. Sci.*, **280–A**, 794–819.

LI, S. AND HART, S. R. 1986. Sources and evolution of Hawaiian volcanism: isotopic constraints. *Earth Planet. Sci. Lett.*, submitted.

MACDONALD, G. A. AND KATSURA, T. 1964. Chemical composition of Hawaiian lavas. *J. Petrol.*, **5**, 82–133.

MINSTER, J. F., MINSTER, J. B., TREUIL, M. AND ALLÈGRE, C. J. 1977. Systematic use of trace elements in igneous processes. II Inverse problem of the fractional crystallization process in volcanic suites. *Contrib. Mineral. Petrol.*, **61**, 49–77.

MINSTER, J. F. AND ALLÈGRE, C. J. 1978. Systematic use of trace elements in igneous processes. III Inverse problem of batch partial melting in volcanic suites. *Contrib. Mineral. Petrol.*, **68**, 37–52.

O'NIONS, R. K., HAMILTON, P. J. AND EVENSEN, N. M. 1977. Variations in $^{143}Nd/^{144}Nd$ and $^{87}Sr/^{86}Sr$ ratios in oceanic basalts. *Earth Planet. Sci. Lett.*, **34**, 13–22.

ONUMA, N., HIGUCH, H., WAKITA, H. AND NAGASAWA, H. 1968. Trace element partition between two pyroxenes and the host lava. *Earth Planet. Sci. Lett.*, **5**, 47–51.

RODEN, M. F., FREY, F. A. AND CLAGUE, D. A. 1984. Geochemistry of tholeiitic and alkalic lavas from the Koolau range, Oahu, Hawaii: implications for Hawaiian volcanism. *Earth Planet. Sci. Lett.*, **69**, 141–158.

RHODES, J. M. 1983. Homogeneity of lava flows: chemical data for historical Mauna Loan eruptions. *J. Geophys. Res.*, **88**, A869–A879.

ROEDER, P. L. AND EMSLIE, R. F. 1970. Olivine-liquid equilibrium. *Contrib. Mineral. Petrol.*, **29**, 275–289.

SHIDO, F., MIYASHIRO, A. AND EWING, M. 1971. Compositional variation in pillow lavas from the mid-Atlantic ridge. *Marine Geol.*, **16**, 177–190.

STAUDIGEL, H. AND BRYAN, W. B. 1981. Contrasted glass-whole rock compositions and phenocryst re-distribution, IPOD sites 417 and 418. *Contrib. Mineral. Petrol.*, **78**, 255–262.

STAUDIGEL, H., ZINDLER, A., HART, S. R., LESLIE, T., CHEN, C. Y. AND CLAGUE, D. 1984. The isotope systematics of a juvenile intraplate volcano: Pb, Nd, and Sr isotope ratios of basalts from Loihi seamount, Hawaii. *Earth Planet. Sci. Lett.*, **69**, 13–29.

STILLE, P., UNRUH, D. M. AND TATSUMOTO, M. 1987. Pb, Sr, Nd, and Hf isotopic constraints on the origin of Hawaiian basalts and evidence for a unique mantle source. *Geochim. Cosmochim. Acta*, in press.

STOLPER, E. 1980. A phase diagram for mid-ocean ridge basalts: preliminary results and implications for petrogenesis. *Contrib. Mineral. Petrol.*, **74**, 13–27.

SUN, S. S., NESBITT, R. W. AND SHARASKIN, A. Y. 1979. Geochemical characteristic of mid-ocean ridge basalts. *Earth Planet. Sci. Lett.*, **44**, 119–138.

TATSUMOTO, M., HEGNER, E. AND UNRUH, M. 1985. Origin of the West Maui volcanics inferred from Pb, Sr, and Nd isotopes and a multi-component model for oceanic basalts. *USGS Prof. Paper*, submitted.

TILLING, R. I., WRIGHT, T. L. AND MILLARD, H. T. 1979. Trace element chemistry of Kilauea and Mauna Loa lava in space and time: a reconnaissance, *USGS Prof. Paper*, **1350**, 641–689.

TORMEY, D. R., GROVE, T. L. AND BRYAN, W. B. 1987. Experimental petrology of normal MORB near the Kane fracture zone: 22°–25°N, mid-Atlantic ridge. *Contrib. Mineral. Petrol.*, **96**, 121–139.

WEST, H. B., GERLACH, D. C., LEEMAN, W. P. AND GARCIA, M. O. 1987. Isotopic constraints on the origin of Hawaiian lavas from the Maui volcanic complex, Hawaii. *Nature*, **330**, 216–220.

WRIGHT, T. L. 1971. Chemistry of Kilauea and Mauna Loa lava in space and time. *USGS Prof. Paper*, **735**, 1–40.

WRIGHT, T. L., SWANSON, D. A. AND DUFFIELD, W. A. 1975. Chemical compositions of Kilauea east–rift lava, 1968–1971. *J. Petrol.*, **16**, 110–133.

ZINDLER, A. 1980. PhD thesis, Massachusetts Institute of Technology.